

**SUPERHYDROPHOBIC AND ICEPHOBIC
SURFACE TREATMENTS FOR OVERHEAD
LINE SYSTEMS**

A thesis submitted to The University of Manchester for the degree of

Doctor of Philosophy

in the Faculty of Science and Engineering

2021

CHENGXING LIAN

School of Engineering

Department of Electrical & Electronic Engineering

TABLE OF CONTENTS

LIST OF TABLES	6
LIST OF FIGURES	9
ABSTRACT	12
DECLARATION	13
COPYRIGHT STATEMENT	14
ACKNOWLEDGEMENTS.....	15
CHAPTER 1 INTRODUCTION	16
1.1 BACKGROUND AND MOTIVATIONS.....	16
1.1.1 <i>Introduction of Overhead Lines</i>	16
1.1.2 <i>Icing Impacts on Overhead Lines</i>	18
1.1.3 <i>Major Icing Events</i>	21
1.2 RESEARCH AIMS AND OBJECTIVES.....	23
1.3 RESEARCH METHODOLOGY	24
1.4 MAIN CONTRIBUTIONS.....	25
1.5 THESIS OUTLINE	26
CHAPTER 2 LITERATURE REVIEW	28
2.1 ICE ADHESION AND PREVENTIVE SOLUTIONS	28
2.1.1 <i>Mechanism of Ice Adhesions</i>	28
2.1.2 <i>Existing Anti-icing/De-icing Solutions</i>	30
2.2 PRINCIPLES OF HYDROPHOBICITY AND ICEPHOBICITY	32
2.2.1 <i>Principles of Hydrophobicity</i>	32
2.2.2 <i>Principles of Icephobicity</i>	38
2.2.3 <i>Correlations between Superhydrophobicity and Icephobicity</i>	38
2.3 PROTECTIVE COATINGS.....	39

2.3.1	<i>Protective Coatings for Overhead Line Equipment</i>	39
2.3.2	<i>Review of Coating Preparation Methods</i>	46
2.3.3	<i>Review of Coating Characterisations and Ageing Tests</i>	47
2.4	LASER PATTERNING	51
CHAPTER 3 SURFACE TREATMENTS		53
3.1	INTRODUCTION.....	53
3.2	TEST SAMPLES AND PREPARATION METHODS.....	53
3.2.1	<i>Test Samples</i>	53
3.2.2	<i>Sample Cleaning and Preparations</i>	57
3.3	CHARACTERISATION METHODS	58
3.3.1	<i>Contact Angle Measurements</i>	58
3.3.2	<i>Surface Morphology Tests</i>	64
3.4	COATING EXPERIMENTS.....	65
3.4.1	<i>Uncoated Substrates</i>	65
3.4.2	<i>HumiSeal IC49</i>	67
3.4.3	<i>Stearic Acid</i>	69
3.4.4	<i>HCl Etching Pre-treatment</i>	70
3.4.5	<i>Stearic Acid with SiO₂ Nanoparticles</i>	74
3.4.6	<i>NeverWet</i>	84
3.4.7	<i>Comparisons of Coatings on Substrates with Different Roughness</i>	93
3.5	LASER PATTERNING	98
3.5.1	<i>Laser Patterning Sample Preparations</i>	99
3.5.2	<i>Laser Patterning Sample Characterisations</i>	100
3.6	CONCLUDING REMARKS.....	104
CHAPTER 4 AGEING TESTS		106
4.1	INTRODUCTION.....	106
4.2	EXPERIMENTAL DESCRIPTIONS	107

4.2.1	<i>Sample Preparations</i>	107
4.2.2	<i>Characterisation Methods</i>	107
4.2.3	<i>Ageing Tests</i>	108
4.3	TEST RESULTS.....	110
4.3.1	<i>Thermal Ageing & Thermal Cycling</i>	110
4.3.2	<i>Ultraviolet (UV) Exposure</i>	115
4.3.3	<i>Outdoor Environmental Exposure</i>	119
4.3.4	<i>Corona Exposure</i>	124
4.4	CONCLUDING REMARKS.....	126

CHAPTER 5 APPLICATIONS AND BENEFITS OF SURFACE

TREATMENTS..... 128

5.1	INTRODUCTION.....	128
5.2	ICEPHOBICITY PERFORMANCE OF SURFACE TREATMENTS	129
5.2.1	<i>Water Drop Freezing Tests</i>	129
5.2.2	<i>Frost Accretion Tests</i>	134
5.3	BENEFITS OF REDUCING ICE ACCRETIONS ON OVERHEAD LINES.....	138
5.3.1	<i>Impacts of Ice Accretions on Overhead Lines</i>	140
5.3.2	<i>Benefits of Applying Surface Treatments</i>	146
5.4	AUDIBLE NOISE REDUCTION ON OVERHEAD LINES	148
5.4.1	<i>Experimental Descriptions</i>	149
5.4.2	<i>Test Results</i>	151
5.5	HEAT DISSIPATION PERFORMANCE OF LASER-TEXTURED SURFACES	156
5.5.1	<i>Benefit of Increasing Heat Dissipation Rate</i>	158
5.5.2	<i>Heat Dissipation Experimental Descriptions</i>	160
5.5.3	<i>Test Results</i>	161
5.6	CONCLUDING REMARKS.....	163

CHAPTER 6 CONCLUSIONS AND FUTURE WORKS 165

6.1	CONCLUSIONS	165
6.1.1	<i>Fabrications of Surface Treatments</i>	165
6.1.2	<i>Sample Characterisations</i>	166
6.1.3	<i>Ageing Tests</i>	167
6.1.4	<i>Applications and Benefits</i>	168
6.1.5	<i>Overall Conclusions</i>	169
6.2	FUTURE WORK.....	170
	REFERENCES	172
	APPENDIX EXPERIMENTAL DATA	184

Word Count: 36048

LIST OF TABLES

<i>Table 1.1 Damage recorded for the power network systems [1].....</i>	<i>23</i>
<i>Table 2.1 Summary of prospective coatings on overhead line insulators</i>	<i>41</i>
<i>Table 2.2 Summary of prospective coatings on overhead line conductors</i>	<i>43</i>
<i>Table 2.3 Summary of different laser patterns on aluminium alloy substrates</i>	<i>51</i>
<i>Table 3.1 Statistic processing of contact angle measurements data using different computing methods and different water drop sizes.....</i>	<i>63</i>
<i>Table 3.2 Average contact angles of uncoated aluminium, silicone rubber, and EPDM rubber substrates with increasing waiting time</i>	<i>66</i>
<i>Table 3.3 Contact angle and coating thickness of HumiSeal coated substrates.....</i>	<i>68</i>
<i>Table 3.4 Contact angles of aluminium substrates after different times of etching, coated with stearic acid</i>	<i>72</i>
<i>Table 3.5 Contact angles for different thicknesses of stearic acid with SiO₂ nanoparticle coating on an etched aluminium substrate.....</i>	<i>76</i>
<i>Table 3.6 Average contact angles of uncoated aluminium substrates</i>	<i>76</i>
<i>Table 3.7 Average contact angles and sliding angles of coatings with different stirring methods and different spray times.....</i>	<i>77</i>
<i>Table 3.8 Average contact angles and sliding angles of coatings with differing flow volumes and spray times</i>	<i>79</i>
<i>Table 3.9 Average contact angles and sliding angles of coatings with different stirring methods and different spray times under high flow volume</i>	<i>80</i>
<i>Table 3.10 Average contact angles and sliding angles of coatings with different spraying distances and different spray times.....</i>	<i>81</i>
<i>Table 3.11 Average contact and sliding angles of coatings using homogeniser with different stirring speeds</i>	<i>81</i>
<i>Table 3.12 Average contact and sliding angles of coatings with different spray times.....</i>	<i>82</i>
<i>Table 3.13 Contact and sliding angle measurements of 48 stearic acid with SiO₂ coated samples using the optimised method.....</i>	<i>83</i>
<i>Table 3.14 Contact angles of NeverWet coated substrates.....</i>	<i>87</i>
<i>Table 3.15 Contact angle and sliding angle measurements of different pre-treated and coated samples ..</i>	<i>97</i>
<i>Table 3.16 Contact angles and processing times of different laser patterned samples</i>	<i>101</i>
<i>Table 4.1 Average contact angle and sliding angle measurements before and after thermal ageing and cycling</i>	<i>111</i>

<i>Table 4.2 Average contact angle and sliding angle measurements before and after the UV test.....</i>	<i>116</i>
<i>Table 4.3 Average contact angle and sliding angle measurements before and after outdoor ageing test.....</i>	<i>120</i>
<i>Table 5.1 Icing test on coated and uncoated substrates with different temperature.....</i>	<i>131</i>
<i>Table 5.2 Frost accretion test results on the uncoated and NeverWet coated samples.....</i>	<i>137</i>
<i>Table 5.3 Parameters of the AAAC Araucaria, AAAC Oak, and ACCC Madrid conductors [140] [141].....</i>	<i>139</i>
<i>Table 5.4 Changes of the ice weight and total weight of conductor lines before and after applying surface treatment.....</i>	<i>147</i>
<i>Table 5.5 Average cooling rates of both laser-textured and untreated samples.....</i>	<i>162</i>

APPENDIX TABLES

<i>Table A 1 Contact angle measurements using different computing methods and different size of water drops</i>	<i>184</i>
<i>Table A 2 Contact angle measurements of uncoated substrates.....</i>	<i>185</i>
<i>Table A 3 Contact angle measurements of HumiSeal coated substrates.....</i>	<i>188</i>
<i>Table A 4 Recovery contact angle measurements of 2 mins etched aluminium substrates at room temperature.....</i>	<i>189</i>
<i>Table A 5 Recovery contact angle measurements of 2 mins etched aluminium substrates at 55 °C.....</i>	<i>190</i>
<i>Table A 6 Recovery contact angle measurements of 4 mins etched aluminium substrates at 55 °C.....</i>	<i>191</i>
<i>Table A 7 Contact angle and sliding angle measurements of coatings with different preparing methods and spray times.....</i>	<i>192</i>
<i>Table A 8 Contact angle and sliding angle measurements of coatings with different flow volumes and spray times.....</i>	<i>193</i>
<i>Table A 9 Contact angle and sliding angle measurements of coatings with different stir methods and spray times under high flow volume</i>	<i>194</i>
<i>Table A 10 Contact angle and sliding angle measurements of coatings with different spray distance and spray times.....</i>	<i>195</i>
<i>Table A 11 Contact angle and sliding angle measurements of coatings using homogeniser with 5000 and 7000 rpm stirring speed.....</i>	<i>196</i>
<i>Table A 12 Contact angle and sliding angle measurements of coatings with different spray times.....</i>	<i>197</i>
<i>Table A 13 Contact angle and sliding angle measurements of coatings with 20s of spray times (4×5s)...</i>	<i>198</i>
<i>Table A 14 Contact angle and sliding angle measurements before and after thermal ageing and thermal cycling</i>	<i>199</i>
<i>Table A 15 Contact angle and sliding angle measurements before and after UV exposure.....</i>	<i>202</i>

Table A 16 Contact angle and sliding angle measurements of stearic acid with SiO₂ coating before and after outdoor exposure..... 204

Table A 17 Contact angle and sliding angle measurements of NeverWet coating and laser patterning before and after outdoor exposure..... 206

Table A 18 Contact angle hysteresis (CAH) measurements of laser patterning before and after outdoor exposure 213

Table A 19 Sag and %RTS of different conductors under different ice accretion thickness with or without wind load..... 217

LIST OF FIGURES

<i>Figure 1.1 Overhead lines supporting structures of (a) pole structure (b) tower structure [3].....</i>	<i>17</i>
<i>Figure 1.2 Ice accretion on overhead lines causing sagging of lines [4].....</i>	<i>18</i>
<i>Figure 1.3 Ice accretion on overhead lines causing tower collapse in 1998, Canada [5].....</i>	<i>19</i>
<i>Figure 1.4 Maximum withstand voltage of an insulator as a function of the ice thickness accreted on the insulator [9].....</i>	<i>20</i>
<i>Figure 1.5 Forces acting on the ice accreted conductor [12].....</i>	<i>21</i>
<i>Figure 1.6 A broken 132 kV overhead transmission line (left) and ice accretion on a 132 kV tower with an ice thickness of 20 to 30 cm (right) [1].....</i>	<i>22</i>
<i>Figure 1.7 Methodology of characterisation and durability experiments on different surface treatments</i>	<i>24</i>
<i>Figure 2.1 Ice adhesion hydrogen Binding in a water molecule [24].....</i>	<i>29</i>
<i>Figure 2.2 The geometric definition of static contact angle of a liquid drop on a smooth surface [39].....</i>	<i>34</i>
<i>Figure 2.3 (a) advancing angle, (b) receding angle (c) a water drop on an inclining surface [41].....</i>	<i>35</i>
<i>Figure 2.4 Demonstrations of (a) Wenzel wetting model and (b) Cassie-Baxter wetting model.....</i>	<i>36</i>
<i>Figure 2.5 Linear correlation between contact angle hysteresis and shear stress [50].....</i>	<i>39</i>
<i>Figure 2.6 Dielectric tester for conductor coatings [1].....</i>	<i>49</i>
<i>Figure 2.7 Image of the corona exposure test [1].....</i>	<i>50</i>
<i>Figure 3.1 Silicone rubber (left), EPDM rubber (middle), and aluminium (right) substrates.....</i>	<i>54</i>
<i>Figure 3.2 Image of an aluminium alloy 6082 substrate.....</i>	<i>55</i>
<i>Figure 3.3 Image of an AAAC conductor line.....</i>	<i>56</i>
<i>Figure 3.4 Image of a Gap-type conductor line.....</i>	<i>56</i>
<i>Figure 3.5 Images of the contact angle measurement equipment.....</i>	<i>59</i>
<i>Figure 3.6 Comparisons of zoomed-in and zoomed-out methods of contact angle measurements using different fittings.....</i>	<i>61</i>
<i>Figure 3.7 Comparison of enlarged images of (3) Zoomed-out manual elliptical fitting and (4) Zoomed-in manual circular fitting.....</i>	<i>62</i>
<i>Figure 3.8 Comparison of contact angles for different coated substrates with different waiting times.....</i>	<i>66</i>
<i>Figure 3.9 MEGA DC 100 Dip Coater.....</i>	<i>68</i>
<i>Figure 3.10 Comparison of water droplet images on (A) uncoated substrate and (B) stearic acid coated aluminium substrate.....</i>	<i>69</i>
<i>Figure 3.11 Comparison of microscopy images of the aluminium substrates under 2 and 4 mins of the etching times.....</i>	<i>71</i>

<i>Figure 3.12 Contact angle and contact angle hysteresis of 2 mins etched aluminium substrates being recovered at room temperature (T) and 55 °C.....</i>	<i>73</i>
<i>Figure 3.13 Contact angle and contact angle hysteresis of 2 and 4 mins etched aluminium substrates being recovered at 55 °C.....</i>	<i>73</i>
<i>Figure 3.14 Different thicknesses of stearic acid with SiO₂ nanoparticle coating on the hydrochloric acid etched aluminium substrates.....</i>	<i>75</i>
<i>Figure 3.15 Microscope images of (a) base layer only (b) base and top layers of the NeverWet coating</i>	<i>85</i>
<i>Figure 3.16 Microscopic images of NeverWet coated aluminium (Al), EPDM rubber, and silicone rubber (SR) substrates.....</i>	<i>86</i>
<i>Figure 3.17 Comparisons of contact angles of uncoated and NeverWet coated substrates</i>	<i>87</i>
<i>Figure 3.18 Experimental set-up of high-speed camera tests.....</i>	<i>88</i>
<i>Figure 3.19 Movement of a water drop on an uncoated aluminium flat sample under the high-speed camera</i>	<i>89</i>
<i>Figure 3.20 Movement of a water drop on a NeverWet coated aluminium flat sample under the high-speed camera</i>	<i>90</i>
<i>Figure 3.21 Movement of a water drop on an uncoated GAP conductor sample under the high-speed camera</i>	<i>91</i>
<i>Figure 3.22 Movement of a water drop on a NeverWet coated GAP conductor sample under the high-speed camera</i>	<i>92</i>
<i>Figure 3.23 Uncoated samples with different pre-treatments under a magnification of 10, 50, and 100 times</i>	<i>94</i>
<i>Figure 3.24 NeverWet coated samples with different pre-treatments under a magnification of 10, 50, and 100 times.....</i>	<i>95</i>
<i>Figure 3.25 Stearic acid with SiO₂ nanoparticle coated samples with different pre-treatments under a magnification factor of 10, 50, and 100 times.....</i>	<i>96</i>
<i>Figure 3.26 Laser patterning test substrates</i>	<i>99</i>
<i>Figure 3.27 3D images of micro-channel laser patterns with different parameters.....</i>	<i>102</i>
<i>Figure 3.28 3D images of micro-pillar laser patterns with different parameters.....</i>	<i>103</i>
<i>Figure 4.1 (A) outdoor exposure sample holder (B) corona exposure set-up.....</i>	<i>110</i>
<i>Figure 4.2 Microscope images of surface treatments before and after thermal ageing and cycling: (A) stearic acid with SiO₂ before ageing, (B) stearic acid with SiO₂ after ageing, (C) NeverWet before ageing, (D) NeverWet after ageing, (E) laser patterning before ageing, and (F) laser patterning after ageing.</i>	<i>112</i>
<i>Figure 4.3 Changes to (A) contact angles and (B) sliding angles before and after thermal ageing and cycling</i>	<i>114</i>
<i>Figure 4.4 Changes to (A) contact angles and (B) sliding angles before and after UV exposure.....</i>	<i>117</i>

<i>Figure 4.5 Microscope images of different surface treatments before and after UV exposure: (A) stearic acid SiO₂ before ageing, (B) stearic acid SiO₂ after ageing, (C) NeverWet before ageing, (D) NeverWet after ageing, (E) laser patterning before ageing, and (F) laser patterning after ageing.....</i>	<i>118</i>
<i>Figure 4.6 Changes to (A) contact angles and (B) sliding angles & contact angle hysteresis before and after outdoor environmental exposure.....</i>	<i>121</i>
<i>Figure 4.7 Microscope images of different surface treatments before and after outdoor environmental ageing: (A) stearic acid SiO₂ before ageing, (B) stearic acid SiO₂ after ageing, (C) NeverWet before ageing, (D) NeverWet after ageing, (E) laser patterning before ageing, and (F) laser patterning after ageing... </i>	<i>123</i>
<i>Figure 4.8 Microscopy images of different surface treatments before and after corona exposure: (A) stearic acid SiO₂ before ageing, (B) stearic acid SiO₂ after ageing, (C) NeverWet before ageing, (D) NeverWet after ageing, (E) laser patterning before ageing, and (F) laser patterning after ageing.....</i>	<i>125</i>
<i>Figure 5.1 Images of Thermotron climate chamber</i>	<i>130</i>
<i>Figure 5.2 Images of uncoated and NeverWet coated substrates after -10 and -20 °C ice accretion tests</i>	<i>132</i>
<i>Figure 5.3 Ice accretion on the NeverWet coated EPDM rubber after freeze and thaw tests.....</i>	<i>133</i>
<i>Figure 5.4 An example of coating damage during the icing test.....</i>	<i>133</i>
<i>Figure 5.5 Microscope images of the damaged area after (a) the 1st freeze/thaw cycle and (b) the 7th freeze/thaw cycle.....</i>	<i>134</i>
<i>Figure 5.6 Temperature changing curves for the sample pre-cooling procedure under -15 °C in the Kasco chamber (3-hour vs. 12-hour of pre-cooling).....</i>	<i>136</i>
<i>Figure 5.7 Changes of conductor sag with increasing ice accretion thickness on (a) AAAC Araucaria conductor, (b)AAAC Oak conductor, and (c) ACCC Madrid conductor with and without wind load</i>	<i>143</i>
<i>Figure 5.8 Changes of %RTS with increasing ice accretion thickness on conductors under conditions of (a) ice accretion only and (b) ice with wind load</i>	<i>145</i>
<i>Figure 5.9 Images of the anechoic chamber</i>	<i>150</i>
<i>Figure 5.10 The experimental set-up diagram of audible noise tests.....</i>	<i>151</i>
<i>Figure 5.11 The Image of the earthed cage set-up inside the chamber.....</i>	<i>151</i>
<i>Figure 5.12 Noise levels at 100 Hz with different levels of electric field on coated and uncoated GAP (left) and ACSR (right) conductors during the light rain condition</i>	<i>152</i>
<i>Figure 5.13 Noise levels at 100 Hz with different levels of electric field on coated and uncoated GAP (left) and ACSR (right) conductors during the heavy rain condition.....</i>	<i>152</i>
<i>Figure 5.14 Images of water drops accretion on the coated and uncoated GAP conductors with and without the electric field of 21 kV/cm.....</i>	<i>154</i>
<i>Figure 5.15 Images of water drop accretion on the coated and uncoated ACSR conductors with and without an electric field of 21 kV/cm.....</i>	<i>155</i>
<i>Figure 5.16 Experimental equipment set-up of heat dissipation tests.....</i>	<i>160</i>

ABSTRACT

Accumulation of ice or snow on overhead lines can significantly threaten the stability and safety of power systems as a result of the extra weight. This can result in severe damage or the collapse of towers. Surface treatments that claim to be superhydrophobic or icephobic have been attracting a great deal of attention for their anti-icing, self-cleaning, noise-reducing, and anti-corrosion properties. If these surface treatments can be applied to overhead lines in a manner that reduces or delays ice accretion, significant improvements in the stability and durability of existing overhead lines can be achieved. New overhead line designs can also benefit from these surface treatments by reducing clearance requirements to allow lower-cost systems to be built.

This research, inspired by the CIGRE TB 631, assesses the viability of the deployment of superhydrophobic surface treatments onto overhead line systems. The wettability performance of superhydrophobic surface treatments was characterised by contact angle measurements. A manual zoomed-in computing method was developed to improve the accuracy of these contact angle measurements. Water drop behaviour on superhydrophobic surfaces was examined under a high-speed camera. The fabrication & application method of various surface treatments were optimised using different parameters to achieve optimal performance with high reproducibility and feasibility. Overall, high levels of superhydrophobicity with low surface hysteresis were achieved on substrates by deploying different protective coatings and laser patterns.

Taking into account the need to examine ageing behaviours of surface treatments before deployment, a range of ageing tests were designed and conducted, including thermal ageing/cycling, ultraviolet exposure, corona exposure, and outdoor environmental exposure. The laser patterning technique was proven to be more robust and durable than the protective coatings used in this research. Each laser patterned sample retained a high level of superhydrophobicity after most of the ageing tests, while different levels of degradation were observed on the samples with protective coatings. In addition, the benefits and applications of surface treatments on overhead line systems were discussed, including anti-icing, anti-frosting, audible noise reduction, and heat dissipation improvement.

DECLARATION

I declare that no portion of the work referred to in the thesis has been submitted in support of an application for another degree or qualification of this or any other university or other institute of learning.

COPYRIGHT STATEMENT

- I. The author of this thesis (including any appendices and/or schedules to this thesis) owns certain copyright or related rights in it (the “Copyright”) and s/he has given The University of Manchester certain rights to use such Copyright, including for administrative purposes.
- II. Copies of this thesis, either in full or in extracts and whether in hard or electronic copy, may be made only in accordance with the Copyright, Designs and Patents Act 1988 (as amended) and regulations issued under it or, where appropriate, in accordance with licensing agreements which the University has from time to time. This page must form part of any such copies made.
- III. The ownership of certain Copyright, patents, designs, trademarks and other intellectual property (the “Intellectual Property”) and any reproductions of copyright works in the thesis, for example graphs and tables (“Reproductions”), which may be described in this thesis, may not be owned by the author and may be owned by third parties. Such Intellectual Property and Reproductions cannot and must not be made available for use without the prior written permission of the owner(s) of the relevant Intellectual Property and/or Reproductions.
- IV. Further information on the conditions under which disclosure, publication and commercialisation of this thesis, the Copyright and any Intellectual Property and/or Reproductions described in it may take place is available in the University IP Policy (see <http://documents.manchester.ac.uk/DocuInfo.aspx?DocID=24420>), in any relevant Thesis restriction declarations deposited in the University Library, The University Library’s regulations (see <http://www.library.manchester.ac.uk/about/regulations/>) and in The University’s policy on Presentation of Theses

ACKNOWLEDGEMENTS

A special thanks to my parents Wei Lian and Jian Wang for raising me and giving me the opportunity to study in the UK. I am forever indebted to them for all their love and support. I would also like to thank the rest of my family and all my dear friends. Matt Alexander, Ziyue Guo & Rongrong Wang whose boundless energy to lift my spirits are second to none. Xiaohan Li, Zong Wen Yan, Xu Hang & Shuyang Shen, whose wonderful support was invaluable to me. Qinghua Han, Yue Wang, and Zihan Gao for being such a fantastic shoulder to lean on & supportive whenever I needed them.

I would like to thank Christopher Emersic, Robert Lowndes, Xu Zhang, and Wenyuan Li for their brilliant support during the course of the work presented in this thesis, and for the long-lasting friendship we've formed. Without their help, this research wouldn't have been possible or anywhere near as enjoyable!

Most importantly, I would like to thank my supervisor Ian Cotton for his invaluable guidance and patient support during this PhD. He inspired me not only in my work but also to follow in his footsteps as a researcher with his unwavering attention to detail & thoughtful approach. Through his kind nature & illustrious sense of humour, he was also largely responsible for ensuring the mental health of students such as myself!

CHAPTER 1 INTRODUCTION

1.1 Background and Motivations

In icing weather, accumulation of snow, ice, or pollution on overhead line transmission and distribution infrastructure can lead to severe damage or failure of power systems due to excessive weight that leads to sagging and galloping of the lines. In particular, icing weather can be critical to overhead line insulators and conductors where flashover and additional mechanical loads can cause serious system failures or even the collapse of entire overhead line towers. A family of protective coatings and surface treatments were introduced in the CIGRE TB 631 [1] that claim to be superhydrophobic or icephobic. These coatings can be applied to overhead lines to potentially reduce ice accretions and flashovers during icing events. The coatings and surface treatments with reasonable longevities aim to optimise the stability and increase the performance of power network systems. With increased electrical demands, more overhead lines are being constructed. If ice accretions can be minimised on overhead lines, new overhead lines could also benefit from new mechanical designs that allow lower clearance distances with lower construction costs.

In this section, the background of overhead lines, icing impacts on power network systems, and the influence of major icing events are reviewed to build a better understanding of research motivations and the importance of finding solutions to minimise these impacts.

1.1.1 Introduction of Overhead Lines

Climate change has become such an important issue worldwide that governments have been devoted to decreasing carbon emissions for the past decade. The usage of fuels, such as oil, gas, and coal, are to be reduced. Renewable energies such as solar or wind will displace conventional fuels, and the use of electric vehicles and heating will increase demands in electricity. As such, the general increasing demand for electrification requires more electrical infrastructure to be built, including overhead transmission and distribution lines. If the design of overhead lines can be optimised in a way that increases the reliability of the

system while minimising the mechanical load and the overall tower height, it will enable a significantly lower cost on the construction of power system infrastructure.

As a vital part of power systems, overhead transmission and distribution lines provide the benefit of much lower cost compared to buried cables. The estimated installation capital cost of 132 kV overhead lines is £150,000 per km, while 132 kV underground cables cost £986,000 per km [2]. In general, overhead transmission lines have voltages of 66 kV and above for long-distance transmissions, while voltages ranging from 11 kV to 66 kV are usually used for short-distance distributions.

Poles and towers as shown in Figure 1.1 (a) and (b), are the two main supporting structures in overhead line systems to support conductor lines, insulators, and other auxiliary facilities. Wooden or concrete supporting poles are efficient and commonly used for residential supply at low voltage levels, such as 415 V, 11 kV, and 33 kV. For a higher voltage level from 66 V to 132 kV, lattice steel towers are used to support overhead lines.

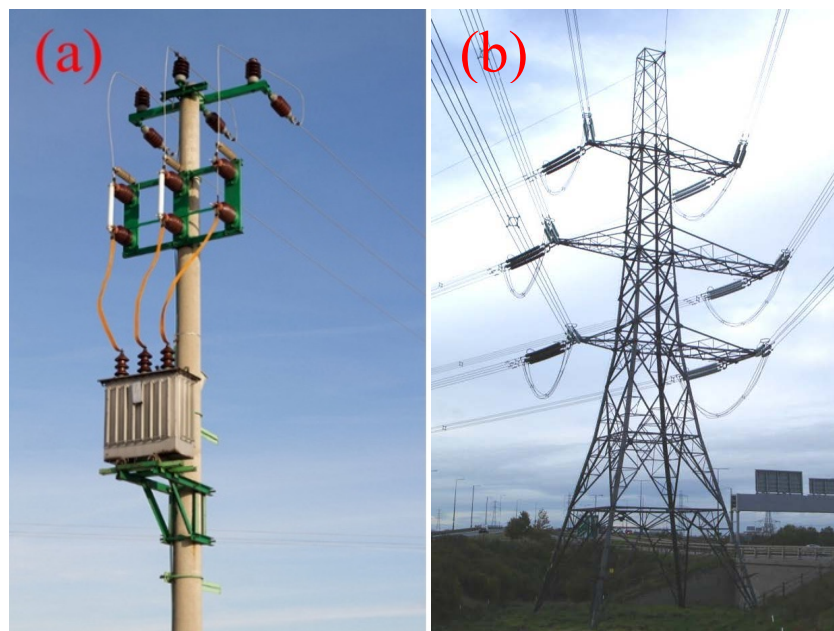


Figure 1.1 Overhead lines supporting structures of (a) pole structure (b) tower structure [3]

Recent improvements in aluminium alloy compositions aim to reduce electrical resistance while maintaining the desirable properties of increased strength and resistance to corrosion.

Traditional steel-centred conductors are gradually replaced by the modern designs using various forms of all aluminium alloy conductors (AAAC), aluminium conductor alloy reinforced (ACAR), or aluminium alloy stranded conductors (AASC). These alloys often contain silicon or magnesium to double the breaking or ultimate tensile strength compared to pure aluminium, while providing a lower resistance when compared with an aluminium conductor steel-reinforced conductor (ACSR). The resistance towards chemicals or saline corrossions of aluminium alloy is also significantly improved over pure aluminium [3].

1.1.2 Icing Impacts on Overhead Lines

In general, icing on overhead lines can cause a range of problems such as sagging of lines and reduced clearance, as shown in Figure 1.2 [4]. Icicles can not only short-circuit the lines from different phases but also add extra weight and lead to tower collapse, as shown in Figure 1.3 [5]. Ice thawing can also cause short-circuits, line galloping, and flashovers. These problems severely threaten the safe operation of overhead line insulators and conductors.

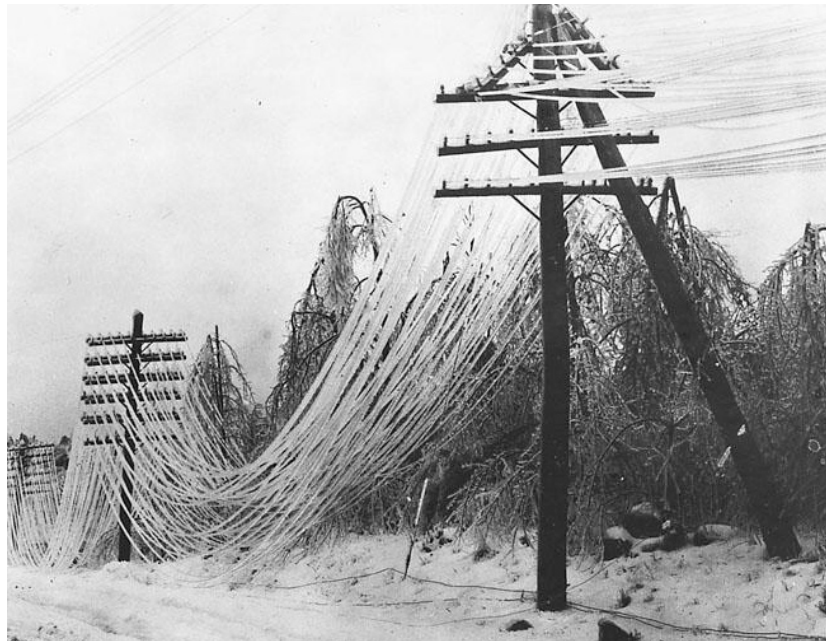


Figure 1.2 Ice accretion on overhead lines causing sagging of lines [4]

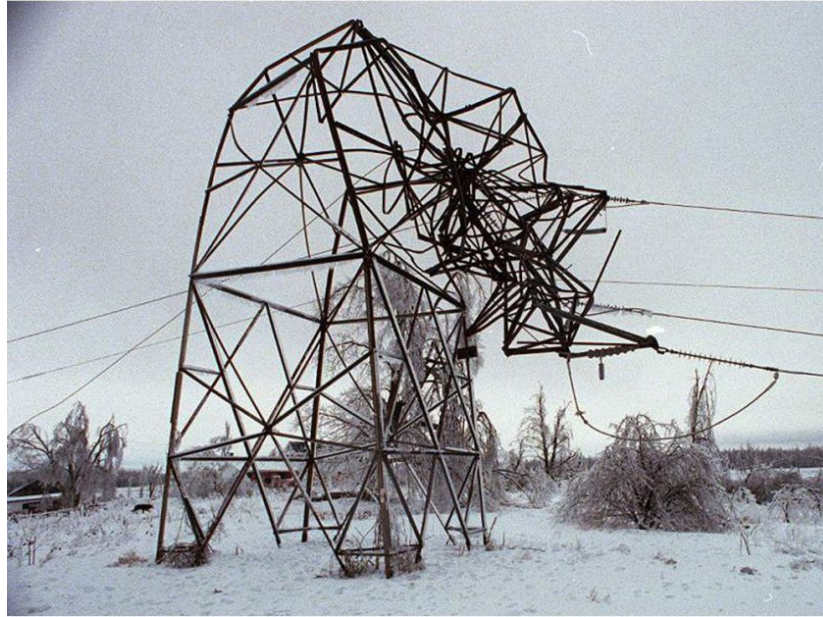


Figure 1.3 Ice accretion on overhead lines causing tower collapse in 1998, Canada

[5]

- **Icing Impacts on Insulators**

For overhead line insulators, the accretions of rime, glazed ice, or frost on high voltage energised insulators can reduce the breakdown strength and lead to flashovers across the energised surfaces. Rime ice occurs when liquid droplets in the air freeze onto a surface and grow into combs, needles, or feathery forms. Glaze ice results from falling rain that freezes on contact with a cold surface and forms clear and uniform coatings. Supercooled water droplets can remain in a liquid state even when the temperature is below 0 °C until they contact with any solid surface and start ice nucleation [6].

Phan's study on minimum flashover voltages indicates that the most severe hard rime ice can be formed on insulators under the temperature of -12 °C with a volumetric ice density of 0.87 g/cm³. Compared with wet accretions, hard rimes formed on insulators can lead to a higher likelihood of flashover occurring with only 40% of the minimum flashover voltage required [7]. Different rime ice densities were tested in Khalifa's study on insulator flashover performances, which indicated the leakage current could increase by approximately 100% when ice density increased from 0.32 to 0.8 g/cm³ [8]. The

relation between the thickness of ice accretions on insulators and maximum withstand voltage was tested in Farzaneh's study as shown in Figure 1.4, in which the maximum withstand voltage dropped as ice thickness increases, until ice thickness is beyond 3 cm and then the insulator lost its function [9].

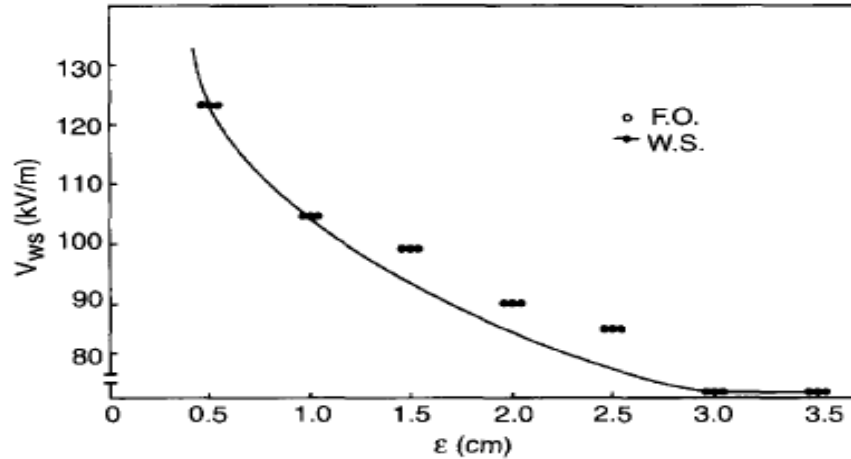


Figure 1.4 Maximum withstand voltage of an insulator as a function of the ice thickness accreted on the insulator [9]

- **Icing Impacts on Conductors & Towers**

Ice or snow accretions on overhead lines can result in a dramatic increment of mechanical loads. The largest load of ice accretion recorded was 305 kg/m on a 22 kV overhead line in Norway 1961 [10]. When ice or snow accretions exceed the weight-bearing limit of an overhead line tower, the whole system may collapse and lead to area power loss and further economic losses.

Increased conductor mass due to ice accretion can also lead to changes in sag and violation of conductor-ground clearance. Extra mechanical load due to ice accretion on the conductor line can increase conductor tension. This leads to the expansion of conductor length in order to release the additional tension and results in sag increasing. Therefore, the increase in sag may infringe on the clearance distance of the conductor to the ground. With the interaction of wind and increased surface area due to ice accretion, higher combined loads can be imposed on conductor lines. Wind forces with ice loads

can also lead to the occurrence of conductor galloping and air gap breakdown due to asymmetric conductor aerodynamics [11]. Conductor galloping is a low frequency (0.1-1 Hz), high amplitude (up to 12 m), and vertical oscillation that appears on single or bundle conductors. The correlation of wind force, iced conductor mass, and ice thickness is shown in Figure 1.5 [12], where the amplitude of the galloping motion increases with the increase of the wind speed, the correlated wind forces, or the ice accretion thickness. If the operating clearance is infringed, the significant amplitude of conductor oscillation can also lead to flashover [13].

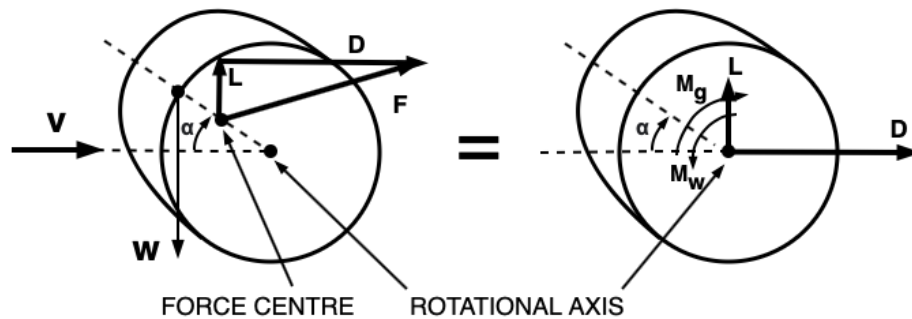


Figure 1.5 Forces acting on the ice accreted conductor [12]

1.1.3 Major Icing Events

Icing events occasionally happen in many different continents including Europe, Asia, and America. These events affect numerous countries by causing power outages and tower collapses, resulting in severe socio-economic losses.

- **Icing Events in the UK**

In 1990, a wet snow event in the UK caused one of the most severe disruptions on power systems. Over 1 million people were cut off from power for up to 9 days. In the midlands and northern areas of the UK, more than 8000 incidents were reported, in which 800 failures on 275 and 400 kV lines and thousands of wooden poles broke due to severe sagging and galloping as a result of ice accretion thickness up to 62 mm [1][14].

- **Icing Events in Europe**

In 1999, the contaminated ice accretions on overhead lines led to 130 - 400 kV power network outages in Sweden for up to 6 h with the average temperature down to $-12.1\text{ }^{\circ}\text{C}$, which was extremely rare in Sweden [15].

In 2012, heavy wet snow in Iceland broke many 66 and 132 kV overhead lines with an ice mass of around 14.5 kg/m and ice thickness of around 20 to 30 cm, as shown in Figure 1.6 [1].



Figure 1.6 A broken 132 kV overhead transmission line (left) and ice accretion on a 132 kV tower with an ice thickness of 20 to 30 cm (right) [1]

- **Icing Events in Asia**

In 2008, China experienced one of the most severe icing events of the past half-century which resulted in a large area power outage for up to two weeks and more than 3.5 billion dollars in direct economic losses. It was reported that 36,740 overhead lines, 2018 transformers, and 8381 power network towers ranging from 110 to 500 kV lost their functions or collapsed [16].

In 2005 in Japan, a total duration of 31 h of power outage affected more than 650,000 households. This was due to the salt contaminated wet snow causing short circuit faults and line galloping [17].

▪ Icing Events in North America and Canada

In 1998, an unprecedented ice storm attacked North America and eastern Canada, which accumulated 110 mm of ice after 80 h of freezing rain. During this ice storm, more than 1.4 million people suffered power outages for up to 4 weeks. Thousands of power network lines and towers were destroyed or damaged, as shown in Table 1.1, which resulted in 6.4 billion dollars of estimated losses [1][18].

Table 1.1 Damage recorded for the power network systems [1]

Voltage level/kV	Total lines	Broken and/or collapsed towers
735	10	149
315	12	58
230	13	306
120	67	1091 (steel and wooden poles)
49	14	1500 (wooden poles)
Total	116	3104

1.2 Research Aims and Objectives

This research aimed to investigate the performance and benefits of a variety of superhydrophobic surface treatments and to examine the long-term durability of those surface treatments before being deployed on overhead lines, as described in the CIGRE TB 631 [1].

Following objectives were specified to support these aims:

- To identify methods of examining the superhydrophobic performance of surface treatments, such as using contact angle measurements, high-speed camera examinations, and surface microscopy to examine the surface geometries and the water drop movements on test samples.
- To optimise the performance of existing superhydrophobic coatings by examining different surface roughness and exploring different experimental factors to achieve a better superhydrophobicity and reproducibility of the coatings.

- To fabricate and examine different laser patterns on aluminium substrates to identify the optimal pattern with the balance of good superhydrophobic performance and short manufacturing time.
- To establish a series of ageing tests for examining the durability of the different surface treatments, including thermal ageing, thermal cycling, corona exposure, ultraviolet exposure, and outdoor environmental exposure.
- To discuss the applications and benefits of superhydrophobic surface treatments on overhead line systems, including anti-icing performance, the benefits of reducing ice accretion, audible noise reduction, and heat dissipation performance on overhead lines.

1.3 Research Methodology

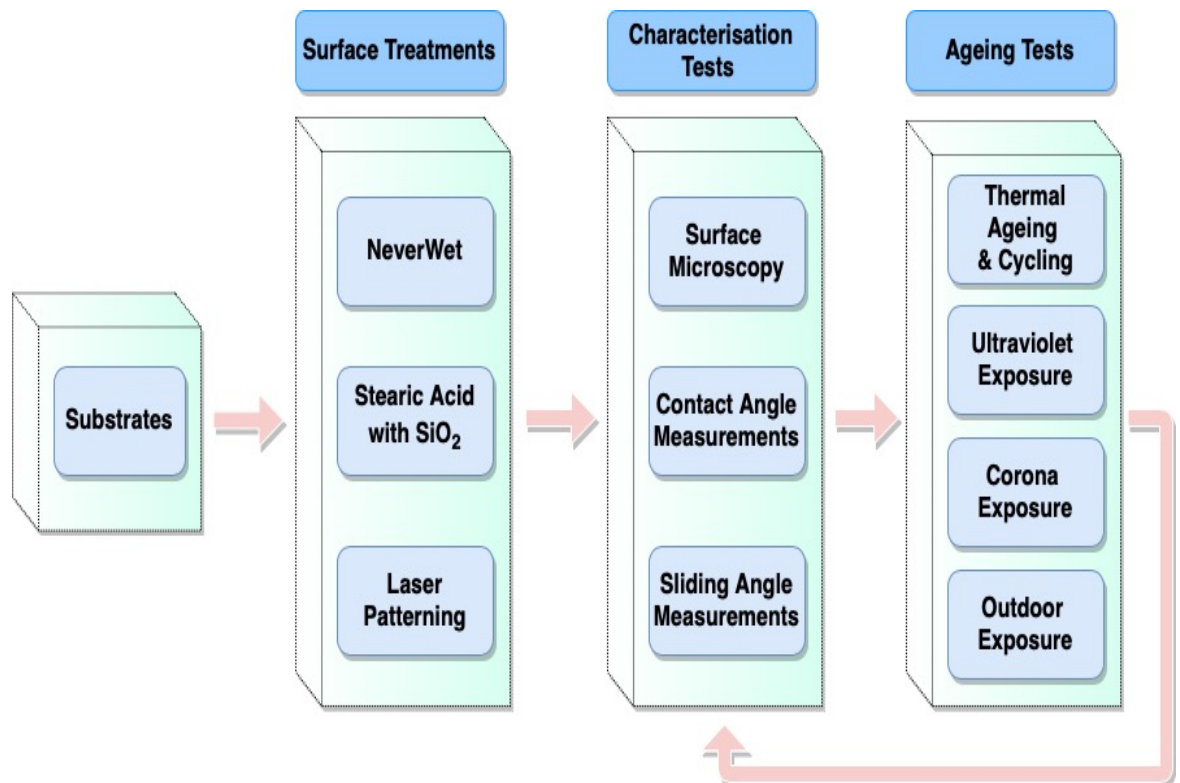


Figure 1.7 Methodology of characterisation and durability experiments on different surface treatments

In this research, different surface treatments were examined using different techniques, covering the performances and longevities of the surface treatments under different situations. The flow chart in Figure 1.7 demonstrates the research methodology and the main experiments of characterisations and durability tests on the different surface treatments. This includes the lists of the different surface treatments, wettability characterisation tests, and durability tests to evaluate the potential water/ice repellent performance and the operating lifespans of the surface treatments on overhead lines.

1.4 Main Contributions

The main contributions of this research are summarised as below:

- A number of superhydrophobic surface treatments were trialled on pieces of aluminium alloy representative of overhead line conductors and on sections of circular conductor. The techniques used included depositing a range of coatings and surface texturing using laser patterning. The fabrication methods were optimised to achieve good superhydrophobicity and reproducibility.
- An improved zoomed-in method of contact angle measurement was developed to increase the resolution used for computing contact angles with a low standard deviation – this ensured subsequent tests could accurately quantify the contact angle measurement.
- No obvious standards were found for examining the durability of surface treatments. As understanding the long-term ageing performance of the coating would be essential in this application, a series of ageing tests were designed to quantify whether these surface treatments would be durable given the different environmental stresses experienced by overhead lines.
- An assessment of the potential applications and benefits of superhydrophobic surface treatments was made including an evaluation of the level of ice and frost accretion,

along with the potential benefits in terms of audible noise reduction and heat dissipation improvements on overhead lines.

1.5 Thesis Outline

This thesis is organised into six chapters:

Chapter 1: Introduction

This chapter introduces the overall research background and motivations of deploying superhydrophobic surface treatments, and presents their potential applications and benefits on overhead line systems. Aims, objectives, and research methodology are also identified.

Chapter 2: Literature Review

This chapter discusses the principles and correlations of hydrophobicity and icephobicity. Ice adhesions on overhead lines, preventative solutions, and protective surface treatments are reviewed.

Chapter 3: Surface Treatments

This chapter introduces test substrates, sample pre-treatments, and different surface treatments. An improved zoomed-in method of contact angle measurement was examined. Different methods were tested to optimise the performance and reproducibility of coatings. Different laser patterned samples with different parameters were fabricated. The performance of the superhydrophobic coatings and the laser patterned samples were characterised.

Chapter 4: Ageing Tests

This chapter introduces a family of ageing tests to examine and compare the durability of different surface treatments under different ageing situations.

Chapter 5: Applications and Benefits of Surface Treatments

This chapter discusses different applications and benefits of superhydrophobic surface treatments, including anti-icing performance, audible noise reduction, and heat dissipation performance. Impacts of icing and potential benefits of using superhydrophobic surface treatments on overhead lines are discussed.

Chapter 6: Conclusions and Further Work

This chapter summarises the main findings and conclusions of the research work presented in this thesis. Some potential opportunities and further work are identified.

CHAPTER 2 LITERATURE REVIEW

In this chapter, the mechanisms of ice adhesion and existing anti-icing / de-icing methods are reviewed for a better understanding to aid in the development of preventive solutions against ice accretions on power network systems. Two crucial principles of hydrophobicity and icephobicity are demonstrated for examining characterisations of water and ice repellent abilities of surfaces. Correlations between hydrophobicity and icephobicity are briefly discussed. Summaries of protective coatings on overhead line insulators and conductors are given. A summary of previous experiments with different protective coatings on conductors and insulators is presented, as well as test methods on coating preparations, characterisation tests, and durability tests. Laser patterning techniques are discussed, and different types of laser patterns from previous studies are also reviewed.

2.1 Ice Adhesion and Preventive Solutions

2.1.1 Mechanism of Ice Adhesions

The mechanism of ice adhesion on surfaces is due to the bonding of different forces and factors including hydrogen bonding, electrostatic forces, Van der Waals forces, and mechanical interlocking [19][20][21].

- **Hydrogen Bonding**

Hydrogen bonding is defined as an attractive interaction between a hydrogen atom and another atom or atoms, between one or more molecules [22]. Hydrogen bonding occurs during the intermolecular or intramolecular binding process of a hydrogen atom from the ice with electronegative atoms from the interface, such as an electronegative oxygen atom [23]. During ice adhesion, intermolecular bonding happens between oxygen atoms from the interface and hydrogen atoms in the ice to form a bridge between them, as shown in Figure 2.1 [24].

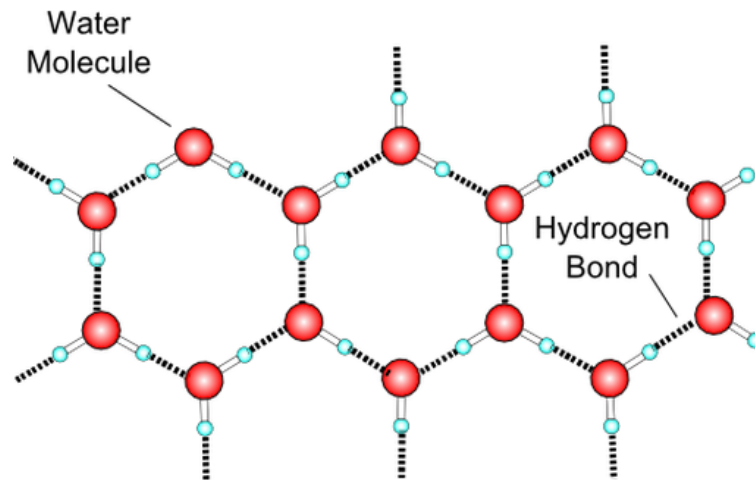


Figure 2.1 Ice adhesion hydrogen Binding in a water molecule [24]

- **Electrostatic Force**

The electrostatic force is one of the strongest interactions that attracts both charges from the ice and the solid substrate interface [25]. A Bjerrum defect is a crystallographic defect of ice, which results in the electrical polarisation of the ice [26]. Because of Bjerrum defects, protonic defects appear on the surface and produce an electrical field which could firmly strengthen the ice bonding on surfaces [19]. Decreasing the electrostatic force can significantly reduce the adhesion of ice by redistributing charges in the substrates and using low dielectric constant substrates [20][27].

- **Van Der Waals Forces**

Van der Waals forces are the interactive forces between two electrical charges from different portions of different molecules, of which the strength is significantly dependant on the distance between two charges [28]. In the ice adhesion process, Van der Waals forces are relatively small compared to the other types of binding forces such as hydrogen bonding [21][29].

- **Mechanical Interlocking**

It is known that water has a larger expansion coefficient than metal substrates. As a result of this expansion and the roughness on metal surfaces, mechanical interlocking occurs

when water infuses into the surface structure gaps and becomes solidified. This results in a firm interlocking between the ice and the surface [19].

2.1.2 Existing Anti-icing/De-icing Solutions

Various strategies have been deployed in the past decades to reduce the probability of failure of power network equipment as a result of ice accretions. A number of techniques have been proposed by others to prevent ice accretion or to actively de-ice overhead lines once ice has accumulated. In this section, four categories of different anti-icing and de-icing methods are discussed. All of these methods are described in CIGRE TB 631 [1].

- **Passive Methods**

Passive methods of anti-icing use natural forces such as wind, gravity, and solar radiation to eliminate ice accretions on energised or non-energised surfaces [19]. Different methodologies are used against icing on surfaces such as (a) reducing the ice bonding forces, (b) preventing water drops from freezing on surfaces, (c) using specific devices to minimise the influence of ice loadings on overhead line systems, and (d) relying on natural energy sources such as wind, solar energy, or gravity to eliminate ice accretion on overhead lines [1]. Superhydrophobic or icephobic coatings and other surface treatments are passive methods that offer the benefits of low-cost, easy-maintenance, and high-efficiency performance. Passive methods that rely on natural forces are likely limited by irregularity of the weather required.

- **Active Coatings**

Energised active coatings can be used to efficiently heat up and melt the ice loads on the substrates. Active coatings can utilise energy loss from the energised conductors and transform this energy onto the surfaces to maintain the temperature above freezing point. However, a much higher frequency of 60,000 Hz is required for this method rather than the traditional 50 or 60 Hz. This could cause some electromagnetic disturbances and other issues to the power system [1]. Also, it will always be a challenge seeking to make

a connection to a heating system onto overhead line conductors operating at voltages in the range of some tens of kilovolts to hundreds of kilovolts.

- **Mechanical Methods**

Mechanical methods have been widely used as de-icing solutions to remove ice loads on overhead lines. Two common methodologies have been used: (a) external forces mechanically shed the ice loads, and (b) forces from shock waves and line vibrations or twisting eliminate the ice loads [30]. Mechanical methods require much less energy than thermal methods to remove ice and are easier to carry out. As such, a mechanical technique is highly recommended as a time-saving and quick intervention on a section of overhead line. Nevertheless, mechanical methods often lack accuracy in practice and may lead to damage to the conductors / structure and are particularly risky when overhead lines are equipped with expensive optical fibres [1]. It is also impractical in extreme weather due to the risk of requiring manual operations on tall and energised lines.

- **Thermal Methods**

Thermal methods require an external source of energy as de-icing or anti-icing tools to accelerate the melting of ice and to prevent supercooled water from freezing on substrates. Anti-icing solutions consume less energy than de-icing solutions. Two types of thermal methods are usually considered to limit ice adhesion and accretion on power network systems: (a) methods using the Joule effect; (b) methods using dielectric wastage, radiative waves, and external energy sources [1][19]. The Joule effect is most likely applicable to overhead line conductors.

Considering the advantages and disadvantages of different anti-icing methods, the passive method of superhydrophobic surface treatments was the primary focus of the work presented in this thesis. Passive methods that prevent the icing of conductors are, in principle, applicable to both new and old overhead lines and are low in complexity with a good cost-benefit.

Active coatings can only function on energised conductors or require external power sources that are complex to install given the operating voltage of the power system. Active coatings may require the use of higher frequencies that could cause disturbance to the power system. Mechanical methods require manual operation that usually lacks accuracy and are generally only used on a short section of lines. Thermal methods usually lack efficiency and require a significant amount of power as anti-icing methods on long overhead lines.

In comparison, passive methods do not require an external power source and can function on both energised and non-energised conductors. A passive coating would therefore be preferable on overhead lines subject to the longevity of the coating being reasonable or the feasibility of reapplying the coating at regular intervals without circuit outage. The lifespan of overhead line conductors are usually shorter than towers, and as such, conductors are usually replaced regularly. If a passive surface coating does not show a longevity commensurate with the timescale, there would be regular opportunity to re-treat the surface with passive coatings while carrying out this maintenance or upgrade.

2.2 Principles of Hydrophobicity and Icephobicity

2.2.1 Principles of Hydrophobicity

Water can sometimes spread out and stick to a surface, while on other occasions water can split into smaller drops and slide off the surface. Cohesive forces within a water drop and adhesive forces between water drops and the contacted surfaces contribute to surface wettability. The ability of a surface to repel water is known as hydrophobicity. On the contrary, the ability of a highly wettable material that allows water to spread out in a larger contact area is called hydrophilicity. Static and dynamic contact angles are used to quantify the degree of surface hydrophobicity or hydrophilicity. Whether a surface is hydrophobic or hydrophilic is determined by two significant parameters: surface energy and surface roughness.

2.2.1.1 Surface Energy

Surface energy is defined as the energy required to form a surface from substances. This type of energy relates to the intermolecular bonds or forces in the substance molecules that form the surface [31]. In Bharathidasan's study, rough superhydrophobic coatings were shown to have different levels of ice adhesion strength which indicate surface energy is more relevant than surface roughness of the coatings [32]. Materials with higher surface energy are more wettable and tend to be more hydrophilic, such as metals, ceramics, and glasses. Materials such as polymers that have less surface energy tend to be more hydrophobic [33]. New overhead line conductors are usually hydrophobic, but they may become more hydrophilic as they age. Thus, superhydrophobic coatings using low surface energy materials could be deployed on overhead lines to increase the surface hydrophobicity.

2.2.1.2 Surface Roughness

The hydrophobicity of a surface can be increased by modifying the surface roughness. It was discovered by Bikerman that the surface roughness might affect the repellence of water drops from the surface [34]. Johnson and Dettre furthered this discovery by concluding that low surface roughness can increase contact angle hysteresis, while higher roughness with nano/micro composite surfaces could reduce hysteresis by preventing water from penetrating the rough surface [35]. Different surface treatments have been used, such as chemical etching, sandblasting, and laser patterning, to increase surface roughness to a certain degree that produces better water or ice repellent abilities [36][37][38].

2.2.1.3 Static and Dynamic Contact Angles

- **Static Contact Angle**

The static contact angle is defined as the angle between the liquid-vapour interface and the solid surface. This is calculated mathematically by recognising a tangent line from triple-points of the three mediums as shown in Figure 2.2. From left to right, each drop shows a contact angle Θ between Y_{lv} and Y_{sl} being below 90° , equal to 90° , and above

90°. The contact angle of 90° has been used as a critical angle. A surface that has a contact angle of less than 90° is called a hydrophilic surface, while a surface has the contact angle higher than 90° is defined as a hydrophobic surface. Moreover, superhydrophobicity is indicated when the contact angle of a surface is larger than 150° [39].

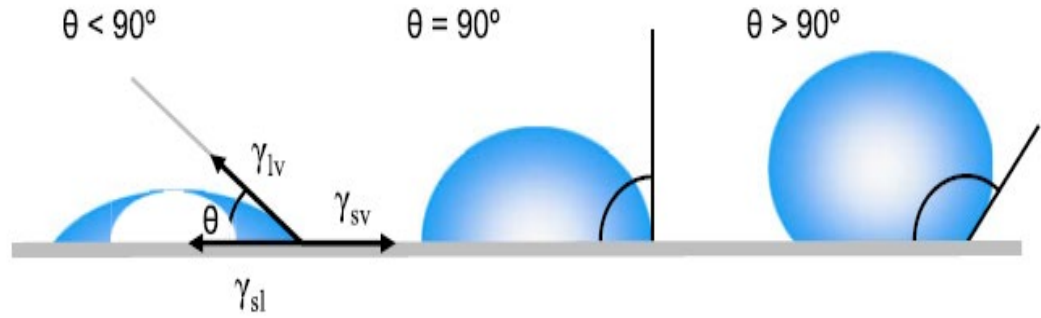


Figure 2.2 The geometric definition of static contact angle of a liquid drop on a smooth surface [39]

Young's equation [40] is the first description of contact angle of a liquid drop on a solid interface with the mechanism of the three interfacial tensions, as in the equation (1) shown below:

$$\gamma_{lv} \cos \theta_Y = \gamma_{sv} - \gamma_{sl} \quad (1)$$

Where γ_{lv} is the liquid-vapour interfacial tension, γ_{sv} is the solid-vapour interfacial tension, γ_{sl} is the solid-liquid interfacial tension, and θ_Y is Young's contact angle [40].

- **Dynamic Contact Angle**

The dynamic contact angle can be used to characterise the icephobicity and dynamic wetting behaviours of a solid surface. According to Figure 2.3, the advancing contact angle θ_A and the receding contact angle θ_R can be defined as the maximum steady angle and the minimum steady angle for a liquid drop to fling off a surface by a driving force such as gravity [41][42]. The definition of contact angle hysteresis is shown as equation (2) below:

$$\text{CAH} = \theta_A - \theta_R \quad (2)$$

Where contact angle hysteresis (CAH) is the difference between the maximum advancing angle θ_A and the minimum receding angle θ_R .

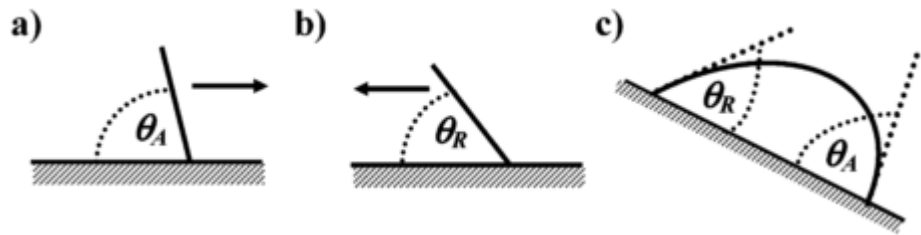


Figure 2.3 (a) advancing angle, (b) receding angle (c) a water drop on an inclining surface [41]

Johnson suggested that contact angle hysteresis is used as a guideline for the sliding ability of a surface [35]. To further explore the sliding ability of a liquid drop on a solid surface, the sliding angle was introduced as the incline angle of the surface required for liquid drops to slide off. Furmidge equation (3) demonstrates the correlation between the sliding angle, gravity force of the liquid drop, and the surface tension of the solid interface:

$$\sigma \cdot L \cdot (\cos\theta_R - \cos\theta_A) = mg \cdot \sin\alpha \quad (3)$$

The left-hand side of the equation stands for the capillary force in which σ is the surface tension coefficient and L is the drop-surface contact length. The right-hand side of the equation represents the vertical proportion of the drop gravity force, in which m is the mass of the drop and α is the sliding angle of the drop on the surface [43].

2.2.1.4 Hydrophobicity Models

The static and dynamic contact angles described in the previous section were based on ideal surfaces, where some factors such as the surface roughness, rigidity, and chemical homogeneity were not considered. In this section, the Wenzel model and the Cassie-Baxter model as shown in Figure 2.4 (a) and (b) were discussed to better illustrate the wetting behaviours of surfaces with the consideration of surface roughness.

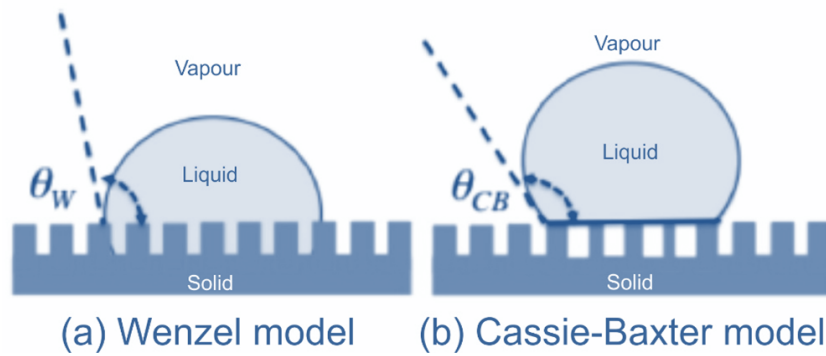


Figure 2.4 Demonstrations of (a) Wenzel wetting model and (b) Cassie-Baxter wetting model

- **Wenzel Model**

Figure 2.4 (a) demonstrates the Wenzel wetting model on a rough solid surface, where the liquid drop can penetrate the tiny surface structural air gaps and be in full contact with the solid surface to produce an entirely wet interface. Equation (4) below shows the correlation of the apparent contact angle θ_W under the Wenzel model [44]:

$$\cos\theta_W = r \cos\theta \quad (4)$$

Where r is the surface roughness factor and θ is the intrinsic contact angle on an ideally smooth surface. The surface roughness factor is equivalent to the ratio of the actual solid-liquid contact area to the projected solid-liquid contact area.

The surface roughness factor r is always larger than 1 in the Wenzel model. When the intrinsic contact angle θ is less than 90° , θ_W decreases with the increase of r . When the intrinsic contact angle θ is larger than 90° , θ_W increases with the increase of r . Thus, under the Wenzel model, a rougher hydrophilic surface leads to a higher hydrophilicity, while a rougher hydrophobic surface leads to higher hydrophobicity. Moreover, due to fact that the actual contact area is usually much larger than the apparent area in the Wenzel model, it produces a large liquid-solid attraction force and leads to a low wet repellence ability with a high surface hysteresis.

- **Cassie-Baxter Model**

When the surface roughness forms a specific cylindrical structure, surface structural gaps can trap vapours below the liquid-solid contacted area and become a vapour-solid composite. This specific surface structure model is called the Cassie-Baxter model as shown in Figure 2.4 (b), from which the apparent contact angle θ_{CB} can be obtained from the equation (5) below [45]:

$$\cos\theta_{CB} = f_1 \cos\theta - f_2 \quad (5)$$

Where θ is the intrinsic contact angle on an ideal smooth surface and f_1 and f_2 are the fractions of the solid-liquid area and the liquid-vapour area, assuming the liquid drop is a perfect sphere. When the surface is rough but not porous, $f_2 = 0$, the Cassie-Baxter equation becomes the Wenzel equation [45][46].

Because the fractions of the solid-liquid area and the liquid-vapour area $f_1 + f_2 = 1$, equation (5) can be rewritten as equation (6) below:

$$\cos\theta_{CB} = f_1(\cos\theta + 1) - 1 \quad (6)$$

From equation (6), it is known that the apparent contact angle θ_{CB} increases with the decrease of the fraction of solid-liquid contact area f_1 . This means a smaller liquid-solid contact area can lead to a larger apparent contact angle in the Cassie-Baxter model, which illustrates that the contact angle can be increased even when the intrinsic contact angle is below 90° . When the solid-liquid area is small enough, f_1 is close to 0 and θ_{CB} is close to 180° . When the solid-liquid area is large enough, f_1 is close to 1. In this situation, the Cassie-Baxter model becomes similar to the Wenzel model. Moreover, the actual liquid-solid contact area for the Cassie-Baxter model is much smaller than that of the Wenzel model due to the presence of air gaps. Thus, the Cassie-Baxter model produces a relatively weaker liquid-solid attractive force and results in a better wet-repellent ability and a lower surface hysteresis.

2.2.2 Principles of Icephobicity

Icephobicity is a property of a surface that repels ice adhesion and accretion on a surface. Superhydrophobic surfaces described by the Cassie-Baxter model have excellent icephobicity that can significantly decrease the ice adhesion strength and delay the freezing time it takes for a liquid drop to become ice. Three anti-icing strategies have been used to improve the icephobicity of surfaces.

- Reduce the adhesion strength of the ice-solid interface. Icephobic surfaces offer low shear strength, usually between 150 and 500 kPa, and sometimes this value can be even down to 15.6 kPa [47]. If the ice formed on a surface, the low shear strength of the surface could allow the ice to be easily removed from it by natural forces such as wind or gravity forces.
- Delay the formation of ice nucleation on surfaces by reducing water drop and surface contact area. A smaller contact area can reduce the heat transfer rate between the drop and the surface, and thus prolong the time it takes for supercooled water drops to be frozen on surfaces with a temperature below 0 °C [48].
- Reduce the water drop rebound time on surfaces. If the time it takes for a drop to rebound is less than the time for ice nucleation, ice formation can be decreased or eliminated [49].

2.2.3 Correlations between Superhydrophobicity and Icephobicity

Although the principle of icephobicity is different from that of the hydrophobicity, several factors correlate them together. Figure 2.5 indicates that lower contact angle hysteresis can result in less shear stress and a higher chance of ice shedding [50]. Other studies also indicate that superhydrophobic surfaces can decrease or eliminate ice formations and accretions with the following factors as below [51] [48] [52]:

- The superhydrophobic surface has a micro or nanostructure that plays a significant role in obstructing the thermal transfer between liquid drops and the solid interface. The reduction of surface contact area reduces heat flow and keeps the drops warmer

than they would be otherwise. This improves the icephobic performance of the surface, making ice formations less likely to occur [51].

- The liquid-solid contact area can be dramatically decreased by using superhydrophobic treatments on surfaces. This can result in a significantly reduced amount of ice nucleation points and larger activation power, which prevents the ice nucleation or crystallisation from happening [48].
- A superhydrophobic surface can increase the mobility of a liquid drop on it and increase the chance of the drop being shed away rapidly after arriving on the surface. The drop can rebound and detach from the superhydrophobic surface before freezing with a shorter time than that on a hydrophilic surface [52].

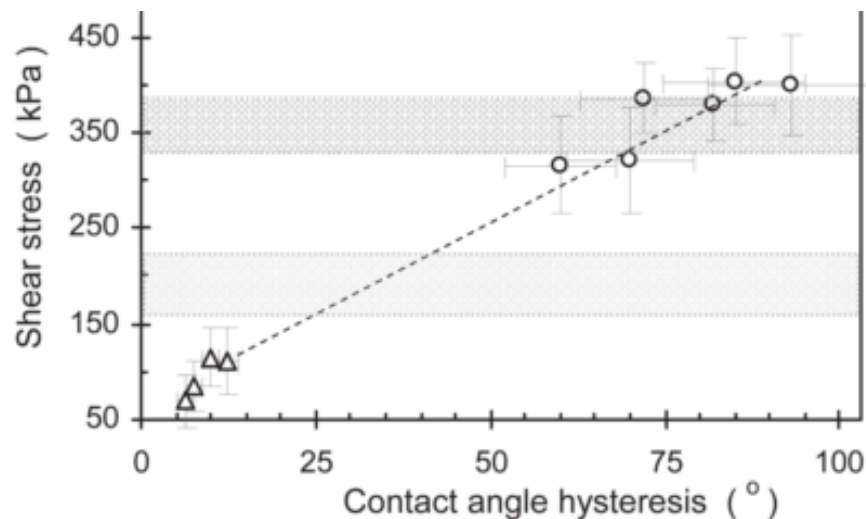


Figure 2.5 Linear correlation between contact angle hysteresis and shear stress

[50]

2.3 Protective Coatings

2.3.1 Protective Coatings for Overhead Line Equipment

CIGRE TB 631 introduces a number of protective coatings with specific abilities that can be engineered into the overhead line systems. In some cold regions, coatings with water or ice repellent ability can be beneficial when applied to overhead line insulators and conductors to prevent ice accretions during extreme weathers.

In general, there are two types of coating that can be used on overhead line insulators and conductors. The first is superhydrophobic coatings, which can be used to repel liquid on surfaces for the purpose of eliminating corrosive liquid pollutants and water drops before freezing. The second type is icephobic coatings. By using the icephobicity of a coating to create a special surface structure, the ice adhesion strength of the surface can be significantly reduced, thus making it easier for the ice to be shed away from the surface. This type of icephobic coating usually relies on external energies to counteract ice adhesion strengths, such as gravity forces or aerodynamic forces [53].

Table 2.1 and Table 2.2 summarise previous studies of the superhydrophobic and icephobic coatings for overhead line insulators and conductors, including coating deployment methods, testing methods, and their achievement on surfaces.

Table 2.1 Summary of prospective coatings on overhead line insulators

Coating Compositions	Deposition Methods	Sample Types	Testing Methods	Achievement and Improvements	Reference
<ul style="list-style-type: none"> ▪ RTV silicon rubber ▪ ATH (Alumina tri-hydrate) ▪ Fluoric nanoparticles 	<ul style="list-style-type: none"> ▪ Spray coating ▪ Brush coating ▪ Dip coating 	<ul style="list-style-type: none"> ▪ Ceramic 	<ul style="list-style-type: none"> ▪ Static and dynamic contact angle tests ▪ Surface morphology ▪ Water recovery test ▪ Adhesion durability test ▪ UV durability test ▪ Erosion and tracking resistance tests 	<ul style="list-style-type: none"> ▪ Achieved 148° contact angle and 3° sliding angle ▪ Better thermal conductivity ▪ Better erosion and tracking resistance ▪ Good durability after the UV test 	[54]
<ul style="list-style-type: none"> ▪ VoltShield 	<ul style="list-style-type: none"> ▪ Spray coating 	<ul style="list-style-type: none"> ▪ Glass ▪ Porcelain 	<ul style="list-style-type: none"> ▪ Corona discharge test ▪ Flashover test ▪ Pollution test 	<ul style="list-style-type: none"> ▪ 18% improvement on the corona and flashover tests ▪ No flashover occurred within 18 months ▪ Better self-cleaning ability 	[55]
<ul style="list-style-type: none"> ▪ PDMS (Polydimethylsiloxane) ▪ FAS (fluorinated alkyl silane) 	<ul style="list-style-type: none"> ▪ Dip coating 	<ul style="list-style-type: none"> ▪ Polyester 	<ul style="list-style-type: none"> ▪ Static and dynamic contact angle tests ▪ Surface morphology ▪ Washing durability test ▪ Abrasion resistance test 	<ul style="list-style-type: none"> ▪ Achieved 171° contact angle and 2° sliding angle ▪ Excellent durability after 500 wash cycles ▪ Excellent abrasion resistance durability after 28,000 cycles of abrasion damage 	[56]

<ul style="list-style-type: none"> ▪ RTV Silicon rubber ▪ SiO₂ or ZnO nanoparticles 	<ul style="list-style-type: none"> ▪ Spray coating 	<ul style="list-style-type: none"> ▪ Glass 	<ul style="list-style-type: none"> ▪ Static and dynamic contact angle tests ▪ Surface morphologies ▪ UV Durability test ▪ Humidity test ▪ Erosion test ▪ Thermal cycling 	<ul style="list-style-type: none"> ▪ 162° contact angle and 7.5° contact angle hysteresis ▪ Good performance after the UV, humidity and erosion tests ▪ Good performance after 700 h of thermal cycling 	[57]
<ul style="list-style-type: none"> ▪ RTV silicon rubber ▪ Stearic acid 	<ul style="list-style-type: none"> ▪ Spray coating 	<ul style="list-style-type: none"> ▪ Glass 	<ul style="list-style-type: none"> ▪ Static and dynamic contact angle tests ▪ Surface morphology 	<ul style="list-style-type: none"> ▪ 165±3° contact angle and 4±1° contact angle hysteresis 	[58]
<ul style="list-style-type: none"> ▪ Fluorinated carbon 	<ul style="list-style-type: none"> ▪ Plasma deposit 	<ul style="list-style-type: none"> ▪ Porcelain 	<ul style="list-style-type: none"> ▪ Static and dynamic contact angle tests ▪ Chemical composition analysis 	<ul style="list-style-type: none"> ▪ Increase the contact angle and decrease the contact angle hysteresis ▪ Higher roughness observed with higher pressure coating 	[59]
<ul style="list-style-type: none"> ▪ OH-PDMS ▪ Silica nanoparticles 	<ul style="list-style-type: none"> ▪ Spray coating 	<ul style="list-style-type: none"> ▪ Glass 	<ul style="list-style-type: none"> ▪ Static contact angle tests ▪ Ice accretion test 	<ul style="list-style-type: none"> ▪ 162° static contact angle ▪ Fewer water drops on the coated substrates ▪ The ice accretion was decreased 50% by using the PDMS modified silica nanoparticles coating 	[60]

Table 2.2 Summary of prospective coatings on overhead line conductors

Coating Compositions	Deposition Methods	Sample Types	Testing Methods	Achievement and Improvements	Reference
<ul style="list-style-type: none"> ▪ Stearic acid 	<ul style="list-style-type: none"> ▪ Chemical etching ▪ Dip coating 	<ul style="list-style-type: none"> ▪ Aluminium 	<ul style="list-style-type: none"> ▪ Static and dynamic contact angle tests ▪ Surface morphology ▪ Ice accretion test 	<ul style="list-style-type: none"> ▪ Reached 150° contact angle and 5° sliding angle ▪ Ice accretion appeared on the part of the sample, particularly at the edges 	[61]
<ul style="list-style-type: none"> ▪ Stearic acid with SiO₂ or CaCO₃ nanoparticles 	<ul style="list-style-type: none"> ▪ Spray coating 	<ul style="list-style-type: none"> ▪ 6061 Aluminium alloy 	<ul style="list-style-type: none"> ▪ Static and dynamic contact angle tests under different temperatures ▪ Surface morphology 	<ul style="list-style-type: none"> ▪ Reached 154° contact angle and 30° sliding angle for the single stearic acid coating at room temperature ▪ Reached 160°/158° contact angle and 3°/4° sliding angle for the stearic acid with SiO₂/CaCO₃ nanoparticles at room temperature ▪ At -10 °C, the contact angles drop to 120° and 133° for the stearic acid coating with or without SiO₂ nanoparticles respectively 	[62]
<ul style="list-style-type: none"> ▪ SLIPS (liquid-infused porous surfaces) 	<ul style="list-style-type: none"> ▪ Oxidative electrochemical deposition 	<ul style="list-style-type: none"> ▪ 1100 Aluminium alloy 	<ul style="list-style-type: none"> ▪ Dynamic contact angle tests ▪ Surface morphology ▪ Ice accretion test ▪ Shear stress test 	<ul style="list-style-type: none"> ▪ Contact angle hysteresis decreased from 41±4° to 2±1° ▪ Critical drop size on SLIP coated aluminium is 8 times smaller than that on the bare aluminium ▪ Good performance during the ice accretion test 	[63]

				<ul style="list-style-type: none"> ▪ Shear stress decreased from 1359 kPa to 15.6 kPa. Better performance during frost weather on SLIP aluminium than on bare aluminium 	
<ul style="list-style-type: none"> ▪ HMDSO (hexamethyl disiloxane) 	<ul style="list-style-type: none"> ▪ Adonisation process ▪ Plasma polymerisation ▪ Gas carrier deposition 	<ul style="list-style-type: none"> ▪ 6061 Aluminium alloy 	<ul style="list-style-type: none"> ▪ Static and dynamic contact angle tests ▪ Chemical composition analysis ▪ Surface morphology ▪ Ice accretion test ▪ Shear stress test 	<ul style="list-style-type: none"> ▪ Reached 158° of contact angle and 8° sliding angle ▪ Coating was damaged after 15 icing accretion events ▪ Coated substrate had a shear stress 3.5 times lower than the uncoated substrate ▪ After the ice accretion test, shear stress increased again but still showed excellent icephobic performance 	[64]
<ul style="list-style-type: none"> ▪ PTFE 	<ul style="list-style-type: none"> ▪ Adonisation process ▪ Dip coating 	<ul style="list-style-type: none"> ▪ 6061 Aluminium alloy 	<ul style="list-style-type: none"> ▪ Static contact angle tests ▪ Chemical composition analysis ▪ Surface morphology ▪ Ice accretion test ▪ Shear stress test 	<ul style="list-style-type: none"> ▪ Reached 130° - 140° contact angle ▪ Thickness of coating was approximately 100 nm ▪ Good performance in that ice accretion test and the ice adhesion was reduced by 2.5 times than that of the uncoated samples ▪ The coating still fully functioned after 7 shear stress tests 	[65]
<ul style="list-style-type: none"> ▪ Fluorolink S10 ▪ Siliclad Glide 10 	<ul style="list-style-type: none"> ▪ Chemical etching ▪ Adhesion promoter 	<ul style="list-style-type: none"> ▪ Aluminium 	<ul style="list-style-type: none"> ▪ Static and dynamic contact angle tests ▪ Surface morphology ▪ Ice accretion test 	<ul style="list-style-type: none"> ▪ Fluorolink S10 showed the low ice adhesion with an adhesion reduction-factor (ARF) of 20 ▪ Contact angle of Fluorolink S10 was 120°. After adding silicon particles, the contact angle increased to 169°, but there was no 	[66]

<ul style="list-style-type: none"> ▪ PDMS (polydimethylsiloxane) 			<ul style="list-style-type: none"> ▪ Shear stress test 	<ul style="list-style-type: none"> reduction in shear stress ▪ Siliclad Glide 10 showed hydrophobicity with 104° of contact angle, and adhesion reduction factor (ARF) was close to 1 ▪ PDMS coating had a high ARF value of around 100, but it also had a low mechanical strength 	
<ul style="list-style-type: none"> ▪ RTV silicone rubber with Al₂O₃ nanoparticles 	<ul style="list-style-type: none"> ▪ Spray coating 	<ul style="list-style-type: none"> ▪ 6061 aluminium alloy ▪ Copper ▪ Stainless steel 	<ul style="list-style-type: none"> ▪ Static and dynamic contact angle tests ▪ Surface morphology ▪ Corrosion resistance test ▪ Ice accretion test 	<ul style="list-style-type: none"> ▪ The contact angles were higher than 160°. The contact angle hysteresis was around 6° to 11°, and the sliding angles were around 2.5° to 4.2° ▪ 95.8% of corrosion protection efficiency was reached with the coated substrates after 20 days of corrosion resistance testing. ▪ Good performance for the ice accretion tests 	[67]
<ul style="list-style-type: none"> ▪ PTES 	<ul style="list-style-type: none"> ▪ Chemical etching ▪ Dip coating 	<ul style="list-style-type: none"> ▪ 1060 Aluminium alloy 	<ul style="list-style-type: none"> ▪ Static and dynamic contact angle tests under different temperatures and humidity ▪ Surface morphology ▪ Ice accretion test ▪ Icing and de-icing durability test 	<ul style="list-style-type: none"> ▪ Contact angle reached 165° with a sliding angle of 1° at room temperature and humidity of 30%. It dropped to 138° with a sliding angle of 20° at -10 °C and humidity of 90% ▪ Drops were still able to slide off before becoming frozen when the temperature was extremely low ▪ Ice accretion was dramatically decreased by 87% ▪ After 40 icing and de-icing tests, the shear stress of the ice was increased by 16% 	[68]

2.3.2 Review of Coating Preparation Methods

2.3.2.1 Pre-treatments

Pre-treatments on the test substrates were used for several purposes before applying coatings, including (a) to remove the external layers or contamination on the surfaces, (b) to produce specific structures on the surfaces for enhancing the roughness, and (c) to increase the molecular interaction on the coating-solid interface [1]. Three types of pre-treatment method are listed below:

- **Degreasing**

Degreasing in organic solutions such as acetone or potassium hydroxide can remove the inhibitor layers on surfaces to ensure the coverage and effectivity of coatings [69].

- **Chemical Etching**

Immersing a substrate into chemical solutions such as hydrochloric acid or hydrofluoric acid can increase the surface hydrophobicity by producing certain surface structures and decreasing surface energy [70].

- **Mechanical Abrasion**

Abrasion techniques such as sandblasting or sandpaper grinding can be used to mechanically generate surface structures before applying coatings [71][72]. These abrasion methods are usually low-cost and convenient to be processed as the pre-treatments.

2.3.2.2 Deposition Methods

- **Conventional Methods**

Conventional coating deposition methods include dip coating, spin coating, spray coating, and brush coating. These methods have been widely used for several decades in the industry to apply thin coatings on substrates, because of their economical and practical benefits.

- **Plasma Treatment**

Plasma is a conductive ionised gas that has been widely used in the electronic industry and coating applications. Plasma treatment is an advantageous method that can be used to modify the two most crucial factors when generating a superhydrophobic surface: the surface energy and the surface roughness. There are three types of plasma treatment in general, including plasma etching, plasma polymerisation, and plasma sputtering. Plasma etching is mostly utilised to produce certain roughness on a surface, while plasma polymerisation and sputtering are usually used to create a thin film with low surface energy on a substrate [1][73].

- **Electrodeposition**

Electrodeposition is an excellent and valuable method to apply materials or generate structures onto any conductive surface. By using electric currents to decrease the cations from a dissolved metal, a corresponding metal coating can be formed and deposited on a base surface [74]. Different materials have been deposited on metal substrates to fabricate superhydrophobic surfaces. For examples, copper oxidation was electrodeposited on aluminium alloys and achieved a 160° surface contact angle [75]. Nickel was electrodeposited on magnesium alloys and achieved a 151.7° surface contact angle [76].

2.3.3 Review of Coating Characterisations and Ageing Tests

- **Static and Dynamic Contact Angle Measurements**

Contact angle measurements are the most straightforward methods to determine coating characterisations. Generally, there are two types of contact angles: static contact angles and dynamic contact angles. The details of both types of contact angles can be found in section 2.2.1.3.

- **Ice Accretion Tests**

Ice accretion tests are used to evaluate and quantify the icing influence and the icephobic performance of treated conductors and insulators. IEEE publications and standards proposed several different icing tests on insulators to evaluate their flashover performance, including ice tests, snow tests, cold-fog tests, and salt-fog tests [77][78]. Several studies carried out different icing accretion tests for evaluating the performance of overhead line insulator and conductor materials under different icing weather. In Li's study, the anti-icing performance of a PDMS/modified nano-silica superhydrophobic coating was tested. The result shows that this coating is an excellent anti-icing method that can effectively delay ice formation and reduce ice adhesion strength on insulators [60]. Phan's study tested the minimum flashover voltage of an iced insulator, where hard rime was the most severe type of icing that can reduce the minimum flashover voltage by 60% compared to a wet insulator [7]. Ice accretion tests in Wang's study show that a stearic acid superhydrophobic coating can effectively reduce ice formation on aluminium substrates at -6 °C [61]. The anti-icing performance of a hydrangea-like micro/nanostructure superhydrophobic treatment on aluminium samples was tested in Wenxuan's study, and results showed that water drop freezing time on the treated samples was delayed by 4 to 5 times compared to that of the untreated samples [79].

- **Dielectric Test**

The dielectric test is a simple method to determine a coating's dielectric strength on overhead line conductors. The dielectric test shown in Figure 2.6 was carried out by connecting the substrate through an electrode to a high voltage source. The dielectric strength of the sample was measured by gradually increasing the testing voltage applied to the sample to its maximum breakdown point [1].



Figure 2.6 Dielectric tester for conductor coatings [1]

▪ **Thermal Cycling**

Thermal cycling is an environmental stress test that aims to examine the performance of treated surfaces under variations of extremely high and low temperatures, according to ANSI C29.2 [80]. One-week of high-temperature thermal cycling was carried out on chromate-free cathodic electrodeposition coated 2024-T3 aluminium alloy samples with the temperature varied from 23 to 85 °C. The coating proved to have excellent thermal corrosion resistance under high temperatures [81]. Low-temperature thermal reliability of 10% and 20% MWNT-silicone composite coatings on aluminium substrates were examined by 4000 h of thermal cycling with the temperature changing from -30 to 20 °C. The results indicated that the contact angle of the 10% MWNT coating dropped to 134° after only 400 thermal cycles, while the 20% MWNT coating maintained its superhydrophobicity after 4000 cycles of thermal cycling. [82].

▪ **Corona Exposure**

Corona exposure aims to examine the influence of corona discharges and their potential damages on surface treatments for overhead line conductors. During the corona exposure, three major by-products affect the durability of surface treatments [1]:

- Ozone generated by corona
- UV-B range light associated with corona
- Chemical acid produced by corona with water

Figure 2.7 shows an example of corona exposure suggested in CIGRE TB 631 with a total duration of 1000 h. It can be carried out with 2 mm distance between the substrates and energised electrodes [1]. Another corona exposure was carried out on fluorinated RTV silicone rubber hydrophobic samples by placing the samples 3 mm under the electrode needles connected to an 8 kV voltage, and after 4 h of the corona exposure, all the samples lost their hydrophobicity [83].

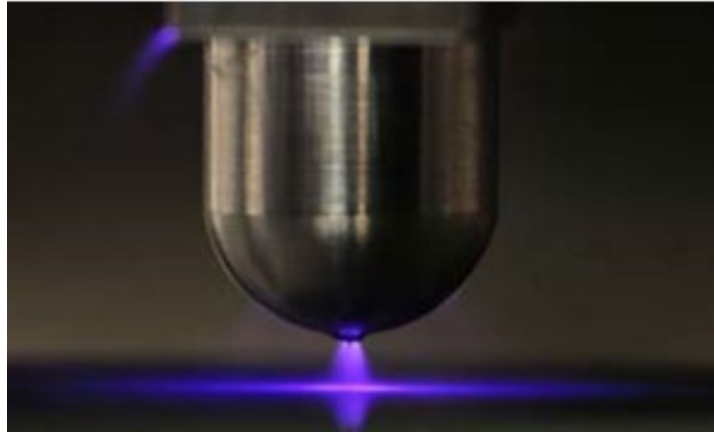


Figure 2.7 Image of the corona exposure test [1]

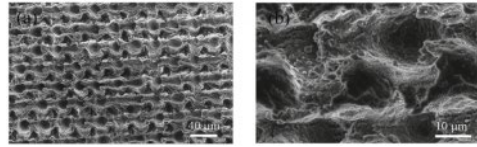
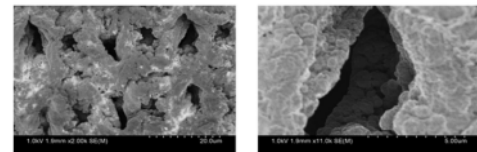
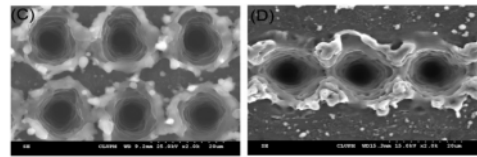
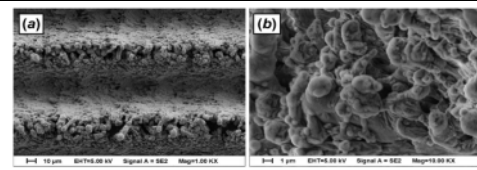
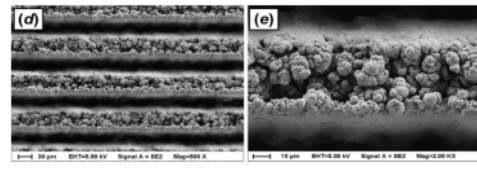
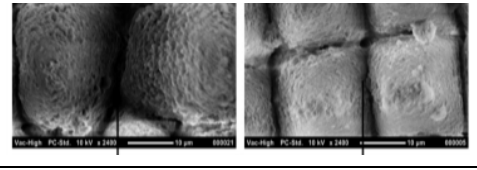
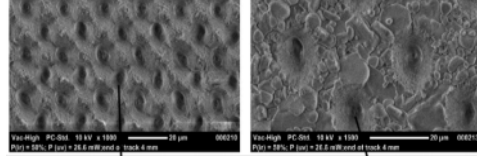
- **Ultraviolet Exposure**

Short wavelength ultraviolet (UV) light has been indicated to cause most of the damage to coatings from exposure to sunlight [1]. Different types of UV exposure can be carried out to examine the UV influence on samples, such as Xenon Arc UV exposure and Fluorescent UV exposure for a duration of 2000 h, according to ASTM G155 [84] and ASTM G154 [85]. Colour variation and gloss retention can be used to examine the damage grade, according to ASTM D4587 [86]. 1000 h of UV exposure was carried out on the superhydrophobic RTV silicone rubber coating, according to ASTM G155, with no significant change in contact and sliding angles recorded [54]. A UV test based on ASTM G154 was carried out on the ZnO-based nanocomposite coatings, and the results showed that all the samples retained their superhydrophobicity after 4 UV exposure cycles [57].

2.4 Laser Patterning

Laser patterning is a sophisticated method to create a superhydrophobic surface with micro or nano structures on overhead line conductors. The superhydrophobic surfaces produced by laser ablations are capable of repelling water or ice on the surfaces. Studies of different laser patterns on aluminium substrates with their surface structure images and hydrophobicity achievements are summarised in Table 2.3.

Table 2.3 Summary of different laser patterns on aluminium alloy substrates

Laser Irradiation	Scanning Structure	Image of the Surface Structure	Contact/Sliding Angle	Reference
Picosecond Laser	Micro-pillars Micro-cavities		$153 \pm 2^\circ$	[87]
Femtosecond Laser	Hierarchical Structure		160°	[88]
Nanosecond Laser	Blind Micro-holes		$148 \pm 3^\circ$	[89]
Nanosecond Laser	Micro-channels		$173.1 \pm 1.2^\circ$ $/2 \pm 0.6^\circ$	[90]
	Intensive Micro-channels		$173.4 \pm 1^\circ$ $/2.4 \pm 1.2^\circ$	
Ultraviolet Laser pulses (On Al ₂ O ₃)	Micro-pillars		151°	[91]
	Blind Micro-holes		151°	

The laser pattern studies in Table 2.3 indicate that most of the laser patterns can produce superhydrophobic structures on aluminium alloy samples, and the micro-channels patterns produced by the nanosecond laser resulted in the largest contact angle of around 173° [90]. Besides the performance of different laser patterns, there are some important considerations as shown below:

- Superhydrophobic performance does not appear directly on the treated surface after laser ablations. Chemical treatment such as immersing in $(\text{CF}_3(\text{CF}_2)_7(\text{CH}_2)_2\text{Si}(\text{OCH}_3)_3$ methanol solution may be required after the laser treatments to reduce surface tensions [92].
- Absorption of organic compounds onto the oxide surface can speed up the transition from superhydrophilic to superhydrophobic on an ablated oxide aluminium substrate [91].

CHAPTER 3 SURFACE TREATMENTS

3.1 Introduction

Superhydrophobic surfaces with surface contact angles larger than 150° and low contact angle hysteresis have been extensively utilised in various situations such as power systems, aerospace, and mining industry. In this chapter, the different test substrates used in this research are discussed, including sample preparation and sample pre-treatment methods. Sample characterisation methods are introduced, including improved methods of contact angle measurement and surface morphology tests. The different coatings used in this research are introduced, including coating materials, deployment methods, and wettability performance of the coatings. Water drop movement on flat and round conductor samples were examined under a high-speed camera with and without superhydrophobic coatings. Different surface roughness and experimental parameters were examined to find out the optimised method of obtaining superhydrophobic coatings with high consistency and good reproducibility. Different laser parameters were used to fabricate various micro-structure patterns on aluminium alloy substrates in order to obtain the optimum pattern while considering superhydrophobic performance and manufactory feasibility.

3.2 Test Samples and Preparation Methods

3.2.1 Test Samples

This section details different test samples used in this research. Flat samples were chosen because of their composition being similar to overhead line conductors and insulators. The contact angles and surface geometric characterisations of flat samples were also easy to measure. Round conductor samples that were available in the laboratory were used to examine water drop behaviour under a high-speed camera.

- **EPDM Rubber, Silicone Rubber, and Aluminium Substrates**

Figure 3.1 shows three different materials representing overhead line insulators and conductors: silicone rubber, EPDM (Ethylene Propylene Diene Monomer) rubber, and aluminium. All three types of substrates have dimensions of $100 \times 50 \times 6$ mm. Polymer composite insulators such as silicone rubber or EPDM rubber offer advantages of lower cost, lighter weight, and better hydrophobicity than traditional porcelain or glass insulators when used in overhead line systems [93][94][95]. EPDM rubber has higher tensile strength and better abrasion resistance than silicone rubber, while silicone rubber offers higher electrical resistivity and tracking resistance compared to EPDM rubber. Aluminium is a common material used for overhead line conductors. Although aluminium is less conductive than copper, it offers the crucial benefits of lower weight and cost effectiveness. As such, these three materials representing overhead line insulators and conductors were chosen to conduct preliminary experiments in this research. With the research focusing largely on conductors, further details of the metallic samples used are provided below.



Figure 3.1 Silicone rubber (left), EPDM rubber (middle), and aluminium (right) substrates

- **Aluminium Alloy 6082**

The aluminium alloy 6082 substrate as shown in Figure 3.2 has good mechanical strength and excellent corrosion resistance among the 6000 series. Because of its higher mechanical strength, aluminium alloy 6082 has been replacing 6061 in many recent applications. Aluminium alloy 6082 substrates with dimensions of $25 \times 25 \times 3$ mm were used in this research because of the similarity in composition to actual overhead line conductors.

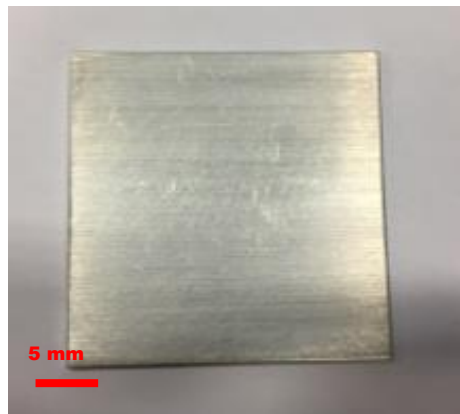


Figure 3.2 Image of an aluminium alloy 6082 substrate

- **All Aluminium Alloy Conductor (AAAC)**

AAAC conductors, like all other overhead lines, are stranded, which provides more flexibility and makes them suitable to be coiled for transporting. AAAC is the most commonly used conductor for overhead transmission systems in the UK. The AAAC conductor shown in Figure 3.3 is a concentric-lay-stranded aluminium alloy conductor with 61 strands. AAAC conductors have advantages of good conductivity, excellent corrosion resistance, and high mechanical strength. The maximum operating temperature of AAAC conductors is $90\text{ }^{\circ}\text{C}$ [96]. AAAC conductors are usually used to replace some ACSR conductors by offering a lower electric loss and a better strength-to-weight ratio [97]. Considering the reasons above, the AAAC conductors with 36 mm in diameter and 100 mm in length were used as test samples in this research.



Figure 3.3 Image of an AAAC conductor line

- **Gap-type Conductor**

The Gap-type Conductor shown in Figure 3.4 consists of trapezoidal aluminium external layers (with 40 strands) and steel internal cores (with 7 strands). With super thermally resistant external Al-Zr alloy layers, the operating temperature of Gap-type conductors can reach a maximum of 210 °C. This super thermally resistant conductor also offers a better thermal expansion characteristic than ACSR conductors, which maintain smaller sag under high temperatures [98]. Because of the complexity of the stringing procedures, Gap-type conductors are more expensive to manufacture and require special installation. Gap-type conductors are a relatively new technology and have a comparably flat surface profile, which makes their surface easier to treat with surface profiling when compared to traditional types of conductors. As a result of these advantages and potential benefits, the Gap-type conductors with 32 mm in diameter and 100 mm in length were used as test samples in this research.



Figure 3.4 Image of a Gap-type conductor line

3.2.2 Sample Cleaning and Preparations

3.2.2.1 Sample Cleaning

Different cleaning methods were used on metal and rubber samples for the purpose of degreasing and removing loose material or debris on surfaces before applying surface treatments.

- **Aluminium Substrates**

An ultrasonic bath filled with acetone was used to clean the aluminium substrates at 25 °C for 10 mins, followed by rinsing in deionized water, dipping in isopropanol, and drying at room temperature for 10 mins.

- **Rubber Substrates**

Silicone or EPDM rubber substrates were cleaned using an ultrasonic bath filled with deionized water at 25 °C for 10 mins, followed by dipping in isopropanol and drying at room temperature for 10 mins.

3.2.2.2 Sample Pre-treatments

Sample pre-treatments are usually used on test substrates before applying coatings. These pre-treatments have different functions such as removing the external layers, producing specific structures, and increasing molecular interaction forces between the coating and the surface [1]. In this research, three types of sample pre-treatments were used on aluminium substrates as below:

- **Hydrochloric Acid Etching**

An 18.5 wt% (weight percentage) of hydrochloric acid (HCl) was prepared by diluting concentrated HCl with distilled water. The diluted HCl solution was transferred into a plastic beaker and allowed to cool down before etching. An aluminium substrate test sample was immersed into the 18.5 wt% HCl solution for 2 to 4 mins in a fume cabinet. Plastic tweezers were used to remove and transfer the substrate from the HCl solution to

an ultrasonic bath filled with deionized water at 25 °C for 3 mins, followed by drying in an oven at 70 °C for 10 h.

- **Sandpaper Grinding**

Different grades of sandpaper were used on aluminium substrates to achieve refined roughness on the surfaces. Samples were treated using the 120-grade sandpaper to grit horizontally and vertically, and then the process was repeated twice with both 800 and 1200 grade sandpaper. Afterwards, the treated samples were cleaned before use.

- **Polishing**

Samples were mechanically polished to achieve a specular gloss configuration. Afterwards, the treated samples were cleaned before use.

3.3 Characterisation Methods

This section introduces different characterisation methods to examine wettability performance and inspects the surface geometrics of the test samples, including different static and dynamic contact angle measurements, optical microscopy, scanning electron microscopy, and confocal laser scanning microscopy.

3.3.1 Contact Angle Measurements

Static contact angles, sliding angles, and contact angle hysteresis measurements are some common methods to characterise the level of hydrophobicity and hysteresis of surfaces [16]. A DataPhysics OCA 15EC goniometer was used to examine various contact angle measurements on samples. A prepared sample was placed on the sample holder with a rotatable surface as shown in Figure 3.5. Deionised water drops were dispensed on samples and images were captured for analysis using SCA20 software. In selecting the technique to be used for contact angle measurement, a technique was developed that was not reliant on the installed software and was different than other methods usually seen in literature.

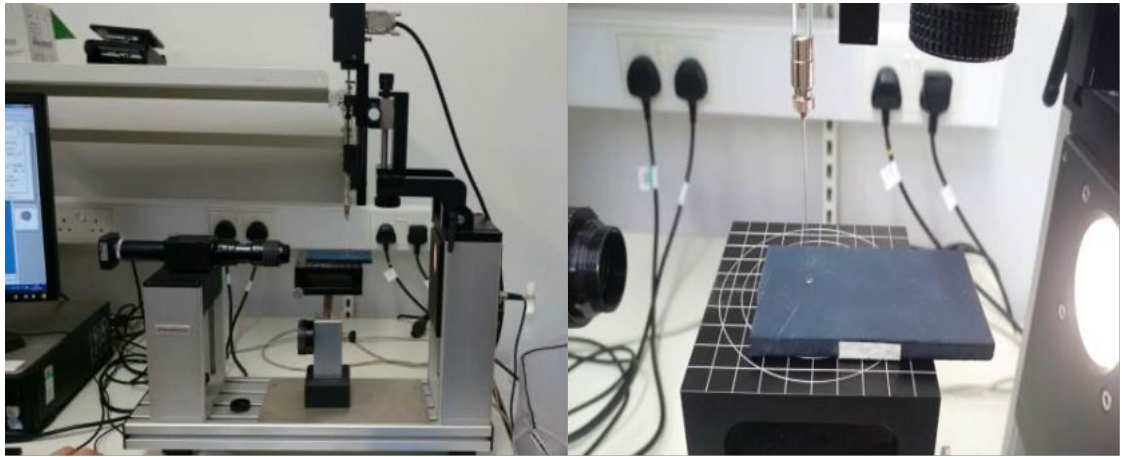


Figure 3.5 Images of the contact angle measurement equipment

- **Static contact angle measurements**

The traditional zoomed-out method (with the whole drop visible) using either auto or manual computation can result in varying contact angles even from the same water drop (this will be discussed further in this section). The reproducibility and accuracy of contact angle measurement mostly depends on the accuracy of mapping the drop profile and the consistency of the operator [99]. The misplacement of baselines and interfacial triple points of liquid, air, and solid interfaces lead to inaccuracy of contact angle analysis. By using a higher magnification of the captured image to allow the detailed investigation of the triple point that defines the contact angle, the accuracy of the contact angle measurement can be improved [100]. The idea for the zoomed-in approach is simply to increase the resolution of the important region: the interfacial triple point. This important region determines the contact angle, which by definition is the angle between the solid-liquid interface and the solid-gas interface. By zooming in and manually curve-fitting at the critical triple point, the liquid-gas interface and the horizontal baseline can be defined much more accurately.

The commercial software available in the laboratory offers different fitting methods for static contact angle measurements, such as Laplace-Young, elliptical, and circular fitting. However, there is no official standard for choosing the fitting method, and thus it is left to sensible discretion. Schmitt et al., 2013 [101] and Heib et al., 2016 [102] indicate most

of these commercial fittings for contact angle analysis lack accuracy and reproducibility especially on evaluating non-axisymmetric drops or superhydrophobic surfaces as the whole drop shape is considered. A zoomed-in method can potentially improve this problem by separating the left and right hand sides of the drop so that both sides can be fitted and analysed individually.

The baseline and outline mapping results for each drop significantly differ depending on the choice of zoomed-in vs. zoomed-out method. This resulted in different locations of triple-points and thus affected the accuracy of contact angles as shown in Figure 3.6. Methods (1) to (3) are the zoomed-out methods using different fittings. Method (4) is the zoomed-in approach using a manual circular fitting. Yellow “O” and “X” marked the actual triple points and the computational triple points respectively.

The Laplace-Young fitting is a mathematical fit that is more commonly used for large bulging drops. The zoomed-out method using the auto Laplace-Young fitting cannot precisely locate the actual triple point due to a lack of resolution, which resulted in a larger contact angle than in reality as shown in method (1).

The zoomed-out method using the auto elliptical fitting ignores the bulge toward the bottom of a water drop and misplaces the triple point as shown in method (2), which results in an outline that deviates from the drop and thus leads to a smaller contact angle.

The same problem applies to the zoomed-out method with manual elliptical fitting, where the actual triple point is further to the right than the computational triple point as shown in method (3), leading to a smaller contact angle than in reality.

The manual circular zoomed-in method solved these problems by zooming in the lens to one side of the drop with approximately 50 pixels per 100 μm as shown in method (4), which provides about 10 times the resolution of the zoomed-out methods. By using the zoomed-in method, the computational triple point coincides with the actual triple point. The triple point region used to define the static contact angle appears circular when using the zoomed-in method, and thus the circular fitting is more suitable to map the triple

point region. These findings portray the key advantage of the zoomed-in method vs. other zoomed-out methods and this information can be utilised to compute contact angles within the critical region of importance. With less deviation presented between the chosen triple point and the actual triple point, the zoomed-in method is more likely to provide greater accuracy in this work.

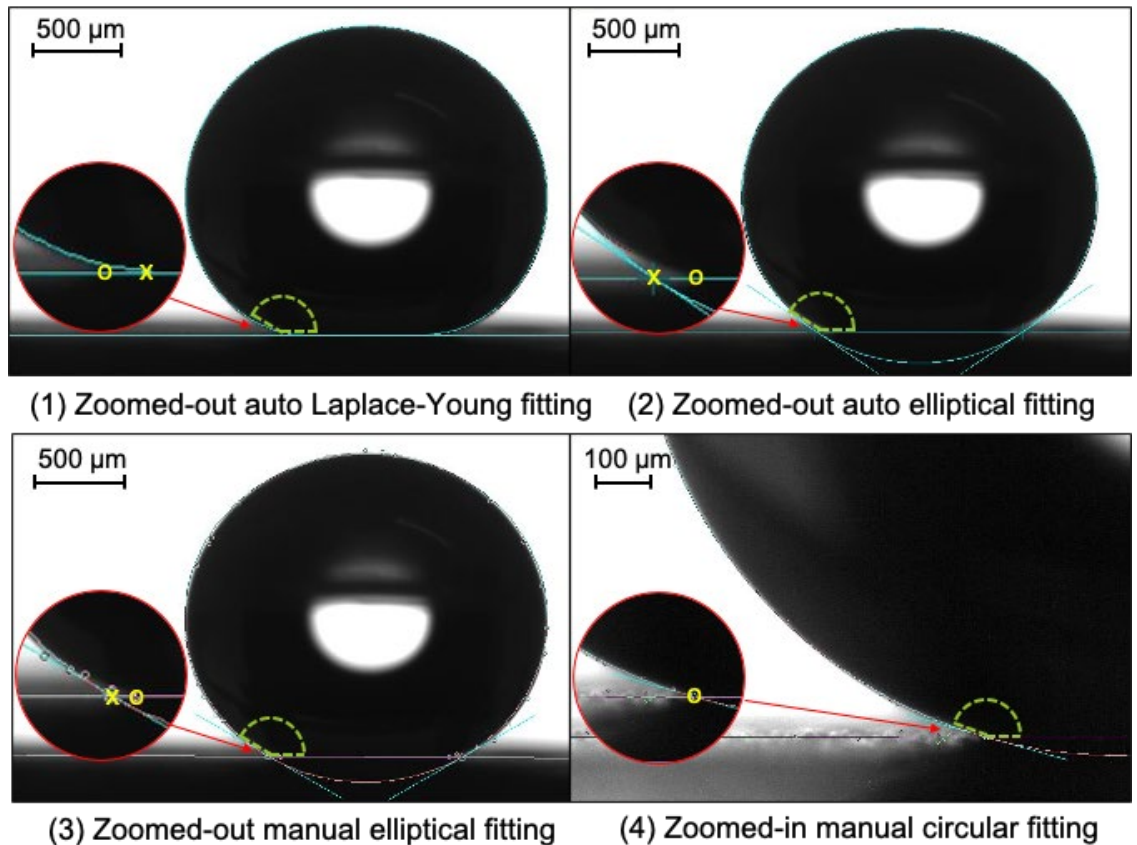


Figure 3.6 Comparisons of zoomed-in and zoomed-out methods of contact angle measurements using different fittings

When the images (3) and (4) from Figure 3.6 were further enlarged to the same drop size level, a clearer comparison can be obtained as shown in Figure 3.7. It is clear that the enlarged image (3) shows larger pixels with lower resolution for the same size of the water drop unit compared to the enlarged image (4). The chosen drop outline in the enlarged image (3) demonstrates a larger error with more black pixels resting on the left

hand side of the outline compared to that of the enlarged image (4). This observation further indicates the potential higher accuracy of the zoomed-in method.

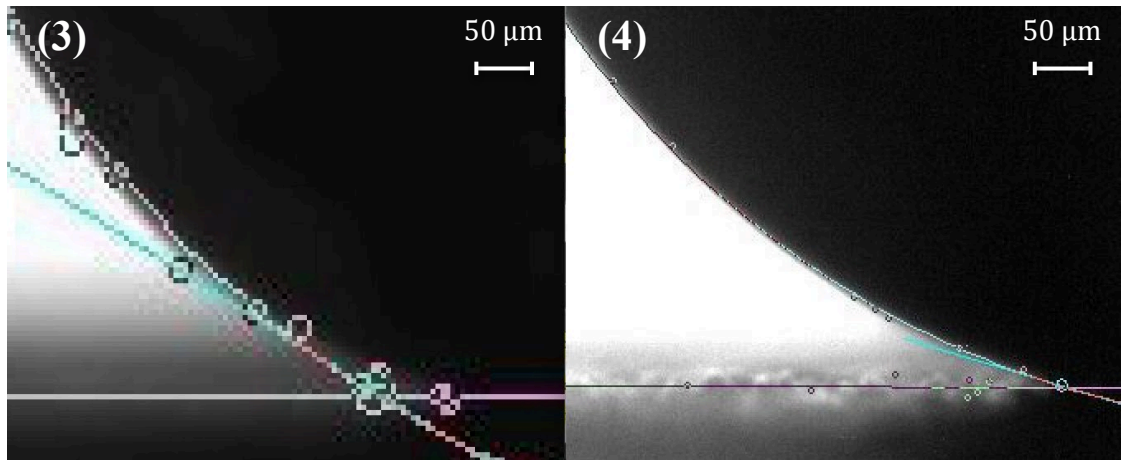


Figure 3.7 Comparison of enlarged images of (3) Zoomed-out manual elliptical fitting and (4) Zoomed-in manual circular fitting

To quantify the reproducibility of the zoomed-in manual method, various statistical metrics were compared with other zoomed-out methods. 12 μL and 4 μL water drops were dispensed on the same location of a laser patterned aluminium substrate to obtain 10 repeated contact angle measurements for each method. Data were statistically processed to calculate the mean contact angle, standard deviation, and data range for each method as shown in Table 3.1.

For both 4 and 12 μL water drops, the zoomed-out method with auto Laplace-Young fitting shows the largest standard deviation and range of contact angles, indicating the poor reproducibility of this method. The zoomed-out method using either auto or manual elliptical fitting demonstrates a low standard deviation and small data range. However, the zoomed-out auto elliptical fitting shows a large inconsistency in mean contact angles with an 8.7° difference between 4 and 12 μL drops.

The zoomed-in manual method shows low standard deviation and a small data range, and this method also appears to equate consistently in static contact angles between drop sizes.

Table 3.1 Statistic processing of contact angle measurements data using different computing methods and different water drop sizes

Methods		Zoomed-out			Zoomed-in
		Auto Laplace-Young Fitting	Auto Elliptical Fitting	Manual Elliptical Fitting	Manual Circular Fitting
12 μ L Drop Size	Mean Contact Angle ($^{\circ}$)	173.7	147.8	154.9	165.8
	Standard Deviation ($^{\circ}$)	6.5	0.8	0.9	1.0
	Data Range ($^{\circ}$)	160.2–179.9	146.2-149	153.6-156.5	164.2-167.4
4 μ L Drop Size	Mean Contact Angle ($^{\circ}$)	175.4	156.5	160.6	169.4
	Standard Deviation ($^{\circ}$)	6.0	1.4	0.3	0.9
	Data Range ($^{\circ}$)	166.2-179.8	154.6-158.7	159.9-160.9	168-170.8

Overall, the zoomed-in method with manual circular fitting demonstrates a good reproducibility with a small standard deviation and data range. While some of the zoomed-out methods (the auto elliptical and the manual elliptical fittings) when zoomed out show a comparable reproducibility, as measured by lower standard deviation and range, the information used to fit the curve is far higher when zoomed in as shown in Figure 3.6. Therefore, the zoomed-in method could only improve the accuracy of contact angle measurements with a higher resolution and comparable reproducibility when compared with the zoomed-out method. Thus, the zoomed-in method was used in this research.

- **Sliding Angle Measurements**

A prepared sample was placed on the rotatable sample holder that rotates the sample from flat to fully inclined. A single drop of deionised water was carefully dispensed on the surface. The angle adjusting knob was rotated to increase the angle between the substrate and horizontal line until the water drop slid off the substrate. The angle

displayed on the protractor was recorded, with an accuracy of 0.1° , as the sliding angle of the surface.

- **Contact Angle Hysteresis (Pendant Dragging Method)**

To measure contact angle hysteresis, a pendant dragging method was used according to [103]. A water drop was dispensed on a sample while it was still attached to the needle. The needle height level was adjusted to maintain the contact of the water drop to the surface without squashing the shape of the drop. The drop was dragged horizontally across the surface to a point where the maximum advancing and minimum receiving angles could be recorded and computed by the manual circular zoomed-in method. The difference between the advancing angle and receiving angle was calculated, which provided the contact angle hysteresis of the surface.

3.3.2 Surface Morphology Tests

- **Optical Microscope**

The Axio Imager MAT reflected-light optical microscope with the AxioVision SE 64 software was used to observe substrates with different pre-treatments and coatings. Enlargement factors of 5, 10, and 50 times were used to obtain different magnifications for the different samples. The thickness of transparent coatings could also be measured using the Z-Position function of the optical microscope. At first, the lens was focused on the base surface to set the Z-Position to zero. Then the height of the sample was adjusted until the top coating could be focused. The value of the Z-axis at this height was equivalent to the thickness of the coating.

- **Scanning Electron Microscope (SEM)**

FEI Quanta 200 & 250 scanning electron microscopes (SEM) were used to examine laser patterned samples before and after ageing tests, with 20 kV of beam voltage and 3.0 mm of spot size in a vacuumed environment.

- **Confocal Laser Scanning Microscope (CLSM)**

A confocal laser scanning microscope (CLSM) was used to map the 3D profile geometry of micro-structured laser patterns on aluminium substrates.

3.4 Coating Experiments

One of the challenges of replicating some of the coatings was the lack of complete information and instructions within the CIGRE TB 631 report and the referenced publications. In this section, different coating materials and surface pre-treatments were deployed on samples. The wettability of these coatings was examined, and the coating replicating procedures were optimised to achieve a better reproducibility and a higher hydrophobic performance.

3.4.1 Uncoated Substrates

The static contact angles and contact angle hysteresis of uncoated aluminium, silicone rubber, and EPDM rubber substrates were measured after allowing the drops to sit on the surface for different lengths of time. This was to test whether drops require time to respond to the surface. Three different samples of each substrate were prepared to test for reproducibility. Each contact angle test was repeated five times on each substrate, and the average result was calculated. Drops 1 μL in volume were used during the measurement.

Table 3.2 shows that the average contact angles and contact angle hysteresis were 108.2° and 24.4° for the uncoated aluminium; 113° and 21.2° for the uncoated silicone rubber; 108.5° and 16.6° for the EPDM rubber, with zero waiting time. The contact angles of the surfaces dropped gradually to 104.2° , 111.8° , and 106.9° respectively after 60 s of the water drops being left on the surfaces. This result indicates that the aluminium, silicone rubber, and EPDM rubber substrates were hydrophobic materials with the contact angles greater than 90° . It is illustrated in Figure 3.8 that the contact angle decreased with the increase of the measurement waiting time, while the contact angle of the uncoated aluminium substrate

dropped faster than that of the silicone rubber and EPDM rubber substrates. This test only measured contact angles changing curves for the first 60 s, where the changes were visible. It was also noted that after a period of 60 s, the shape of the drops tended to be stabilised such that the reduction rate of contact angles became slow and insignificant.

Table 3.2 Average contact angles of uncoated aluminium, silicone rubber, and EPDM rubber substrates with increasing waiting time

Waiting Time (s)	Contact Angles (°)					Contact Angle Hysteresis (°)
	0	15	30	45	60	
Aluminium	108.2	107.0	106.8	105.2	104.2	24.4
Silicone Rubber	113.0	112.6	112.6	111.9	111.8	21.2
EPDM Rubber	108.5	107.9	107.7	107.0	106.9	16.6

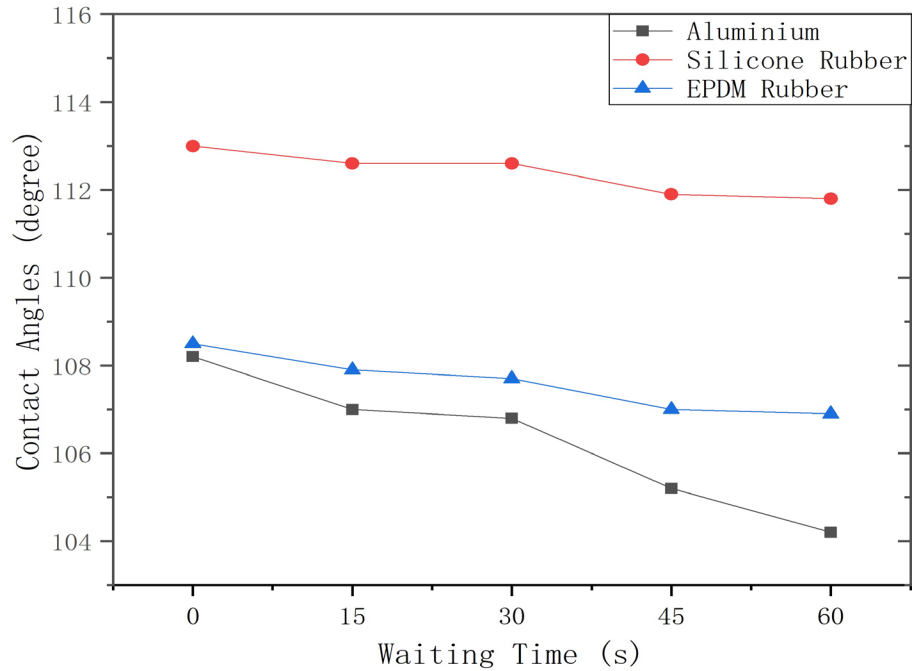


Figure 3.8 Comparison of contact angles for different coated substrates with different waiting times

It is known that liquid surface tensions usually keep water drops spherical, while gravity forces contribute to the flattening of the drops. On a surface with higher hydrophobicity, the liquid drop surface tension is higher than the interfacial tension between the surface and the liquid [104]. The more spherical shape of the drop on the surface, the less liquid-solid contact area. This contributes to a lower heat transfer rate and less ice nucleation points between the drop and the surface, resulting ice formations being less likely to occur [51][48]. Thus, different hydrophobic or superhydrophobic surface treatments were deployed and examined in further tests to achieve a better water-repellent ability and a potential anti-icing ability on the samples.

3.4.2 HumiSeal 1C49

HumiSeal 1C49 is a room temperature vulcanised (RTV) silicone rubber liquid with high viscosity that consists of methyloximosilane. Different concentrations of the HumiSeal coating solution were obtained by dilution with acetone solvent. A Mega DC 100 dip coater was used for applying HumiSeal coatings, as shown in Figure 3.9. The coating solution was transferred to an appropriate size container that allowed the whole sample to be dipped in. The container and the dip coater were set up to an appropriate position. A cleaned substrate was clamped and adjusted onto the dip coater to make sure it could be dipped into the container without touching any edges. Dipping occurred at a speed of 10 mm/min, and the sample was submerged for 20 s. The removal occurred at the same rate, and the coated substrate was allowed to dry at room temperature for 24 h.

Aluminium, silicone rubber, and EPDM rubber substrates were dip-coated in a pure HumiSeal coating solution. After the coating dried, the contact angle and coating thickness on the different substrates were measured. Each of the contact angle and the coating thickness measurements were repeated five times, and the average result was calculated. 4 μL of water drop size was used during the measurement.



Figure 3.9 MEGA DC 100 Dip Coater

Table 3.3 shows that all the HumiSeal dip-coated substrates had reduced contact angle performances compared with the uncoated substrates (reduced by 14.6°, 22.0°, and 0.6° respectively). The coating thicknesses of the different substrates were varied from 167.5 μm to 185.4 μm . Due to the high viscosity of the coating solution, samples were easily contaminated with ambient dirt during measurement. The HumiSeal coating tended to decrease the water and dust repellent ability of the substrates, and thus this type of coating was ruled out as an ineffective solution to achieve superhydrophobicity.

Table 3.3 Contact angle and coating thickness of HumiSeal coated substrates

Substrate Types		Aluminium	Silicone Rubber	EPDM Rubber
Contact Angle (°)	Uncoated Samples	108.2	113.0	108.5
	Coated Samples	93.6	91.0	107.9
Coating Thickness (μm)		167.5	174.2	185.4

3.4.3 Stearic Acid

Stearic acid is a waxy solid saturated fatty acid with a chemical formula of $C_{17}H_{35}CO_2H$, which can be used as a coating solvent to produce hydrophobic surfaces by providing necessary surface roughness and low surface energy [105]. One gram of stearic acid was dissolved in 50 ml of acetone to make the coating solution. The stearic acid coating was sprayed on the etched aluminium substrates. After the coating dried, contact angles on the stearic acid coated aluminium substrates were measured. Each of the contact angle measurements was repeated five times, and the average result was calculated. 4 μ L water drops were used during the measurements.

Figure 3.10 indicates that the average contact angle of the stearic acid coated aluminium substrates was 130.5° . Compared with the uncoated aluminium substrate, the average contact angle of the stearic acid coated substrate had a 22.3° increase. However, the sliding angles of the coated substrates could not be measured, indicating the large hysteresis of the coated surfaces.

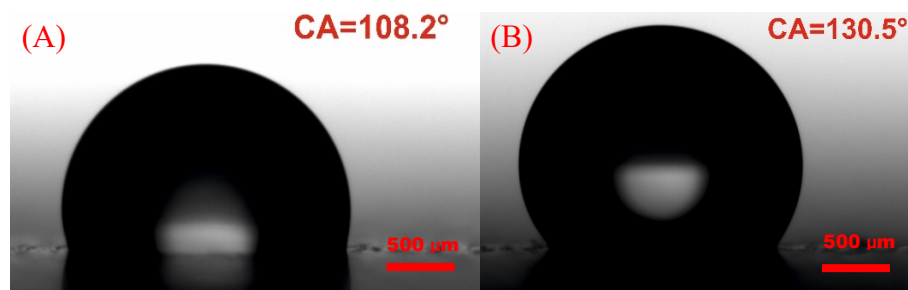


Figure 3.10 Comparison of water droplet images on (A) uncoated substrate and (B) stearic acid coated aluminium substrate

Overall, the stearic acid coating only achieved a low hydrophobic performance on the substrates. Jafari's study shows the stearic acid coating achieves 154° of the contact angle on a polished aluminium substrate, but it also has a large surface hysteresis [62]. However, the stearic acid coating in this experiment did not achieve the superhydrophobic performance on the samples, which might be due to the differences in the surface roughness of base aluminium substrates and other deviations during the coating deployment and sample

measurements. Some studies suggest different approaches to improve the performance of stearic acid coating on aluminium substrates, such as etching the substrates in hydrochloric acid (HCl) as a pre-treatment to modify the roughness of the base substrates, or combining the stearic acid with nanoparticles to achieve nano/micro-structures on the surfaces [62][106][107]. As such, further experiments regarding HCl etching pre-treatment and nano/micro-structure coating are discussed in the next two sections.

3.4.4 HCl Etching Pre-treatment

3.4.4.1 Etching Performance

In Sarkar's study, aluminium substrates were etched in HCl for 4 mins and then immersed in the stearic acid solution for 30 mins, which achieved contact angles higher than 170° on the surfaces [107]. In Zang's study, polished aluminium substrates were etched in HCl for 1.5 mins and then modified with stearic acid in N,N0-dimethylformamide water mixture at 99°C for 30 mins. This achieved contact angles of up to 167.3° [106]. This experiment aimed to identify whether the simple pre-treatment of the HCl etching on aluminium substrates can help to generate some surface structures and improve the wettability performance of the stearic acid spray coating.

Different HCl etching times (from 2 to 4.5 mins) were used on the untreated aluminium substrates according to the etching procedures in section 3.2.2.2. During the etching pre-treatment, the first minute of etching produced no hydrogen gas because the HCl initially reacted with the surface oxide layer of the aluminium substrate. When hydrogen bubbles started to show up, the surface etching process began. The etching reaction became the strongest between 2 and 4 mins. The longest etching time used in this experiment was 4.5 mins. Surface microscopies were examined on the untreated, the 2 mins etched, and the 4 mins etched aluminium substrates. The stearic acid coating was then applied on the etched aluminium substrates. Contact angles were measured five times on each of the coated samples using $4\ \mu\text{L}$ droplets.

Figure 3.11 compares the microscopy images of the untreated aluminium substrate after etching in the HCl solution for 2 and 4 mins. Before the etching, the untreated aluminium substrate showed some strip patterns on the surface due to the mechanical cutting. After 2 mins of the etching, the top layer of the aluminium substrate was damaged from reacting with the hydrochloric acid, and the strip patterns were lost partially. With 4 mins of the etching, the damage on the surface became sufficiently severe that few strip patterns could be observed, and irregular textures were displayed on the surface.

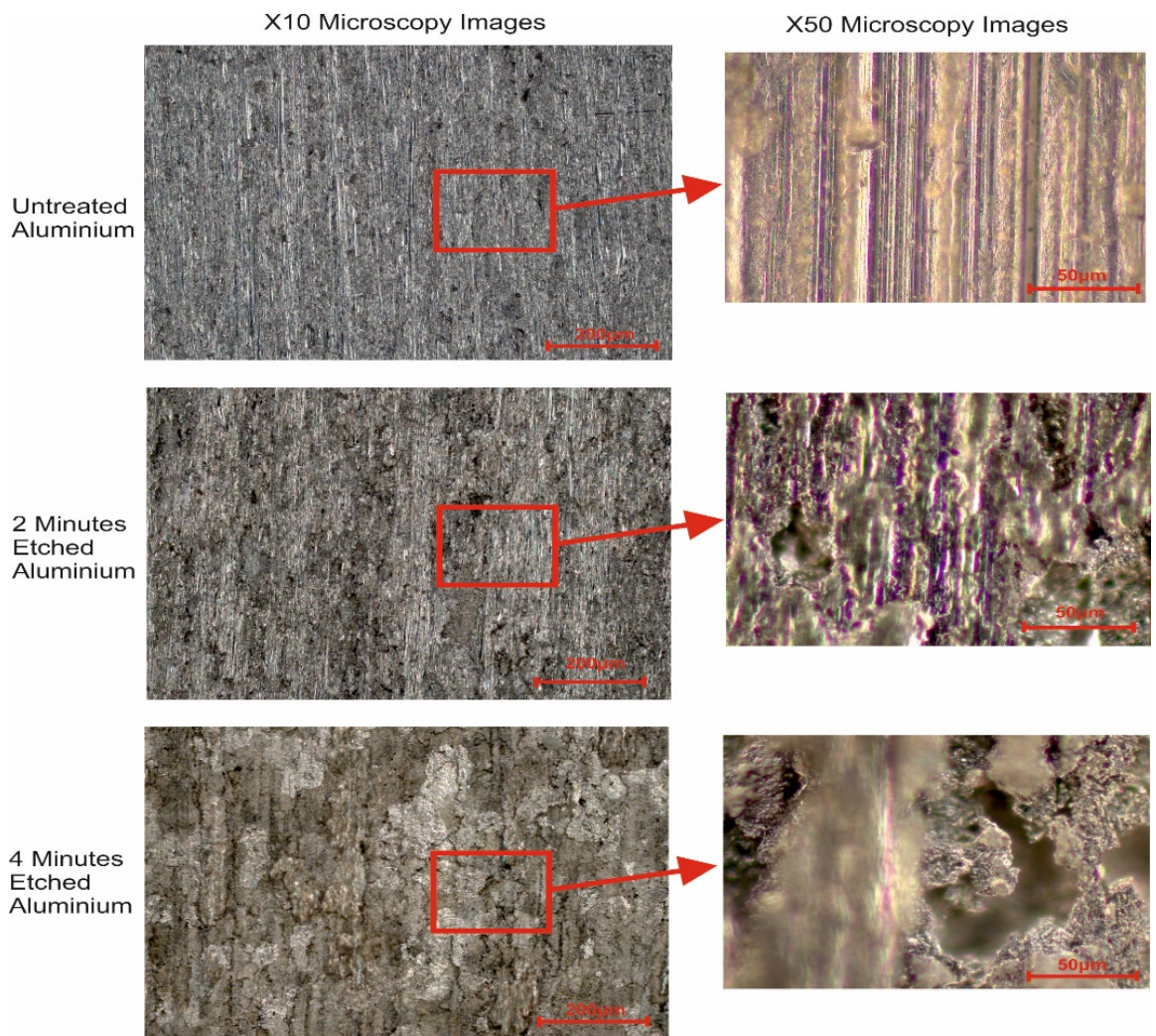


Figure 3.11 Comparison of microscopy images of the aluminium substrates under 2 and 4 mins of the etching times

Table 3.4 shows the contact angles on the HCl etched and the stearic acid coated aluminium substrates with the different etching times. It is noted that the highest contact angle of 130.5°

was reached on the 4 mins etched and the stearic acid coated substrate. However, this highest contact angle was identical to that of the stearic acid coated aluminium substrates without the etching pre-treatment. The result proves that the HCl etching pre-treatment was ineffective in improving the hydrophobicity of the stearic acid coating in this experiment. Superhydrophobicity was not achieved in this study by using the HCl etching pre-treatment as described in the Sarkar's and the Zang's studies [107][106], which may be due to the difference in the substrate roughness levels, combinations of coating materials, and the coating deposition methods.

Table 3.4 Contact angles of aluminium substrates after different times of etching, coated with stearic acid

Etching Time (mins)	2	3	3.5	4	4.5
Contact Angle (°)	120.1	118.2	127.3	130.5	128.8

3.4.4.2 Etching Recovery

It is also noted that after the HCl etching process on the untreated aluminium substrates, they became immediately hydrophilic and then gradually recovered over time with an increase of hydrophobic performance. An etching recovery test was carried out by placing each of the 2 and the 4 mins HCl etched aluminium substrates at room temperature and at 55 °C respectively to see how quickly hydrophobicity of the surface could be recovered after etching. Contact angles and contact angle hysteresis were measured frequently until the samples reached their steady states.

Figure 3.12 compares both the contact angle (CA) and the contact angle hysteresis (CAH) recovery curves of the 2 mins etched aluminium substrates at room temperature and at 55 °C. At room temperature, it took approximately 20 days for both the contact angle and the contact angle hysteresis to reach their steady states at 118° and 19°. This recovery time was shortened to just 2 days at 55 °C, achieving similar steady state values of the contact angle (120°) and contact angle hysteresis (19°). This result proves that the hydrophobic recovery

of the samples after the etching is faster at a higher temperature. Thus, another experiment was carried to compare the recovery rates of the contact angles and contact angle hysteresis of both the 2 and 4 mins etched aluminium substrates at 55 °C, as shown in Figure 3.13. The 4 mins etched substrate recovered in around 50 h, with a contact angle that increased from around 0° to 135°, and contact angle hysteresis that decreased from around 40° to 10°. The 2 mins etched substrate recovered in a similar timescale, with contact angle increasing from around 70° to 120°, and hysteresis decreasing from around 45° to 19°. The 2 mins etched substrate had an initially higher but eventually lower contact angle than that of the 4 mins etched substrates, due to the 2 mins etching being insufficient to modify the surface structure to reach a higher hydrophobicity.

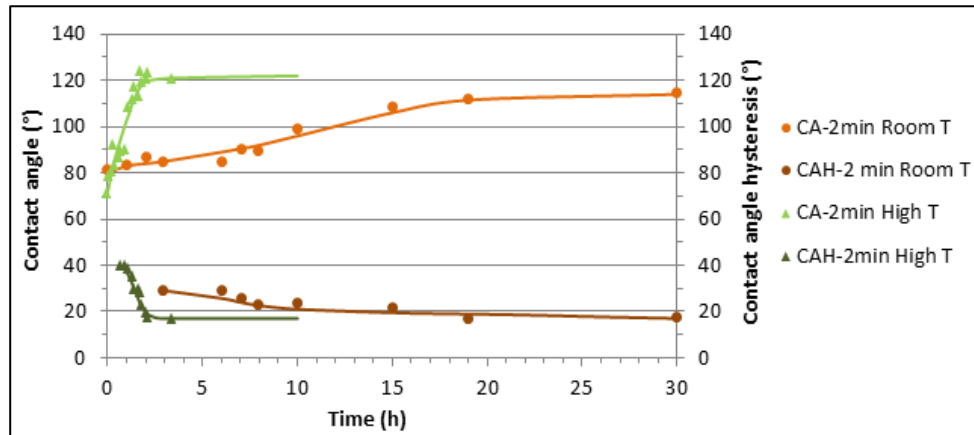


Figure 3.12 Contact angle and contact angle hysteresis of 2 mins etched aluminium substrates being recovered at room temperature (T) and 55 °C

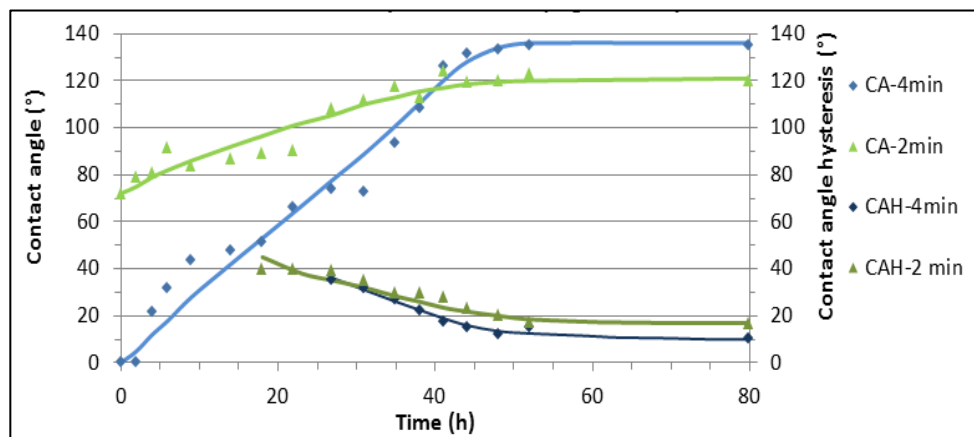


Figure 3.13 Contact angle and contact angle hysteresis of 2 and 4 mins etched aluminium substrates being recovered at 55 °C

Overall, the 4 mins etching on the aluminium substrates produces a higher hydrophobicity level than the 2 mins etching after the surface recovery. Additionally, the higher temperature of 55 °C contributes to a quicker recovery process of the etched surfaces and achieves a better hydrophobic performance than the room temperature. In order to speed up the recovery time or to further improve the hydrophobicity after etching, other methods may also be used for the recovery process. A HCl etched aluminium substrate was firstly immersed in the potassium permanganate solution for 180 mins and then immersed in the ethanol solution of trichloro (1H,1H,2H,2H-heptadecafluorodecyl) silane for more than 10 h, which achieved a maximum contact angle of 153.5° [108]. A treated aluminium substrate achieved a high contact angle of 161.9°, which was firstly etched in CuCl₂ and HCl solutions, and then modified by hexadecyltrimethoxy silane at room temperature for 60 mins and recovered at 90 °C for 30 mins [36].

3.4.5 Stearic Acid with SiO₂ Nanoparticles

SiO₂ nanoparticles have been widely used to form microstructures on surfaces to increase their hydrophobicity [109][110][111]. 1 g of stearic acid and 0.2 g of SiO₂ nanoparticles (with a diameter of approximately 500 nm) were dissolved in 100 ml of acetone. A water bath was used to heat the solution to 30 °C, and then the solution was mixed using a magnetic stirrer at 800 rpm for 1 h. The coating solution was transferred to a Metabo FSP 600 spray gun, supplied by an air compressor with 4 bars of air pressure. The coating was evenly sprayed on the substrate at a distance of 25 cm, followed by drying at room temperature overnight.

3.4.5.1 Performance of Stearic Acid with SiO₂ Nanoparticle Coating after Etching

A HCl acid etched aluminium substrate was divided into three areas as shown in Figure 3.14, in the interest of exploring the performance of the stearic acid with SiO₂ nanoparticle coatings with different thicknesses. Three coating thicknesses on the substrate were obtained by applying 2, 5, or 10 spray layers. Contact angle measurement was repeated three times on each of the coating areas, and the average result was calculated. 4 μ L water drop size was used during measurement.

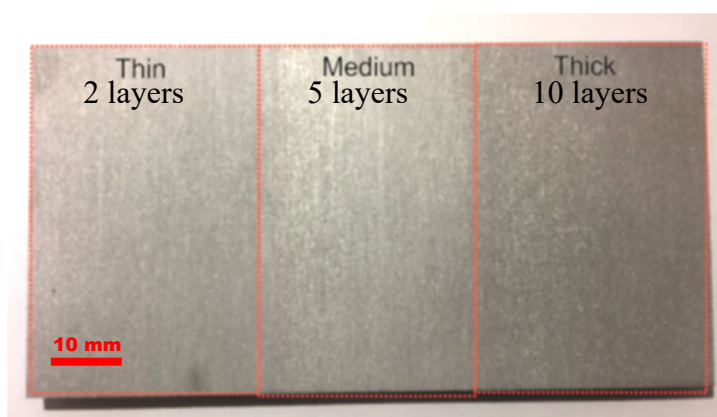


Figure 3.14 Different thicknesses of stearic acid with SiO₂ nanoparticle coating on the hydrochloric acid etched aluminium substrates

Table 3.5 indicates that increasing coating thickness increases the degree of the hydrophobicity. The thin coating with only 2 sprayed layers had the least average contact angle of 127.4°, while the 5 layers of the coating increased the surface contact angle to 136.0°. The 10 layers of spraying showed the best performance that achieved the average contact angle of 142.4°. These results indicate that the coating with 10 spray layers was more effective than the coatings with 2 or 5 spray layers to produce certain surface roughness with reduced energy on the surface. However, none of the coatings achieved superhydrophobicity by using this method. The sliding angles were larger than 60° for all the coated substrates, meaning all the surfaces were the Wenzel model with large surface hysteresis. Under this circumstance, an optimised coating deployment system was investigated to improve the hydrophobicity and to reduce surface hysteresis on the samples.

Table 3.5 Contact angles for different thicknesses of stearic acid with SiO₂ nanoparticle coating on an etched aluminium substrate

Coating Layers	2		5		10	
	Left	Right	Left	Right	Left	Right
Contact Angle (°)	126.0	126.1	136.3	136.3	141.6	141.7
	127.5	127.7	133.9	134.1	142.1	142.1
	128.5	128.7	137.7	137.8	143.5	143.1
Average (°)	127.4		136.0		142.4	

3.4.5.2 Optimised Spray Coating of Stearic Acid with SiO₂ Nanoparticles

Different methods and parameters were used to optimise the experimental procedure for deployment of the stearic acid with SiO₂ nanoparticle coating by using a high-pressure spray gun. The contact angles of uncoated and unaltered AA6082 aluminium alloy substrates were first measured to derive the reference contact angle using the zoom-in method described in Section 3.3.1. 6 aluminium samples were used in total, and each sample had five repeat measurements to calculate the average contact angle. The results shown in Table 3.6 indicate that uncoated aluminium substrates have an average contact angle of 87°, which is close to the threshold of hydrophobicity.

Table 3.6 Average contact angles of uncoated aluminium substrates

Sample	1	2	3	4	5	6	Average
Contact angle (°)	87.1	87.4	87.5	86.7	87.3	86.1	87.0

a) Varying coating stirring methods and different spray times

Whether stearic acid and SiO₂ nanoparticles in the coating solution should be stirred and dissolved together or separately might affect the final performance of the coating. Different coating spray times can produce different coating thicknesses and surface geometries. In this experiment, two coating solutions were prepared. The first one was a twice-mixed solution by stirring the stearic acid first and then adding the SiO₂ nanoparticles to be remixed, and

the second one was a single-mixed solution by stirring the stearic acid and SiO₂ nanoparticles together at the same time. Different spraying times (10, 30, and 50 s) were used on each of the coating solutions, with an extra 70 s of spraying time on the single-mixed solution. Except for the coating stirring methods and the spraying times, the rest of the parameters were kept the same. 7 aluminium samples were used in total, and the contact angles of each sample were measured 5 times per sample. The sliding angle measurements were each taken 3 times per sample.

The result in Table 3.7 indicates that the single-mixed coating solution produced an overall better performance with larger contact angles and smaller sliding angles than that of the separate stirring method. For the twice-mixed solutions, the water drops did not slide on any of the samples, which indicates all the samples were the Wenzel model with large surface hysteresis. In terms of different spray times, the samples with 30, 50, and 70 s spray times using the single-mixed solution achieved superhydrophobic performance with contact angles larger than 160°. The sample with a 70 s spray time, resulted in the smallest sliding angle of 4.5°. This result indicates coatings with less spray time may not create sufficient water-repellent surface structures, and a thicker coating may be required to increase the superhydrophobicity of the surfaces.

Table 3.7 Average contact angles and sliding angles of coatings with different stirring methods and different spray times

Spray Time (s)	Twice-mixed Solution			Single-mixed Solution			
	10	30	50	10	30	50	70
Contact Angle (°)	120.1	150.6	130.3	148.2	163.9	165.6	163.8
Sliding Angle (°)	Did Not Slide	Did Not Slide	Did Not Slide	Did Not Slide	9.0	11.7	4.5

Overall, the single-mixed solution achieved better superhydrophobic performance than the twice-mixed solution. The single-mixed solution was used for future experiments. The thicker coating with longer spray time produced a smaller sliding angle. In the following test, to further optimise the sliding angle performance, a spray gun was tested with a higher flow volume to increase coating thickness.

b) Varying flow volumes of the spray gun and different spray times

It was shown in the last experiment that the thicker spray coating produced the smaller sliding angle of the surface. In this experiment, thicker coatings were produced by using longer spray times or a higher flow volume to further improve the superhydrophobic performance of the samples. In the first test, 30, 50, 70, and 90 s spray times were used with the original flow volume setting. In the second test, a higher flow volume setting with 5, 10, 15, and 20 s spray times were used. The flow regulating screw on the spray gun was opened by approximately 1/4 rotation for the original flow volume, and 1/2 rotation for the higher flow volume. Aside from flow volumes and spray times, the remaining parameters were kept the same. 8 aluminium samples were used in total and their contact angles were measured 5 times. Their sliding angles were measured 3 times.

Table 3.8 indicates that under the original flow volume setting, spray times of 70 and 90 s both achieved better superhydrophobic performance with the large contact angles and small sliding angles compared to the shorter spray times. All the samples under the high flow volume setting achieved superhydrophobicity, and 10 s spray time achieved superhydrophobicity with the smallest sliding angle of 5.8°.

Table 3.8 Average contact angles and sliding angles of coatings with differing flow volumes and spray times

	Original Flow Volume (1/4 Rotation)				Higher Flow Volume (1/2 Rotation)			
	30	50	70	90	5	10	15	20
Spray Time (s)	30	50	70	90	5	10	15	20
Contact Angle (°)	136.5	163.0	165.0	164.3	163.7	160.0	158.6	158.1
Sliding Angle (°)	Did Not Slide	Did Not Slide	9.3	7.5	7.8	5.8	7.7	10.8

Overall, the higher the flow volume setting (1/2 rotation of the regulating screw), the better the performance and reproducibility. This result was used for future experiments.

c) Using a homogeniser with different spray times

It was noticed from the previous experiments that the stearic acid with SiO₂ nanoparticle coating solution could not always be adequately mixed using the magnetic stirrer and large visible particles remained suspended in the solution. In this experiment, a homogeniser was used to further improve the quality of the coating solution. Two coating solutions were prepared with and without the homogeniser. The first solution was prepared using a homogeniser at a speed of 5000 rpm for 10 mins after 2 h of magnetic stirring at 800 rpm, followed by heating the solution in a water bath at 30 °C for 5 mins and magnetic stirring at 800 rpm for 1 h. The second solution was prepared by using the magnetic stirrer without the homogeniser, with the rest of the procedures unchanged. Different spray times of 5, 10, 15, and 20 s were used to deploy both coating solutions. Aside from the homogeniser and spray time settings, all other parameters were kept the same. 8 aluminium samples were used in total, and the contact angle and sliding angle of each sample was measured 5 times.

As shown in Table 3.9, both preparation methods with and without the homogeniser achieved superhydrophobic performance on all the samples, with a contact angle higher than

160°. Compared to the method using a magnetic stirrer only, the sliding angles of the samples under all the spray times were much lower (less than 7.3°) after use of the homogeniser.

Table 3.9 Average contact angles and sliding angles of coatings with different stirring methods and different spray times under high flow volume

	Spray Time (s)	5	10	15	20
Magnetic Stirrer Only	Contact Angle (°)	160.8	163.2	162.5	163.3
	Sliding Angle (°)	Did Not Slide	11.2	10.0	18.7
Magnetic Stirrer & Homogeniser	Contact Angle (°)	165.2	162.9	162.9	165.4
	Sliding Angle (°)	5.6	5.8	7.3	5.3

Overall, by using a combination of magnetic stirrer and homogeniser to prepare the coating solution, better superhydrophobic performance and higher reproducibility of the coatings were achieved. This coating preparation method was used for future experiments.

d) Varying spray distance and spray times

In order to further improve the reproducibility of the stearic acid with SiO₂ nanoparticle coating, a spray board was designed to control spray distance from the spray gun nozzle to the substrates. Two different spray distances (15 and 25 cm) and four different spray times (5, 10, 15, and 20 s) were used to deploy the coating. Except for the spray distance and spray time, the rest of the parameters were kept the same. 8 aluminium samples were used in total, and for each sample the contact angles and the sliding angles were measured 5 times.

Table 3.10 demonstrates that a 25 cm spray distance produced a more stable performance with contact angles larger than 160° and sliding angles less than 10°, compared with that of the 15 cm spray distance. The overall best superhydrophobic performance was achieved using a 25 cm spray distance and 20 s spray time, of which the surface performed the smallest sliding angle of 4.0°.

Table 3.10 Average contact angles and sliding angles of coatings with different spraying distances and different spray times

Spray Distance (cm)	Spray Time (s)	5	10	15	20
15	Contact Angle (°)	162.8	162.9	163.3	163.4
	Sliding Angle (°)	9.9	8.1	Did Not Slide	11.3
25	Contact Angle (°)	168.3	163.5	165.5	168.1
	Sliding Angle (°)	9.3	8.9	5.4	4.0

A spray distance of 25 cm shows overall better superhydrophobic performance and higher reproducibility, which may generate a more uniformed coating on the surface. Therefore, a spray distance of 25 cm was used for further experimentation.

e) Varying stirring speeds of homogeniser

In this experiment, homogeniser stirring speeds of 5000 rpm and 7000 rpm were used to optimise the performance of the coating solution. All other parameters were kept the same. 2 aluminium samples were used in total, and the contact and sliding angles of each sample were measured 5 times.

Table 3.11 indicates the sample using the homogeniser with 5000 rpm stirring speed achieved better performance than the sample with 7000 rpm. A larger contact angle of 168.3° was achieved, and a smaller sliding angle of 5.1°.

Table 3.11 Average contact and sliding angles of coatings using homogeniser with different stirring speeds

Stirring Speed (rpm)	5000	7000
Contact Angle (°)	168.3	166.4
Sliding Angle (°)	5.1	6.0

As the coating solution produced using the homogeniser with a speed of 5000 rpm performed overall better superhydrophobic performance than that of the 7000 rpm, the 5000 rpm speed was used for further experimentation.

f) Varying spray times

In this experiment, different spray times (15, 20, 25, and 30 s) were used to optimise the performance of the coating with a spray distance of 25 cm and homogeniser stirring speed of 5000 rpm. Aside from spray time, the remaining parameters were kept the same. 4 aluminium samples were used in total, and the contact and sliding angles of each sample were measured 5 times.

The results in Table 3.12 show that all the samples produced by different spray times achieved superhydrophobic performance, with contact angles larger than 165°, and the sliding angles less than 10°. As the 20 s spray time achieved the best performance with the smallest sliding angle of 4.7°, these parameters were used for future experiments.

Table 3.12 Average contact and sliding angles of coatings with different spray times

Spray Time (s)	15	20	25	30
Contact Angle (°)	169.7	169.3	166.2	167.0
Sliding Angle (°)	6.1	4.7	7.7	9.4

It was noted that the spray volume distributed by the spray gun was not always consistent during the 20 s spray time. This may be due to air pressure in the spray gun varying during application. In order to maintain a uniform coating, the 20 s spray time was divided into 4 separate 5 s sprays in order to allow the air pressure in the gun to be refilled to a consistent level.

g) Reproducibility of the optimised method

To calibrate the reproducibility of the optimised method, a total of 48 samples were made using the optimised method. The contact and sliding angles were measured 3 times per sample. Table 3.13 shows the contact and sliding angle measurements of the 48 stearic acid with SiO₂ coated samples produced using the optimised procedures. All the samples achieved superhydrophobic performance with an average contact angle of 164.4° and an average sliding angle of 4.7°. Both the contact angle and sliding angle demonstrate small

standard deviations of 1.9° and 1.0°, respectively. These results indicate the optimised method has a good reproducibility for the deployment of the stearic acid with SiO₂ coating, as it consistently achieves a high level of superhydrophobicity on samples.

Table 3.13 Contact and sliding angle measurements of 48 stearic acid with SiO₂ coated samples using the optimised method

Sample	1	2	3	4	5	6	7	8	9	10	11	12
Contact Angle (°)	168.3	167.1	166.8	168.9	168.0	167.1	164.6	162.4	163.7	161.4	163.5	163.0
Sliding Angle (°)	3.8	3.8	3.8	4.2	3.5	3.9	4.5	4.2	4.7	4.7	6.3	6.2
Sample	13	14	15	16	17	18	19	20	21	22	23	24
Contact Angle (°)	164.3	163.6	164.2	161.2	162.5	163.5	160.2	164.1	166.0	166.3	166.3	163.6
Sliding Angle (°)	6	6.2	6.5	5.8	6.2	6.5	5.8	5.5	5.8	5.5	5.5	5.5
Sample	25	26	27	28	29	30	31	32	33	34	35	36
Contact Angle (°)	164.6	163.8	165.4	164.5	161.3	164.7	164.6	166.9	165.7	162.7	163.7	164.6
Sliding Angle (°)	4.0	3.8	4.2	3.3	5.3	3.5	4.2	4.0	3.7	4.8	4.0	4.2
Sample	37	38	39	40	41	42	43	44	45	46	47	48
Contact Angle (°)	163.8	167.4	164.8	163.4	164.6	163.8	165.1	163.2	165.9	161.9	164.5	163.5
Sliding Angle (°)	5.7	3.5	4.7	5.0	3.7	3.8	4.0	4.2	3.7	4.7	4.2	4.0

Overall findings: By carrying out all the experiments above, an optimised experimental procedure was obtained for deploying the stearic acid with SiO₂ nanoparticle coating. Several main conclusions and the chosen parameters for the optimised procedure are listed as below:

- The stearic acid and SiO₂ nanoparticles should be stirred together to prepare the coating solution.
- A higher flow volume setting with 1/2 rotation of the regulating screw should be used on the spray gun.

- The combination of the magnetic stirrer at 800 rpm and the homogeniser at 5000 rpm should be used to mix the coating solution.
- A spray distance of 25 cm between the sample and the spray gun nozzle should be used to spray the coating.
- A total coating spray duration of 20 s should be divided into 4 distinct 5 s sprays to achieve a stable spray size and a uniform coating.

3.4.6 NeverWet

NeverWet (full name: NeverWet multi-surface liquid repelling treatment) is a commercial coating produced by Rust Oleum. This coating has a two-step spray process and can achieve superhydrophobic performance with a surface contact angle of approximately 160° . The base layer mainly consists of aliphatic hydrocarbons, which can be used to produce microstructures on surfaces. The main components of the top layer include acetone, propane, n-Butane, and silicone, where silicone particles can be used to fill the gaps among the base layer microstructures to improve superhydrophobic performance.

A cleaned substrate test sample was placed in the fume cabinet, and the two-step NeverWet coating was ready to be sprayed at a distance of 25 cm. The base coating was sprayed twice on the surface with 15 mins in between each spray. The substrate was then allowed to dry for 30 mins. The top coating was applied twice with 15 mins in between. 30 mins were allowed for the samples to dry completely before testing.

3.4.6.1 Characterisation Tests on NeverWet

The NeverWet coating was sprayed on cleaned and untreated aluminium, silicone rubber, and EPDM rubber substrates to produce superhydrophobic surfaces. The contact angles and sliding angles on each of the sample were measured 3 times to calculate the average results. 4 μL of water droplet size was used during the measurements.

Figure 3.15 demonstrates the base and top layers of the NeverWet coating under optical microscopy. After the base layer was sprayed, several micro-sized particles were noticed in Figure 3.15 (a), forming bumps randomly distributed on the substrate. Those bumps formed micro-geometric structures on the surface and increased the surface roughness to the micro-level, which prevents water drops penetrating the gaps on the surface and contributes to the increase in surface hydrophobicity [35]. The top layer was sprayed after the base layer and formed a white coating on the substrate, as shown in Figure 3.15 (b). The top coating appears to fill the gaps of the base layer and complete the surface roughness to achieve a refined surface geometry. This may help to build a Cassie-Baxter model on the surface by trapping air in gaps on the surface to further increase hydrophobicity and reduce surface hysteresis [45][112].

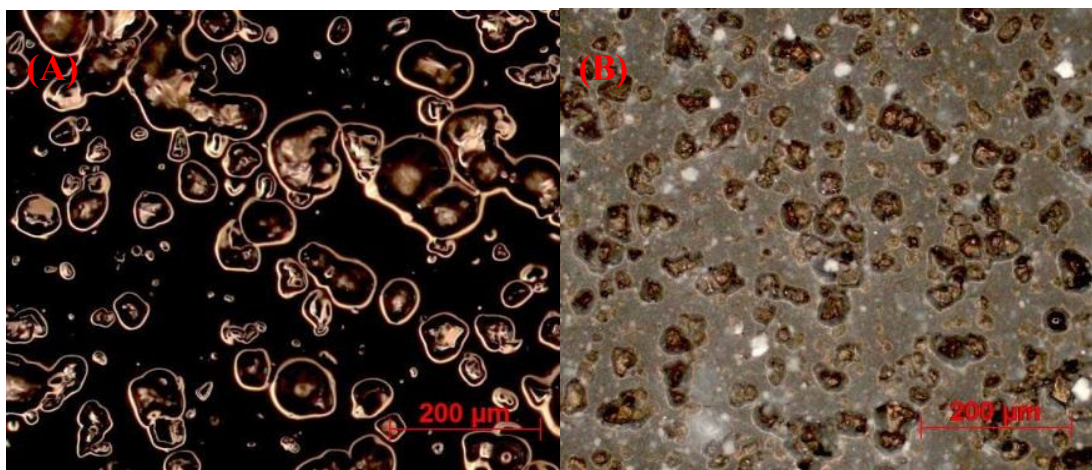


Figure 3.15 Microscope images of (a) base layer only (b) base and top layers of the NeverWet coating

Figure 3.16 compares microscope images of uncoated and NeverWet coated aluminium, EPDM, and silicone rubber substrates. Comparing the coated and uncoated substrates, the mechanical cutting patterns on the aluminium alloy substrate were still visible after coating, while both EPDM and silicon rubber samples showed smoother base surfaces after coating. All NeverWet coated samples showed randomly distributed micro-sized particles on the surface, which leads to a micro-structured roughness and delivers water repellence.

Table 3.14 shows the average contact and sliding angles of NeverWet coated aluminium, silicone rubber, and EPDM rubber substrates. Compared with the uncoated substrates, as

showed in Figure 3.17, the contact angles of all the NeverWet coated substrates achieved significant increases of 54.7° , 41.4° and 51.1° . The sliding angles of all the NeverWet coated substrates are quite similar, varying from 2.9° to 3.8° . The differences in the contact angles of the different substrates may be due to the distinct initial surface roughness of the substrates. Overall, the results indicate that the NeverWet coating can produce superhydrophobic surfaces for all the provided substrates with good water sliding ability.

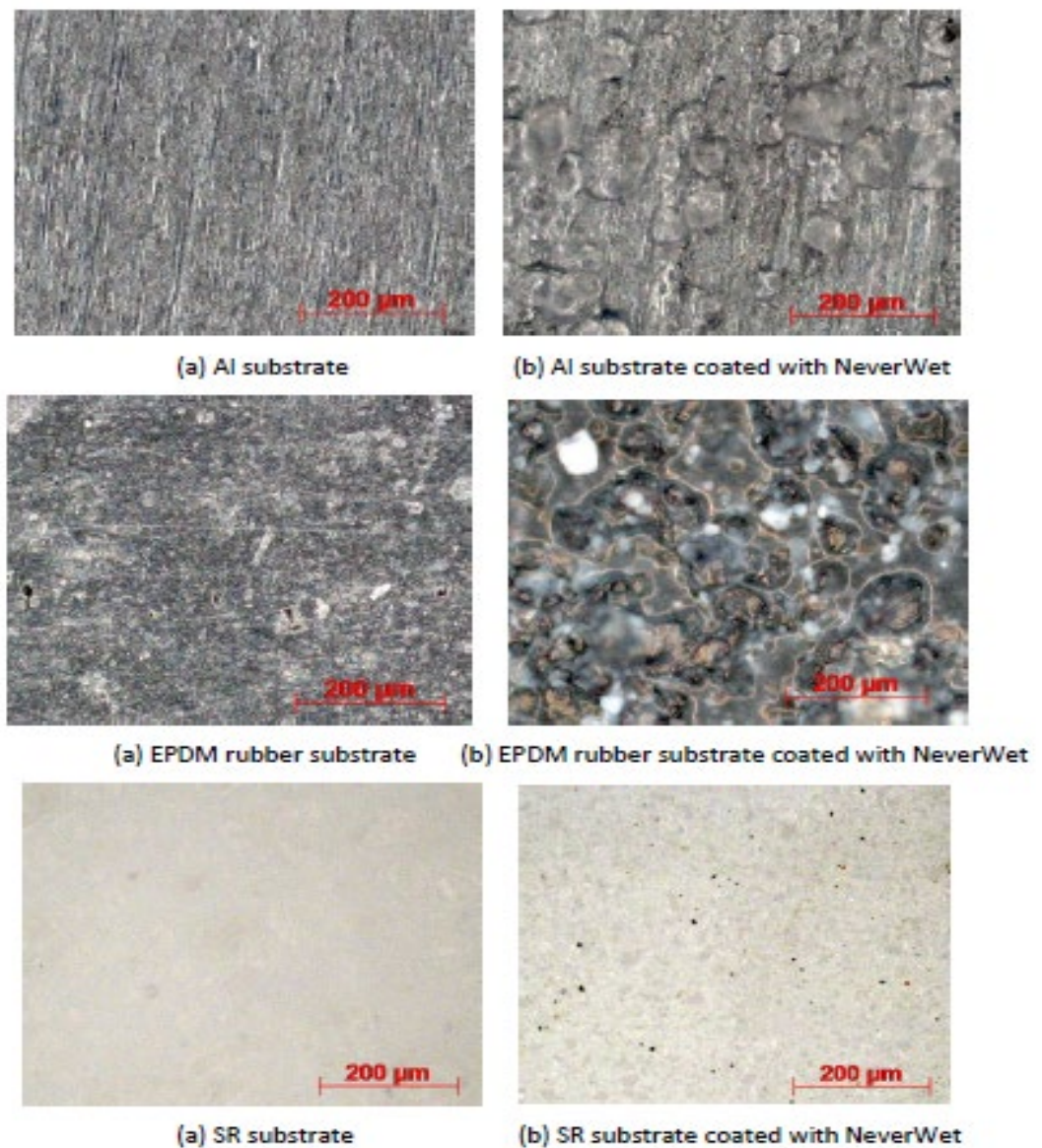


Figure 3.16 Microscopic images of NeverWet coated aluminium (Al), EPDM rubber, and silicone rubber (SR) substrates

Table 3.14 Contact angles of NeverWet coated substrates

	Contact Angle (°)			Sliding Angle (°)		
	Aluminium	Silicone	EPDM	Aluminium	Silicone	EPDM
1	161.6	153.9	160.8	3.0	2.9	3.8
2	163.8	153.9	159.7	2.5	2.8	3.0
3	163.4	155.5	158.2	3.5	3.0	3.9
Average	162.9	154.4	159.6	3.0	2.9	3.6

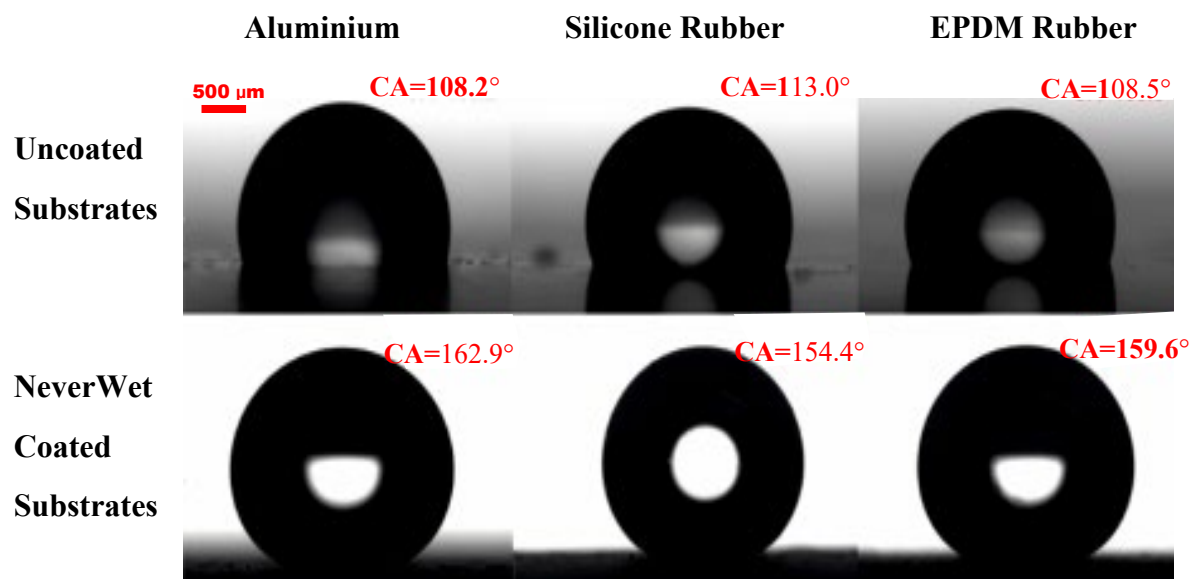


Figure 3.17 Comparisons of contact angles of uncoated and NeverWet coated substrates

3.4.6.2 High-speed Camera Tests on NeverWet Coated and Uncoated Samples

Using a high-speed camera, this test aimed to observe the dynamic behaviour of water drops on flat aluminium surfaces and round overhead conductors. The uncoated and NeverWet coated flat aluminium alloy samples and the GAP-type conductor samples were used in this test. The set-up for this experiment is shown in Figure 3.18. A transparent sample holder was used to secure the conductor samples. While water drops were dispensed onto the samples, slow-motion videos of water drop movement were recorded.

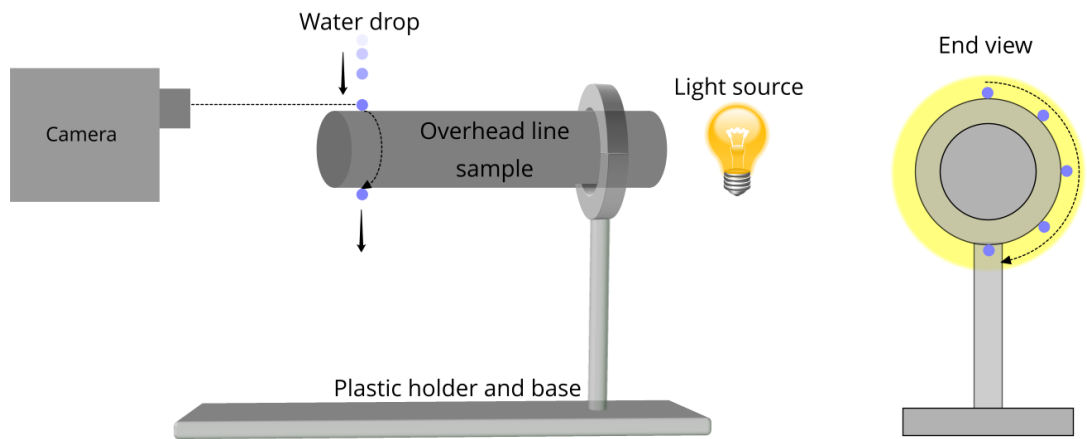


Figure 3.18 Experimental set-up of high-speed camera tests

- **Uncoated Flat Aluminium Alloy Sample**

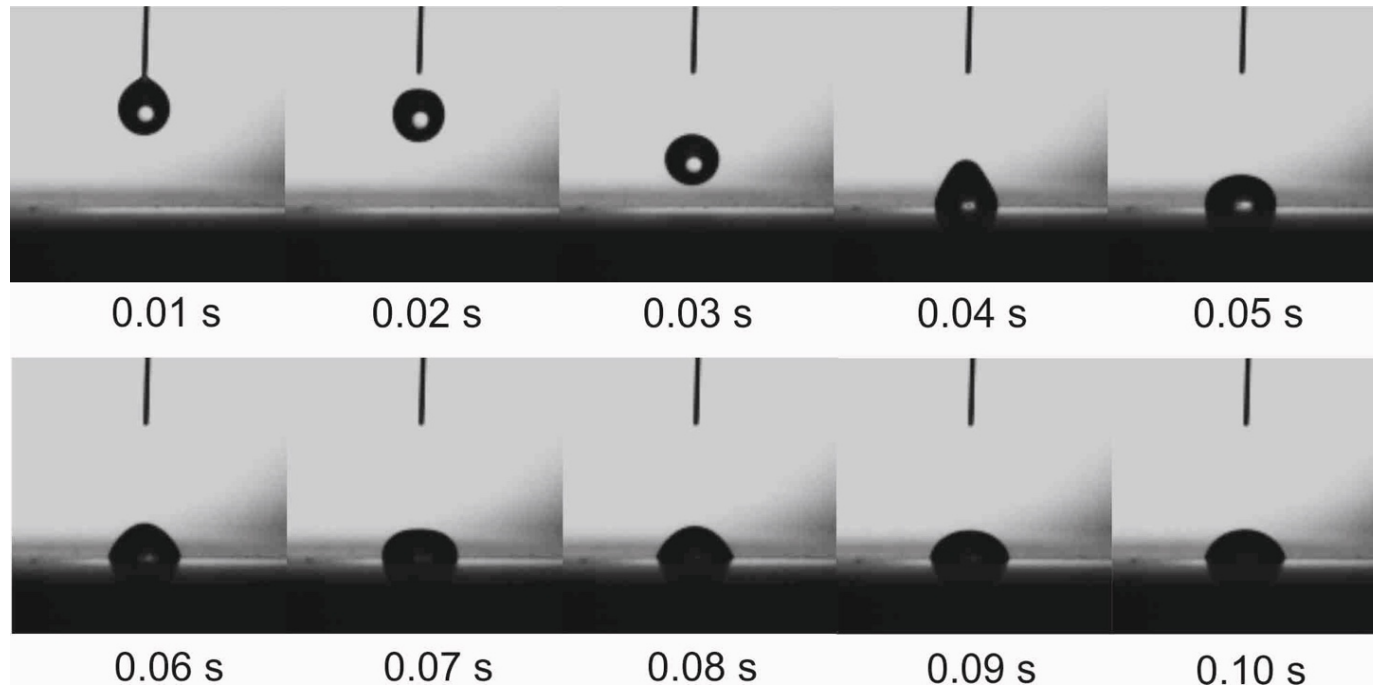


Figure 3.19 Movement of a water drop on an uncoated aluminium flat sample under the high-speed camera

Figure 3.19 shows the movement of a water drop dispensed on an uncoated aluminium flat sample under the high-speed camera. Initially, the water drop landed directly on the surface and attached to the surface. The drop then vibrated on the surface several times, alternating between a hemisphere and a cone shape. Meanwhile, the drop continued to sink and flatten, resulting in the reduction of the contact angle to a minimum value.

- **NeverWet Coated Flat Aluminium Alloy Sample**

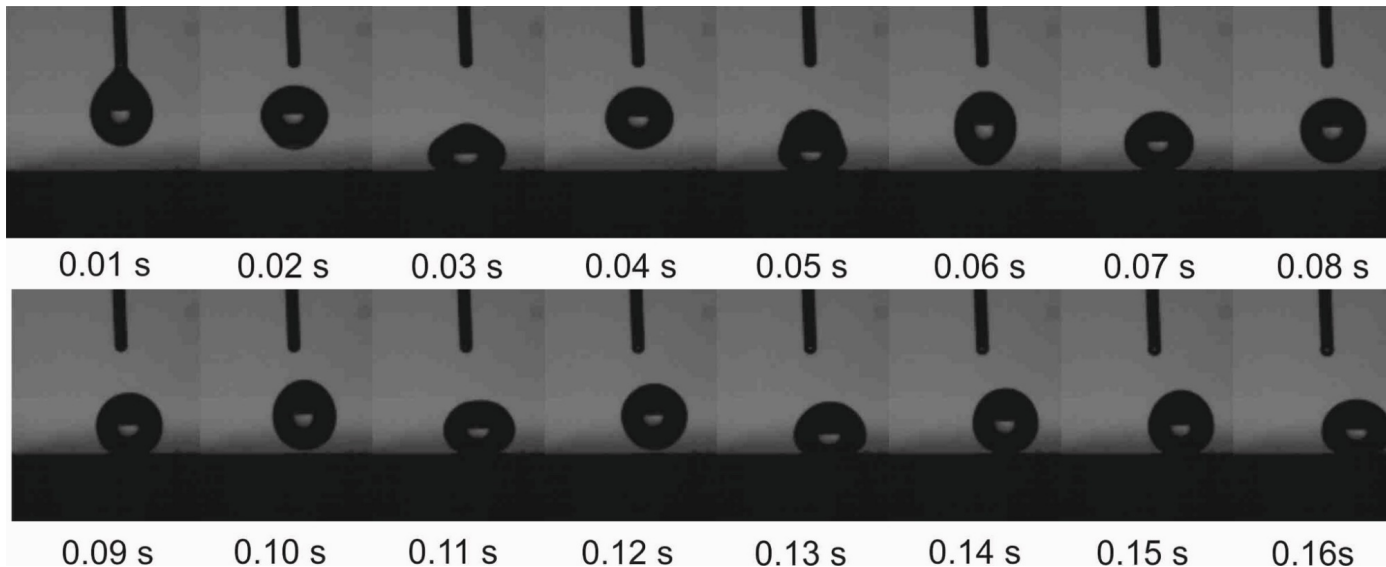


Figure 3.20 Movement of a water drop on a NeverWet coated aluminium flat sample under the high-speed camera

Figure 3.20 demonstrates the movement of a water drop on a NeverWet coated flat aluminium sample under the high-speed camera. Unlike the uncoated sample, the drop initially landed on the NeverWet coated surface and then bounced back to a certain height without sticking firmly to the surface. This bouncing movement repeated several times with the bounce height decreasing each time until the drop eventually landed and attached to the surface. At this moment, the drop displayed a near ellipsoid form with a small surface contact area. The drop also showed a much longer sinking time than that of the uncoated sample.

- **Uncoated GAP-type Conductor Sample**

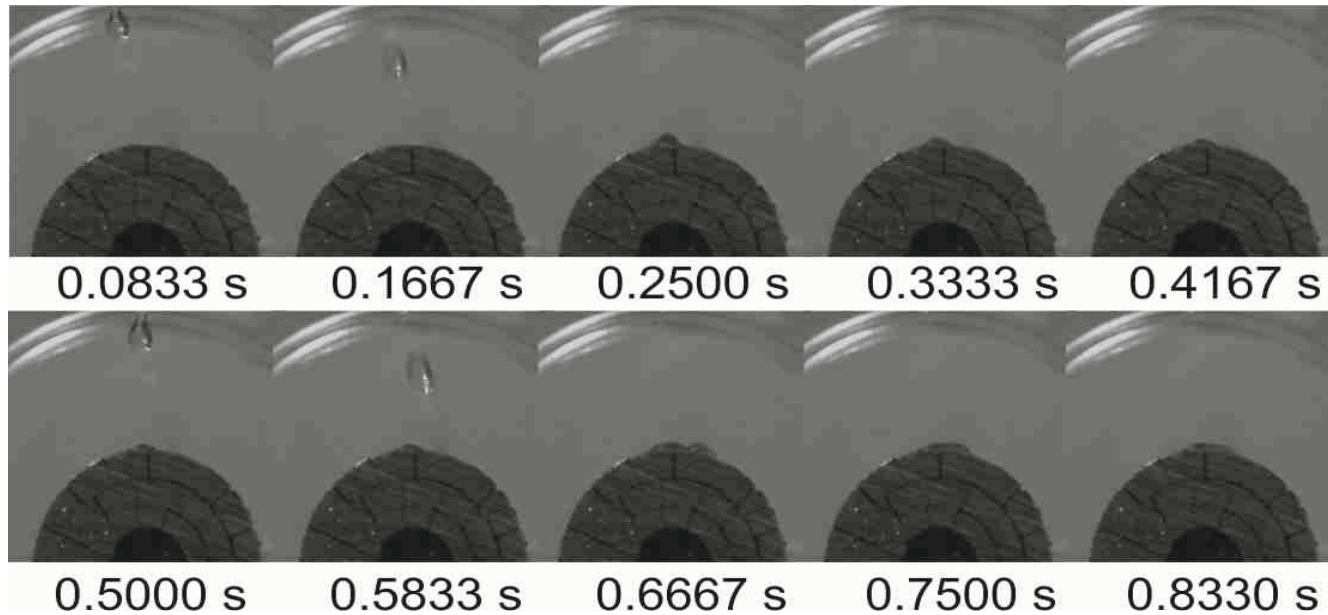


Figure 3.21 Movement of a water drop on an uncoated GAP conductor sample under the high-speed camera

Figure 3.21 shows the movement of water drops dispensed on an uncoated GAP-type conductor sample under the high-speed camera. With a similar result to the uncoated flat sample, the first water drop directly landed on the top of the surface and showed a hemispheric form with the interface side attaching to the surface. The drop continued vibrating and gradually sunk on the surface. The vibration became more noticeable when the second drop landed on top of the first and merged into a larger drop.

- **NeverWet Coated GAP-type Conductor Sample**

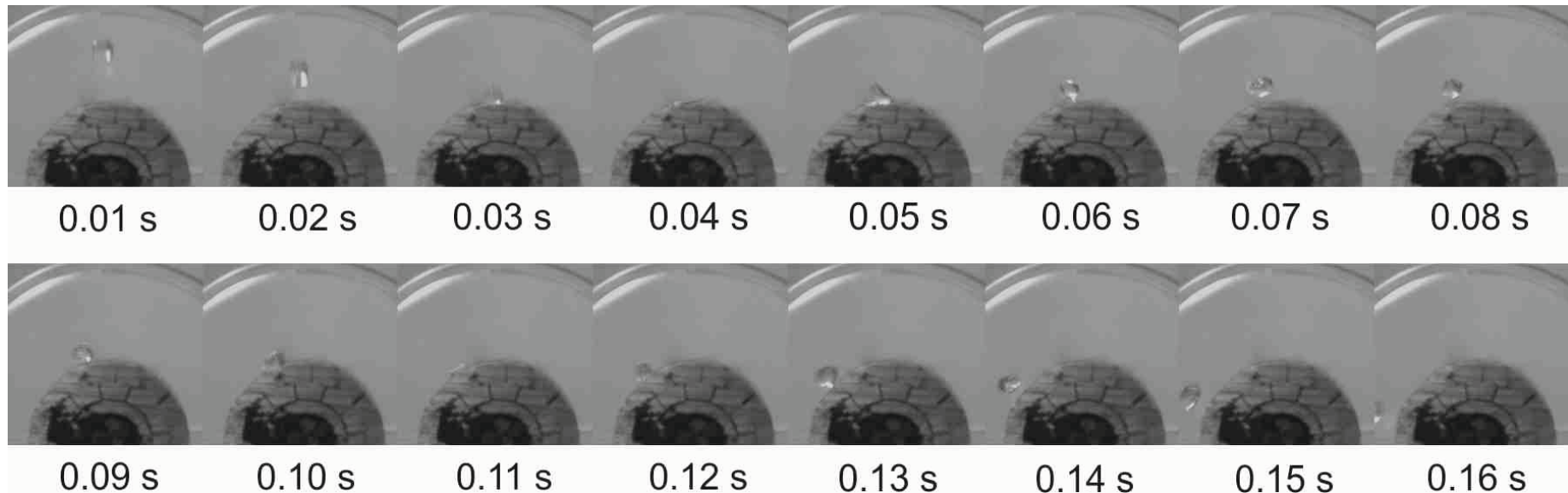


Figure 3.22 Movement of a water drop on a NeverWet coated GAP conductor sample under the high-speed camera

Figure 3.22 demonstrates the movement of a water drop on a NeverWet coated GAP-type conductor sample under the high-speed camera. With a different result to the uncoated conductor sample, the drop landed on the surface of the NeverWet coated conductor, and the shape of the drop was squeezed to an almost flat ellipsoid. The drop then bounced up toward one side of the conductor and landed back on the surface. Finally, the drop bounced up a second time and moved away from the conductor sample without further contacting the surface.

To sum up, both the NeverWet coated flat sample and the NeverWet coated GAP-type conductor sample showed better water-repellent abilities than that of the uncoated samples. With the use of the superhydrophobic treatment on the flat sample, the water drop took longer to finally rest on the surfaces. The likelihood of the drop rolling off the superhydrophobic surface was higher as a result of the smaller sliding angle and larger contact angle. It was also much less likely for water drops to accumulate on the superhydrophobic treated conductor sample as the curve of the surface further assists water drops to slide off. This result proves that the number of water drops on superhydrophobic coated overhead line conductor can be significantly reduced, which can potentially reduce the chance of ice formations and delay ice accumulation on the conductor [52]. The higher contact angle of the superhydrophobic treated surface resulted in a smaller liquid-solid contact area. This may be beneficial during icing weather as a result of the reduced ice adhesion strength [48]. Overall, the high-speed camera tests indicated the potential benefits of superhydrophobic coatings on overhead conductors, including water-repellent, self-cleaning, and anti-icing abilities. Full video of the high-speed camera tests can be found in [113]

3.4.7 Comparisons of Coatings on Substrates with Different Roughness

It is unclear whether different surface roughness can affect the surface wettability performance of stearic acid with SiO₂ nanoparticles or the NeverWet coated samples. This experiment aimed to examine the superhydrophobic performance of coatings on pre-treated surfaces with different roughness. Three types of aluminium surfaces were used, including unaltered, polished, and sandpaper treated samples. The samples were composed of untreated aluminium alloy 6082. The polished samples were prepared by polishing until their surface appeared to have a gloss texture. The sandpaper treated samples were prepared by using 120-grade sandpaper to sand each sample horizontally and vertically, and then the samples were further sanded with both 800 and 1200 grades. Each sample was coated with the NeverWet coating or stearic acid with SiO₂ nanoparticle coating. In total, 6 samples were prepared. This is the minimum number of the samples required to cover the geometry and

chemistry parameters. Surface optical microscopy, contact angle measurements, and sliding angle measurements were carried out on each sample in order to examine the samples' characterisations with the different surface roughness.

Figure 3.23 shows optical microscope images of the uncoated samples with different surface pre-treatments. The unaltered sample has parallel patterns on the surface as a result of the cutting process during manufacture. The polished sample shows a mirror-like surface and has a much smoother surface roughness compared to the unaltered sample, and only a small number of scratches or lines can be observed under high magnification. The sandpaper treated sample shows a much rougher surface with much denser scratches or lines from different orientations than that of the unaltered sample.

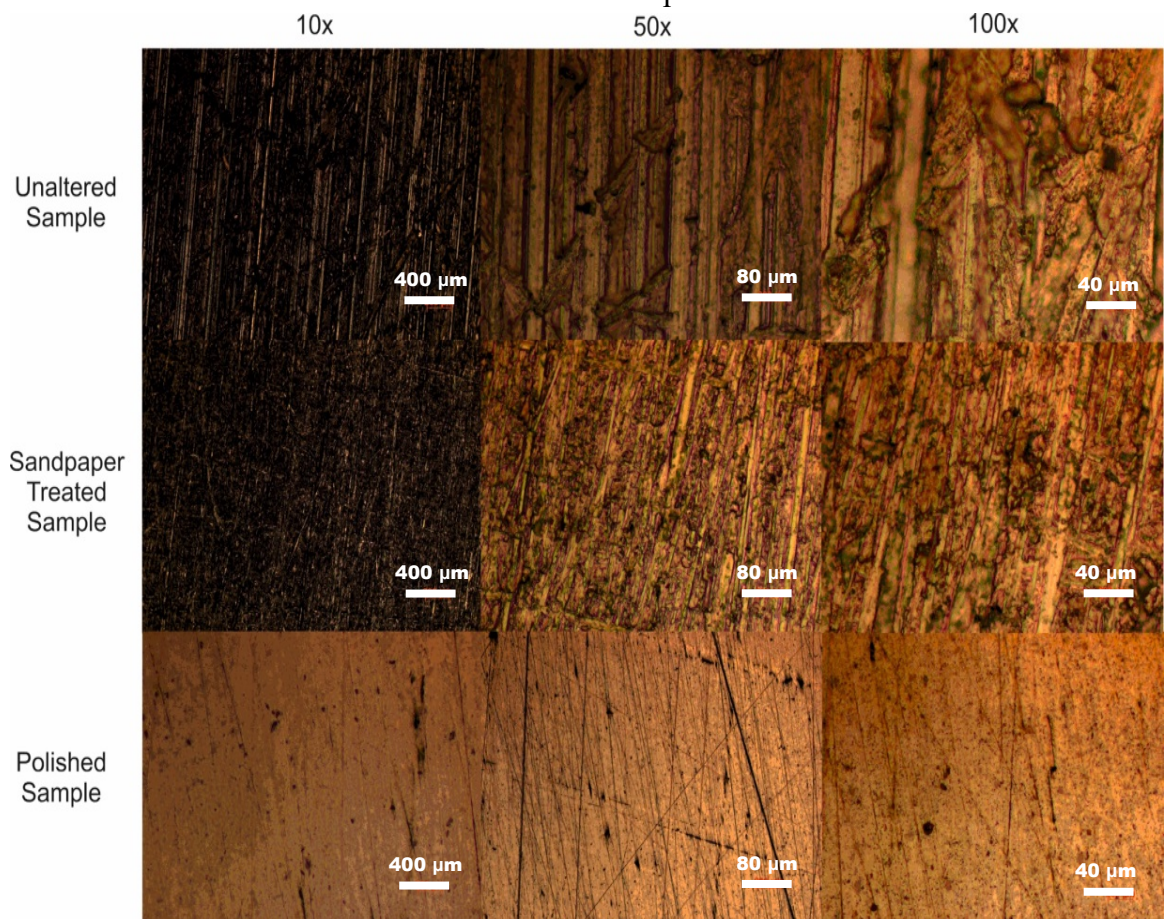


Figure 3.23 Uncoated samples with different pre-treatments under a magnification of 10, 50, and 100 times

Figure 3.24 shows microscope images of the NeverWet coated samples with different surface pre-treatments. Under a magnification factor of 10, the NeverWet coating demonstrates a semi-transparent and granular form of appearance, and more patterns were observed through the coating on the unaltered sample than on the sandpaper treated and polished samples. With higher magnifications of 50 and 100 times, coating appeared “misty” on all the three types of the samples, and no pattern could be observed on all samples.

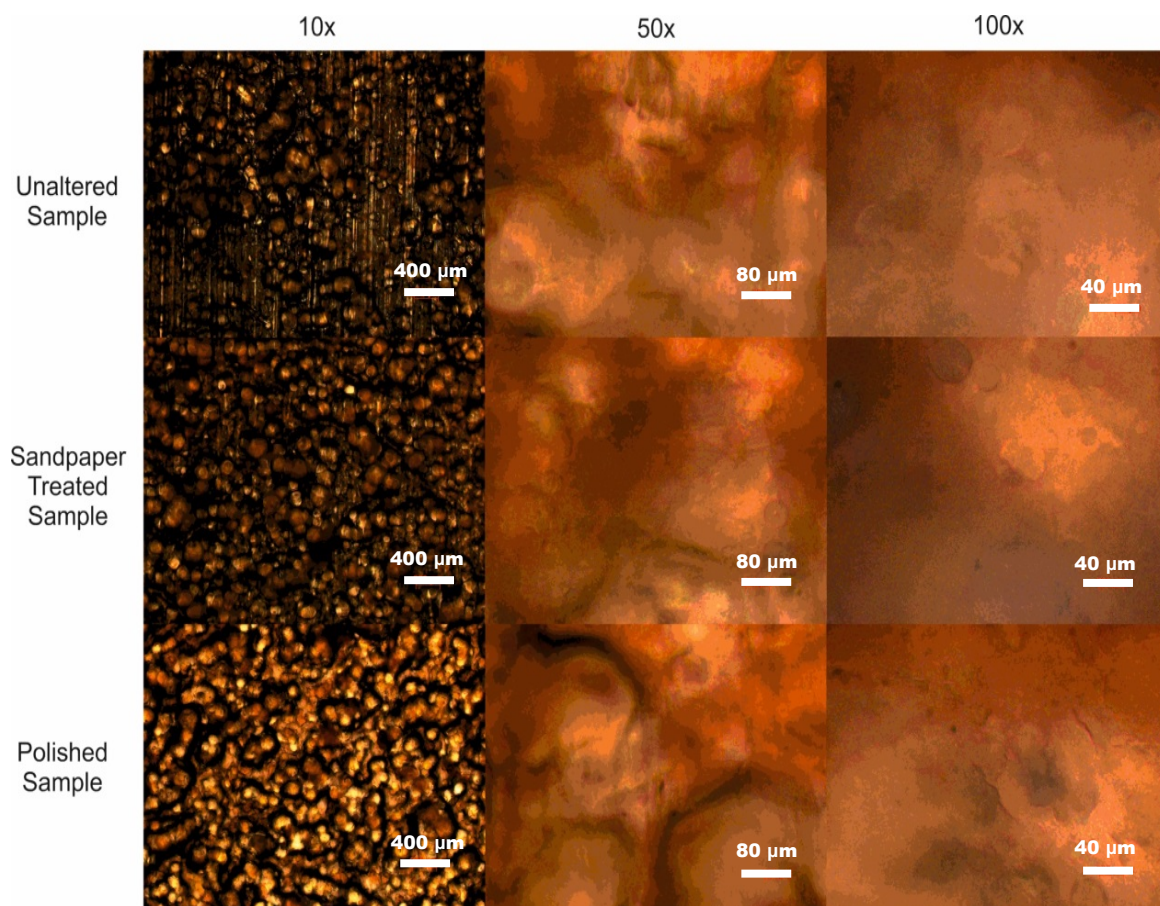


Figure 3.24 NeverWet coated samples with different pre-treatments under a magnification of 10, 50, and 100 times

Figure 3.25 shows optical microscope images of the stearic acid with SiO₂ nanoparticle coated samples with different surface pre-treatments. Stearic acid with SiO₂ nanoparticles shows a “clotty” form of appearance under microscopy. With higher magnifications of 50 and 100 times, larger clots of coating particles with irregular shapes were observed on all the three types of samples. However, the coating clots did not appear to cover as much of

the surface area than the NeverWet coating, and the original surface patterns or scratches could be still observed on all samples.

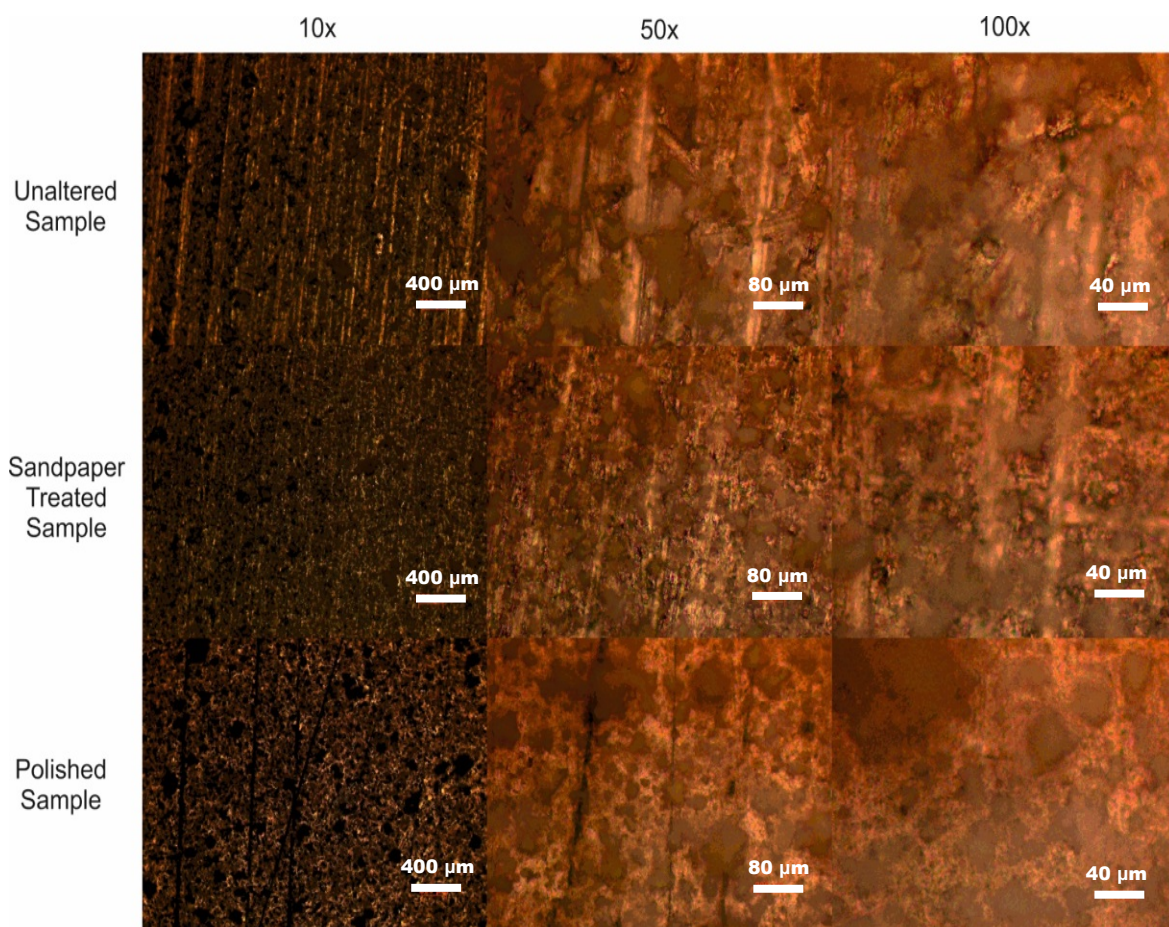


Figure 3.25 Stearic acid with SiO₂ nanoparticle coated samples with different pre-treatments under a magnification factor of 10, 50, and 100 times

Table 3.15 shows the results of the contact angle and sliding angle measurements of NeverWet and the stearic acid with SiO₂ nanoparticle coating with different surface pre-treatments. All the samples in this experiment achieved superhydrophobic performance with average contact angles above 160°, and average sliding angles less than 10°. The overall superhydrophobic performance of the NeverWet coating was better than that of the stearic acid with SiO₂ nanoparticle coating. Whilst observing sliding angle measurements, the NeverWet coating achieved angles between 2° and 3°, while the sliding angles of the stearic acid with SiO₂ nanoparticle coating were between 8° and 9°.

Table 3.15 Contact angle and sliding angle measurements of different pre-treated and coated samples

Coating Type	Pre-treatment	Contact Angle (°)			Average Contact Angle (°)	Average Sliding Angle (°)
		1	2	3		
NeverWet	Polish	164.5	165.2	165.4	165.0	2.5
	Sandpaper	169.7	166.0	168.0	167.9	2.0
	Unaltered	161.6	163.8	163.4	162.9	3.0
Stearic Acid with SiO ₂	Polish	163.1	160.6	162.2	162.0	9.0
	Sandpaper	166.5	164.6	164.7	165.3	8.0
	Unaltered	163.4	162.8	161.0	162.4	9.0

The sandpaper pre-treated samples demonstrated the best superhydrophobic performance with the highest average contact angles and lowest average sliding angles for both types of coatings. In contrast to this, the polished samples had the least performance with the lowest average contact angles and highest average sliding angles. This may be because the polished samples had the smoothest surfaces and so the surface mechanical interlocking and friction forces were relatively low [114]. This results in the coating being less firmly on each surface and more likely to become removed. Nevertheless, the differences in the average contact and sliding angles for both coatings among all the three types of surfaces were not significant.

Overall, the NeverWet coating had overall better superhydrophobicity with lower surface hysteresis than the stearic acid with SiO₂ nanoparticle coating on all types of the surfaces. Ding's study shows that surface roughness can enhance surface hydrophobicity, particularly where surface roughness involves cylindrical-shaped structures, which can help to stabilise the Cassie-Baxter state [115]. Cansoy's study investigated a number of square-shaped and cylindrical-shaped pillars with different sizes and distances, and they found that surface contact angle hysteresis tended to decrease with increasing separation distance (up to a maximum of 40 µm) between the pillars [116]. It was also noticed that square-shaped pillars

had a stronger pinning force to water drops and larger surface hysteresis than that of the cylindrical-shaped pillars with curved tops, due to the fact that the sharp edges of the square pillars can pin to contact angle lines [116][117]. However, the superhydrophobic performance of all the three types of surface with different roughness was similar for both types of coatings in this study. This may be because the surface geometries of all samples in this research were irregular without a cylindrical-shape, and thus it is likely that these geometries did not significantly contribute to superhydrophobic performance. It was also noted that the substrate geometries were not discernible under microscope after the coatings were applied. This means the coating materials were the main contributor to surface superhydrophobicity.

3.5 Laser Patterning

Conventional coatings might be worn away by daily operation while physical surface fabrications could provide long-term solutions for overhead lines. Aside from the surface coatings mentioned, superhydrophobicity can also be achieved with a certain degree of surface roughness and low surface energy. Methods for modifying surface geometries by mechanically or chemically producing micro or nano structures on the surfaces are quite promising in terms of superhydrophobic performance [118]. Laser patterning techniques have been widely used in order to mechanically fabricate nanometre or micrometre geometric patterns to achieve superhydrophobic performance on aluminium surfaces [26][27]. In this section, a number of micro-channels and micro-pillars patterned surfaces with a comparably high level of superhydrophobicity and low surface hysteresis, were applied to aluminium substrates, using different laser parameters. Using contact angle measurements and surface microscopy, the superhydrophobic performance of these aluminium substrates were examined and compared.

3.5.1 Laser Patterning Sample Preparations

Different laser patterns with different microstructures (10 x 10 mm) were engraved on a single aluminium substrate (100 × 50 × 6 mm) as shown in Figure 3.26 to select the best parameter that achieved superhydrophobicity for the further tests. Different parameters were used to produce different micro-channels and micro-pillars patterns, including hatch distances, scanning speeds, and scanning passes.

Before the laser treatment, the aluminium substrate was immersed in 1 M of Potassium hydroxide (KOH) solution for 10 s, followed by ultrasonically cleaning in deionised water and drying at room temperature. A nanosecond laser ablation (Laserlines Laserval Violino, Nd: YVO4 laser) was used to engrave patterns on the substrate, with a 532 nm wavelength, 30 kHz repetition rate, 55 µm focused spot size, and 9.26 J/cm² laser fluence. After the laser treatment, the sample was ultrasonically cleaned in ethanol for 5 mins and then sterilised in UV ozone for 30 mins to remove any debris or contaminations. Finally, the sample was immersed into a 1 % hetadecafluoro-1,1,2,2-tetrahydro-decyl-1-trimethoxysilane methanol solution for 150 mins to reduce the surface tension, followed by drying in an oven at 80 °C for 30 mins.

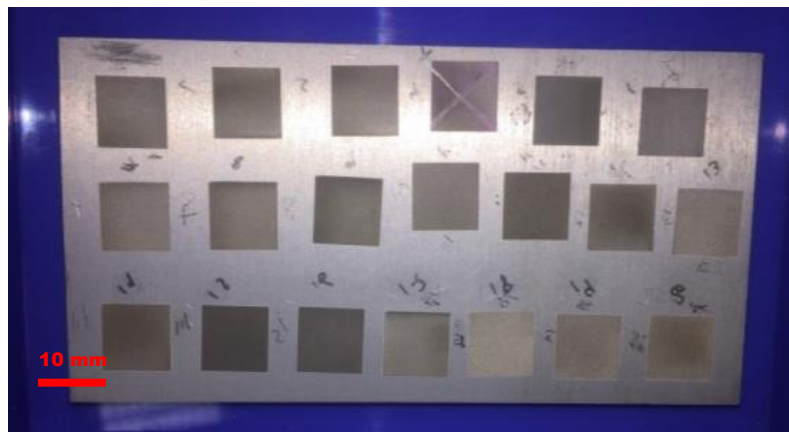


Figure 3.26 Laser patterning test substrates

The parameters used in the laser treatment are listed below:

- Pattern Type: micro-channels or micro-pillars
- Hatch Distance: spot-to-spot size 50 or 100 µm

- Scanning Speed: 10, 50 or 100 mm/s
- Scanning Pass: 1, 5, 10 or 20 times

After the chemical treatment, the contact angle measurement and scanning electron microscope (SEM) were carried out on the laser patterned samples to examine their surface characterisations. The contact angle was measured three times on each of the samples using 10 μ L water drops, and the average result was calculated.

3.5.2 Laser Patterning Sample Characterisations

Table 3.16 shows the contact angles and the processing times for both micro-channel and the micro-pillar laser patterns with different hatch distances, scanning speeds, and scanning passes. The results show that the contact angles of all the micro-channel and micro-pillar patterns with the different parameters were above 150° and achieved superhydrophobic performance. It was noted that the contact angle tended to increase with an increase in the number of scanning passes or decrease in scanning speed. The higher the number of the scanning passes, the deeper the valley between channels. The higher the scanning speed, the shallower valley. In terms of hatch distance, patterns with 50 μ m distance resulted in slightly higher overall contact angles than those with 100 μ m distance. This means the smaller hatch distance can lead to a more suitable surface structure and achieve a better superhydrophobicity. Nearly double the processing time was required to create micro-pillar laser patterns than micro-channel patterns. In contrast, the overall contact angle of micro-pillar patterns was higher than that of the micro-channel patterns. Note that the surface after laser treatment was superhydrophilic, as a result of the increase in surface tension with the laser processing. Hydrophobicity will increase with time and may switch to superhydrophobicity within around a month. However, it is unstable and may easily lose its hydrophobicity with a large amount of water or contamination due to high surface tension. Therefore, for application purpose in the case of metals, reducing surface tension using chemical treatments such as heptafluoro-1,1,2,2-tetrahydro-decyl-1-trimethoxysilane solutions, is essential in order to stabilise wettability [92].

Table 3.16 Contact angles and processing times of different laser patterned samples

	Hatch Distance (μm)	50					100				
	Scanning Speed (mm/s)	10	50			100	10	50			100
	Scanning Pass	1	5	10	20	10	1	5	10	20	10
Micro-channels	Processing Time (s)	200	210	406	813	207	105	105	210	419	104
	Contact Angle ($^{\circ}$)	163.8	157.7	163.4	164.2	162.7	161.9	156.9	161.1	163.7	160.5
Micro-pillars	Processing Time (s)	400	405	810		408	204	205	411		207
	Contact Angle ($^{\circ}$)	169.3	166.5	169.9		163.3	165.8	160.0	162.7		161.8

Figure 3.27 and Figure 3.28 show the 3D images of different micro-channel and micro-pillar patterns with 50 and 100 μm hatch distances; 50 and 100 mm/s scanning speeds; and 5, 10, & 20 scanning passes. The two patterns from both images in (a) in both figures have irregular spherical shaped particles due to the resolidification of the aluminium vapour from fast and shallow laser engraving. However, the rest of the patterns have parallel shaped channels or pillars. It is noted that the depth between channels increases with an increase in the number of scanning passes and decreasing scanning speeds, but unaffected by hatch distance. The patterns with 10 scanning passes were also found to have more uniformity than the patterns with 5 or 20 passes.

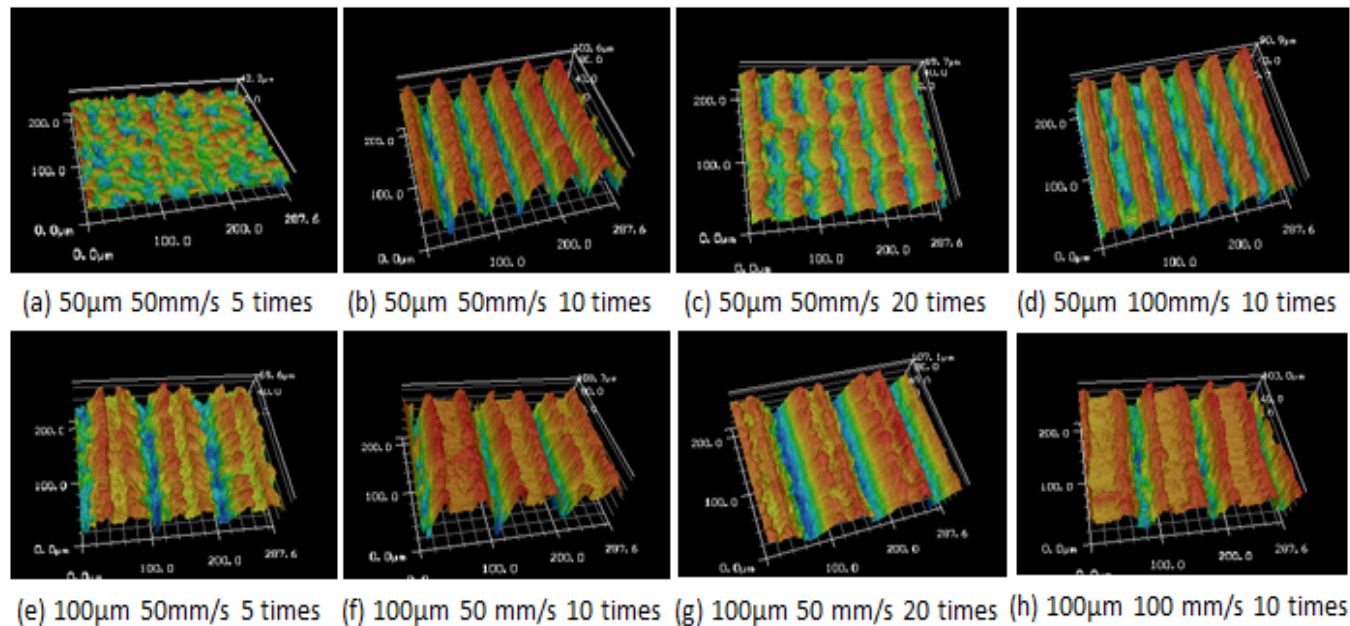


Figure 3.27 3D images of micro-channel laser patterns with different parameters

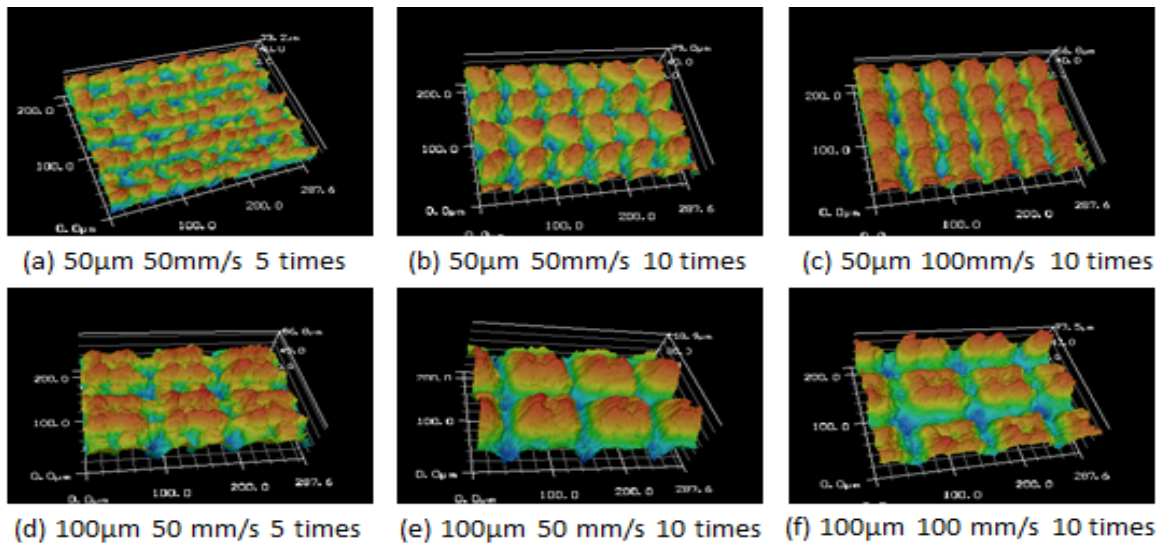


Figure 3.28 3D images of micro-pillar laser patterns with different parameters

Overall, the treatment of micro-structured laser patterns on aluminium substrates was verified as a robust and precise technique that can produce a tremendously high level of superhydrophobicity on surfaces. Different laser patterning parameters can generate different sizes of the pillars or channels to achieve different wettability performance, which suggests the surface wettability can be significantly affected by the surface structures. Smaller pillars or channels can lead to a smaller water drop contact area with a weaker liquid-solid attraction force, resulting in smaller surface hysteresis and the better potential icephobicity [1]. The reduction of water-surface contact area on a micro-structured superhydrophobic surface can also lead to a slower heat-transmission rate between water drops and the surface, which may increase the time it takes for water drops to become frozen on surfaces. This anti-icing property was verified in Milles's study that shows the freezing time of an 8 μL water drop on a laser patterned superhydrophobic aluminium surface was delayed by up to 3 times than that of an untreated sample [121]. Because of the comparable superhydrophobicity of all the patterns, the micro-channel laser pattern with 100 μm hatch distance, 100 mm/s scanning speed, and 10 scanning passes, was chosen to carry out further tests in this research, considering its higher uniformity and higher efficiency with the quickest processing time. Ta's study shows that laser patterns with a hatch distance larger than 200 μm could result in non-superhydrophobic surfaces [122]. Furthermore, laser

patterns with wider hatching distances than 100 μm or a faster scanning speed than 100 mm/s may be investigated to achieve an optimum pattern considering superhydrophobic performance and feasibility of manufacture. This could benefit the application of laser patterns on overhead line conductors by minimising manufacturing time and costs.

While micro-structured laser patterns provide robust superhydrophobic performance and potential long-lasting durability on aluminium surfaces, the cost and processing time may raise concerns in practice. To calculate the laser pattern processing time of an overhead line conductor, the micro-channel pattern with a scanning speed of 104 s/cm² and a 150 m span of a Gap-type conductor with diameter of 31.48 mm, can be used as an example. The 150 m long conductor has a surface area of approximately 14.84 m², which takes around 4287 h to pattern the whole conductor. If multiple lasers can be used simultaneously during manufacture, process time could be shortened to increase productivity.

Alternative methods that produce micro or nanostructures on surfaces physically or chemically could also be promising in virtue of less time consumption. Nano-pattern surface structures on aluminium were achieved using a Nickel template with nano-sized structures to directly emboss upon softened aluminium surfaces [123]. Micro/nano binary surface structures were obtained on aluminium surfaces by CuCl₂ and HCl chemicals etching, which showed superhydrophobic and anti-icing performance on some level [36].

3.6 Concluding Remarks

This chapter introduced test substrates, sample preparation methods, and a number of hydrophobic and superhydrophobic surface treatments, including the HumiSeal coating, the NeverWet coating, the stearic acid with/without SiO₂ nanoparticle coatings, and the laser patterning techniques. The manual circular zoomed-in method used in this research was statically examined and indicated a small deviation and reliable accuracy of measuring contact angles. The water drop movements on the samples were compared under the high-speed camera and both the NeverWet coated flat and GAP type round conductor samples

showed better water-repellent ability than that of the uncoated samples. The water drops rolled off more easily on superhydrophobic surfaces because of lower sliding angles and larger contact angles. The spray coating procedures of stearic acid with SiO₂ nanoparticles was optimised, achieving a high reproducibility of the superhydrophobic coating with low surface hysteresis. Different surface pre-treatments that produced different surface roughness were proven to have similar superhydrophobic performance when coated with the NeverWet coating or stearic acid with SiO₂ nanoparticle coating. Overall, the NeverWet coating had better superhydrophobic performance than that of the stearic acid with SiO₂ nanoparticle coating. The laser fabrication of micro-channel and micro-pillar patterns was verified to be a robust and precise technique to produce tremendously effective superhydrophobic surfaces on aluminium substrates. As a result of the comparable superhydrophobic performance of all laser patterns, the micro-channel laser pattern with the fastest processing time was chosen to carry out further tests for higher efficiency.

CHAPTER 4 AGEING TESTS

4.1 Introduction

Superhydrophobicity on surfaces can be achieved using different methods such as traditional protective coatings, chemical etching, or physical fabrications, and each of them provides different benefits and lifespans for practical applications. The stearic acid based superhydrophobic coating introduced in the CIGRE TB 631 report has potential value for use on overhead lines because of its organic and eco-friendly nature. A commercially available superhydrophobic coating, NeverWet, has been widely used to create superhydrophobic surfaces on different materials because of its high efficiency and excellent water repellent ability. Conventional coatings can be worn away and aged thermally or chemically through daily operation, while physical surface fabrications such as laser patterning might be longer lasting when deployed on overhead lines. The laser patterning method has been reported to be an excellent technique that can produce a range of nano or microstructures on surfaces to achieve superhydrophobicity on aluminium substrates [119][120].

Taking into account of the need described in the CIGRE brochure for further examination of the long-term durability of surface treatments before deployment, a family of durability tests were designed and performed to examine the longevity of different surface treatments on aluminium alloy substrates, including thermal ageing/cycling, corona exposure, ultraviolet exposure, and outdoor environmental ageing. Results of the ageing impacts on the three types of surface treatments were compared to determine their advantages and disadvantages against each other when deploying on overhead line conductors.

4.2 Experimental Descriptions

4.2.1 Sample Preparations

Flat aluminium alloy 6082 substrates ($25 \times 25 \times 3$ mm) were used in this chapter. Aluminium alloy 6082 was chosen because its alloy compositions are similar to overhead line aluminium conductors. Flat substrates were used to measure contact angles and to characterise surface geometry more easily. Substrates were cleaned according to Section 3.2.2.1

The NeverWet coated samples were prepared using the 2-step coating method, according to Section 3.4.6.

The stearic acid with SiO₂ coated sample was produced using the optimised method described in Section 3.4.5.2. The single-mixed solution, magnetic stirring at 800 rpm, homogeniser at 5000 rpm, higher spray gun flow volume setting, a spray distance of 25 cm, and 4 separate 5 s spray durations, were chosen for sample preparation.

The micro-channel laser pattern with 100 μ m hatch distance, 100 mm/s scanning speed, and 10 scanning passes, was chosen to carry out the ageing tests, considering its high uniformity and high efficiency. The laser patterned samples were produced according to Section 3.5.1.

4.2.2 Characterisation Methods

Different contact angle measurements were used on samples before, during, and after each of the ageing tests. Each measurement was repeated 3 times on samples to obtain the average results. The manual circular zoomed-in method of the static contact angle measurement, the sliding angle measurement, and the pendant dragging method of the contact angle hysteresis measurement were used according to Section 3.3.1. Deionised water drops (5 μ L) were dispensed on the samples.

Confocal laser scanning microscope (CLSM) and FEI Quanta 200 & 250 scanning electron microscopes (SEM) were used to examine the laser patterned samples before and after the ageing tests, with a 20 kV beam voltage and 3.0 mm spot size in a vacuumed environment.

Optical microscopy was used to examine the NeverWet coated and the stearic acid with SiO₂ coated samples before and after each of the ageing tests.

4.2.3 Ageing Tests

A series of ageing tests were designed and carried out to examine the durability of different surface treatments, including thermal ageing, thermal cycling, ultraviolet exposure, outdoor environmental ageing, and corona exposure. 4 of each of the NeverWet coated, the stearic acid with SiO₂ coated, and the laser patterned samples were prepared, giving 12 test samples in total for each of the ageing tests.

4.2.3.1 Thermal Ageing & Thermal Cycling

The purpose of thermal ageing and thermal cycling is to accelerate the ageing process on different treated superhydrophobic surfaces to observe surface durability and its changing characteristics. Thermal ageing tests allow chemical reactions to take place that would otherwise not happen at lower temperatures. Thermal cycling results in differential thermal expansion of coating and sample, imposing specific mechanical forces. The test substrates were placed into a Thermotron environmental chamber at room temperature. The chamber was increased to 80 °C and left running for a week, which is likely enough to allow any expected chemical reaction to take place on a thin coating. A temperature of 80 °C was set because it is just above the typical operating temperature of 75 °C, and lower than the highest rated temperature of 100 °C for aluminium conductor steel-reinforced (ACSR) overhead lines [124]. To accomplish the thermal cycling test, a programme was set to change the temperatures in the chamber repeatedly. During a single cycle, the chamber was cooled to -20 °C in 55 mins and left a further 5 mins to thermally equilibrate. The chamber was then heated to 80 °C in 55 mins and left a further 5 mins to thermally equilibrate. This cycle was programmed to repeat 500 times for 1000 h. A temperature of -20 °C was used according to the lowest snowing overnight temperature in the UK [125]. The substrates were characterised by static contact angle and sliding angle measurements weekly.

4.2.3.2 Ultraviolet (UV) Exposure

The purpose of UV exposure was to evaluate the damage of short wavelength ultraviolet lights to the surface treatments by simulating exposure to the sunlight. A Q-Sun Xe-1 Xenon test chamber was used for the UV ageing test. A 340 nm sensor measuring narrow bands of wavelength centred on 340 nm, with a half-bandwidth of 10 nm was used to simulate the material damaged by short-wavelength UV light. A DAYLIGHT-Q filter was used to produce a spectral power distribution (SPD) equivalent to summer noon sunlight in an outdoor environment according to the ASTM G155-13 standard [126]. The test substrates were placed into the chamber and exposed under an irradiance narrowband of $0.51 \text{ W/m}^2 \cdot \text{nm}$ and the black-panel temperature of $63 \text{ }^\circ\text{C}$ for a total duration of 4 weeks based on the European standard EN ISO 4892- 2:2013 [127]. The substrates were characterised by static contact angle and sliding angle measurements weekly.

4.2.3.3 Outdoor Environmental Exposure

The purpose of outdoor environmental exposure was to examine the impact of a realistic outdoor environment on the performance and durability of different surface treatments. The test substrates were mounted on a perforated sample holder with an angle of 45° facing upwards, as shown in Figure 4.1 (A). The sample holder was placed in a roofless outdoor environment facing a motorway in Manchester to ensure the samples were exposed to pollution and other weather conditions such as rain, snow, and frost. A total duration of 1 year (52 weeks) of outdoor environmental exposure was carried out on different substrates. The static contact angles, sliding angles, and contact angle hysteresis of the samples were measured at weekly time intervals for the first 4 weeks, then at 2-week intervals until the 12th week, and then at 4-week intervals after the 12th week.

4.2.3.4 Corona Exposure

Corona exposure is a method used to examine the changes of superhydrophobicity of different surface treatments influenced by corona discharges. There is currently no specific standard about corona exposure ageing for coatings or surface treatments on overhead lines.

Therefore, a corona exposure ageing test was designed as shown in Figure 4.1 (B) and carried out in an ASM-3B10-L 3 kV voltage amplifier cage. A function generator was used to generate a 10 V input sinewave voltage to produce a 3 kV peak output voltage on electrode needles. The test substrates were placed on top of an earthed mount. The electrode needles were oriented 3 mm above the substrates to ensure a sufficient corona exposing area on the substrates. Visible corona discharges can be observed at the tip of the electrode needles during the test. A total duration of 168 h of corona exposure was carried out on different substrates. The substrates were characterised by static contact angles and sliding angle measurements after the corona ageing.

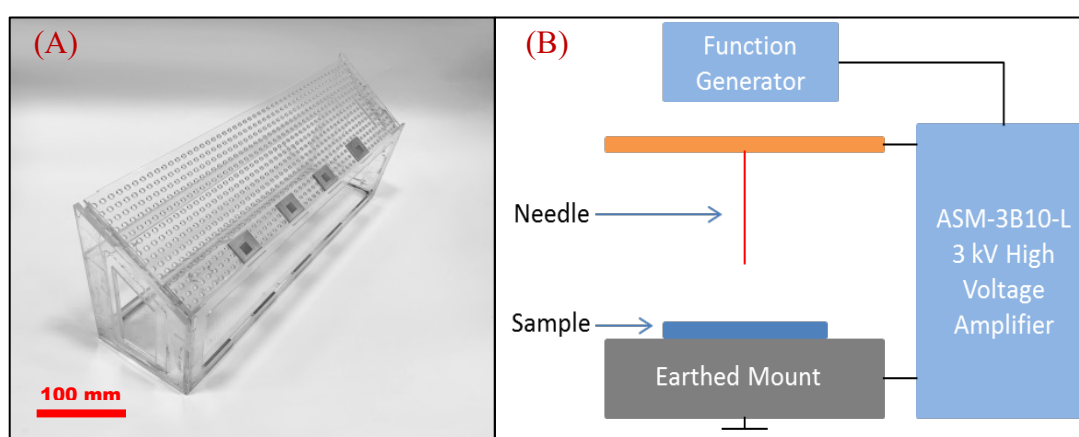


Figure 4.1 (A) outdoor exposure sample holder (B) corona exposure set-up

4.3 Test Results

4.3.1 Thermal Ageing & Thermal Cycling

4.3.1.1 Thermal Ageing

For the stearic acid with SiO₂ nanoparticle coating, although the temperature setting of 80 °C was higher than the melting point (63 °C) of the stearic acid, it was intended to test whether the coating material would still be attached to the surface after the thermal ageing. As a result of the high temperature, all the stearic acid with SiO₂ nanoparticles coated substrates lost their superhydrophobicity with contact angles decreased to less than 90° and sliding angles increased to more than 30° after 1 week of thermal ageing. Hardly any coating particles were

observed on the stearic acid with SiO₂ nanoparticles coated surface as shown in Figure 4.2 (B) after the ageing. The original mechanical cutting patterns were clearly exposed on the surface. This observation verifies the hypothesis that this coating material may be lost due to high temperature and no longer visible on the samples.

Table 4.1 shows the result of the contact angle and sliding angle measurements of different surface treatments before and after thermal ageing and thermal cycling. After 1 week of the thermal ageing, insignificant change was noted on the Neverwet coated substrates in terms of the contact and sliding angles. The laser patterned substrates showed a high level of superhydrophobic performance before and after thermal ageing. Prior to the thermal ageing test, the superhydrophobic performance of the laser patterned substrates was so high that water drops did not remain on the laser patterned areas, preventing the quantification of contact and sliding angles. After thermal ageing, the laser patterned substrates still performed such a high level of superhydrophobicity that neither the contact angles nor the sliding angles could be measured.

Table 4.1 Average contact angle and sliding angle measurements before and after thermal ageing and cycling

Thermal Ageing & Cycling		NeverWet		Laser Patterning	
		Contact Angle (°)	Sliding Angle (°)	Contact Angle (°)	Sliding Angle (°)
Before Ageing		167.1	1.7	Cannot be Measured	
After Thermal Ageing		166.7	1.7		
Thermal Cycling (week)	1	165.0	2.1	164.8	2.5
	2	165.0	2.5	166.5	2.5
	3	163.4	3.7	165.8	2.8
	4	163.0	4.3	165.0	2.8
	5	162.8	5.0	164.9	2.7
	6	162.0	5.9	165.2	2.7

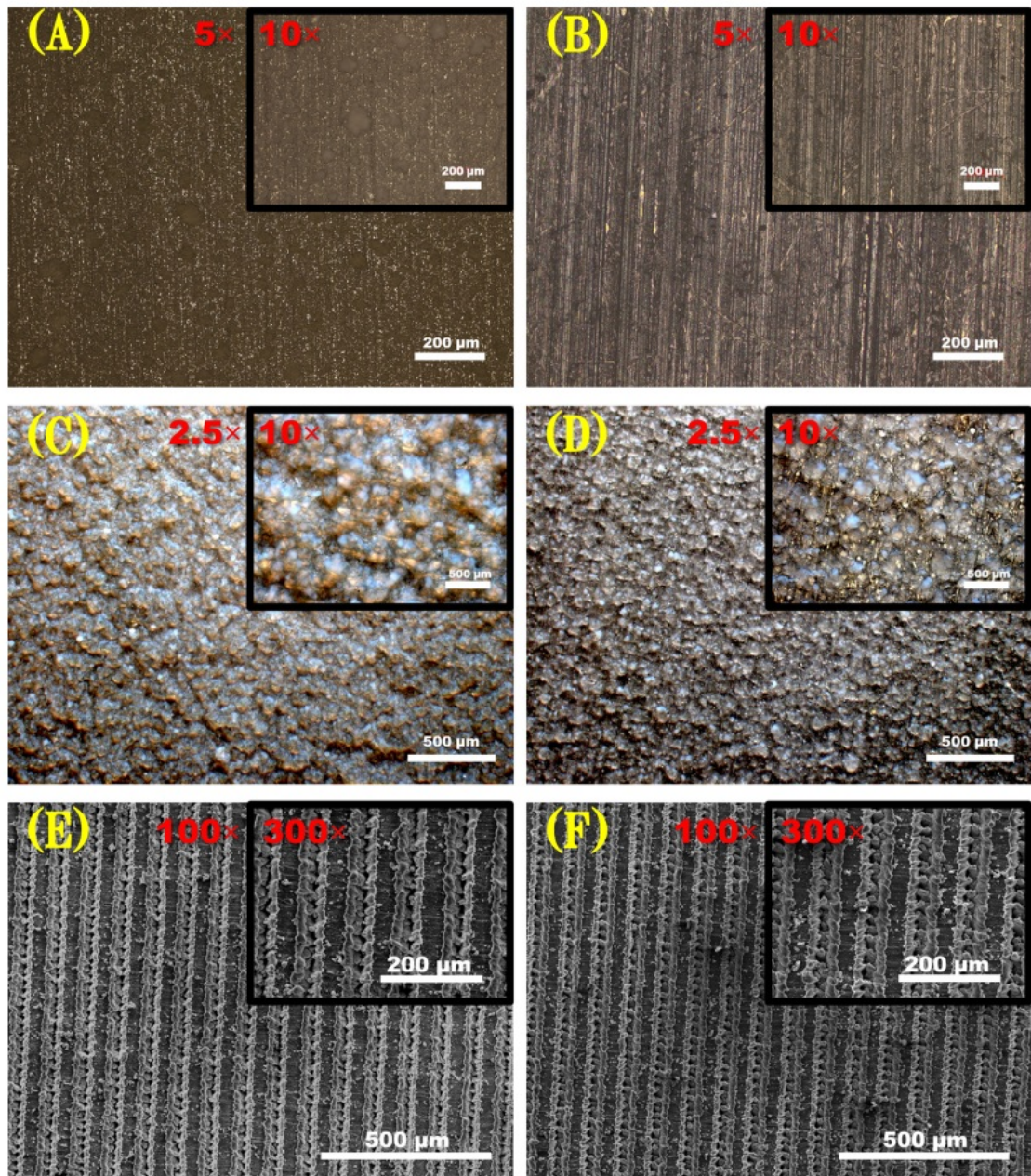
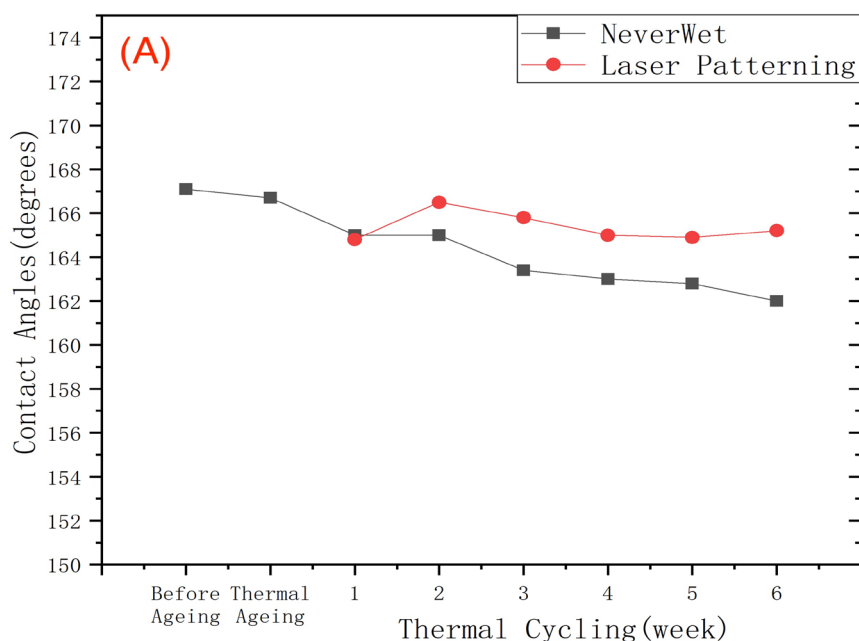


Figure 4.2 Microscope images of surface treatments before and after thermal ageing and cycling: (A) stearic acid with SiO₂ before ageing, (B) stearic acid with SiO₂ after ageing, (C) NeverWet before ageing, (D) NeverWet after ageing, (E) laser patterning before ageing, and (F) laser patterning after ageing.

4.3.1.2 Thermal Cycling

After the 1st week of the thermal ageing, the stearic acid with SiO₂ nanoparticles coated samples lost their hydrophobicity, while insignificant changes were noticed for both the NeverWet coated and laser patterned samples. To further examine the influence of extreme temperatures on the surface treatments, thermal cycling was carried out on the same NeverWet coated and laser patterned samples.

Figure 4.3 demonstrates the changes in contact angles and sliding angles of the NeverWet coated and laser patterned samples before and after different periods of thermal ageing and cycling. The average contact angle of the NeverWet coated samples decreased slightly from 167.1° to 162.0° after the ageing, and the average sliding angle increased slightly from 1.7° to 5.9° at the end of the testing. Nevertheless, all the NeverWet coated samples maintained their superhydrophobicity with average contact angle larger than 160° and average sliding angle less than 6°. The contact angles and sliding angles of the laser patterned samples were measurable after the first week of the thermal cycling. After 6 weeks of thermal cycling, the laser patterned samples still maintained their high level of superhydrophobicity with a contact angle of around 165° and a sliding angle less than 3°.



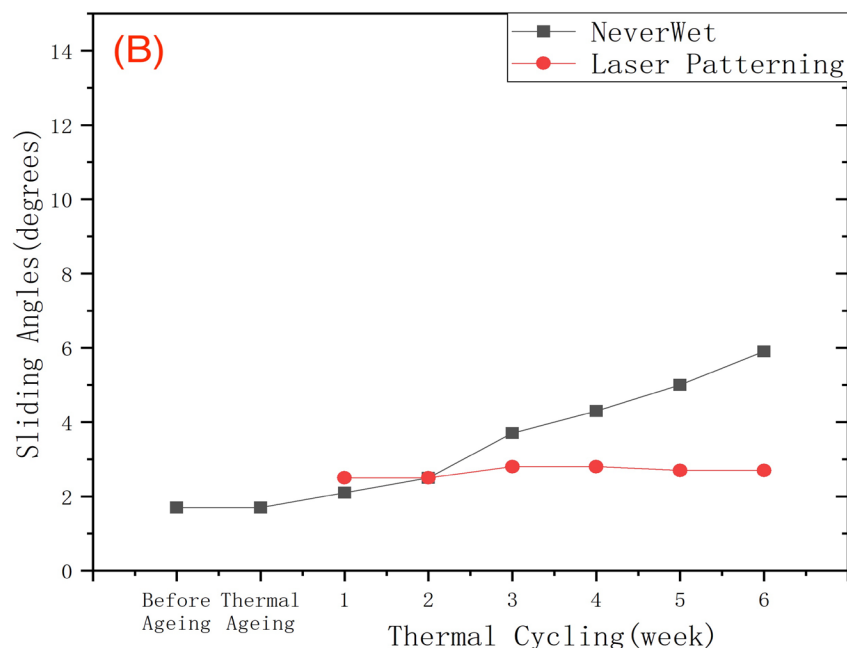


Figure 4.3 Changes to (A) contact angles and (B) sliding angles before and after thermal ageing and cycling

Figure 4.2 (C) and (D) compare the optical microscope images of a NeverWet sample before and after thermal ageing and cycling. Image (C) shows a slightly varied surface geometry after ageing with less luminescent spots being observed on the uneven surface compared to image (D). This observation indicates the possibility of less coating material being left on the samples, which supports the resulting contact angle measurements and slightly reduced superhydrophobicity after the ageing test. Figure 4.2 (E) and (F) compare the SEM images of a laser patterned sample before and after the thermal ageing and cycling tests. Despite some debris on the surface, no geometric change was observed after the ageing. This observation is supported by the contact angle measurements and the fact that the laser patterned sample retained comparable superhydrophobic performance after the ageing.

Overall, the laser patterned samples showed the best superhydrophobic performance and the most substantial durability. Insignificant changes were noticed on the samples after thermal ageing and cycling. Following the NeverWet coating, only a slight decrease in superhydrophobic performance was noticed on the samples after thermal ageing and cycling.

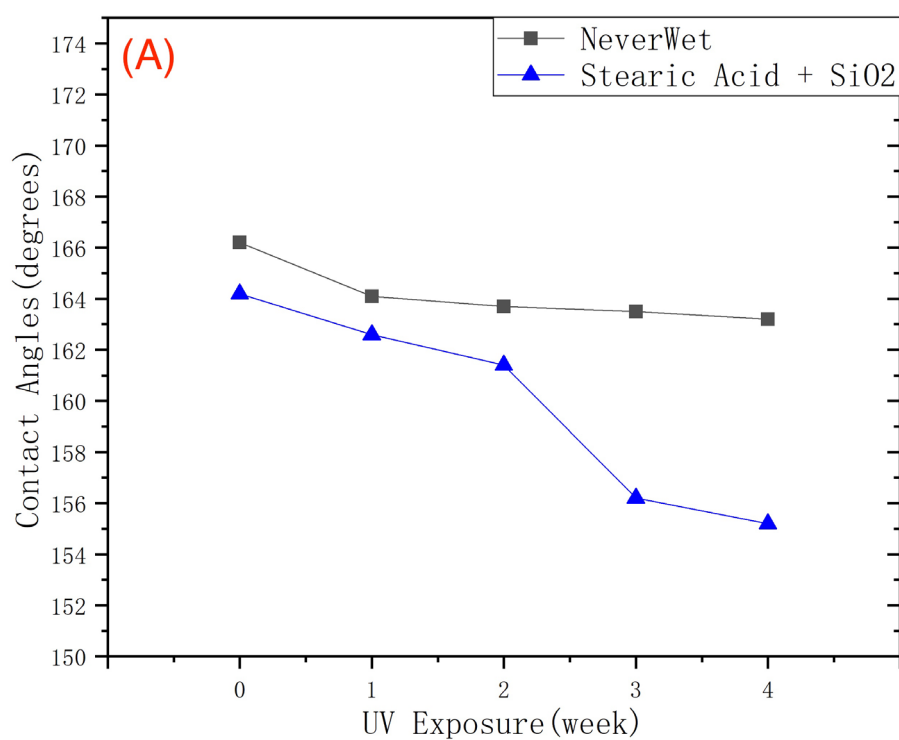
The stearic acid with SiO₂ coating showed the worst durability and the coating lost its superhydrophobicity under high temperature after 1 week of thermal ageing.

4.3.2 Ultraviolet (UV) Exposure

Table 4.2 and Figure 4.4 show the result of the contact and sliding angle measurements of the different surface treatments before and after UV exposure. For the laser patterned substrates, the surfaces showed a high level of superhydrophobic performance before and after UV exposure. Because the surface hysteresis was minimal and the water drops could not stay on the laser patterned areas, neither the contact angles nor the sliding angles could be measured on the laser patterned surfaces before and after UV exposure. Therefore, the UV exposure ageing had such little effect on the laser patterned samples that all the samples remained the high level of superhydrophobicity. For the stearic acid with SiO₂ nanoparticles coated samples, the average contact angle decreased from 164.2° to 155.2 after the 4th week of UV exposure. The average sliding angle increased dramatically from 5.7° to 22.1° after the 4th week of UV exposure. Although the contact angle was still above 150°, the sliding angle increased to over 20°. This result meant that the surface wetting behaviour potentially transformed from the Cassie-Baxter model to the Wenzel model and water drops could easily become trapped between surface protrusions, resulting in an increase in surface hysteresis and sliding angle [1][45][112]. The average contact angle of the NeverWet coated substrates only decreased slightly from 166.2° to 163.2°, and the average sliding angle increased from 1.9° to 2.2° after 4 weeks of the UV exposure. Therefore, all the NeverWet samples still performed with a good level of superhydrophobicity after UV exposure.

Table 4.2 Average contact angle and sliding angle measurements before and after the UV test

UV Exposure (week)	NeverWet		Stearic Acid with SiO ₂	
	Contact Angle (°)	Sliding Angle (°)	Contact Angle (°)	Sliding Angle (°)
Before Ageing	166.2	1.9	164.2	5.7
1	164.1	2.0	162.6	7.9
2	163.7	2.1	161.4	8.9
3	163.5	2.1	156.2	17.0
4	163.2	2.2	155.2	22.1



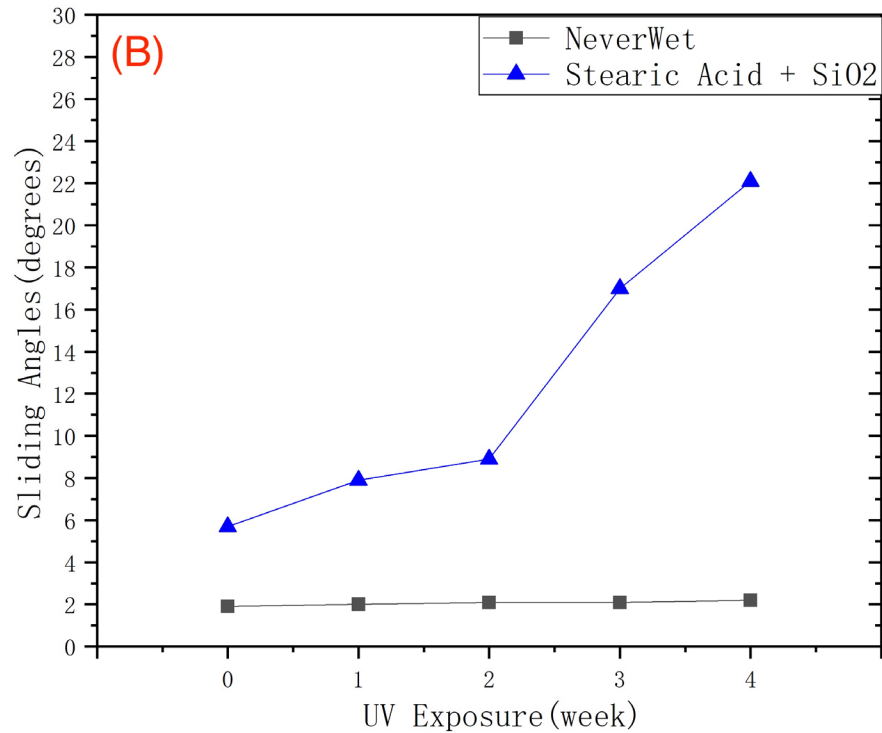


Figure 4.4 Changes to (A) contact angles and (B) sliding angles before and after UV exposure

Figure 4.5 compares the surface microscopy of different treatments before and after UV exposure. For the stearic acid with SiO₂ nanoparticles coated sample as shown in image (B), it is clear that coating particles were partially lost on the surface after UV exposure and the aluminium machine-cutting patterns were exposed. Images (D) and (F) show the NeverWet coated and laser patterned samples after UV exposure. No noticeable surface geometric changes were observed on the samples compared to images (C) and (E) before ageing. These microscopy results verify that contact and sliding angle measurements for both the NeverWet coating and laser patterning, retained a good level of superhydrophobicity after UV exposure.

Overall, all three types of surface treatments still performed with superhydrophobicity, with contact angle above 150° after UV exposure. The laser patterning performed with the best superhydrophobicity and the longest durability after UV exposure with no observable changes. The NeverWet coating demonstrated such a good performance against UV exposure that insignificant changes were noticed after ageing. The stearic acid with SiO₂

coating showed the least durability with a reduced superhydrophobic performance after UV ageing. The contact angle hysteresis on stearic acid with SiO₂ coated samples increased to quite a high level and resulted in a reduced water repellent ability.

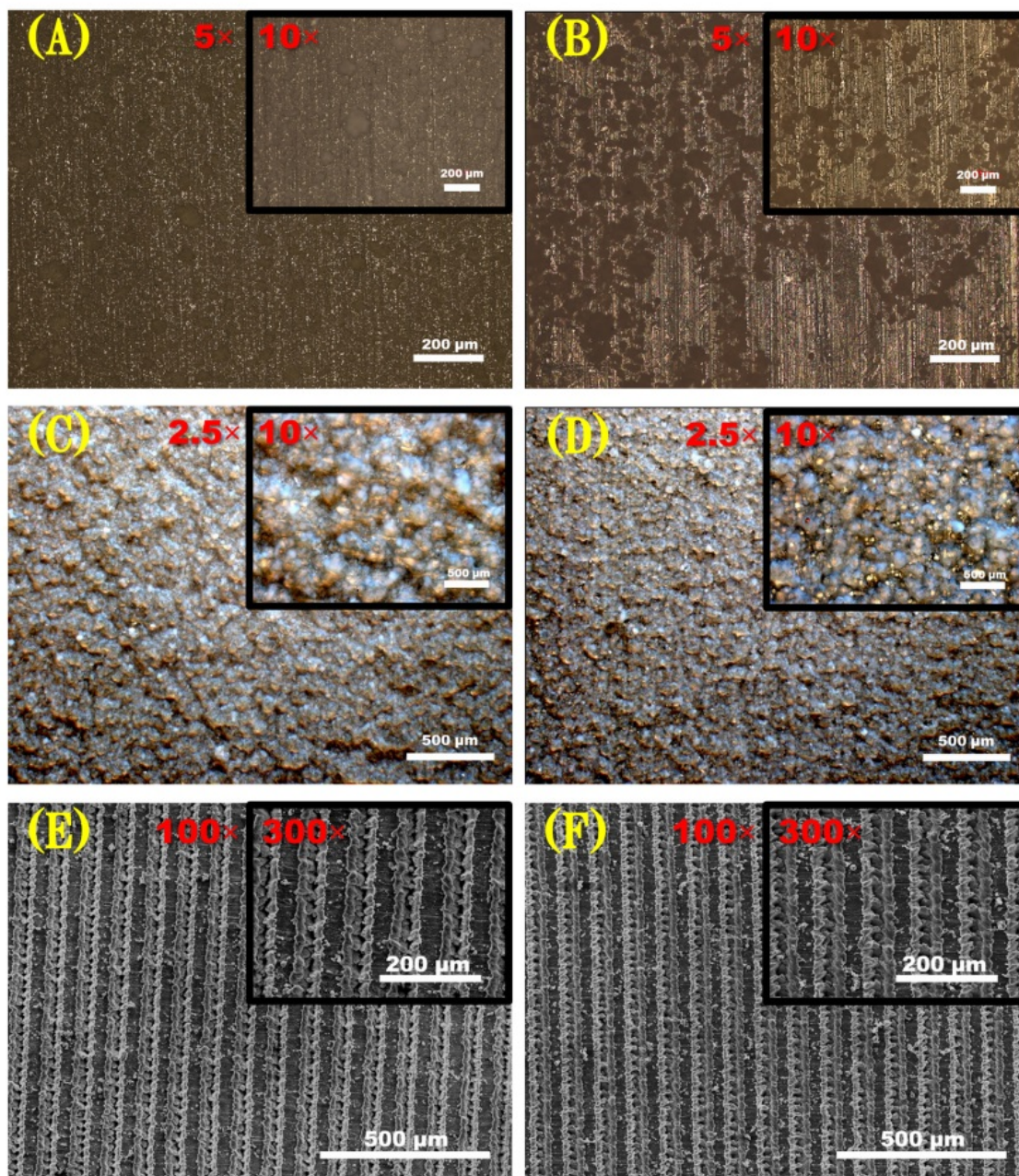


Figure 4.5 Microscope images of different surface treatments before and after UV exposure: (A) stearic acid SiO₂ before ageing, (B) stearic acid SiO₂ after ageing, (C) NeverWet before ageing, (D) NeverWet after ageing, (E) laser patterning before ageing, and (F) laser patterning after ageing.

4.3.3 Outdoor Environmental Exposure

Table 4.3 and Figure 4.6 show the changes in contact angles and sliding angles of different surface treatments before and after different periods of outdoor environmental exposure. Only 4 weeks of outdoor exposure was carried out on the stearic acid with SiO₂ nanoparticles coated samples, due to their rapidly reducing performance. The average contact angle decreased from 163.6° to 157.7 ° after 4 weeks of the outdoor exposure. However, the average sliding angle increased dramatically from 6.2° to 29.9° within the first week and then increased to 30.8° after 4 weeks of ageing tests. Although the contact angle was still above 150°, the sliding angle increased to over 30°. This result supports Miwa's theory that a high contact angle does not always lead to a high sliding angle [112]. In this situation, the wetting behaviour of stearic acid with SiO₂ nanoparticles coated samples might transform from the Cassie-Baxter model to the Wenzel model, resulting in increased surface hysteresis and sliding angles [45][112]. Both the average contact angle and the average sliding angle of the NeverWet coated samples remained relatively unchanged before the 32nd week. The changes on the NeverWet samples became visible from the 32nd week to the 52nd week. Although the average contact angle was still above 150°, the average sliding angle increased from 3.7° to 13.4° at the end of outdoor exposure, resulting in a slightly reduced superhydrophobic performance with a higher surface hysteresis. All the laser patterned surfaces maintained such a high level of superhydrophobicity before the 12th week of ageing that contact angle hysteresis could only be measured using the pendant dragging method. The contact angles and sliding angles were measurable from the 16th week. The average contact angle hysteresis was gradually increased from 0.3° to 8.9° at the end of the 52nd week of outdoor exposure. The average contact angle dropped to 161.2°, and the average sliding angle increased to 7.2° at the end of the 52nd week. These results indicate the laser patterned samples retained a good level of superhydrophobicity with average contact angle above 160° and average sliding angle and contact angle hysteresis below 10° after 1 year of outdoor environmental exposure.

Table 4.3 Average contact angle and sliding angle measurements before and after outdoor ageing test

Outdoor Ageing	Stearic Acid with SiO ₂		NeverWet		Laser Patterning		
	Contact Angle (°)	Sliding Angle (°)	Contact Angle (°)	Sliding Angle (°)	Contact Angle (°)	Sliding Angle (°)	Contact Angle Hysteresis (°)
Before	163.6	6.2	166.1	2.3			0.3
1	160.6	29.9	164.9	2.3			0.4
2	160.1	30.2	164.1	2.3			0.6
3	158.9	30.5	163.8	2.3			0.7
4	157.7	30.8	163.5	2.4			0.8
6			163.4	2.5			0.9
8			163.3	2.5			1.0
10			162.9	2.5			1.1
12			162.7	2.6			1.3
16			162.6	2.7	165.1	1.8	1.7
20			162.2	3.2	164.7	2.3	3.4
24			162.1	3.5	164.2	3.0	5.3
28			162.1	3.5	163.7	3.4	6.1
32			161.9	3.7	163.5	4.4	6.9
36			159.7	6.1	163.0	4.6	7.6
40			159.4	9.1	162.7	4.7	8.0
44			159.2	11.2	162.1	5.8	8.4
48			158.4	11.8	161.7	6.1	8.8
52			157.9	13.4	161.2	7.2	8.9

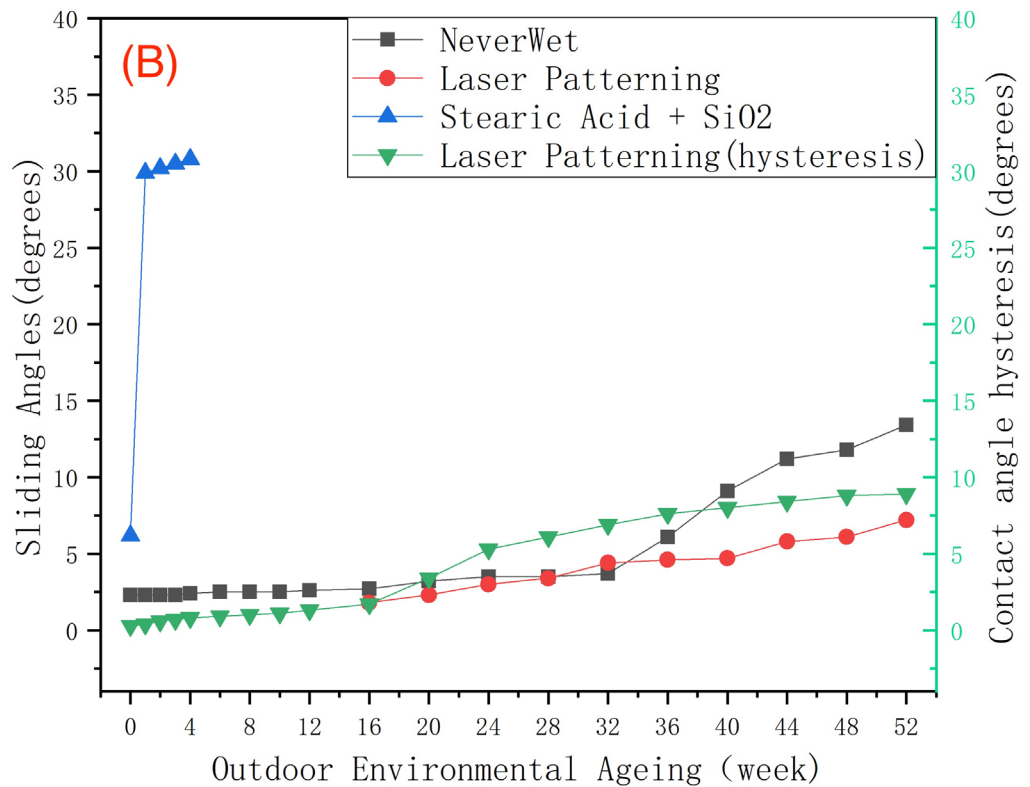
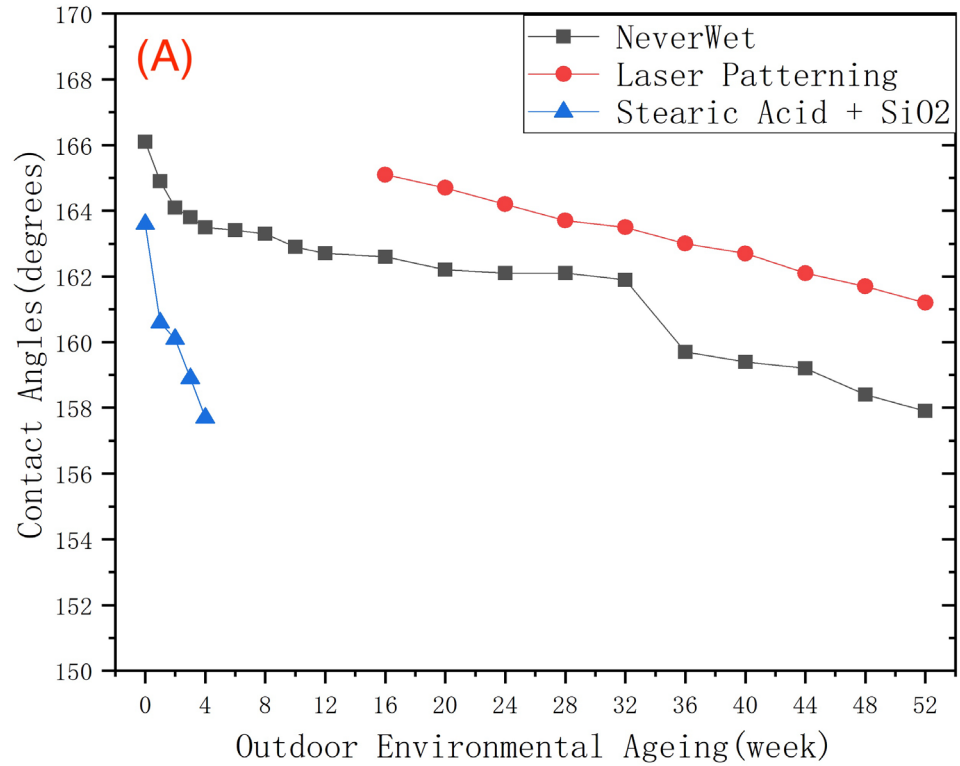


Figure 4.6 Changes to (A) contact angles and (B) sliding angles & contact angle hysteresis before and after outdoor environmental exposure

Figure 4.7 shows the surface microscopy of the different treatments before and after outdoor environmental exposure. Compared to image (A) of the stearic acid with SiO₂ nanoparticles coated sample before ageing, regions of contaminations were observed in image (B) after ageing. Those contaminations trapped between the coating particles may result in a change of surface geometry and lead to a reduction in water repellent ability. Image (C) shows a slightly varied surface geometry of the NeverWet coated sample after outdoor ageing. Fewer pale blue spots were observed on the uneven surface compared to image (D) before ageing. This observation indicates the possibility of the coating material being worn off due to oxidation or other types of chemical changes occurring on the sample. This result supports the change in contact angle measurements and the reduced superhydrophobicity after the ageing test. Images (E) and (F) compare the SEM images of the laser patterned sample before and after outdoor exposure. It is noted that the samples were placed relatively low compared to overhead lines in practice, therefore, it is likely to have experienced an increased level of contamination compared to real-world applications. Despite some debris on the surface, no geometric change was observed after the ageing process. This also supports the contact angle measurements of the laser patterns after outdoor exposure, including the slight reduction in superhydrophobic performance of the laser patterned samples, which was noticed after outdoor exposure.

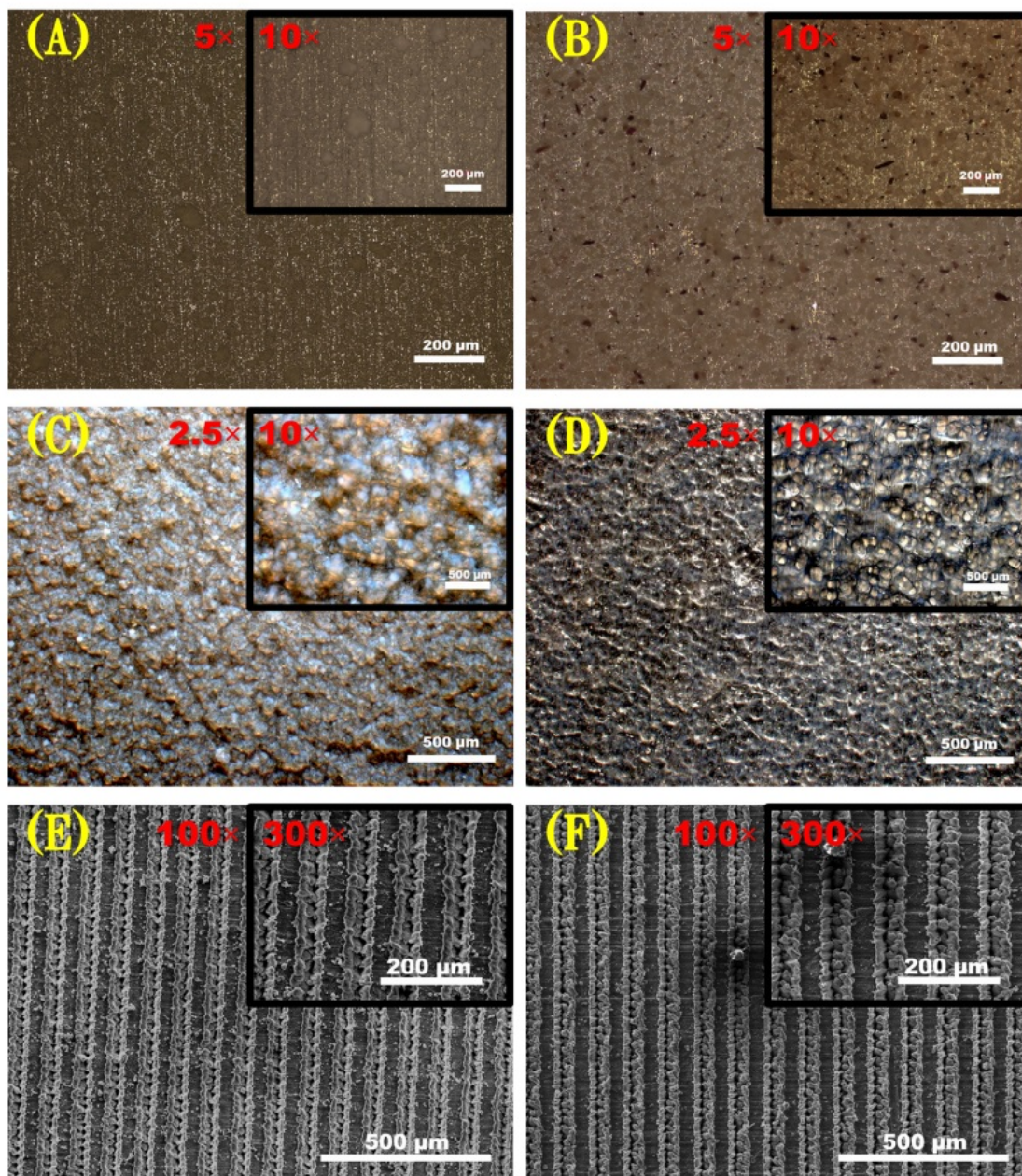


Figure 4.7 Microscope images of different surface treatments before and after outdoor environmental ageing: (A) stearic acid SiO₂ before ageing, (B) stearic acid SiO₂ after ageing, (C) NeverWet before ageing, (D) NeverWet after ageing, (E) laser patterning before ageing, and (F) laser patterning after ageing.

Overall, the laser patterned samples demonstrated the strongest tolerance towards outdoor environmental exposure. All the samples retained a good level of superhydrophobicity after 1 year of outdoor exposure. The superhydrophobic performance of the NeverWet coating was reduced due to outdoor exposure. Although the average contact angle was still above

150° and remained superhydrophobic, the average sliding angle of the NeverWet samples increased to over 13°, indicating an increased surface hysteresis. The stearic acid with SiO₂ coated samples showed the worst durability after 4 weeks of outdoor exposure. Although the average contact angle was still above 150°, the average sliding angle increased to more than 30°, resulting in a significantly reduced water shedding ability of the surfaces.

4.3.4 Corona Exposure

After the corona exposure, all the samples showed superhydrophilic performance during the contact angle measurements. When water drops were applied to the samples, the drops immediately sank and became so flattened on the surface that the contact angles were approximately 0°. Therefore, the sliding angles could not be measured under these conditions. This could be because the corona discharge led to some chemical reactions of the coatings and the chemical treatment on the laser patterning, and thus changed their wetting behaviours.

Figure 4.8 shows microscope images of the samples with different surface treatments before and after corona exposure. In image (B), the stearic acid with SiO₂ nanoparticles coated sample showed an obvious circular area under the corona exposed area with little coating left on it, and even the aluminium surfaces seemed to be so affected by the corona exposure that they no longer had metal lustre. In the image (D), the NeverWet coated sample demonstrated a yellowing circular area under the electrode needle after corona exposure. The 10 times zoomed-in microscope image showed coating particles under the area of the corona exposure becoming sparse, and the aluminium mechanical cutting lines appeared through the coating. In image (F), the laser patterned sample also showed a circular area under the corona exposed area, and some convoluted surface structures were found in between and on the top of the micro-patterns as shown in the image. It would appear the laser patterns remained on the surface after the corona exposure when compared to the image (E) before ageing. These surface changes indicate the occurrence of some chemical reactions caused by the corona discharge on the surfaces, resulting in a tremendous transformation of the surface characterisation from water repellence to water absorptive.

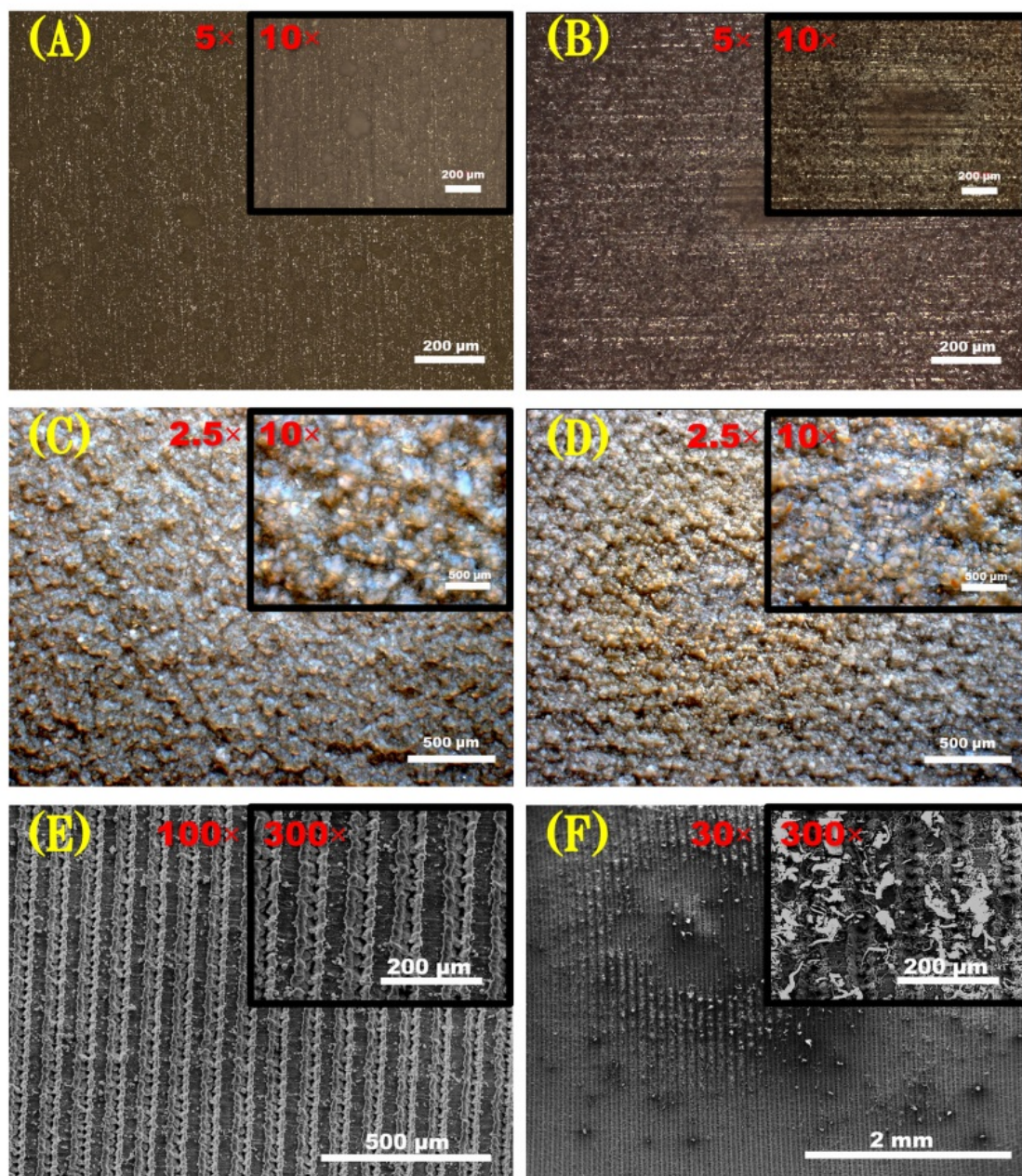


Figure 4.8 Microscopy images of different surface treatments before and after corona exposure: (A) stearic acid SiO₂ before ageing, (B) stearic acid SiO₂ after ageing, (C) NeverWet before ageing, (D) NeverWet after ageing, (E) laser patterning before ageing, and (F) laser patterning after ageing.

The corona exposure method used in this research was indicated to be the most destructive ageing method. However, this specific corona ageing methodology was likely to cause much more damage than that in a practical operation due to the use of sharp needles to generate the intensely focused corona discharges on the samples. Because there is no test standard for

this specific corona ageing on overhead lines, a more represented method may be developed to better simulate the corona ageing on a more appropriate level. For instance, alternate corona ageing can be carried out by examining the ageing behaviour of energised cylindrical conductors with different superhydrophobic treatments in a sense that coronas may be generated in a similar way to that of a practical overhead line system.

Overall, the corona discharge was proven to be such a severe threat to superhydrophobic surface treatments that all the samples were damaged and lost their superhydrophobicity and transformed into superhydrophilic surfaces after 168 h of the corona exposure test. Other more representative corona ageing methods may be carried out to better understand the actual damage the corona discharge could cause to different superhydrophobic surface treatments.

4.4 Concluding Remarks

In this chapter, a family of surface longevity ageing tests were designed and tested on the different surface treatments to examine and to compare their longevities. The NeverWet coating, the stearic acid with SiO₂ nanoparticles coating, and the laser patterning surface treatments demonstrated high levels of superhydrophobicity with low surface hysteresis before ageing. After the ageing experiments, different levels of degradation resulted in different surface treatments under the varied ageing factors. The treatment of the micro-channel laser patterned aluminium alloy substrates was a precise and robust technique, which was proven to be the most resistant surface treatment among the other two coatings against most of the ageing factors. The NeverWet coating was an efficient method to achieve superhydrophobic performance on the aluminium alloy samples. Although it was not as durable as the laser patterning technique, the NeverWet coating was verified as an effective superhydrophobic treatment that survived most of the ageing conditions. On the other hand, the stearic acid with SiO₂ nanoparticle coating was shown to be the least enduring surface treatment compared to the other two techniques, and the coated samples lost their water

repellent ability after most of the ageing tests. Overall, the laser patterning or the NeverWet coating can effectively achieve superhydrophobicity on surfaces with durable ageing performance, which can be potentially deployed on overhead lines to increase reliability and lifespans of systems under different ageing conditions. However, the stearic acid with SiO₂ nanoparticle superhydrophobic coating demonstrated poor durability under most of the ageing conditions and may have a limited application on overhead lines due to its poor ageing performance. The reliability of this coating, however, could change once other methods can be found to prevent its long-term degradation under different ageing conditions.

CHAPTER 5 APPLICATIONS AND BENEFITS OF SURFACE TREATMENTS

5.1 Introduction

Superhydrophobic surface treatments can be a promising approach in the field of reducing or delaying ice accretion on overhead lines [128][129]. The reduction in water-surface contact area on a micro-structured superhydrophobic surface can lead to a slower heat-transmission rate between water drops and the surface, resulting in a longer water drop freezing time. A study of anti-icing shows the freezing time of an 8 μL water drop on a laser patterned superhydrophobic aluminium surface was delayed by up to 3 times compared to an untreated sample [121]. A water drop presented on a Cassie model superhydrophobic surface showed a delayed freezing time of 3 to 5 times longer than that of a similar drop on a smooth hydrophobic surface [48]. Several studies show that superhydrophobic surface treatments can considerably reduce ice adhesion strength and thus increases ice shedding ability on surfaces [25][130][131]. If the superhydrophobic surface treatments can be applied on overhead lines in a way that reduces ice accretion and increases ice shedding ability, not only does the design of new overhead line systems benefit from the reduced loading requirement, but also the reliability of existing aged overhead lines.

Superhydrophobic surfaces can help to reduce audible noise on overhead lines [132]. The audible noise generated by overhead conductor lines can be quite disturbing, especially during wet conditions such as rain or snow. With extra water drops presenting on the conductor line and vibrating under the energised condition, noise can be produced at double the normal frequency (100 Hz / 120 Hz for a 50 Hz / 60 Hz power system) [99][125]. These water drops can also increase the local electric field and lead to corona discharges that generate a high-frequency noise [126][127].

Laser-textured surface treatments can also potentially increase heat dissipation rate on surfaces because of the increasing surface area from the laser patterns. A study shows that

by engraving the laser patterns on metal samples to create micro-structured surfaces, the convective heat transfer coefficient is almost doubled compared to a smooth surface [137].

In this chapter, different applications of superhydrophobic surface treatments are discussed. The icephobicity performance of surface treatments was examined, including water drop freezing tests and frost accretion tests. The benefits of reducing ice accretion on overhead lines are discussed. The performance of the audible noise reduction by a superhydrophobic coating was tested under different wet conditions. Moreover, the convective heat dissipation performance of laser-textured surfaces was examined and compared with untreated surfaces.

5.2 Icephobicity Performance of Surface Treatments

5.2.1 Water Drop Freezing Tests

5.2.1.1 Experimental Procedures

Samples were placed inside sealable sample bags, and mass of each sample with the bag was measured using an electronic scale before the water drop freezing test. A Thermotron SM 8-3800 climate chamber as shown in Figure 5.1 was pre-cooled to either -10 or -20 °C depending on the test. The substrate was placed in the chamber using a clamp and oriented 45° upwards and facing a spraying nozzle. The substrate was allowed to reach thermal equilibrium in the climate chamber for 30 mins prior to the test.

During the test, 12 ml of deionised water was sprayed onto the sample through the nozzle on the chamber door. The sample was left in the chamber for 30 mins to allow ice accretion on the surface. Images were taken after testing for visual comparison. The ice accreted sample was then transferred into the same sealed sample bag. The bag with the sample was allowed to reach room temperature to remove condensation formed on the bag before being weighed. The sample with the sealed bag was then weighed again to determine the mass of ice accretion.



Figure 5.1 Images of Thermotron climate chamber

5.2.1.2 Test Results

In the early stage, a small volume of 2.5 or 4 ml of deionised water was sprayed on substrates, resulting in significant deviations in the results, due to the inaccuracy occurring during dispensing such a small amount of water in each spray. The pre-existed high humidity in the chamber before testing also resulted in a significantly inaccurate outcome. To increase accuracy and maintain the humidity level in the chamber before each test, methods were used to optimise the ice accretion test. Firstly, 12 ml of deionised water was used to provide an even and sufficient amount of water to be sprayed on the substrate to reduce deviation. Secondly, the chamber was dried out under high temperature before each test to maintain a similar level of humidity. Thirdly, tissues were placed and replaced in the chamber regularly to collect extra water from spraying.

Table 5.1 shows the result of the water drop freezing test on uncoated and NeverWet coated substrates under the testing temperatures of -10 and -20 °C. Under the temperature of -10 °C, the amount of water frozen on the NeverWet coated aluminium, silicone rubber and EPDM rubber substrates were 95.6%, 91.6%, and 97.5% less than that of the uncoated substrates respectively, which indicates the NeverWet coated samples have high water and ice repellent abilities. When the testing temperature was decreased to -20 °C, the amount of water frozen

on the NeverWet coated aluminium, silicone rubber and EPDM rubber substrate decreased by 82.3%, 67.1%, and 64.3% respectively, compared with that of the uncoated substrates. This result indicates the NeverWet coating was slightly less effective under the lower testing temperature, but it could still reduce a significant amount of ice accretion.

Figure 5.2 compares the visual inspection of the ice accretion test on the uncoated and NeverWet coated substrates at -10 and -20 °C. Under the temperature of -10 °C, big ice pillars covered a particular area of the uncoated substrate, while hardly any ice was noticed on the NeverWet coated substrate. An excellent icephobicity of the NeverWet coating was observed at -10 °C on all the three types of substrates. When the testing temperature decreased to -20 °C, bigger ice pillars covered a larger area of the uncoated substrates. Moreover, a small amount of ice also started to accumulate on the edge of the NeverWet coated substrate, although the size of ice balls was still much smaller than that on the uncoated substrates. The anti-icing performance of the NeverWet coating was reduced under -20 °C on all the substrates. However, it still distinctly enhanced the icephobicity on the surface compared with the uncoated substrates.

Table 5.1 Icing test on coated and uncoated substrates with different temperature

Coating Type	Temperature (°C)	Mass of Frozen Water Drops (g)		
		Aluminium	Silicone Rubber	EPDM Rubber
Uncoated	-10	0.319	0.308	0.361
NeverWet		0.014	0.026	0.009
Uncoated	-20	0.372	0.346	0.420
NeverWet		0.066	0.114	0.150

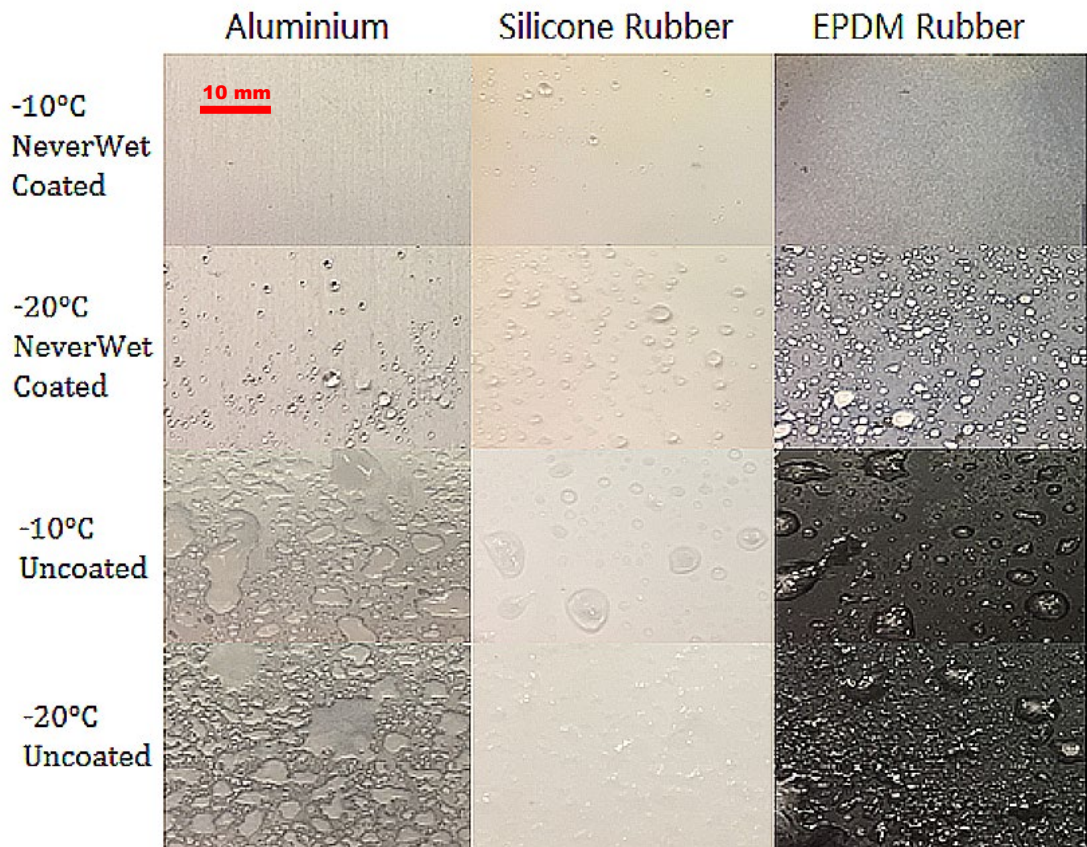


Figure 5.2 Images of uncoated and NeverWet coated substrates after -10 and -20 °C ice accretion tests

5.2.1.3 Repeated Water Drop Freeze and Thaw Tests

The water drop freeze and then thaw procedure was repeated 7 times on the NeverWet coated EPDM rubber substrate under a temperature of -10 °C to examine the influence of repeatedly freezing and thawing of the samples on the stability of the coating. Visual inspections and surface microscopy were taken after each freeze and thaw cycle.

Figure 5.3 shows the images of a sample after repeated water drop freezing tests. It shows that there was hardly any ice accreted on the substrate during the first cycle, except the fact that an ice pillar was found on the edge of the substrate as shown in the figure with a red highlight. From the third to the seventh cycle, small ice drops gradually appeared on the surface, and the size of the ice pillar on the highlighted part was gradually increased.

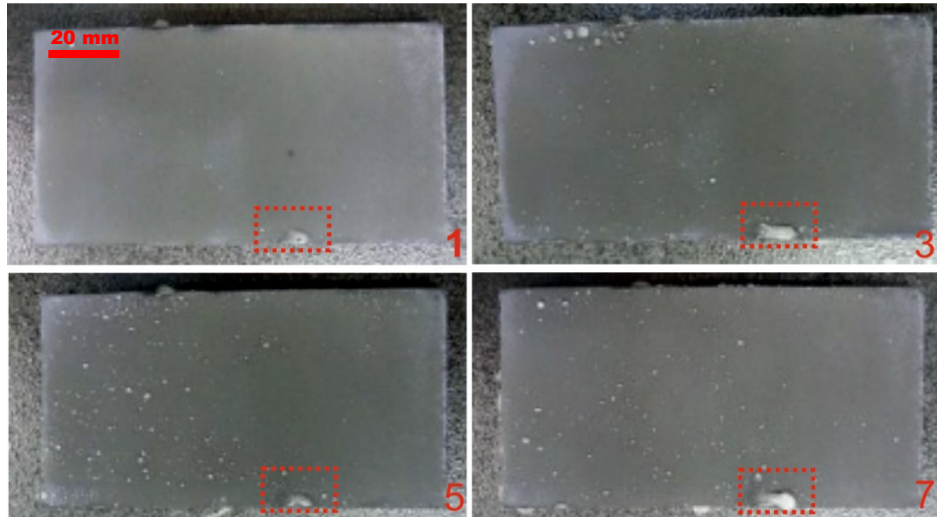


Figure 5.3 Ice accretion on the NeverWet coated EPDM rubber after freeze and thaw tests

Figure 5.4 highlights a severely damaged area of the test sample. It shows a colour change on the part of the substrate after seven times of freeze and thaw cycles. To further examine the severely damaged area on the sample, surface microscopy was examined on the damaged area with 50 times magnification as shown in Figure 5.5 before and after the freeze and thaw cycle. The red and yellow highlighted parts assisted in relocating the damaged area after each cycle. The red and yellow highlighted areas in image (a) show some small cellular patterns on the base layer of the substrate. In image (b), the outlines of the same cellular patterns in the highlighted area seem to be sharper and more apparent compared to image (a). This observation may be because the top layer of coating material was worn off after 7 freeze and thaw cycles, and thus the cellular patterns of the base layer were revealed.



Figure 5.4 An example of coating damage during the icing test

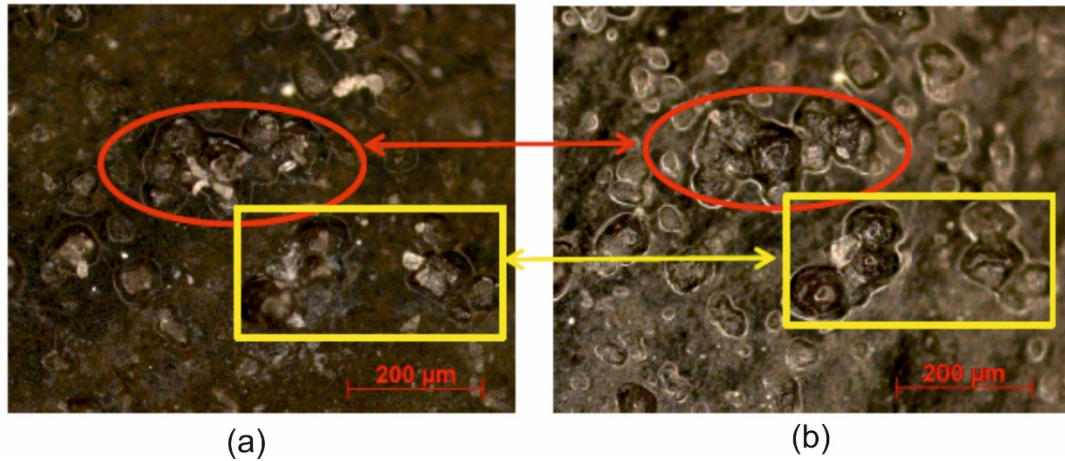


Figure 5.5 Microscope images of the damaged area after (a) the 1st freeze/thaw cycle and (b) the 7th freeze/thaw cycle

Overall, the coating was slightly damaged on most parts of the sample, while a specific area on the edge of the sample was severely damaged after 7 freeze and thaw cycles. This result indicates that although the coating is likely to deliver a reduction in ice accretion, the longevity of the coating could become an issue for practical applications. Therefore, more robust superhydrophobic surface treatments are required in order to deliver longer-lasting lifespans.

5.2.2 Frost Accretion Tests

Frost can be described as a thin layer of frozen water vapour that is produced when vapours above 0 °C environment come across a solid surface with a temperature below 0 °C [138]. A study shows the ice formation on a surface can directly come from the vapours of a supersaturated ambient environment [139]. If frost accretion on a surface can be reduced or delayed, it can also help in reducing or delaying further ice formation on the sample. Therefore, it is essential to gain a better understanding of whether superhydrophobic surfaces can minimise or delay frost formation. In this section, the frost repellent ability of the NeverWet superhydrophobic coated aluminium alloy samples was examined by comparing the relative mass of frost growth to that of the uncoated samples.

5.2.2.1 Experimental Procedures

A Mercatus freezer room with dimensions of 2 x 1.7 x 2.1 m (W x D x H) was used in this test to simulate a cold environment with a temperature of 2 °C for the frost accretion tests. A sealed cloud chamber with dimensions of 1 x 1 x 1 m (W x D x H) was placed inside the freezer room. A large amount of water was sprayed around the inner walls of the cloud chamber to generate a supersaturated environment for the frost test. 5 of each uncoated and NeverWet coated aluminium alloy samples were prepared for this experiment. Samples were weighed in their respective sealable bags and then transferred onto a big steel block with large heat capacity. The steel block with samples on it was sealed with a big sample bag to prevent pre-frosting, and then it was placed into a pre-cooled Kasco chamber at -15 °C. After a specific time in the Kasco chamber to reach thermal equilibrium, the block and samples were quickly transferred to the cloud chamber, and then removed from the bag. The samples were left inside the cloud chamber to grow frost for 20 mins. The frosted samples were sealed into their respective bags again using a tweezer with minimal contact to the samples for accuracy. The samples with bags were removed from the freezer room and allowed to reach room temperature until condensation that formed on the outside of the bag dried out. The mass of each sample with the sealed bag was measured to determine the mass of the accreted frost. The frost accretion test was repeated on each of the uncoated and coated samples 5 times. The mass of each sample was measured 3 times before and after the frost accretion test.

5.2.2.2 Pre-cooling Calibration

This calibration aimed to obtain a sufficient pre-cooling duration for the samples to reach a stable temperature changing curve for each frost test. 2 pre-cooling calibration tests were carried out inside the Kasco chamber. Each of the tests was repeated once more to ensure accuracy. A thermal meter was attached to the samples to record the temperature changing curves.

Test 1 A sample was pre-cooled under $-15\text{ }^{\circ}\text{C}$ for 3 h, then transferred to the climate chamber under $2\text{ }^{\circ}\text{C}$ for 20 mins.

Test 2 A sample was pre-cooled under $-15\text{ }^{\circ}\text{C}$ for 12 h, then transferred to the climate chamber under $2\text{ }^{\circ}\text{C}$ for 20 mins.

Pre-cooling temperature changing curves of 3 and 12 h were compared, as shown in Figure 5.6. The sample after the 3 h of pre-cooling showed a starting temperature between -8 and $-9\text{ }^{\circ}\text{C}$. After 20 mins in the freezer room, the temperature gradually increased to between -2 and $-3\text{ }^{\circ}\text{C}$, which was still below $0\text{ }^{\circ}\text{C}$ thus validating the test was suitable for frost formation. With 12 h of pre-cooling, the sample experienced an overall lower temperature with a similar trend in temperature changing. The test with 3 h of pre-cooling showed a slightly less deviation than that of the 12 h one. For higher efficiency and accuracy, a 3 h pre-cooling time was chosen to carry out the frost accretion tests.

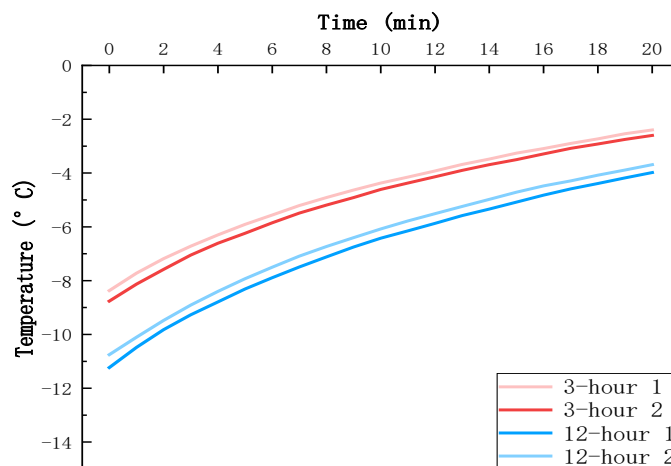


Figure 5.6 Temperature changing curves for the sample pre-cooling procedure under $-15\text{ }^{\circ}\text{C}$ in the Kasco chamber (3-hour vs. 12-hour of pre-cooling)

5.2.2.3 Test Results

Table 5.2 shows the result of the frost accretion measurements for both the uncoated and NeverWet coated samples. The uncoated samples had an average mass of 0.0089 g , and the NeverWet coated samples had an average mass of 0.0078 g after the frost accretion test. These results show that the use of NeverWet superhydrophobic coating on the samples can reduce the average frost accretion mass by 13.18% .

Table 5.2 Frost accretion test results on the uncoated and NeverWet coated samples

Sample Mass (g)	Uncoated Samples		NeverWet Samples	
	Before Frosting	After Frosting	Before Frosting	After Frosting
Sample 1	5.3895	5.3987	5.4317	5.4394
Sample 2	5.4079	5.4163	5.4398	5.4468
Sample 3	5.4084	5.4187	5.4455	5.4536
Sample 4	5.4077	5.4163	5.4461	5.4544
Sample 5	5.4012	5.4095	5.4328	5.4405
Average (g)	5.4029	5.4119	5.4392	5.4469
Frost Mass (g)	0.0089		0.0078	
Frost Reduction Percentage	13.18%			

Overall, the frost accretion test demonstrates that NeverWet superhydrophobic coating can provide the potential benefit of reducing frost accretion on the aluminium alloy surfaces during frosting weather. This result matches Yang’s and Yoonchul’s studies such that frost accumulation can be reduced and slowed down to some degree by the use of superhydrophobic coatings [79][82]. While the mass of the frost accretion can be reduced when using the superhydrophobic coating, there remains a risk of further ice build-up. The delay of frost formation may also aid in the delay of further ice accretion. A future test could be carried out to examine whether superhydrophobic coatings can contribute to a reduction in the ice adhesion strength of surfaces. If the ice adhesion strength of a conductor can be reduced to a point where the self-weight of any ice accretion can cause it to shed before forming a full annular ice ring around the conductor, an improvement of ice shedding ability of overhead lines can be achieved.

5.3 Benefits of Reducing Ice Accretions on Overhead Lines

Overhead lines can be vulnerable under the circumstance of the accumulation of ice and snow, due to the excessive weight added to conductor lines that lead to sagging of the lines and reduction of clearance distance. When the extra load of ice accretion goes beyond the loading-capacity of the tower, the entire system can collapse. This can cause great danger to the surroundings and continuous power outages of substantial areas, resulting in economic loss and increased reconstruction expenditure. The combination of ice accretion and wind forces can result in even larger stresses being applied to overhead lines and towers, leading to severe damage to overhead line infrastructures [11].

Overhead line mechanical loads and thermal expansion lead to the occurrence of sag. There are a few factors affecting sag on overhead line conductors, including conductor weight and ice loading, conductor span length, conductor tension, wind force, and temperature. The sag is in direct proportion to the conductor weight, the ice loading, and the span length, and inversely proportional to the conductor tension. The sag length of an overhead conductor line can significantly affect the line clearance distance and the overall height of the tower. Ice accretion on a conductor line deploys extra mechanical weight on the line and thus increases the conductor tension. Exceeding the maximum percentage of rated tensile strength (%RTS) can cause severe damage, especially on the wood poles used on distribution lines where a high %RTS is likely to pull the poles down and break the conductors. With lattice towers, conductor failure is a more likely outcome if the maximum %RTS is exceeded. In order to release the extra tension, a conductor expands its length which also results in the sag increasing. If any surface treatment can be applied on overhead lines to reduce ice accretions and thus reduce the extra tension and line sagging, tower height can be significantly reduced, and the system designs can benefit from lower-cost and visual amenity. To better understand the impact of icing on overhead line systems, the influence of ice accretion on sag and %RTS of different types of overhead line conductors are discussed in this section. This provides a quantification of the relationship between ice accretion

thickness and maximum clearance or tensile strength of overhead lines. This also indicates the need for a solution on reducing ice accretions on overhead lines to prevent potential damages during icing events. Thus, calculations are presented to quantify the potential benefits of using a superhydrophobic surface treatment to reduce ice accretion thickness on overhead lines.

In this study, three types of conductors that are commonly used on the high voltage power system are chosen as examples: Araucaria (a large AAAC conductor typically used in transmission systems), Oak (a smaller AAAC conductor typically used in distribution systems), and Madrid (an ACCC conductor similar to Araucaria). The parameters of the conductors are shown in Table 5.3, according to British Standard EN 50182 [140] and CTC Global [141].

Table 5.3 Parameters of the AAAC Araucaria, AAAC Oak, and ACCC Madrid conductors [140] [141]

Conductor Types	Conductors per Phase	Ruling Span (m)	Diameter (mm)	Mass (kg/km)	Conductor Rated Strength (kN)
AAAC Araucaria	3	300	37.26	2269.4	242.2
AAAC Oak	1	100	13.95	324.5	35.1
ACCC Madrid	3	300	38.20	2977.0	219.7

The parameters list below are used, according to British Standard EN 50341 [142], to simulate the sag lengths of conductors under different ice thickness R_o without wind force, and R_w with wind force. A wind speed of 30 m/s is chosen based on the maximum wind speed in the UK. A temperature of -10 °C is considered for both icing in still air and combined wind and ice in the UK.

$$\text{Installation Temperature (}^\circ\text{C)} = 5$$

$$\text{Coefficient of Thermal Expansion (}/^\circ\text{C)} = 0.000023$$

$$\text{Ice Density (kg/m}^3\text{)} = 913.1$$

$$\text{Installation Tension (\%RBS)} = 20\%$$

The ice thicknesses are set from 0 to 80 mm (at 5 mm intervals). These represent real case values found in BS EN 50341[142]. A value of $R_o = 80$ mm (without wind) or $R_w = 30$ mm (with wind) for the maximum radial thickness of ice accretion is used in the British power system. Section 4.2.3 of BS EN 50341 also details the ice loading expected for overhead lines in the Finland power system, in which a maximum ice thickness of 63 mm would be used with an Oak conductor to assess the combined load on the line as a result of ice and wind. Therefore, ice thicknesses over 30 mm and up to 80 mm for the ice and wind condition are also demonstrated to reflect conditions that could be expected in countries with more severe winter climates.

5.3.1 Impacts of Ice Accretions on Overhead Lines

5.3.1.1 Sag vs. Ice Accretion Thickness

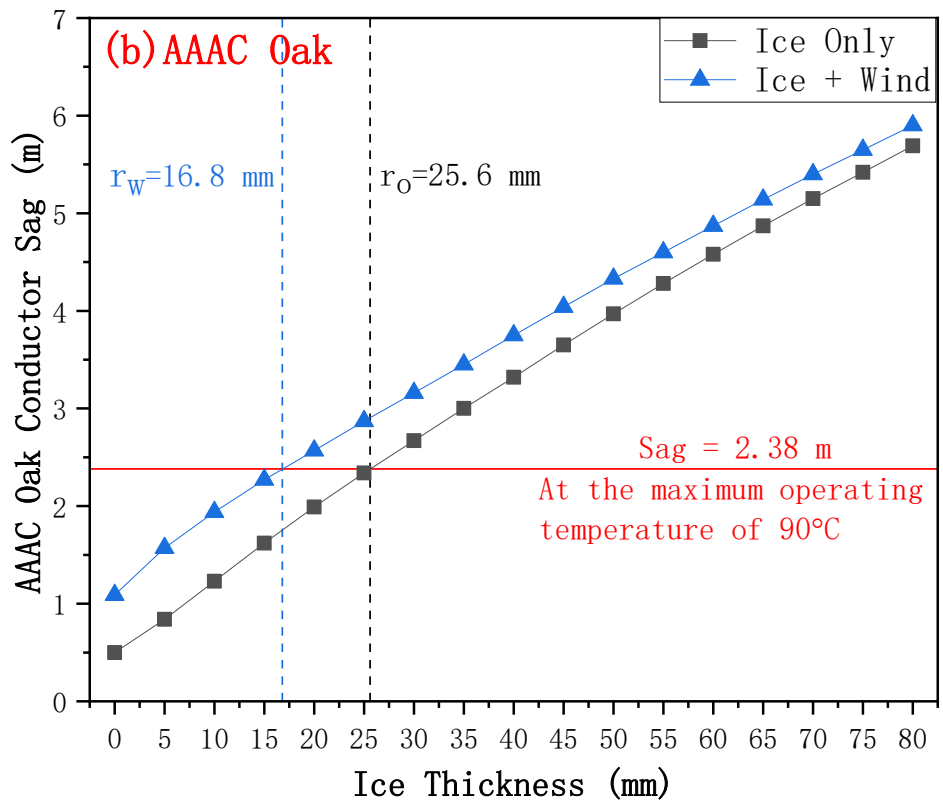
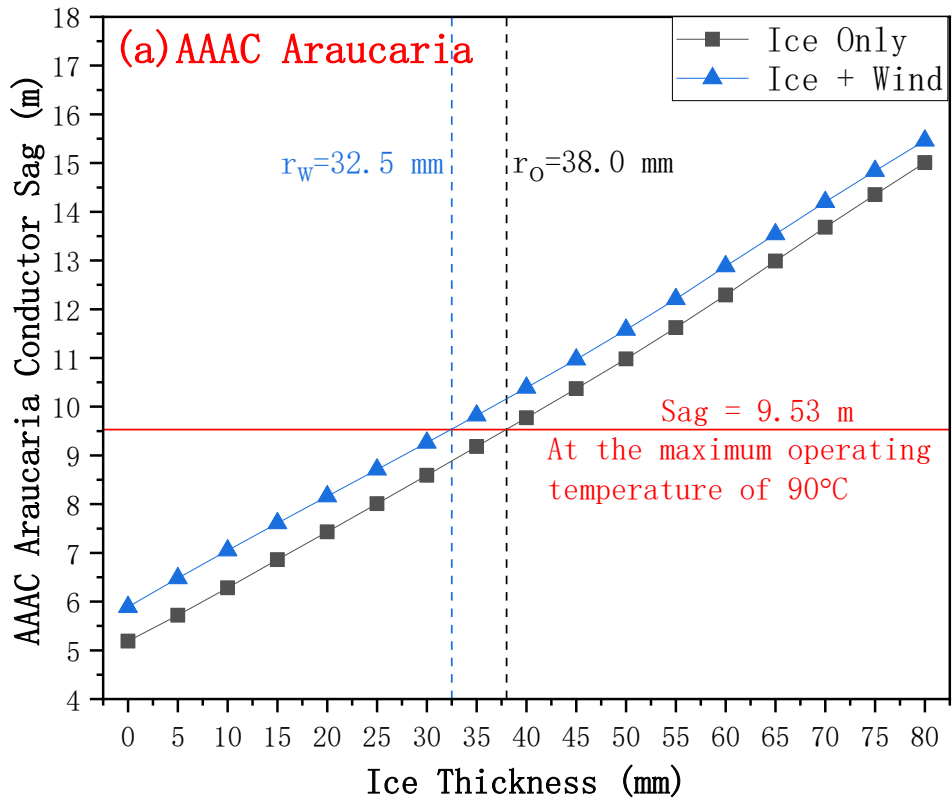
Figure 5.7 shows the expected sag for ice thicknesses of up to 80 mm with or without wind loads of three types of conductors: (a) AAAC Araucaria, (b) AAAC Oak, and (c) ACCC Madrid. With a combination of icing and wind loads, the sag of a conductor line is usually higher than that of the ice accretion only case. This is due to the extra force of wind load being applied to the conductor, and thus increases the sag level. An overhead line will have a specific level of sag at its maximum operating temperature as a result of conductor expansion. Ideally, the ice and wind load would not increase the sag beyond this level (indicated by the red line in the figure). If the ice and wind load can be managed to ensure the sag does not exceed this level, the height of the overhead line tower can be controlled to the lowest possible value.

In Figure 5.7 (a), an almost linear growth trend is shown such that the sag of the AAAC Araucaria conductor increases with the increase of ice thickness. The red guideline in the figure defines the maximum allowable sag of 9.53 m on the Araucaria conductor under the maximum operating temperature of 90 °C. If the sag level is below 9.53 m as a result of ice accretion with or without wind load, which is equivalent to $R_w < 32.5$ mm or $R_o < 38.0$ mm,

the conductor line remains within the safety clearance. If the ice thickness $R_w > 32.5$ mm or $R_o > 38.0$ mm, the sag level is beyond 9.53 m. At this point, the ice load contributes to an increase in line sagging and therefore the safety clearance is breached. In this situation, the overhead line would need to be designed to have the conductors positioned higher off the ground.

In Figure 5.7 (b), the maximum allowable sag of the AAAC Oak conductor is 2.38 m at the maximum operating temperature of 90 °C as the red guideline shows. This specific sag value is equivalent to the sag caused by ice accretion at the critical point when $R_w = 16.8$ mm or $R_o = 25.6$ mm. When R_o or R_w is beyond this point, the clearance distance of the conductor line is infringed. Compared to the Araucaria conductor with larger radial size and longer ruling span, the Oak conductor is more affected by ice and wind loads under the same icing weather. This is because of the shorter tower height of the Oak conductor lines, which provides less clearance. When the same thickness of ice accretion on the Oak conductor lines causes sagging, the clearance of the shorter overhead line tower is violated more easily, and the chance of tower collapse is also higher during extreme icing weather.

In Figure 5.7 (c), the ACCC Madrid conductor offers a higher maximum operating temperature of 200 °C. At this temperature, the maximum sag level of the conductor is 10.73 m as the red guideline shows in the figure. This sag value is equivalent to the sag caused by ice accretion when $R_o = 24.5$ mm or $R_w = 18.7$ mm. Compared to the AAAC Araucaria conductor with a similar radial size and the same ruling span, the ACCC Madrid conductor is heavier in weight than the Araucaria conductor (2977 vs. 2269 kg/km). With the same ice accretion thickness, the heavier weight Madrid conductor has a larger sag value than the AAAC Araucaria conductor. Thus, under the same icing weather, the ACCC Madrid conductor will be affected more significantly in terms of line sagging.



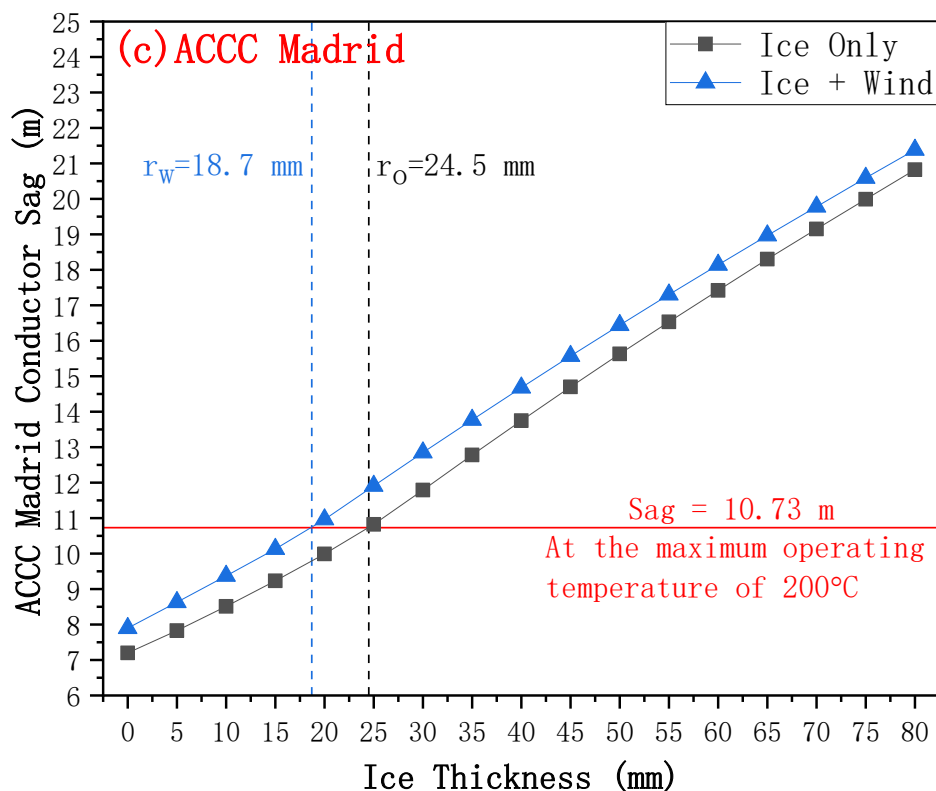


Figure 5.7 Changes of conductor sag with increasing ice accretion thickness on (a) AAAC Araucaria conductor, (b) AAAC Oak conductor, and (c) ACCC Madrid conductor with and without wind load

5.3.1.2 %RTS vs. Ice Accretion Thickness

Figure 5.8 shows the expected %RTS for ice thicknesses up to 80 mm of three types of conductors under these conditions: (a) ice accretion only and (b) ice accretion with wind loads. With a combination of icing and wind loads, the %RTS of a conductor line is usually higher than that of the ice accretion only case due to the extra force of wind load being applied to the conductor. According to CIGRE TB 324 [143] and IEC 60826 [144], %RTS of conductors should not exceed 50% under the situation of ice and wind loads to avoid conductor tensile failure. The maximum allowable %RTS of 50% is shown in the figure as the red guideline.

Among all the three types of conductors, the %RTS of the Oak conductor shows a much faster increment rate with increased ice thickness under both conditions. The maximum

allowable rated tensile strength of 50% the AAAC Oak conductor is breached when ice thickness $R_o > 23.1$ mm or $R_w > 14.1$ mm. The maximum allowable %RTS of the AAAC Araucaria conductor is breached when $R_o > 31.3$ mm or $R_w > 25.4$ mm. The ACCC Madrid conductor shows the lowest %RTS increasing rate among all three types of conductors. The maximum allowable %RTS is breached when $R_o > 47.9$ or $R_w > 43.1$ mm.

The ice thicknesses that breach the maximum %RTS (as shown in Figure 5.8) are lower than the ice thicknesses that breach the maximum sag levels (as shown in Figure 5.7) for both the AAAC Araucaria and Oak conductors with and without wind load. This indicates these two types of conductors are much more affected in terms of %RTS under icing weather than the maximum allowable %RTS is breached before the maximum sag is breached. On ACCC Madrid conductors, the ice accretion thickness expected to breach the maximum %RTS is much higher than the level required to breach the maximum sag. This may be because the composite carbon fibre cores in ACCC conductors have advantages of high-strength and high-flexibility, allowing the conductors to stretch further without breaking under icing and wind loading weather. Thus, the sag of the Madrid conductor is more affected by ice accretion, and the maximum safety clearance of the line is breached before the maximum %RTS is breached.

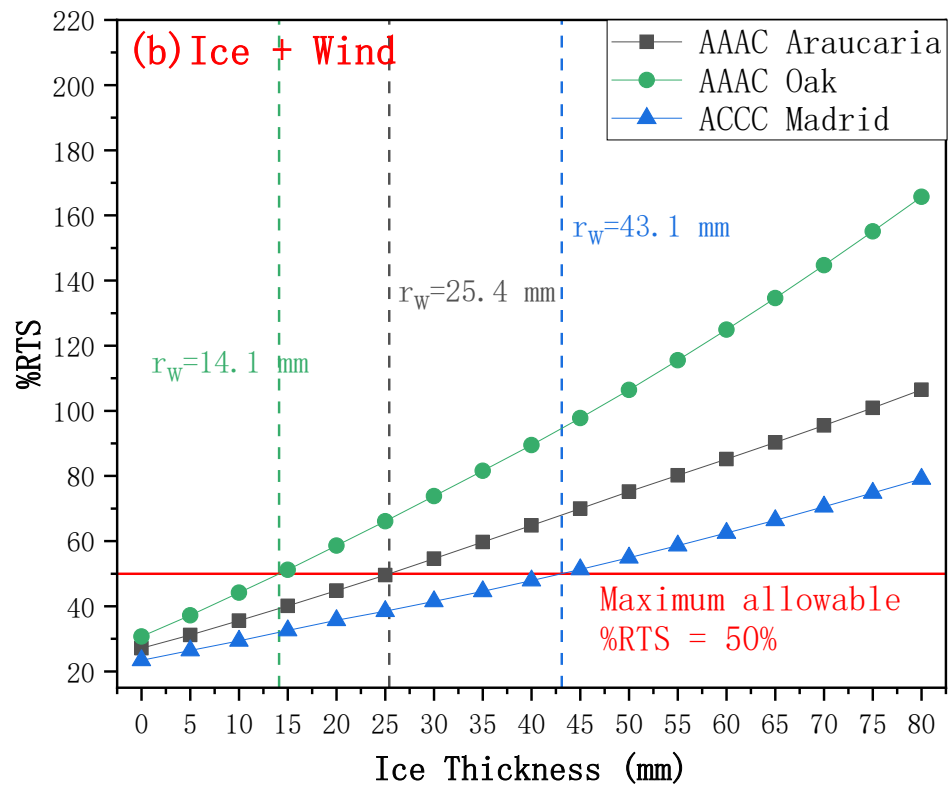
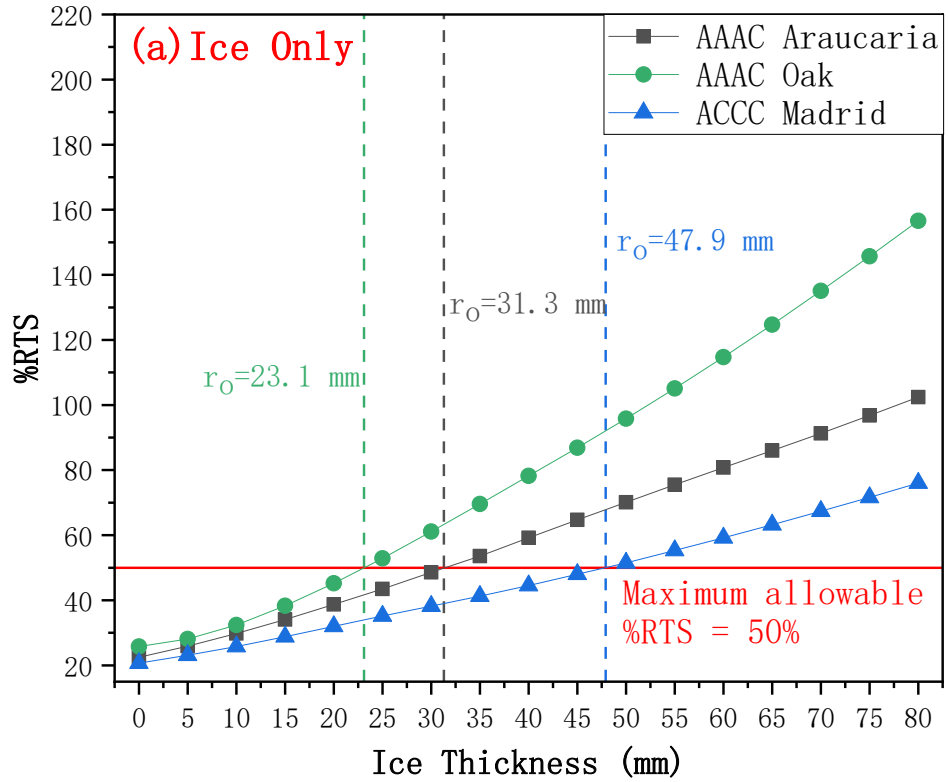


Figure 5.8 Changes of %RTS with increasing ice accretion thickness on conductors under conditions of (a) ice accretion only and (b) ice with wind load

Overall, the impact of icing on sag and %RTS of overhead lines are compared using three different types of conductors. The sag of the smaller size AAAC Oak conductor and the heavier weight ACCC Madrid conductor are concluded to be more affected by the same amount of ice accretion than that of the AAAC Araucaria conductor. The ACCC Madrid conductor shows a lower %RTS than that of the AAAC Araucaria or the Oak conductor under the same ice accretion thickness because of its high strength and flexibility.

When designing an overhead line, ideally, the sag expected on an overhead line when the line is ice-loaded should be lower than the value of sag at its maximum operating temperature. If the sag as a result of ice load is higher than this value, this will be the factor that determines the tower height and increases the size and cost of the overhead line. The same principle applies to %RTS when designing an overhead line. If the %RTS of an overhead line as a result of ice load is higher than its maximum allowable tensile strength, the designer of the overhead line would have to specify a smaller span length in its design. This would lead to an increased cost as more poles would be required to support the line. As such, it is crucial to control ice accretion on overhead lines to ensure a safe operation within the limitations of clearance distance and tensile strength. It is only necessary to control ice accretion within the safe region that is below the breaching points of the maximum allowable sag and %RTS, other than to eliminate it. Therefore, minimising ice loads through the use of surface treatments would be a sensible solution to ensure the safe operation and optimal design of overhead lines.

5.3.2 Benefits of Applying Surface Treatments

If any surface treatment can be applied on overhead lines in a way that effectively reduces or delays ice accretion, the sagging of conductor lines can be decreased. If ice thickness can be controlled within the critical point mentioned above, it will increase the safety of overhead line systems and prevent catastrophic situations such as tower collapse. The deployment of advanced superhydrophobic or icephobic surface treatment can result in a decrease in maximum sag, which leads to a reduction in the required tower clearance. This can also

decrease the financial cost of future construction of towers by creating a lower height tower design.

To quantify the potential benefit of using surface treatments on reducing ice accretions on overhead lines, ice accretion weight is calculated on Araucaria, Oak, and Madrid conductors with and without surface treatment. Assuming conductors have an ice accretion thickness of 25 mm with ice density of 913.1 kg/m³, if a surface treatment can be used to reduce ice accretion on the conductors by 10 mm, the weight reductions on the conductors are calculated in Table 5.4.

Table 5.4 Changes of the ice weight and total weight of conductor lines before and after applying surface treatment

Weight (kg/m)	Conductor	Ice Accretion		In Total		Total Weight Reduction (%)
		0	25	15	25	
AAAC Araucaria	2.269	2.249	4.465	4.518	6.734	32.9
AAAC Oak	0.325	1.246	2.793	1.571	3.118	49.6
ACCC Madrid	2.977	2.289	4.532	5.266	7.509	29.9

Without any surface treatment, a 25 mm ice load adds an additional weight of 4.465 kg/m on the Araucaria conductor, which is almost 2 times its bare conductor weight. The same 25 mm thickness adds on 4.532 kg/m in additional weight on to the ACCC Madrid conductor, which is equivalent to 1.5 times of its conductor weight. It is even higher on the AAAC Oak conductor that a 25 mm ice load increases the weight of the line by 2.793 kg/m, which is nearly 8.6 times of the weight of a bare Oak conductor line. With a surface treatment that reduces ice accretion by 10 mm, the total weight is reduced by 32.9% (from 6.734 to 4.518 kg/m) on the Araucaria conductor. The weight reduction is also more significant on the Oak conductor because of the surface treatment, resulting in 49.6% total mass drop (from 3.118

to 1.571 kg/m). The weight reduction on the Madrid conductor is 29.9% (from 7.509 to 5.266 kg/m), which is the least among all three types of conductors.

Overall, the amount of ice accretion can be reduced significantly on different overhead conductor lines by applying the surface treatment. The benefits of reducing ice accretion are arguably more effective at the distribution line level such as the Oak conductor with a smaller size at the lower voltage level. The deployment of surface treatments on existing conductor lines can also assist in reducing stress and tension on overhead line towers, foundations, and other fittings and insulators. This will help to increase lifespan and enhance the reliability of existing overhead line systems. If the advantages of surface treatments can be considered in future overhead line designs, a reduction in mechanical strength with smaller cores and a reduction in line sagging can be achieved with lower construction cost, and lower financial losses during icing events.

5.4 Audible Noise Reduction on Overhead Lines

The accumulation of water drops or other pollution on conductors caused by different weather such as rain or snow can result in the generation of audible noises on overhead lines due to an increased electrical field [3]. Audible noise within the frequency range 20 Hz to 20 kHz can be detected by human ears [149]. The audible noises generated on AC transmission overhead lines can be divided into two spectrums: a wide spectrum crackling noise with frequency ranging from 1 to 20 kHz, and a low spectrum humming noise with frequency primarily at 100 Hz [135][150][151]. The wide spectrum crackling noise was mainly due to a defect on overhead lines causing corona discharge [152]. Different research offers differing opinions on the 100 Hz humming noise. Straumann believes it is due to the drifting of ions from partial discharge under the AC voltage that results in a doubled frequency of the noise [153][154]. Teich and Weber concluded that a 100 Hz humming noise can exist without the partial discharge and could be caused by the periodic movement of water drops with a frequency of 100 Hz [133]. Other studies also tested the vibration of

water drops on surfaces of overhead lines and discovered a frequency of twice of the AC voltage [155][156].

To demonstrate whether the presence of water drops on energised overhead lines was the cause of the increased noise level at 100 Hz, a test was carried out prior to this study to compare the 100 Hz noise emitted from energised conductors under both dry and wet conditions. The test concluded that the noise level under the dry condition was similar to the background noise (around 30 dB), while the noise level under the wet condition was much higher (around 50 dB). This result is further evidence to indicate that the 100 Hz noise was emitted due to the presence of water drops on the conductors.

The audible noise study described in this section is collaborative research between the author of this thesis and Xu Zhang. This study aims to examine whether a superhydrophobic coating could help to reduce audible noise levels on overhead lines. The NeverWet coating was used to produce superhydrophobic surfaces in this study. The noise levels of overhead line conductors with and without the superhydrophobic coating were recorded and compared in an anechoic chamber under energetic and wet conditions.

5.4.1 Experimental Descriptions

An anechoic chamber with dimensions 10.5 x 4.3 x 3 m (W x D x H), as shown in Figure 5.9, was used in this research to minimise the background noise and noise reflections for better accuracy in the experiments. The chamber was assembled with a 0.7 mm thickness of insulation panels and 50 mm inner cross-layered mineral wool. The inside walls of the chamber were covered by wedges with porous foam for sound absorptions and a reduction of sound wave reflections. Background noise levels were tested inside and outside of the chamber. At 100 Hz, the average noise reduction was 17 dB inside the chamber.

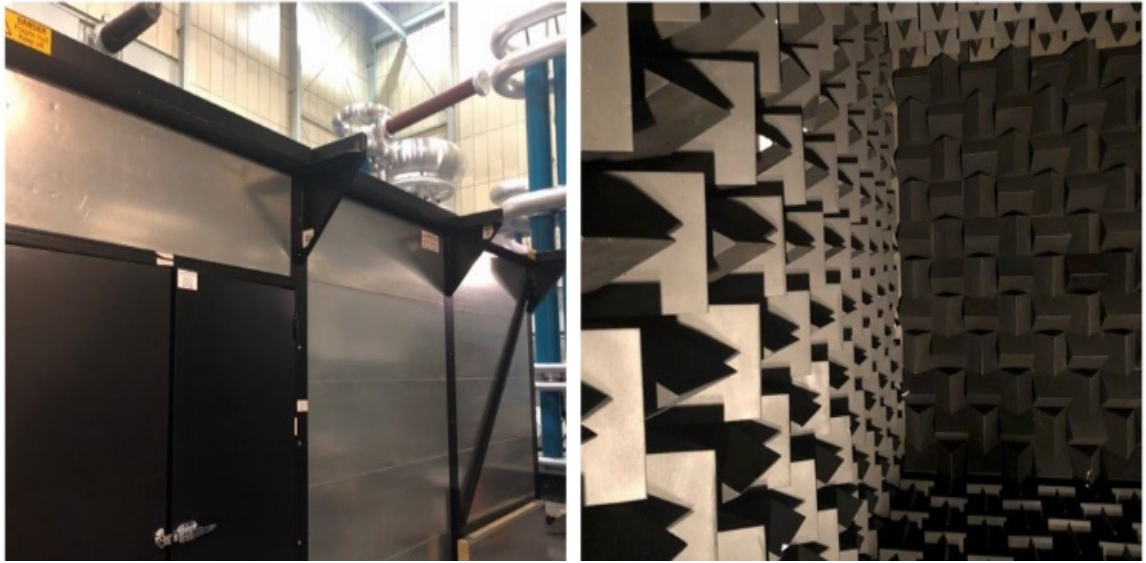


Figure 5.9 Images of the anechoic chamber

Two of each the aluminium conductor steel reinforced (ACSR) and the GAP type super thermal-resistant ACSR conductors were used in this study. Both types of conductors have a similar diameter of 32 mm and a length of 4 m. The NeverWet superhydrophobic coating was applied on one of each type of the conductors, and the rest of the two conductors remained untreated for comparison.

Figure 5.10 shows the experimental set-up of the test. A 0-150 kV transformer was installed and connected to the inside of the chamber via a bushing to create a 110 kV (RMS) power supply. Two spheres were used on both sides of the conductor line to ensure the electric field was uniform. An earthed cage with a diameter of 150 cm, as shown in Figure 5.11, was designed to generate a surface electric field of 18 kV/cm. This is equivalent to the average gradient on a 400 kV twin bundle conductor line. Uni-spray Mark 1 nozzles were used to generate different wet conditions with different flow rates and water pressures. Light rain with a flow rate of 20 mm/h was generated using 2 nozzles under a water pressure of 0.7 bar, and heavy rain with a flow rate of 70 mm/h was generated using 4 nozzles under a water pressure of 1 bar.

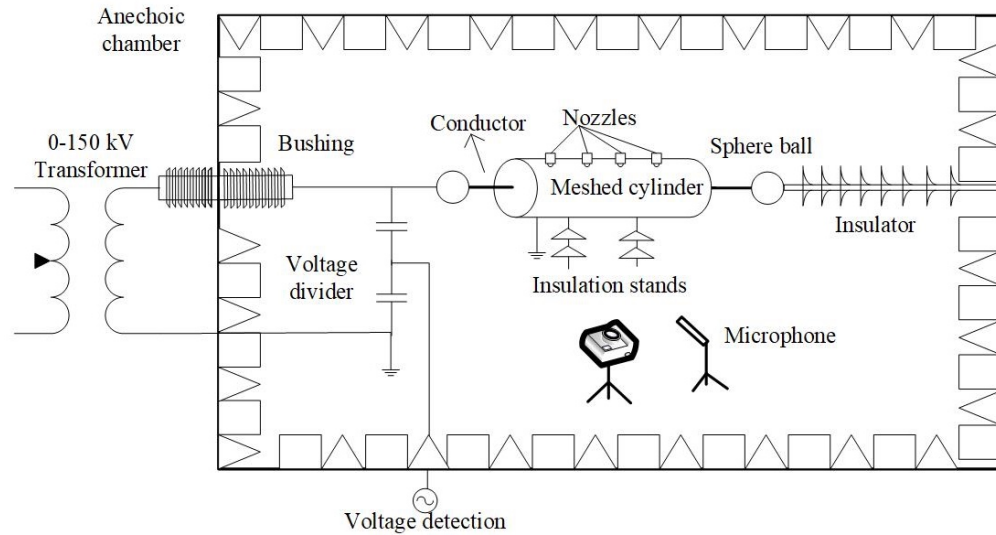


Figure 5.10 The experimental set-up diagram of audible noise tests

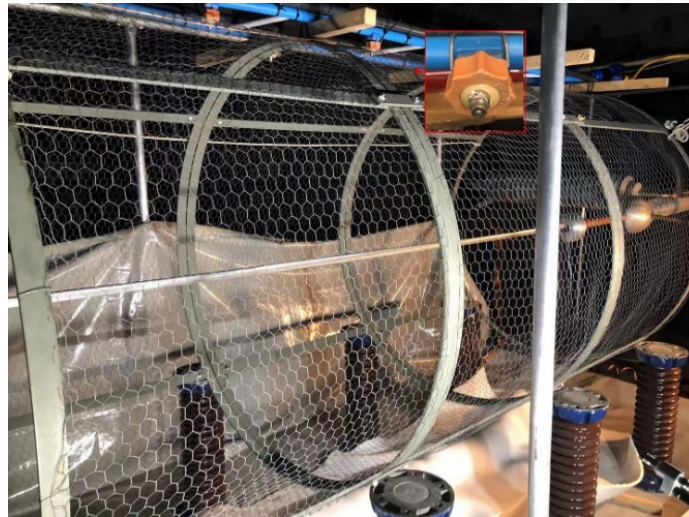


Figure 5.11 The Image of the earthed cage set-up inside the chamber

5.4.2 Test Results

100 Hz is the most concerning noise during wet weather due to its abilities to travel long distances and to last a long time [134]. Superhydrophobic coatings can reduce water accretion on conductor lines and thus can potentially reduce the noise level of conductors during wet conditions. To test the influence of the superhydrophobic coating on this 100 Hz noise, NeverWet coated and the uncoated conductor samples were recorded and compared under different levels of the electric field. Light and heavy rain conditions were simulated as shown in Figure 5.12 and Figure 5.13.

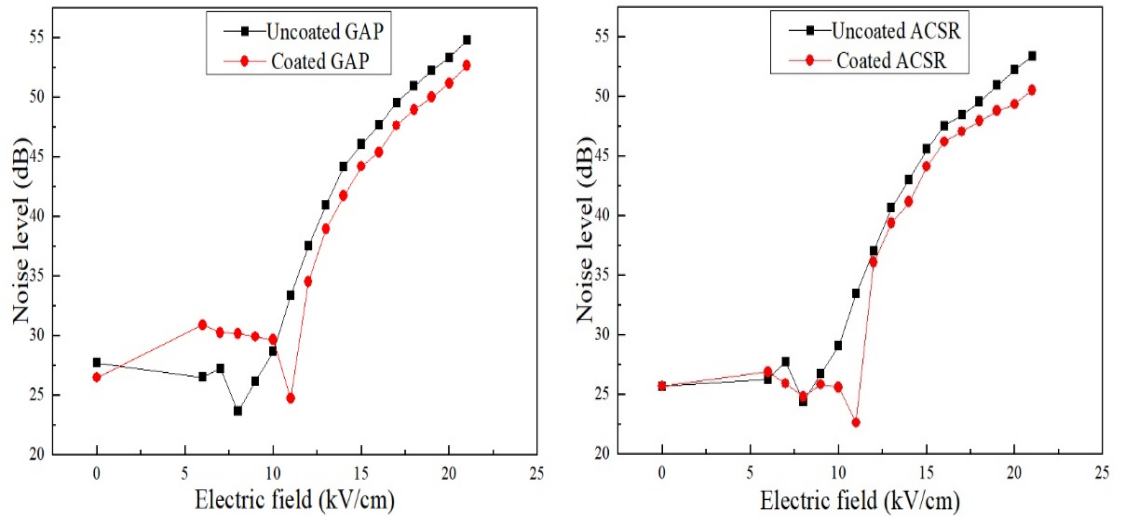


Figure 5.12 Noise levels at 100 Hz with different levels of electric field on coated and uncoated GAP (left) and ACSR (right) conductors during the light rain condition

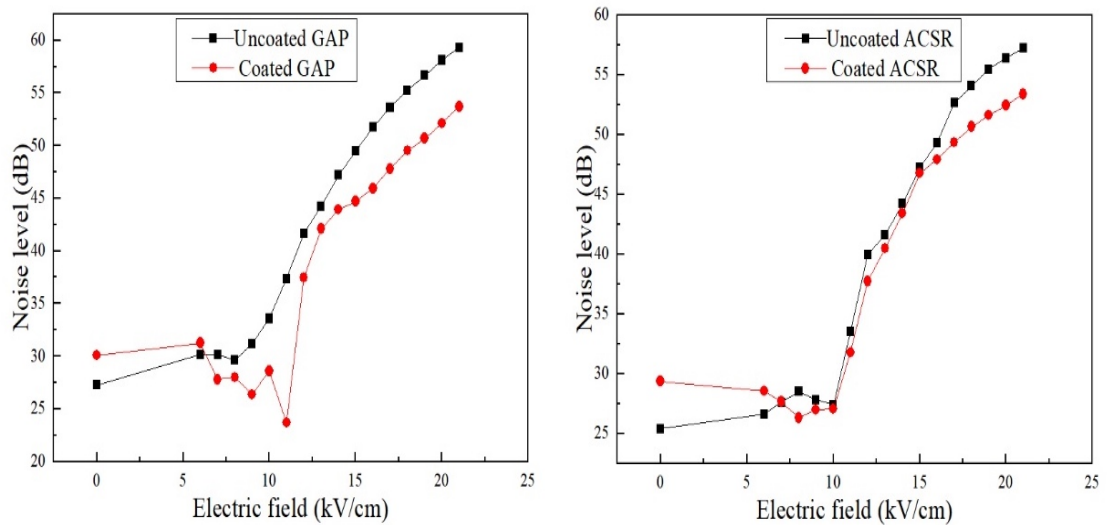


Figure 5.13 Noise levels at 100 Hz with different levels of electric field on coated and uncoated GAP (left) and ACSR (right) conductors during the heavy rain condition

In Figure 5.12, the 100 Hz noise levels of the coated and uncoated GAP and ACSR conductors under different levels of electric fields were compared during light rain. The noise level of the coated GAP conductor was higher than that of the uncoated GAP conductor when the electric field was below 10 kV/cm. Under higher levels of electric field (from 10

to 21 kV/cm), the noise level of the coated conductor was lower than the uncoated conductor. Taking 18 kV/cm of the electric field as an example, the noise level of the coated conductor had a reduction of 2 dB. The ACSR conductor showed similar noise levels between the uncoated and coated conductors, when the electric field was below 10 kV/cm. When the electric field was between 10 and 21 kV/cm, the coated ACSR conductor showed a lower noise level than that of the uncoated conductor. With an electric field of 18 kV/cm, there was a 1.6 dB noise reduction on the coated conductor.

During the heavy rain condition in Figure 5.13, both the types of conductors have similar noise levels at lower electric fields. At a higher electric field (mainly above 10 kV/cm), the noise levels on the coated conductors were lower than that of the uncoated conductors. The reduction in noise levels on the coated conductors was larger during heavy rain than in light rain. At an electric field of 18 kV/cm, the noise level reductions on the coated GAP and ACSR conductors were 5.7 and 3.8 dB respectively. Those results indicate that the superhydrophobic coating can be an effective method to reduce the noise level on conductor lines at 100 Hz.

To evaluate the benefit of this superhydrophobic coating on conductors, water drop behaviours on the coated and uncoated conductors were compared with the same amount of water sprayed on their surface. Images as shown in Figure 5.14 and Figure 5.15 were taken of both coated and uncoated GAP and ACSR conductor samples with water drops remaining on each sample, under no electric field and under an electric field of 21 kV/cm.

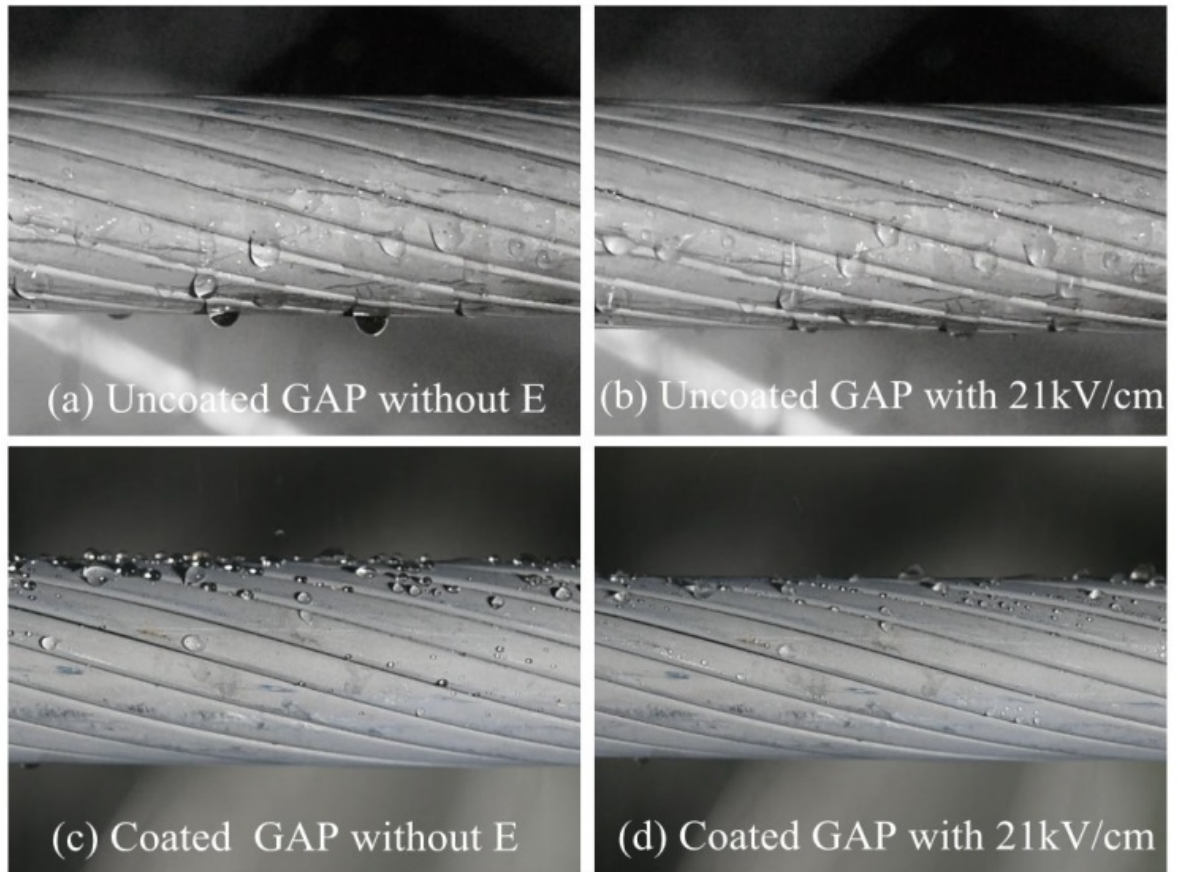


Figure 5.14 Images of water drops accretion on the coated and uncoated GAP conductors with and without the electric field of 21 kV/cm

In Figure 5.14, the coated conductor without electric field in image (c) had less water with smaller drop sizes on the top of the conductors, compared to the uncoated conductor in image (a), where bigger drops were observed on the side and the bottom of the conductor. Under 21 kV/cm of the electric field, the water drops on the uncoated conductor in image (b) changed their shapes from hemisphere to a more flattened form, compared to image (a). The coated conductor under the electric field exhibited fewer water drops, as shown in image (d), compared with image (c) without the electric field.

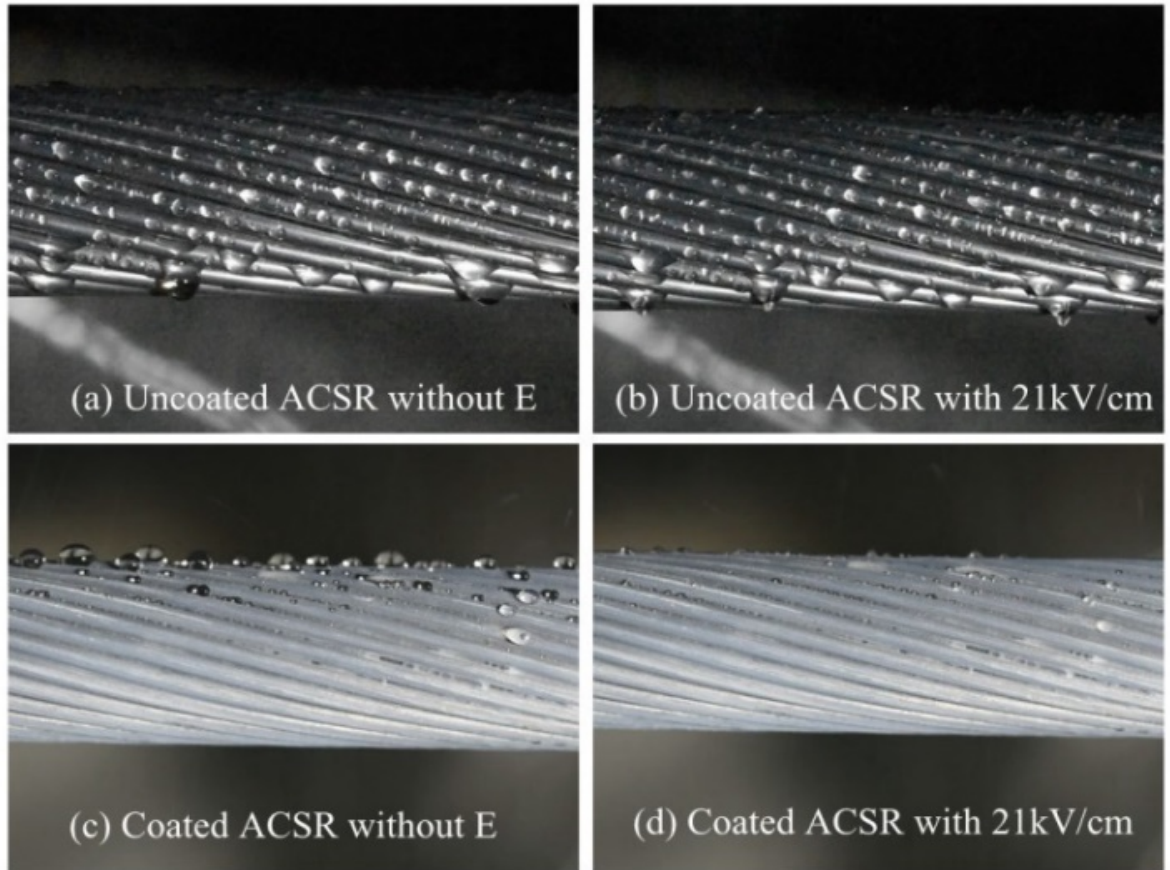


Figure 5.15 Images of water drop accretion on the coated and uncoated ACSR conductors with and without an electric field of 21 kV/cm

In Figure 5.15, similar water drop behaviour was noted on the ACSR conductors. Comparing images (a) and (c), the coated ACSR conductor without the electric field exhibited a lesser volume of water and smaller size of water drops on top of the conductors, while larger water drops were noted all around the uncoated conductor trapped between strings. Under 21 kV/cm of the electric field, the water drops on the uncoated ACSR conductor in image (b) changed from the hemisphere shape to the conical shape, compared to the water drops in image (a). Similarly, smaller water drops were noted on the coated conductor with the electric field in image (d) than that of the coated conductor without the electric field in image (c).

Overall, fewer water drops were noticed on both types of superhydrophobic coated conductors. This might be the result of vibrations of the conductors under the electric field,

and thus the water drops rolled off the surfaces. These observations in water drop behaviour support the results of the noise level tests: the coated conductors can offer a better noise performance with less noise than the uncoated conductors.

In conclusion, the noise reduction performance of NeverWet superhydrophobic coatings on the GAP and ACSR conductors were examined in this research. The anechoic chamber was used to reduce the background noise and noise reflections to achieve better accuracy of noise measurements. To investigate the noise reduction performance of the superhydrophobic coating, noises from the uncoated and coated conductors at 100 Hz were compared under light and heavy rain conditions. The results show that superhydrophobic coated conductors can offer effective audible noise reductions at 100 Hz under both conditions. The behaviour of water drops on the NeverWet coated and uncoated GAP and ACSR conductors were compared. The superhydrophobic coating allowed fewer and smaller water drops to rest on the coated conductors and provided a better noise reduction performance during wet conditions.

5.5 Heat Dissipation Performance of Laser-Textured Surfaces

Laser-textured surfaces can offer not only superhydrophobic performance but also other advantages and applications. Laser patterns on a surface can increase the surface to air contact area, and thus potentially increase the heat dissipation performance of the surface. There are three types of heat transfer mechanisms: conduction, radiation, and convection. Conduction heat transfer is energy movement due to molecular motion and interaction. The amount of conduction heat transfer is a function of the temperature difference and the thermal conductivity of the material. This mode of heat transfer is not significant in the context of an overhead line conductor transferring heat to air.

Heat transfer by radiation relies on electromagnetic waves or photons from a surface or volume and does not require a medium. The amount of radiation heat transfer is proportional

to the surface area, temperature, and the emissivity of the material. Radiative heat transfer exists from an overhead line in all weather conditions.

Convective heat transfer is energy movement due to bulk fluid motion. The amount of convective heat transfer is proportional to the temperature difference across the fluid to the solid surface, the surface area, and the heat transfer coefficient of the fluid. Convective heat transfer from an overhead line conductor increases as a function of windspeed.

As briefly described above, conductive heat transfer only occurs within the strand matrix of a conductor and is insignificant in terms of the transfer of heat to the air given the low thermal conductivity of air. It is therefore ignored when calculating the steady state temperature of overhead line conductors [157][158]. Radiative heat transfer in contrast is important as conductors emit heat to the surroundings at a rate proportional to $(T_c^4 - T_a^4)$ where T_c is the conductor temperature and T_a is the ambient temperature. Radiative heat transfer is also important in terms of temperature rise as a result of the conductor receiving solar radiation. Convective heat transfer occurs from a conductor surface to the ambient air surrounding the conductor. In an overhead line, natural convection occurs when there is no wind speed while the presence of wind leads to forced convection. The wind speed is usually a more important factor than the ambient temperature when calculating overhead line ratings (a windy summer day may result in an overhead line being able to carry more current than a still winter day).

The laser patterning of metallic materials has the potential to increase the rating of the conductor by increasing the amount of heat dissipated through convection and radiation, as a result of increased surface area and contact with the surrounding medium [137][159]. In this section, calculations were made to demonstrate the potential benefit of using laser patterning techniques to increase current ratings on conductors. Measurements were taken to examine and quantify the influence of a laser-patterned surface on heat loss for the forced convection method.

5.5.1 Benefit of Increasing Heat Dissipation Rate

During the operation of overhead lines, thermal loss and gain can affect the conductor temperature and current rating. If the heat dissipation rate can be improved, it can enable an increase in the current rating of conductors. A study tested the force convective heat transfer enhancement on laser treated flat aluminium alloy samples (with dimensions of $11.1 \times 11.1 \times 5$ mm), and concluded that the increased roughness with micro structures created on the surfaces resulted in an increase of the convective heat transfer by 63% on average compared to smooth surfaces [159]. To demonstrate the potential impact of this 63% of the convective heat transfer enhancement could have on increasing the current rating of overhead lines, a calculation is made using the equations of thermal equilibrium below according to IEEE standard 738 [160]:

$$q_c + q_r = q_s + I^2 R_{T_c} \quad (1)$$

$$q_c = 387(1000DV_w)^{0.45}(T_c - T_a) \quad (2)$$

$$q_r = 11D \times 10^{-5}[(T_c + 273)^4 - (T_a + 273)^4] \quad (3)$$

Where q_c is convection heat loss (W/km), q_r is radiated heat loss (W/km), q_s is solar heat gain (W/km), I is conductor current (A), R_{T_c} is conductor resistance (Ω /km) at conductor temperature T_c ($^{\circ}$ C), T_a is the ambient temperature ($^{\circ}$ C), D is conductor diameter (m), and V_w is wind speed (m/s).

Equation (1) is the heat balance equation for an overhead line in thermal equilibrium. The left hand side represents the power loss through convection and radiation while the right hand side represents the power gain owing to joule heating of the conductor and any incident solar radiation. Equations (2) and (3) can be used to calculate the power loss through convection and radiation for an overhead line.

Taking the Araucaria conductor with the parameters as shown in Table 5.3 as an example, ignoring solar gain and assuming $T_a = 20$ $^{\circ}$ C, $T_c = 90$ $^{\circ}$ C, $R_{T_c} = 0.05067$ Ω /km, and $D = 0.03726$ m, the increase in current rating of the conductor using laser patterning can be

calculated as below using equation (1), (2), and (3). A 90 °C conductor temperature is chosen according to the maximum operating temperatures of AAAC conductors. Two wind speeds are used to simulate a worst-case rating at a wind speed of 0.5 m/s versus a common wind speed of 10 m/s.

When $V_w = 0.5$ m/s:

$$q_c = 387(1000DV_w)^{0.45}(T_c - T_a) = 101019 \text{ W/km}$$

$$q_r = 11D \times 10^{-5}[(T_c+273)^4 - (T_a+273)^4] = 40957 \text{ W/km}$$

$$I = \sqrt{(q_c + q_r)/R_{T_c}} = 1674 \text{ A}$$

If q_c can be increased by 63% after laser patterning,

$$q_c' = 164661 \text{ W/km}$$

$$I' = \sqrt{(q_c' + q_r)/R_{T_c}} = 2014 \text{ A}$$

Current rating increase = 20.3%

When $V_w = 10$ m/s:

$$q_c = 387(1000DV_w)^{0.45}(T_c - T_a) = 388904 \text{ W/km}$$

$$q_r = 11D \times 10^{-5}[(T_c+273)^4 - (T_a+273)^4] = 40957 \text{ W/km}$$

$$I = \sqrt{(q_c + q_r)/R_{T_c}} = 2913 \text{ A}$$

If q_c can be increased by 63% after laser patterning,

$$q_c' = 633914 \text{ W/km}$$

$$I' = \sqrt{(q_c' + q_r)/R_{T_c}} = 3650 \text{ A}$$

Current rating increase = 25.3%

The rated current can be up to 4000 A on a 400 kV transmission line [161], and therefore the increased current based on the calculation above of 3650 A is realistic. These results demonstrate that if the convective heat dissipation of overhead line conductors can be

increased by an average of 63% through laser patterning, the current rating of the conductors can be increased by 20.3% at a wind speed of 0.5 m/s and 25.3% at a wind speed of 10 m/s.

5.5.2 Heat Dissipation Experimental Descriptions

The forced-convection method was introduced to better investigate the heat loss from a laser patterned surface. Two almost identical aluminium alloy samples were used in this research. One sample had 9 patches of 1 cm² laser-textured areas on the surface, and another sample was untreated. The experimental set-up is shown in Figure 5.16.

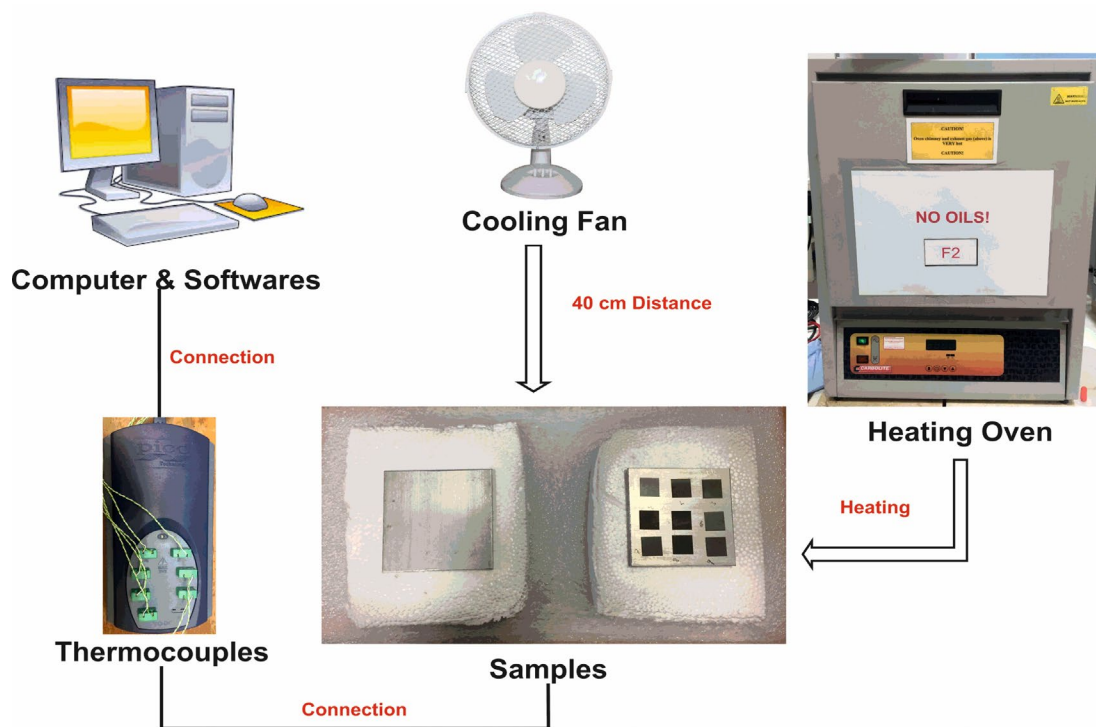


Figure 5.16 Experimental equipment set-up of heat dissipation tests

Samples masses and dimensions are shown below:

- The untreated sample: Mass: 21.8 g Size: 5.09 x 5.13 x 0.32 cm

Total top surface area: 26.1 cm²
- The laser-textured sample: Mass: 21.7 g Size: 5.09 x 5.07 x 0.32 cm

Total top surface area: 25.8 cm²

Patterned area: 9 cm² (35% coverage of top surface)

Calibrated fast-response thermocouples were attached to the samples, and temperatures were recorded. Samples were placed on two polystyrene-insulated bases sufficiently far apart from each other to avoid any thermal influence. Samples with bases were placed into a heating chamber at 50 °C. This temperature was set to allow a fast-enough cooling rate to allow measurement of any significant difference in thermal behaviour. It was also chosen for experimental convenience in order to avoid hot sample handling and the risk of burning other materials in the hot environment. Samples were allowed to heat up until thermal equilibrium and then placed in ambient temperature. The forced-convection method was achieved using a fan placed 40 cm from the samples. An average air speed of 4.65 m/s was produced by the fan above both the laser-textured and the untreated samples, measured by a hot wire probe. The fan was positioned to ensure the same wind speed above both of the samples. Tests were repeated ten times for accuracy purposes. The ambient temperature of the experiment environment was 26 °C.

5.5.3 Test Results

The cooling rates of the samples were determined by measuring the temperature change over a period of 60 s from the time when the sample was at 45 °C. The cooling rate was non-linear, and 60 s was a short enough period to be quasi-linear, enabling a simple mean average to be taken. The measurement was started from 45 °C because heating within the oven was not homogeneous due to the placement of the internal heating elements, and so thermal equilibrium temperatures were not identical for both samples. A fixed start temperature of 45 °C ensured a fair test given the fact that the cooling rate is dependent on temperature.

Whilst cooling occurred both radiatively and convectively, convective cooling, particularly in the forced-convection case, was likely to be dominant. Aside from the laser-textured face, heat loss occurred from all remaining faces of both the samples at approximately the same rate, due to their similar dimensions and masses. As such, this was a fair test that measured comparative heat loss caused by the presence of the laser-textured surface.

Table 5.5 shows the average heat dissipation speeds of both the laser textured and untreated samples from 10 repeated tests. Different results were obtained from each test and occasionally the laser sample cooled faster than the untreated sample, and vice versa. Insignificant differences were observed in terms of the average cooling speeds for both the laser textured and untreated samples. This result might be due to the cover rate of the laser patterned surface area being insufficient to overcome the other environmental deviations, or the accuracy of measuring equipment being insufficient to detect such a small change, in order to obtain an effective result.

Table 5.5 Average cooling rates of both laser-textured and untreated samples

	Cooling Rate (°C / s)	
	Laser Patterned Sample	Untreated Sample
Test 1	0.103	0.098
Test 2	0.103	0.097
Test 3	0.093	0.100
Test 4	0.112	0.093
Test 5	0.093	0.102
Test 6	0.090	0.098
Test 7	0.102	0.105
Test 8	0.098	0.105
Test 9	0.100	0.108
Test 10	0.100	0.107
Average	0.099	0.101

Overall, it is unlikely there is sufficient coverage of laser-textured surface to modify cooling rates for the samples tested, particularly for flat samples. A study showed an increased cooling rate from laser-texturing by placing the samples on heat sinks with fins and other larger structures to maximise heat transfer coefficients [159]. It is possible the improved cooling rates could be measured under the forced convection method using a section of an

overhead conductor line that was fully laser-textured, which may provide distinct differences in cooling rates.

5.6 Concluding Remarks

In this chapter, the water drop freezing test and the frost accretion test on different superhydrophobic surface treatments were carried out. The superhydrophobic coating was proven to be an effective method to reduce the number of frozen drops on the surface. The superhydrophobic coating was also proven to have potential influence on reducing or delaying frost formation on the samples. The relationships between sag, %RTS, and ice accretion thickness are compared using three different types of conductor lines. The sag of the smaller sized Oak conductor and heavier weight Madrid conductor could be more affected under the same ice accretion thickness, compared to that of the Araucaria conductor. The ACCC Madrid conductor shows a lower %RTS than that of the AAAC Araucaria conductor or the Oak conductor under the same ice accretion thickness because of its high strength and flexibility. It is only necessary to control ice accretion within the safe region that is below the breaching points of the maximum allowable sag and %RTS, other than to eliminate it. A calculation result shows that the overall weight of conductors can be significantly reduced if a surface treatment can be applied on conductors to reduce ice accretion thickness by 10 mm. This weight reduction can potentially ensure a safe operation of existing overhead lines during icing weather, and enable lower costs and better designs for new overhead lines. The audible noise performance of superhydrophobic coated overhead line conductors was tested under different rain conditions. The results show that effective noise reduction can be achieved using the superhydrophobic treatment on conductors during both light and heavy rain conditions. The forced convection heat dissipation test was carried out on laser-textured aluminium surfaces to evaluate the influence of laser patterns on increasing heat dissipation rates. However, due to insufficient coverage of laser patterns on the surfaces, little difference was noticed on the cooling rate of

the samples. Further research is suggested by using a reasonable section of a fully laser-textured overhead line conductor for forced convection heat dissipation tests to better quantify the heat dissipation performance of laser patterns.

CHAPTER 6 CONCLUSIONS AND FUTURE WORKS

6.1 Conclusions

This research investigated a range of superhydrophobic surface treatments including the NeverWet coating, stearic acid with SiO₂ nanoparticle coating, and laser patterning. An improved zoomed-in method of computing contact angles was developed to increase the accuracy of the contact angle measurement. The behaviour of water drops on superhydrophobic coated and uncoated samples were compared under a high-speed camera. Different experimental parameters were used to optimise the performance and reproducibility of surface treatments. A series of ageing tests examined whether surface treatments were likely to be robust once deployed onto overhead line conductors and in operation. The examination of icephobicity included water drop freezing tests and frost accretion tests. The benefits and potential applications of superhydrophobic surface treatments were examined including reduced ice and frost accretion, audible noise reduction, and improved heat dissipation of laser-textured surfaces. The main results and findings in this research are summarised below.

6.1.1 Fabrications of Surface Treatments

Different types of surface treatments were investigated, including chemical coatings and physical laser patterning techniques. The HumiSeal and stearic acid coatings did not achieve superhydrophobicity. SiO₂ nanoparticles were then blended into the stearic acid solution to improve the coating hydrophobicity. An optimised method of deploying this coating was obtained by examining different procedures and parameters. This optimised method achieved superhydrophobic performance on the stearic acid with SiO₂ nanoparticle coating, with an average contact angle of 164.4° and an average sliding angle of 4.7°. A good reproducibility was also achieved with standard deviations of 1.9° for contact angles and 1.0° for sliding angles. The NeverWet coating was tested on aluminium, silicone rubber,

and EPDM rubber substrates. All of the samples achieved superhydrophobicity with contact angles larger than 154° , and sliding angles less than 4° .

Different surface pre-treatments were tested to produce different surface structures on aluminium substrates prior to the application of coatings. The results showed that a similar superhydrophobicity was observed with all of the surface pre-treatments after the deployment of the NeverWet and the stearic acid with SiO_2 nanoparticle coatings. This observation indicates that original surface geometries may not significantly contribute to superhydrophobic performance when a chemical coating is used. However, surface pre-treatments may affect the long-term adhesion of a coating on the surface.

Laser patterning proved to be a robust and precise technique to produce micro-channel and micro-pillar patterns on aluminium substrates for the purpose of achieving superhydrophobicity. Different laser parameters were used to achieve different surface profiles on the samples. As a result of the comparable superhydrophobic performance of all laser patterns tested, the micro-channel pattern with the fastest production time was chosen for the further tests.

6.1.2 Sample Characterisations

An improved manual zoomed-in method of contact angle measurement was introduced to increase the resolution of the region used to map drop profiles and interfacial triple-points. This zoomed-in method provides approximately 10 times the resolution compared to the zoomed-out methods and is therefore more likely to achieve higher accuracy for contact angle measurement. The statistical test result shows that the zoomed-in method also has good reproducibility with a standard deviation of 1° when measuring contact angles. Therefore, the improved manual zoomed-in method was used to progress this research.

Water drop behaviours on the NeverWet coated and uncoated flat and round conductor samples were examined using a high-speed camera. The result shows the NeverWet coated flat and round conductor samples demonstrated a better water-repellent performance than the uncoated samples, which indicates potential benefits in the application of

superhydrophobic coatings on overhead lines, such as water-repellent, self-cleaning, and anti-icing abilities.

6.1.3 Ageing Tests

168 h of thermal ageing at 80 °C and 1000 h of thermal cycling with the temperature varied between -20 °C and 80 °C had minimal influence on the laser patterned samples, with average contact angles higher than 165° and sliding angles less than 3° after the tests. A slight impact was noticed on the NeverWet coated samples after ageing, with average contact angles reduced from 167° to 162° and sliding angles increased from 2° to 6°. The stearic acid with SiO₂ coating did not survive the high temperature and all of the coated samples lost their superhydrophobicity after 1 week of thermal ageing.

UV exposure had little effect on the laser patterned or NeverWet coated samples. All the samples performed with a high level of superhydrophobicity after 4 weeks with average contact angles higher than 163° and sliding angles less than 3°. Reduced superhydrophobic performance was observed on the stearic acid with SiO₂ coated samples after UV exposure with average contact angles decreased from 164° to 155°. The sliding angles of the stearic acid with SiO₂ coated samples increased from 6° to 22°, which resulted in reduced water-repellence.

An entire year of outdoor environmental exposure had a slight influence on the laser patterned samples. All the laser patterned samples remained superhydrophobic after the test, with average contact angles higher than 161° and contact angle hysteresis less than 9°. The NeverWet coated samples remained superhydrophobic after outdoor exposure, with average contact angles decreased from 166° to 158°, however, the sliding angle increased from 2° to 13°. The performance of the stearic acid with SiO₂ coated samples dropped significantly after only 4 weeks of outdoor exposure, with average contact angles increased from 164° to 158° and sliding angles increased from 6° to 31°, resulting in considerably reduced water-repellent ability.

The corona exposure used in this research was a significant source of degradation for all superhydrophobic surface treatments. After 168 h of corona exposure, all three types of samples were damaged and transitioned from superhydrophobic to superhydrophilic surfaces, which indicates that this specific corona ageing method was a severe threat to all surface treatments used in this research. However, there is a possibility that this specific ageing method may not be indicative of real-world corona surface ageing on overhead lines.

6.1.4 Applications and Benefits

Two types of ice accretion tests were carried out in this research. During the water drop freezing test, the amount of water frozen on the samples was reduced by up to 96% at -10 °C, and up to 82% at -20 °C through use of a superhydrophobic coating. During the frost accretion tests, the average frost accretion mass on the samples was reduced by 13% through use of a superhydrophobic coating. These results indicate that an effective reduction in frozen water drops and frost accretion can be achieved on aluminium alloy samples by applying superhydrophobic surface treatments.

The relationships among sag, %RTS, and ice accretion thickness of overhead lines were plotted and compared using three different types of conductors. The sag of the smaller size AAAC Oak conductor and the heavier weight ACCC Madrid conductor were concluded to be more affected by the same amount of ice accretion than that of the AAAC Araucaria conductor. The ACCC Madrid conductor shows a lower %RTS than that of the AAAC Araucaria or the Oak conductor under the same ice accretion thickness because of its high strength and flexibility. A higher strength and flexibility allows a conductor to stretch further without breaking under icy and windy weather. To ensure the safe operation of overhead line systems, it is only necessary to control ice accretion below the breaching points of the maximum allowable sag and %RTS rather than to eliminate it completely.

Calculations were made to demonstrate the potential benefit of superhydrophobic surface treatments on reducing ice accretion on overhead lines. By applying a surface treatment to reduce ice accretion on the conductors by 10 mm, the overall weight on Oak, Araucaria, and

Madrid conductors can be reduced by 49.6%, 32.9%, and 29.9%, respectively. This weight reduction would significantly increase the stability of overhead line systems during icing events and enable future overhead line designs with lower costs and more reliable performance.

The effect of superhydrophobic coatings on reducing audible noise on overhead lines was tested under different wet conditions. The results show that superhydrophobic coatings can effectively reduce the noise level at 100 Hz on both the GAP and ACSR conductors by around 2 dB under the light rain condition, and up to 5.7 dB under the heavy rain condition.

The heat dissipation performance of laser patterned samples was tested and showed an insignificant difference in heat dissipation rate between the laser patterned samples and untreated samples. This finding may be due to the coverage rate of laser patterns being insufficient to vary the heat dissipation rate, or due to the accuracy of the measuring equipment being insufficient to detect such a small change.

6.1.5 Overall Conclusions

Overall, the research aim of examining the performance, durability, potential benefits, and applications of superhydrophobic surface treatments on overhead lines was achieved. Objectives and contributions towards the research area were achieved, including the fabrication and optimisation of surface treatments, the design of surface characterisation methods, the investigation of long-term durability, and the discussion of potential applications and benefits of surface treatments on overhead lines. Based on the findings in this research, the stearic acid with SiO₂ nanoparticle coating may have a limited application on overhead lines due to its poor ageing performance unless other methods can be found to prevent its long-term degradation under different ageing conditions. The laser patterning technique and the NeverWet coating demonstrated adequate durability and resilience against a range of representative ageing conditions. Both methods appear to feasibly produce superhydrophobic surfaces on overhead lines, providing potential benefits such as to reduce or delay ice accretion, self-cleaning, and audible noise reduction to ensure the safe operation

of overhead line systems under different weather conditions. Mechanical profiling such as laser patterning would be more suitable for new installations or for upgrades to existing overhead lines to produce a robust and long-lasting superhydrophobic performance. The spray coating technique is likely to be feasible for deployment on existing overhead lines without disassembling conductors from the towers.

6.2 Future Work

While results presented in this report have demonstrated characterisations and durability of selected surface treatments, many opportunities for extending the scope of this research remain. Some of the extensions that deserve further consideration are presented below:

- The research on different laser patterns can be expanded to further improve superhydrophobic performance and to minimise manufacturing time and cost, and the cost to deploy on overhead lines. This includes investigations into patterns with a wider hatching distance (larger than 100 μm) or a faster scanning speed (larger than 100 mm/s), as well as deployment and characterisation techniques of laser patterning on round overhead line conductors.
- The corona ageing methodology in this research has most likely caused more damage to samples than would occur during practical operations, due to the sharp needles used in the test. Other methods may be developed to better represent corona ageing on overhead lines, such as examining the ageing behaviour of energised cylindrical conductors with superhydrophobic treatments. Energised cylindrical conductors may generate corona discharge with a similar effect to real-life situations in overhead line systems.
- Ice adhesion strength is a crucial parameter to determine the ability of a surface to shed accumulated ice. Future tests may be carried out to examine the ice shedding ability of different superhydrophobic surface treatments, such as using a centrifuge to test ice adhesion strengths of ice accreted surfaces.

- Further research into heat dissipation may be carried out with a larger coverage of laser patterns on samples in order to sufficiently measure the heat exchange rate. A full section of laser-textured conductor sample would be beneficial to be utilised in the forced convection heat dissipation tests. This would better quantify heat dissipation improvement of laser patterns on overhead lines.

REFERENCES

- [1] Working Group B2.44, “CIGRE TB631: Coatings for Protecting Overhead Power Network Equipment in Winter Conditions,” 2015, no. September, p. 115.
- [2] Western Power Distribution, “Lifetime Costs Report: Brechfa Forest Connection Project,” 2014.
- [3] I. Cotton and H. Li, “Power System Plant & Protection Lecture Notes.” 2016.
- [4] J. Casey, “SLD Icing demonstration,” 2016. [Online]. Available: <http://flycasey.com/sld-icing-demonstration/>.
- [5] P. MCGRATH, “Remember The Ice Storm of ’98? It was the most devastating and least ferocious of Canadian disasters,” *OTTAWA CITIZEN*, 2016. .
- [6] C. Bell, “Hoar Frost and Rime Ice: What’s the Difference?” 2013.
- [7] L. C. Phan and H. Matsuo, “Minimum flashover voltage of iced insulators,” *IEEE Trans. Dielectr. Electr. Insul.*, vol. EI-18, no. 6, pp. 605–618, 1983, doi: 10.1109/TEI.1983.298699.
- [8] M. M. Khalifa and R. M. Morris, “Performance of Line Insulators Under Rime Ice,” 1967.
- [9] M. Farzaneh and J. Kiernicki, “Flashover problems caused by ice build up on insulators,” *IEEE Electr. Insul. Mag.*, vol. 11, no. 2, pp. 5–17, 1995, doi: 10.1109/57.372510.
- [10] M. A. Drage, *Atmospheric icing and meteorological variables – Full scale experiment and testing of models*. 2005.
- [11] Products Preformed Line, “Conductor Galloping Basics,” vol. EN-ML-1166, no. February, 2016.
- [12] O. Nigol and D. G. Havard, “Control of torsionally induced conductor galloping with detuning pendulums,” in *IEEE PES winter meeting*, 1978.
- [13] H. M. Ryan, *High Voltage Engineering and Testing*, vol. 15, no. 3. 1995.
- [14] BBC, “UK Heavy snow hits much of Britain,” *BBC News*, 02-Feb-2009. [Online]. Available: <http://news.bbc.co.uk/1/hi/uk/7864395.stm>.
- [15] Svenska Kraftnat, “Ice accretion on insulator strings 400 kV in Skane and Halland.pdf,” *Report of Svenska Kraftnat*, 1999.
- [16] China Meteorological Centre, “A rare ice storm in the south China 2008,” *Weather.com.cn*, 2008.
- [17] T. Onodera, H. Inukai, and T. Odashima, “Overview of Power Outage in the Niigata Kaetsu Area Caused by a Snowstorm,” *12th Int. Work. Atmos. Icing Struct.*, no. October, 2007.
- [18] RMS Special Report, “The 1998 Ice Storm : 10-Year Retrospective RMS Special Report,” *Risk Manag. Solut.*, pp. 1–14, 2008.

- [19] M. Farzaneh, *Atmospheric icing of power networks*. 2008.
- [20] I. A. Ryzhkin and V. F. Petrenko, “Physical Mechanisms Responsible for Ice Adhesion,” *J. Phys. Chem. B*, vol. 101, no. 32, pp. 6267–6270, 1997, doi: 10.1021/jp9632145.
- [21] V. F. Petrenko and S. Peng, “Reduction of ice adhesion to metal by using self-assembling monolayers (SAMs),” *Can. J. Phys.*, vol. 81, no. 1–2, pp. 387–393, 2003, doi: 10.1139/p03-014.
- [22] E. Arunan *et al.*, “Definition of the hydrogen bond (IUPAC Recommendations 2011),” *Pure Appl. Chem.*, vol. 83, no. 8, pp. 1637–1641, 2011, doi: 10.1351/PAC-REC-10-01-02.
- [23] T. D. Knuth, “Ice Adhesion Strength Modeling Based on Surface Morphology Variations,” no. August, 2015.
- [24] W. Seagrave, *History of the Universe-Ice*. Penny Press Ltd, 2012.
- [25] N. Saleema, M. Farzaneh, R. W. Paynter, and D. K. Sarkar, “Prevention of Ice Accretion on Aluminum Surfaces by Enhancing Their Hydrophobic Properties,” *J. Adhes. Sci. Technol.*, vol. 25, no. 1–3, pp. 27–40, 2011, doi: 10.1163/016942410X508064.
- [26] N. Bjerrum, “Structure and properties of ice,” *Science*. 1952, doi: 10.1126/science.115.2989.385.
- [27] D. K. Sarkar and M. Farzaneh, “Superhydrophobic Coatings with Reduced Ice Adhesion,” *J. Adhes. Sci. Technol.*, vol. 23, no. 9, pp. 1215–1237, 2009, doi: 10.1163/156856109X433964.
- [28] W. Forces, *Van der Waals Forces 6.1*. 2011.
- [29] L. A. Wilen, J. S. Wettlaufer, M. Elbaum, and M. Schick, “Dispersion-force effects in interfacial premelting of ice,” *Phys. Rev. B*, vol. 52, no. 16, pp. 12426–12433, 1995, doi: 10.1103/PhysRevB.52.12426.
- [30] C. Volat, M. Farzaneh, and A. Leblond, “De-icing / Anti-icing Techniques for Power Lines : Current Methods and Future Direction,” *11 th Int. Work. Atmos. Icing Struct.*, no. June, 2005.
- [31] L. Emilio Marcus de Castro, “Determination of Surface Free Energies and Aspect Ratio of Talc,” pp. 67–127, 2004.
- [32] T. Bharathidasan, S. V. Kumar, M. S. Bobji, R. P. S. Chakradhar, and B. J. Basu, “Effect of wettability and surface roughness on ice-adhesion strength of hydrophilic, hydrophobic and superhydrophobic surfaces,” *Appl. Surf. Sci.*, vol. 314, pp. 241–250, 2014, doi: 10.1016/j.apsusc.2014.06.101.
- [33] M. Ulbricht, “Advanced functional polymer membranes,” *Polymer (Guildf.)*, vol. 47, no. 7, pp. 2217–2262, 2006, doi: 10.1016/j.polymer.2006.01.084.
- [34] J. J. Bikerman, “Sliding of drops from surfaces of different roughnesses,” *J. Colloid Sci.*, vol. 5, no. 4, pp. 349–359, 1950, doi: 10.1016/0095-8522(50)90059-6.
- [35] R. Johnson and R. Dettre, “Contact angle hysteresis,” *Contact angle, wettability, Adhes.*, vol. 43, pp. 136–144, 1964, doi: 10.1021/ba-1964-0043.ch007.

- [36] R. Liao, Z. Zuo, C. Guo, Y. Yuan, and A. Zhuang, "Fabrication of superhydrophobic surface on aluminum by continuous chemical etching and its anti-icing property," *Appl. Surf. Sci.*, vol. 317, pp. 701–709, 2014, doi: 10.1016/j.apsusc.2014.08.187.
- [37] B. T. Tepzz, "Method for fabricating superhydrophobic surface Verfahren," vol. 1, no. 19, pp. 1–13, 2013, doi: 10.1021/la061372.
- [38] B. K. Nayak, P. O. Caffrey, C. R. Speck, and M. C. Gupta, "Superhydrophobic surfaces by replication of micro/nano-structures fabricated by ultrafast-laser-microtexturing," *Appl. Surf. Sci.*, vol. 266, pp. 27–32, 2013, doi: 10.1016/j.apsusc.2012.11.052.
- [39] Y. Yuan and T. R. Lee, "Contact Angle and Wetting Properties," in *Surface Science Techniques*, vol. 51, no. 1, 2013, pp. 3–5.
- [40] T. Young, "An Essay on the Cohesion of Fluids," *Philos. Trans. R. Soc. London*, vol. 95, no. 0, pp. 65–87, 1805, doi: 10.1098/rstl.1805.0005.
- [41] G. McHale, N. J. Shirtcliffe, and M. I. Newton, "Contact-angle hysteresis on superhydrophobic surfaces," *Langmuir*, vol. 20, no. 23, pp. 10146–10149, 2004, doi: 10.1021/la0486584.
- [42] A. Published, C. Link, and D. Terms, "Accessed Contact angle hysteresis: A review of fundamentals and applications," 2016.
- [43] K. Kawasaki, "Study of wettability of polymers by sliding of water drop," *J. Colloid Sci.*, vol. 15, no. 5, pp. 402–407, 1960, doi: DOI: 10.1016/0095-8522(60)90044-1.
- [44] R. N. Wenzel, "Resistance of solid surfaces to wetting by water," *Ind. Eng. Chem.*, 1936, doi: 10.1021/ie50320a024.
- [45] B. D. Cassie, A. B. D. Cassie, and S. Baxter, "Wettability of porous surfaces," *Trans. Faraday Soc.*, vol. 40, no. 5, pp. 546–551, 1944, doi: 10.1039/tf9444000546.
- [46] N. Dalali and P. Separation, *Encyclopedia of Membranes*, no. i. 2016.
- [47] V. Hejazi, K. Sobolev, and M. Nosonovsky, "From superhydrophobicity to icephobicity: forces and interaction analysis," *Sci. Rep.*, vol. 3, no. 1, p. 2194, 2013, doi: 10.1038/srep02194.
- [48] P. Tourkine, M. Le Merrer, and D. Quéré, "Delayed freezing on water repellent materials," *Langmuir*, vol. 25, no. 13, pp. 7214–7216, 2009, doi: 10.1021/la900929u.
- [49] L. Mishchenko, B. Hatton, V. Bahadur, J. A. Taylor, T. Krupenkin, and J. Aizenberg, "Design of ice-free nanostructured surfaces based on repulsion of impacting water droplets," *ACS Nano*, 2010, doi: 10.1021/nn102557p.
- [50] S. A. Kulinich and M. Farzaneh, "How wetting hysteresis influences ice adhesion strength on superhydrophobic surfaces," *Langmuir*, vol. 25, no. 16, pp. 8854–8856, 2009, doi: 10.1021/la901439c.
- [51] A. Alizadeh *et al.*, "Dynamics of ice nucleation on water repellent surfaces," *Langmuir*, vol. 28, no. 6, pp. 3180–3186, 2012, doi: 10.1021/la2045256.

- [52] C. Antonini, M. Innocenti, T. Horn, M. Marengo, and A. Amirfazli, "Understanding the effect of superhydrophobic coatings on energy reduction in anti-icing systems," *Cold Reg. Sci. Technol.*, vol. 67, no. 1–2, pp. 58–67, 2011, doi: 10.1016/j.coldregions.2011.02.006.
- [53] C. Antonini, "Superhydrophobicity as a strategy against icing: Analysis of the water/surface dynamic interaction for icing mitigation," 2011.
- [54] S. A. Seyedmehdi, H. Zhang, and J. Zhu, "Superhydrophobic RTV silicone rubber insulator coatings," *Appl. Surf. Sci.*, vol. 258, no. 7, pp. 2972–2976, 2012, doi: 10.1016/j.apsusc.2011.11.020.
- [55] J. Blackett, "Voltshield - anti-pollutant treatment for glass and glazed porcelain insulators," *IET Conf. Publ.*, no. 1055, pp. 1055–1055, 2009, doi: 10.1049/cp.2009.1137.
- [56] H. Zhou, H. Wang, H. Niu, A. Gestos, X. Wang, and T. Lin, "Fluoroalkyl silane modified silicone rubber/nanoparticle composite: A super durable, robust superhydrophobic fabric coating," *Adv. Mater.*, vol. 24, no. 18, pp. 2409–2412, 2012, doi: 10.1002/adma.201200184.
- [57] G. Momen and M. Farzaneh, "A ZnO-based nanocomposite coating with ultra water repellent properties," *Appl. Surf. Sci.*, vol. 258, no. 15, pp. 5723–5728, 2012, doi: 10.1016/j.apsusc.2012.02.074.
- [58] G. Momen and M. Farzaneh, "Simple process to fabricate a superhydrophobic coating," *Micro Nano Lett.*, p. 405, 2011, doi: 10.1049/mnl.2011.0222.
- [59] H. Ji *et al.*, "Hydrophobic fluorinated carbon coatings on silicate glaze and aluminum," *Thin Solid Films*, vol. 405, pp. 104–108, 2002, doi: 10.1016/S0040-6090(01)01707-2.
- [60] J. Li, Y. Zhao, J. Hu, and L. Shu, "Anti-icing Performance of a Superhydrophobic PDMS / Modified Nano-silica Hybrid Coating for Insulators," *J. Adhes. Sci. Technol.*, vol. 26, no. May, pp. 665–679, 2012, doi: 10.1163/016942411X574826.
- [61] F. Wang, C. Li, Y. Lv, F. Lv, and Y. Du, "Ice accretion on superhydrophobic aluminum surfaces under low-temperature conditions," *Cold Reg. Sci. Technol.*, vol. 62, no. 1, pp. 29–33, 2010, doi: 10.1016/j.coldregions.2010.02.005.
- [62] R. Jafari and M. Farzaneh, "A Simple Method to Create Superhydrophobic Aluminium Surfaces," *Mater. Sci. Forum*, vol. 706–709, pp. 2874–2879, 2012, doi: 10.4028/www.scientific.net/MSF.706-709.2874.
- [63] P. Kim *et al.*, "Liquid-Infused Nanostructured Surfaces with Extreme Anti-Ice and Anti-Frost Performance," *ACS Nano*, vol. 6, no. 8, pp. 6569–6577, 2012, doi: 10.1021/nn302310q.
- [64] L. Foroughi Mobarakeh, R. Jafari, and M. Farzaneh, "The ice repellency of plasma polymerized hexamethyldisiloxane coating," *Appl. Surf. Sci.*, vol. 284, pp. 459–463, 2013, doi: 10.1016/j.apsusc.2013.07.119.
- [65] R. Menini and M. Farzaneh, "Elaboration of Al₂O₃/PTFE icephobic coatings for protecting aluminum surfaces," *Surf. Coatings Technol.*, vol. 203, no. 14, pp. 1941–1946, 2009, doi: 10.1016/j.surfcoat.2009.01.030.

- [66] M. Susoff, K. Siegmann, C. Pfaffenroth, and M. Hirayama, "Evaluation of icephobic coatings - Screening of different coatings and influence of roughness," *Appl. Surf. Sci.*, vol. 282, pp. 870–879, 2013, doi: 10.1016/j.apsusc.2013.06.073.
- [67] G. Momen and M. Farzaneh, "Facile approach in the development of icephobic hierarchically textured coatings as corrosion barrier," *Appl. Surf. Sci.*, vol. 299, pp. 41–46, 2014, doi: 10.1016/j.apsusc.2014.01.179.
- [68] Y. Wang, J. Xue, Q. Wang, Q. Chen, and J. Ding, "Verification of Icephobic/Anti-icing Properties of a Superhydrophobic Surface," 2013.
- [69] T. S. N. S. Narayanan, "Surface pretreatment by phosphate conversion coatings - A review," *Rev. Adv. Mater. Sci.*, vol. 9, no. 2, pp. 130–177, 2005, doi: 10.1016/0033-0655(81)80009-X.
- [70] L. Li, V. Breedveld, and D. W. Hess, "Creation of superhydrophobic stainless steel surfaces by acid treatments and hydrophobic film deposition," *ACS Appl. Mater. Interfaces*, vol. 4, no. 9, pp. 4549–4556, 2012, doi: 10.1021/am301666c.
- [71] Y. Shen, J. Tao, H. Tao, S. Chen, L. Pan, and T. Wang, "Nanostructures in superhydrophobic Ti6Al4V hierarchical surfaces control wetting state transitions," *Soft Matter*, vol. 11, no. 19, pp. 3806–3811, 2015, doi: 10.1039/C5SM00024F.
- [72] Z. S. Saifaldeen, K. R. Khedir, M. F. Cansizoglu, T. Demirkan, and T. Karabacak, "Superamphiphobic aluminum alloy surfaces with micro and nanoscale hierarchical roughness produced by a simple and environmentally friendly technique," *J. Mater. Sci.*, vol. 49, no. 4, pp. 1839–1853, 2014, doi: 10.1007/s10853-013-7872-x.
- [73] M. Avram, A. M. Avram, A. Bragaru, A. Ghiu, and C. Iliescu, "Plasma surface modification for selective hydrophobic control," *Rom. J. Inf. Sci. Technol.*, vol. 11, no. 4, pp. 409–422, 2008.
- [74] W. Schwarzacher, "Electrodeposition: A Technology for the Future," *Electrochem. Soc. Interface*, vol. 15, no. 1, pp. 32–35, 2006.
- [75] M. H. Kwon, W. Y. Jee, and C. N. Chu, "Fabrication of hydrophobic surfaces using copper electrodeposition and oxidation," *Int. J. Precis. Eng. Manuf.*, vol. 16, no. 5, pp. 877–882, 2015, doi: 10.1007/s12541-015-0115-0.
- [76] B. Han, Y. Yang, L. Fang, G. Peng, and C. Yang, "Electrodeposition of super-hydrophobic nickel film on magnesium alloy AZ31 and its corrosion resistance," *Int. J. Electrochem. Sci.*, vol. 11, no. 11, pp. 9206–9215, 2016, doi: 10.20964/2016.11.23.
- [77] M. Farzaneh *et al.*, "Insulator icing test methods and procedures a position paper prepared by the IEEE task force on insulator icing test methods," *IEEE Trans. Power Deliv.*, vol. 18, no. 4, pp. 1503–1515, 2003, doi: 10.1109/TPWRD.2003.817808.
- [78] IEEE-SA Standards Board, "Guide for test methods and procedures to evaluate the electrical performance of insulators in freezing conditions," *IEEE standard 1783*, no. October. pp. 1–32, 2009.

- [79] Y. Wenxuan, Y. Yuan, L. Guoyong, Z. Bing, and Y. Rongkai, "The anti-icing/frosting aluminum surface with hydrangea-like micro/nano structure prepared by chemical etching," *Mater. Lett.*, vol. 226, pp. 4–7, 2018, doi: 10.1016/j.matlet.2018.04.100.
- [80] ANSI C29, "Insulator - Wet Process Porcelain and Toughened Glass - Suspension Type," *Natl. Inf. Stand. Organ.*, 1992.
- [81] G. P. Bierwagen, L. He, J. Li, L. Ellingson, and D. E. Tallman, "Studies of a new accelerated evaluation method for coating corrosion resistance - thermal cycling testing," *Prog. Org. Coatings*, vol. 39, no. 1, pp. 67–78, 2000, doi: 10.1016/S0300-9440(00)00106-5.
- [82] Y. Sohn *et al.*, "Anti-frost coatings containing carbon nanotube composite with reliable thermal cyclic property," *J. Mater. Chem. A*, vol. 2, no. 29, p. 11465, 2014, doi: 10.1039/c4ta01398k.
- [83] B. X. Du and Z. L. Li, "Hydrophobicity, surface charge and DC flashover characteristics of direct-fluorinated RTV silicone rubber," *IEEE Trans. Dielectr. Electr. Insul.*, vol. 22, no. 2, pp. 934–940, 2015, doi: 10.1109/TDEI.2015.7076794.
- [84] ASTM G155, "Standard Practice for Operating Xenon Arc Light Apparatus for Exposure of Non-Metallic Materials," *Annu. B. ASTM Stand.*, 2013.
- [85] ASTM G154, "Standard Practice for Operating Fluorescent Ultraviolet (UV) Lamp Apparatus for Exposure of Nonmetallic Materials," *Natl. Inf. Stand. Organ.*, 2012.
- [86] ASTM D4587, "Standard Practice for Fluorescent UV-Condensation Exposures of Paint and Related Coatings," *Annu. B. ASTM Stand.*, 2011.
- [87] J. Long, M. Zhong, H. Zhang, and P. Fan, "Superhydrophilicity to superhydrophobicity transition of picosecond laser microstructured aluminum in ambient air," *J. Colloid Interface Sci.*, vol. 441, pp. 1–9, 2015, doi: 10.1016/j.jcis.2014.11.015.
- [88] M. V. Rukosuyev, J. Lee, S. J. Cho, G. Lim, and M. B. G. Jun, "One-step fabrication of superhydrophobic hierarchical structures by femtosecond laser ablation," *Appl. Surf. Sci.*, vol. 313, pp. 411–417, 2014, doi: 10.1016/j.apsusc.2014.05.224.
- [89] R. Jagdheesh, J. J. García-Ballesteros, and J. L. Ocaña, "One-step fabrication of near superhydrophobic aluminum surface by nanosecond laser ablation," *Appl. Surf. Sci.*, vol. 374, pp. 2–11, 2016, doi: 10.1016/j.apsusc.2015.06.104.
- [90] L. B. Boinovich, A. M. Emelyanenko, A. D. Modestov, A. G. Domantovsky, and K. A. Emelyanenko, "Synergistic Effect of Superhydrophobicity and Oxidized Layers on Corrosion Resistance of Aluminum Alloy Surface Textured by Nanosecond Laser Treatment," *ACS Appl. Mater. Interfaces*, vol. 7, no. 34, pp. 19500–19508, 2015, doi: 10.1021/acsami.5b06217.
- [91] R. Jagdheesh, "Fabrication of superhydrophobic Al₂O₃ surface using ps laser pulses," *Langmuir*, vol. 30, pp. 12067–73, 2014.
- [92] J. Long *et al.*, "Superhydrophobic surfaces fabricated by femtosecond laser with tunable water adhesion: From lotus leaf to rose petal," *ACS Appl. Mater. Interfaces*, vol. 7, no. 18,

- pp. 9858–9865, 2015, doi: 10.1021/acsami.5b01870.
- [93] M. Cojan, C. Malaguti, P. Nicolini, J. S. T. Looms, A. W. Stannett, and J. Perret, “POLYMERIC TRANSMISSION INSULATORS: THEIR APPLICATION IN FRANCE, ITALY AND THE UK.,” in *International Conference on Large High Voltage Electric Systems*, 1980.
- [94] G. Heger, H. J. Vermeulen, J. P. Holtzhausen, and W. L. Vosloo, “A comparative study of insulator materials exposed to high voltage AC and DC surface discharges,” *IEEE Transactions on Dielectrics and Electrical Insulation*, vol. 17, no. 2, pp. 513–520, 2010, doi: 10.1109/TDEI.2010.5448107.
- [95] A. Ul-Hamid, K. Y. Soufi, and I. Al-Hamoudi, “Evaluation of silicone rubber insulators used in high-voltage transmission lines,” *J. Mater. Eng. Perform.*, vol. 17, no. 2, pp. 280–286, 2008, doi: 10.1007/s11665-007-9142-z.
- [96] PES Transmission and Distribution, *IEEE 1283 - IEEE Guide for Determining the Effects of High Temperature Operation on Conductors, Connectors, and Accessories*, vol. 2002, no. January. 2013.
- [97] J. M. Hesterlce, E. T. Sanders, and F. R. Thrash, “Bare overhead transmission and distribution conductor design overview,” *IEEE Trans. Ind. Appl.*, vol. 32, no. 3, pp. 709–713, 1996, doi: 10.1109/28.502185.
- [98] A. J. Mazón *et al.*, “Gap-type conductors: Influence of high temperature in the compression clamp systems,” *2003 IEEE Bol. PowerTech - Conf. Proc.*, vol. 2, no. March 2015, pp. 1029–1033, 2003, doi: 10.1109/PTC.2003.1304687.
- [99] R. S. Hebbar, A. M. Isloor, and A. F. Ismail, *Contact Angle Measurements*. Elsevier B.V., 2017.
- [100] T. T. Chau, “A review of techniques for measurement of contact angles and their applicability on mineral surfaces,” *Miner. Eng.*, vol. 22, no. 3, pp. 213–219, 2009, doi: 10.1016/j.mineng.2008.07.009.
- [101] M. Schmitt and F. Heib, “High-precision drop shape analysis on inclining flat surfaces: Introduction and comparison of this special method with commercial contact angle analysis,” *J. Chem. Phys.*, vol. 139, no. 13, 2013, doi: 10.1063/1.4822261.
- [102] F. Heib and M. Schmitt, “Statistical Contact Angle Analyses with the High-Precision Drop Shape Analysis (HPDSA) Approach: Basic Principles and Applications,” *Coatings*, vol. 6, no. 4, p. 57, 2016, doi: 10.3390/coatings6040057.
- [103] M. Sun *et al.*, “Artificial lotus leaf by nanocasting,” *Langmuir*, vol. 21, no. 19, pp. 8978–8981, 2005, doi: 10.1021/la050316q.
- [104] M. Bortolotti, M. Brugnara, C. Della Volpe, and S. Siboni, “Numerical models for the evaluation of the contact angle from axisymmetric drop profiles: A statistical comparison,” *J. Colloid Interface Sci.*, vol. 336, no. 1, pp. 285–297, 2009, doi: 10.1016/j.jcis.2009.03.055.

- [105] H. Mojiri and M. Aliofkhazraei, *Effect of Surface Roughness on Wetting Properties*, vol. 3–3. Elsevier Ltd., 2017.
- [106] D. Zang, R. Zhu, W. Zhang, J. Wu, X. Yu, and Y. Zhang, “Stearic acid modified aluminum surfaces with controlled wetting properties and corrosion resistance,” *Corros. Sci.*, vol. 83, pp. 86–93, 2014, doi: 10.1016/j.corsci.2014.02.003.
- [107] D. K. Sarkar and M. Farzaneh, “Superhydrophobic aluminum surfaces obtained by chemical etching,” *Contact Angle, Wettability Adhes.*, vol. 5, pp. 271–278, 2008.
- [108] X. Li *et al.*, “Fabrication of superhydrophobic surface with improved corrosion inhibition on 6061 aluminum alloy substrate,” *Appl. Surf. Sci.*, vol. 342, pp. 76–83, 2015, doi: 10.1016/j.apsusc.2015.03.040.
- [109] B. Xu, Z. Cai, W. Wang, and F. Ge, “Preparation of superhydrophobic cotton fabrics based on SiO₂ nanoparticles and ZnO nanorod arrays with subsequent hydrophobic modification,” *Surf. Coatings Technol.*, 2010, doi: 10.1016/j.surfcoat.2009.09.086.
- [110] T. Soeno, K. Inokuchi, and S. Shiratori, “Ultra-water-repellent surface: Fabrication of complicated structure of SiO₂ nanoparticles by electrostatic self-assembled films,” in *Applied Surface Science*, 2004, doi: 10.1016/j.apsusc.2004.06.041.
- [111] S. Ammar, K. Ramesh, B. Vengadaesvaran, S. Ramesh, and A. K. Arof, “A novel coating material that uses nano-sized SiO₂ particles to intensify hydrophobicity and corrosion protection properties,” *Electrochim. Acta*, 2016, doi: 10.1016/j.electacta.2016.10.099.
- [112] M. Miwa, A. Nakajima, A. Fujishima, K. Hashimoto, and T. Watanabe, “Effects of the surface roughness on sliding angles of water droplets on superhydrophobic surfaces,” *Langmuir*, vol. 16, no. 13, pp. 5754–5760, 2000, doi: 10.1021/la991660o.
- [113] C. Lian, “Video of comparing uncoated and NeverWet superhydrophobic coated flat aluminium and round conductor samples under a high-speed camera,” 2020. [Online]. Available: <https://www.youtube.com/watch?v=69fGg6zcGGg>.
- [114] N. P. Suh and H. C. Sin, “The genesis of friction,” *Wear*, 1981, doi: 10.1016/0043-1648(81)90315-X.
- [115] Y. Ding *et al.*, “Modifying the anti-wetting property of butterfly wings and water strider legs by atomic layer deposition coating: Surface materials versus geometry,” *Nanotechnology*, vol. 19, no. 35, 2008, doi: 10.1088/0957-4484/19/35/355708.
- [116] C. E. Cansoy, H. Y. Erbil, O. Akar, and T. Akin, “Effect of pattern size and geometry on the use of Cassie-Baxter equation for superhydrophobic surfaces,” *Colloids Surfaces A Physicochem. Eng. Asp.*, vol. 386, no. 1–3, pp. 116–124, 2011, doi: 10.1016/j.colsurfa.2011.07.005.
- [117] M. Nosonovsky and B. Bhushan, “Roughness optimization for biomimetic superhydrophobic surfaces,” *Microsystem Technologies*. 2005, doi: 10.1007/s00542-005-0602-9.
- [118] M. H. Shim, J. Kim, and C. H. Park, “The effects of surface energy and roughness on the

- hydrophobicity of woven fabrics,” *Text. Res. J.*, vol. 84, no. 12, pp. 1268–1278, 2014, doi: 10.1177/0040517513495945.
- [119] L. R. de Lara, R. Jagdheesh, and J. L. Ocaña, “Corrosion resistance of laser patterned ultrahydrophobic aluminium surface,” *Mater. Lett.*, vol. 184, pp. 100–103, 2016, doi: 10.1016/j.matlet.2016.08.022.
- [120] X. Li, Q. Xu, Z. Li, and W. Huang, “Al superhydrophobic surfaces fabricated with femtosecond laser pulses,” *ICEOE 2011 - 2011 Int. Conf. Electron. Optoelectron. Proc.*, vol. 2, no. Iceoe, pp. 109–112, 2011, doi: 10.1109/ICEOE.2011.6013188.
- [121] S. Milles, M. Soldera, B. Voisiat, and A. F. Lasagni, “Fabrication of superhydrophobic and ice-repellent surfaces on pure aluminium using single and multiscaled periodic textures,” *Sci. Rep.*, vol. 9, no. 1, pp. 1–13, 2019, doi: 10.1038/s41598-019-49615-x.
- [122] V. D. Ta *et al.*, “Laser textured superhydrophobic surfaces and their applications for homogeneous spot deposition,” *Appl. Surf. Sci.*, vol. 365, pp. 153–159, 2016, doi: 10.1016/j.apsusc.2016.01.019.
- [123] S. C. Oh, B. J. Bae, K. Y. Yang, M. H. Kwon, and H. Lee, “Fabrication of aluminum nano-scale structures using direct-embossing with a nickel template,” *Met. Mater. Int.*, vol. 17, no. 5, pp. 771–775, 2011, doi: 10.1007/s12540-011-1012-4.
- [124] K. Kopsidas and S. M. Rowland, “A performance analysis of reconductoring an overhead line structure,” *IEEE Trans. Power Deliv.*, vol. 24, no. 4, pp. 2248–2256, 2009, doi: 10.1109/TPWRD.2009.2021042.
- [125] Press Association, “UK’s coldest December for 100 years,” *The Guardian*, 05-Jan-2011. [Online]. Available: <https://www.theguardian.com/uk/2011/jan/05/december-coldest-uk-month-100-years>. [Accessed: 22-Jul-2019].
- [126] ASTM, “ASTM G155-13 Standard Practice for Operating Xenon Arc Light Apparatus for Exposure of Non-Metallic Materials,” *Astm*, pp. 1–11, 2013, doi: 10.1520/G0155-13.
- [127] ISO 4892-3, “Plastics – Methods of exposure to laboratory light sources – Part 2: Xenon-arc lamps,” *Int. Organ. Stand.*, vol. 3, 2013.
- [128] F. Wang, C. Li, Y. Lv, and Y. Du, “Reducing ice accumulation on aluminum conductor by applying superhydrophobic coating,” *Annu. Rep. - Conf. Electr. Insul. Dielectr. Phenomena, CEIDP*, pp. 311–314, 2009, doi: 10.1109/CEIDP.2009.5377882.
- [129] M. Farzaneh, F. Jakl, M. Arabani, and A. Eliasson, “Systems for Prediction and Monitoring of Ice Shedding, Anti-Icing and De-Icing for Overhead Power Line Conductors and Ground Wires,” *CIGRE, Electra*, no. 253, pp. 0–3, 2010.
- [130] F. Wang, F. Lv, Y. Liu, C. Li, and Y. Lv, “Ice adhesion on different microstructure superhydrophobic aluminum surfaces,” *J. Adhes. Sci. Technol.*, vol. 27, no. 1, pp. 58–67, 2013, doi: 10.1080/01694243.2012.701506.
- [131] S. Tarquini, C. Antonini, A. Amirfazli, M. Marengo, and J. Palacios, “Investigation of ice

- shedding properties of superhydrophobic coatings on helicopter blades,” *Cold Reg. Sci. Technol.*, vol. 100, pp. 50–58, 2014, doi: 10.1016/j.coldregions.2013.12.009.
- [132] X. Zhang, C. Lian, C. Emersic, and I. Cotton, “Acoustic noise emitted from overhead line conductors with superhydrophobic coating,” *2019 IEEE Electr. Insul. Conf. EIC 2019*, no. June, pp. 87–90, 2019, doi: 10.1109/EIC43217.2019.9046573.
- [133] T. H. Teich and H.-J. Weber, “Origin and abatement of tonal emission from high voltage transmission lines,” *e i Elektrotechnik und Informationstechnik*, vol. 119, no. 1, pp. 22–27, Jan. 2002, doi: 10.1007/BF03161466.
- [134] Q. Li, S. M. Rowland, I. Dupere, and R. Shuttleworth, “Acoustic noise evaluation for overhead line conductors using an anechoic chamber,” *IEEE Trans. Power Deliv.*, vol. 32, no. 4, pp. 1835–1843, 2017, doi: 10.1109/TPWRD.2016.2558153.
- [135] Z. Engel and T. Wszolek, “Audible noise of transmission lines caused by the corona effect: Analysis, modelling, prediction,” *Appl. Acoust.*, vol. 47, no. 2, pp. 149–163, Feb. 1996, doi: 10.1016/0003-682X(95)00041-7.
- [136] M. Sforzini, R. Cortina, G. Sacerdote, and R. Piazza, “Acoustic noise caused by a.c. corona on conductors: Results of an experimental investigation in the anechoic chamber,” *IEEE Trans. Power Appar. Syst.*, vol. 94, no. 2, pp. 591–601, Mar. 1975, doi: 10.1109/T-PAS.1975.31887.
- [137] L. Ventola, L. Scaltrito, S. Ferrero, G. Maccioni, E. Chiavazzo, and P. Asinari, “Micro-structured rough surfaces by laser etching for heat transfer enhancement on flush mounted heat sinks,” *J. Phys. Conf. Ser.*, vol. 525, no. 1, 2014, doi: 10.1088/1742-6596/525/1/012017.
- [138] K. S. Lee, W. S. Kim, and T. H. Lee, “A one-dimensional model for frost formation on a cold flat surface,” *Int. J. Heat Mass Transf.*, vol. 40, no. 18, pp. 4359–4365, 1997, doi: 10.1016/S0017-9310(97)00074-4.
- [139] H. A. Stone, “Ice-phobic surfaces that are wet,” *ACS Nano*, vol. 6, no. 8, pp. 6536–6540, 2012, doi: 10.1021/nn303372q.
- [140] Witthinrich, “British Standard All aluminium alloy conductor AAAC - BS AL3.” EN 50182.
- [141] CTC Global, *Engineering Transmission Lines with High Capacity Low Sag ACCC Conductors*, vol. 2011. 2011.
- [142] British Standard, “Overhead electrical lines exceeding AC 45 kV — Part 3: Set of National Normative Aspects,” *BS EN 50341-32001*, 2001.
- [143] Cigré WG.B2.12.3, *Sag-tension calculation methods for overhead lines, Technical brochure 324*, no. June. 2007.
- [144] I. eletrotechnical C. IEC, “IEC 60826: Design criteria of overhead transmission lines,” *Notes*, 2003.
- [145] H. N. Scherer and G. S. Vassell, “Transmission of Electric Power at Ultra-High Voltages: Current Status and Future Prospects,” *Proc. IEEE*, vol. 73, no. 8, pp. 1252–1278, 1985, doi:

10.1109/PROC.1985.13280.

- [146] R. Tadeusiewicz, T. Wszolek, A. Izvorski, and W. Wszolek, "Recognition of defects in high voltage transmission lines using the acoustic signal of corona effect," *Neural Networks Signal Process. X. Proc. 2000 IEEE Signal Process. Soc. Work. (Cat. No.00TH8501)*, vol. 2, no. C, 2000, doi: 10.1109/NNSP.2000.890167.
- [147] T. Lines, "Tonal Component of the Audible Noise From UHV-Ac," pp. 1–5, 2009.
- [148] G. W. Juetten and L. E. Zaffanella, "Radio Noise, Audible Noise, and Corona Loss of EHV and UHV Transmission Lines Under Rain: Predetermination Based on Cage Tests," *IEEE Trans. Power Appar. Syst.*, 1970, doi: 10.1109/TPAS.1970.292728.
- [149] A.-P. Benguerel, "Signals and Systems for Speech and Hearing," *Lang. Speech*, vol. 34, no. 4, pp. 381–382, Oct. 1991, doi: 10.1177/002383099103400407.
- [150] H. Kirkham and W. Gajda, "A Mathematical Model of Transmission Line Audible Noise Part 1: Background and Model Development," *IEEE Trans. Power Appar. Syst.*, vol. PAS-102, no. 3, pp. 710–717, 1983, doi: 10.1109/TPAS.1983.318032.
- [151] G. W. Juetten and L. E. Zaffanella, "Radio Noise Currents and Audible Noise on Short Sections of UHV Bundle Conductors," *IEEE Trans. Power Appar. Syst.*, vol. PAS-89, no. 5, pp. 902–913, 1970, doi: 10.1109/TPAS.1970.292653.
- [152] R. E. Carberry, J. H. Davey, T. J. DuBois, P. Heroux, D. N. Keast, and R. A. Popeck, "Measurement of audible noise from transmission lines," *IEEE Trans. Power Appar. Syst.*, vol. PAS-100, no. 3, pp. 1440–1452, 1981, doi: 10.1109/TPAS.1981.316619.
- [153] U. Straumann, "Mechanism of the tonal emission from ac high voltage overhead transmission lines," *J. Phys. D. Appl. Phys.*, vol. 44, no. 7, 2011, doi: 10.1088/0022-3727/44/7/075501.
- [154] U. Straumann, "Simulation of the space charge near coronating conductors of ac overhead transmission lines," *J. Phys. D. Appl. Phys.*, vol. 44, no. 7, 2011, doi: 10.1088/0022-3727/44/7/075502.
- [155] Q. Li, S. M. Rowland, I. Dupere, and R. Morris, "The impact of water droplet vibration on corona inception on conductors under 50 Hz AC fields," *IEEE Trans. Power Deliv.*, no. c, pp. 1–9, 2018, doi: 10.1109/TPWRD.2018.2825886.
- [156] O. Fujii, K. Honsali, Y. Mizuno, and K. Naito, "Vibration of a water droplet on a polymeric insulating material subjected to AC voltage stress," *IEEE Trans. Dielectr. Electr. Insul.*, vol. 17, no. 2, pp. 566–571, 2010, doi: 10.1109/TDEI.2010.5448113.
- [157] G. J. Anders, *Rating of electric power cables in unfavorable thermal environment*. 2010.
- [158] D. Enescu, P. Colella, and A. Russo, "Thermal assessment of power cables and impacts on cable current rating: An overview," *Energies*, vol. 13, no. 20, 2020, doi: 10.3390/en13205319.
- [159] L. Ventola *et al.*, "Rough surfaces with enhanced heat transfer for electronics cooling by direct metal laser sintering," *Int. J. Heat Mass Transf.*, vol. 75, no. March, pp. 58–74, 2014, doi: 10.1016/j.ijheatmasstransfer.2014.03.037.

- [160] IEEE Power Engineering Society., *IEEE standard for calculating the current-temperature relationship of bare overhead conductors*, vol. 2006, no. January. 2007.
- [161] G. Schoffner, “Gas insulated transmission lines - successful underground bulk power transmission for more than 30 years,” *8th IEE Int. Conf. AC DC Power Transm.*, pp. 271–275, 2006, doi: 10.1049/cp:20060055.

APPENDIX EXPERIMENTAL DATA

Table A 1 Contact angle measurements using different computing methods and different size of water drops

Measurements (°)	12 μ L drop size				4 μ L drop size			
	Auto computation (Laplace-Young fitting)	Auto computation (Ellipse fitting)	Manual elliptical fit with whole drop	Manual circular zoomed in method	Auto computation (Laplace-Young fitting)	Auto computation (Ellipse fitting)	Manual elliptical fit with whole drop	Manual circular zoomed in method
1	174.5	147.7	156.5	167.4	166.2	154.9	160.9	169.2
2	160.2	146.2	154.1	165.9	167.8	156.8	160.4	169.6
3	169.2	147.7	154.2	164.9	179.7	155.8	160.7	168.5
4	179.9	148.6	155.7	166.1	179.7	158.4	160.7	170.8
5	179.7	147.4	153.9	166.7	179.7	157.1	160.3	168.0
6	169.7	148.0	154.9	166.1	167.4	155.3	160.8	169.2
7	172.7	147.5	155.0	165.5	173.8	156.8	159.9	170.2
8	171.5	148.2	154.8	164.4	179.7	158.7	160.5	170.3
9	179.9	149.0	155.9	164.2	179.7	156.5	160.9	168.9
10	179.8	148.0	153.6	166.6	179.8	154.6	160.7	169.5

Table A 2 Contact angle measurements of uncoated substrates

Uncoated Substrates			0 s		15 s		30 s		45 s		60 s	
			left	right	left	right	left	right	left	right	left	right
Aluminium	Sample 1	1	107.2	107.6	105.9	106.2	105.2	105.4	104.2	104.3	102.7	102.9
		2	100.4	100.4	99.9	99.9	99.1	99.1	98.2	98.2	97.0	97.0
		3	105.6	105.7	103.9	104.1	104.1	104.3	102.5	102.7	102.2	102.3
		4	118.9	120.0	118.2	118.9	118.1	119.2	116.2	117.2	114.9	114.7
		5	109.7	109.6	105.1	107.3	106.9	107.6	105.8	105.6	103.8	103.6
		Average	108.5		106.9		106.9		105.5		104.1	
	Sample 2	1	100.9	106.7	100.0	106.7	97.4	105.5	93.5	100.6	92.7	99.6
		2	108.5	111.8	105.1	108.7	105.9	109.4	105.4	108.1	104.5	108.3
		3	107.6	107.7	107.0	107.0	107.4	107.5	105.4	105.4	104.5	104.5
		4	113.2	113.4	113.0	113.1	112.5	112.6	111.9	112.0	110.6	110.7
		5	110.9	110.7	109.9	109.6	107.8	107.5	107.7	107.2	106.2	105.8
		Average	109.1		108.0		107.4		105.7		104.7	
	Sample 3	1	97.3	98.1	96.0	96.8	97.0	97.8	94.0	94.8	92.6	93.5
		2	116.8	116.6	114.5	114.3	115.0	114.8	113.1	112.7	112.7	112.3
		3	103.8	103.0	103.7	102.7	103.3	102.4	101.2	100.2	101.0	100.0
		4	105.5	105.3	105.4	105.5	104.7	104.8	102.7	102.8	102.2	102.2
		5	112.2	112.5	111.5	111.7	111.0	111.3	110.4	110.9	109.8	110.2
		Average	107.1		106.2		106.2		104.3		103.7	
Silicone Rubber	Sample 1	1	111.1	111.1	111.7	111.5	112.7	113.2	111.5	111.0	110.7	111.2
		2	109.8	109.9	107.6	107.8	109.6	109.7	109.5	109.5	108.2	108.2

		3	105.4	105.6	104.9	105.1	104.2	104.4	104.5	104.7	103.4	103.6	
		4	110.7	110.7	110.3	110.3	110.6	110.5	109.3	109.2	109.1	109.1	
		5	112.7	112.8	113.3	114.4	113.4	113.6	113.3	114.7	113.2	113.2	
		Average	110.0		109.7		110.2		109.7		109.0		
	Sample 2	1	111.8	112.2	111.9	112.2	111.2	111.5	110.4	110.7	111.2	111.5	
		2	117.9	118.6	117.9	118.0	116.7	117.2	115.5	116.8	115.4	116.2	
		3	111.7	111.5	113.9	113.3	112.7	112.4	111.1	110.2	113.8	112.3	
		4	115.3	115.0	112.8	113.0	113.7	113.9	112.8	113.0	113.4	113.6	
		5	115.4	114.8	113.0	112.8	114.0	113.6	114.0	112.9	112.1	111.7	
		Average	114.4		113.9		113.7		112.7		113.1		
	Sample 3	1	116.0	116.6	116.5	116.5	116.0	116.1	115.5	115.6	115.5	115.7	
		2	118.7	119.1	117.2	118.4	117.6	118.1	116.5	118.2	117.5	118.0	
		3	112.6	112.9	112.6	112.8	112.0	112.2	112.0	112.1	111.4	111.5	
		4	111.5	111.6	111.1	111.2	110.7	110.9	110.0	110.2	109.9	110.2	
		5	113.1	113.3	113.2	113.4	112.4	112.6	111.8	112.1	111.6	111.9	
		Average	114.5		114.3		113.9		113.4		113.3		
	EPDM Rubber	A	1	108.6	108.7	106.8	107.0	105.8	106.1	105.6	105.8	106.7	106.9
			2	108.5	108.7	108.0	108.1	107.8	107.9	108.2	108.3	106.4	106.5
3			106.5	108.3	107.1	108.4	106.6	108.3	105.6	104.8	107.3	108.0	
4			108.2	108.3	108.0	108.1	108.3	108.5	107.0	107.2	107.0	107.1	
5			108.5	108.3	107.8	107.6	107.2	107.0	106.9	106.7	107.3	107.1	
Average			108.3		107.7		107.4		106.6		107.0		
B		1	106.8	106.5	106.5	106.4	104.9	104.7	103.5	103.4	102.9	103.0	
		2	108.1	108.1	107.5	107.5	107.7	107.7	107.8	108.0	108.0	108.0	

		3	110.4	110.5	110.1	110.1	108.9	109.0	108.9	109.2	109.0	109.1
		4	109.5	109.6	109.4	109.4	109.2	109.2	108.9	109.0	108.2	108.3
		5	110.8	110.8	110.2	110.1	109.6	109.6	109.2	109.2	110.3	110.3
		Average	109.1		108.7		108.1		107.7		107.7	
	C	1	108.1	108.3	107.8	107.9	108.3	108.5	106.4	106.6	104.9	105.0
		2	109.0	107.8	105.6	105.0	106.7	106.9	107.2	105.7	104.7	104.8
		3	109.8	109.8	109.9	109.9	110.5	110.5	109.2	109.2	109.1	109.1
		4	105.5	105.5	104.9	104.9	104.4	104.4	104.5	104.4	103.9	103.9
		5	108.4	108.4	107.8	107.8	108.0	108.0	107.3	107.3	106.6	106.6
		Average	108.1		107.2		107.6		106.8		105.9	

Table A 3 Contact angle measurements of HumiSeal coated substrates

HumiSeal	Aluminium		Silicone Rubber		EPDM Rubber	
	left	right	left	right	left	right
1	105.1	104.9	108.6	109.7	110.3	110.4
2	82.4	89.1	81.1	92.9	110.1	110.1
3	90.4	99.8	86.4	86.4	104.2	102.7
4	86.9	86.1	84.3	88.5	109.0	108.8
5	99.5	91.6	85.7	85.9	106.1	106.8
Average	93.6		91.0		107.9	

Table A 4 Recovery contact angle measurements of 2 mins etched aluminium substrates at room temperature

Time (Days)	Contact Angle (°)											Contact Angle Hysteresis (°)
	1		2		3		4		5		Average	
	left	right	left	right	left	right	left	right	left	right		
0	80.7	77.8	74.2	81.0	87.6	90.0	68.9	77.2	87.8	86.5	81.2	
1	90.5	90.9	85.3	85.2	93.1	91.8	73.1	69.1	74.2	77.5	83.1	
2	84.4	91.1	93.5	91.0	76.7	75.4	82.7	78.0	97.3	94.2	86.4	
3	89.7	89.3	87.0	79.4	79.2	83.4	80.1	85.1	92.5	81.0	84.7	29
6	85.0	86.2	78.3	86.5	75.2	80.8	84.8	83.1	97.8	96.3	85.4	29
7	102.9	101.2	75.6	77.5	81.6	81.2	85.0	89.0	105.7	105.3	90.5	26
8	91.4	89.3	85.2	82.8	91.6	95.6	86.2	87.0	90.7	91.6	89.1	23
10	91.4	89.8	110.2	109.7	92.2	82.5	91.6	88.8	115.9	115.8	98.8	24
15	105.0	102.5	111.5	112.8	104.9	105.0	103.0	102.0	118.6	117.9	108.3	21
19	114.1	115.2	116.6	117.0	110.2	109.8	109.2	109.2	112.1	111.7	112.5	17
30	117.1	117.6	104.6	104.8	125.0	125.6	113.3	114.7	112.3	110.1	114.5	18

Table A 5 Recovery contact angle measurements of 2 mins etched aluminium substrates at 55 °C

Time (h)	Contact Angle (°)											Contact Angle Hysteresis (°)
	1		2		3		4		5		Average	
	left	right	left	right	left	right	left	right	left	right		
0	72.5	75.0	62.9	62.9	68.1	70.0	80.3	75.6	74.4	72.5	71.4	
2	72.6	87.2	73.3	73.6	82.1	84.9	80.2	84.7	75.2	74.1	78.8	
4	78.0	79.8	79.7	78.5	82.3	76.6	87.7	80.5	81.8	81.8	80.7	
6	76.1	84.5	81.5	84.5	93.8	93.2	99.0	102.4	102.1	100.0	91.7	
9	82.1	73.8	75.7	77.4	86.2	91.5	92.8	93.4	80.5	80.5	83.4	
14	81.6	95.4	80.4	87.5	77.8	78.5	94.8	90.3	91.4	91.2	86.9	
18	85.3	83.2	88.8	88.1	95.8	94.2	90.5	93.0	88.0	89.5	89.6	40
22	95.6	95.1	71.4	78.3	98.3	99.5	80.3	89.8	94.5	97.1	90.0	40
27	104.0	105.6	114.4	113.4	109.5	109.6	108.5	110.0	104.1	105.6	108.5	39
31	109.1	108.3	106.8	106.4	121.7	122.5	110.0	112.8	111.9	113.4	112.3	35
35	120.0	120.0	119.0	118.8	118.2	117.4	113.1	114.7	114.8	114.0	117.0	30
38	119.6	119.8	107.3	105.8	120.5	120.6	103.3	101.2	118.0	110.8	112.7	30
41	123.8	129.8	125.1	125.1	120.9	120.9	127.0	127.3	120.1	119.2	123.9	28
44	124.4	124.4	120.8	122.0	112.3	109.9	115.9	116.0	122.4	121.0	118.9	23
48	121.1	121.9	114.4	114.3	124.9	122.9	117.7	114.7	126.6	127.6	120.6	20
52	125.7	125.6	119.4	119.6	125.1	125.2	122.0	122.4	120.1	126.9	123.2	18
80	119.3	119.1	114.3	113.7	116.4	117.7	125.9	125.8	125.9	126.2	120.4	17

Table A 6 Recovery contact angle measurements of 4 mins etched aluminium substrates at 55 °C

Time (h)	Contact Angle (°)											Contact Angle Hysteresis (°)
	1		2		3		4		5		Average	
	left	right	left	right	left	right	left	right	left	right		
4	15.5	15.5	20.8	20.8	21.1	21.1	27.1	27.1	23.8	23.8	21.7	
6	22.6	24.5	35.8	35.8	30.7	30.7	31.3	31.3	34.8	34.8	31.2	
9	33.3	33.3	36.2	36.2	59.8	59.8	33.3	33.3	59.6	48.7	43.4	
14	49.4	31.3	37.2	42.6	63.9	64.5	41.3	43.1	53.2	43.4	47.0	
18	46.0	43.9	51.2	51.2	65.1	68.1	45.7	35.0	51.3	56.9	51.4	
22	50.8	43.6	62.4	60.4	79.1	80.0	64.7	66.4	73.8	76.3	65.8	
27	65.4	61.2	74.8	74.3	78.9	78.1	70.5	69.4	80.3	81.0	73.4	35
31	73.8	71.5	75.0	71.5	85.1	83.0	55.7	58.1	74.0	82.5	73.0	32
35	86.0	80.7	77.0	79.3	112.9	110.3	69.4	69.4	121.7	122.5	92.9	27
38	107.5	103.8	99.2	98.3	125.4	125.5	85.1	80.6	129.4	129.0	108.4	22
41	123.8	123.6	119.6	119.9	137.0	137.1	118.0	115.2	132.4	132.5	125.9	18
44	130.9	130.5	128.4	129.0	136.7	136.7	124.5	126.3	134.6	134.6	131.2	15
48	130.3	129.1	137.9	138.0	133.0	133.4	130.0	130.3	137.0	136.2	133.5	12
52	131.7	131.5	131.2	131.3	137.0	136.9	138.5	138.6	135.6	135.7	134.8	15
80	136.1	136.1	133.6	133.7	137.0	136.8	136.9	137.2	133.3	133.6	135.4	10

Table A 7 Contact angle and sliding angle measurements of coatings with different preparing methods and spray times

		Twice-mixed Solution						Single-mixed Solution							
Spray Time (s)		10		30		50		10		30		50		70	
Contact Angle (°)	1	164.8	163.1	163.5	166.0	165.5	164.9	123.5	127.4	158.6	148.6	131.2	131.2	164.3	167.4
	2	140.5	144.9	162.3	158.1	164.8	163.7	116.2	122.8	156.2	153.8	135.1	133.1	162.1	159.7
	3	153.8	161.8	164.7	164.9	167.6	166.9	121.0	123.8	151.3	149.2	131.0	130.5	161.0	162.7
	4	134.4	136.3	163.7	162.6	162.7	163.0	116.0	111.8	144.6	144.5	126.6	131.5	165.9	162.3
	5	141.5	141.2	167.9	165.3	172.1	165.0	117.9	120.5	150.8	148.6	125.4	127.6	166.9	165.2
	Average	148.2		163.9		165.6		120.1		150.6		130.3		163.8	
Sliding Angle (°)	1	Did Not Slide		9.5		12.0		Did Not Slide		Did Not Slide		Did Not Slide		4.5	
	2			8.5		11.5								4.0	
	3			9.0		11.5								5.0	
	Average			9.0		11.7								4.5	

Table A 8 Contact angle and sliding angle measurements of coatings with different flow volumes and spray times

		Original Flow Volume (1/4 Rotation)								Higher Flow Volume (1/2 Rotation)							
Spray Time (s)		30		50		70		90		5		10		15		20	
Contact Angle (°)	1	132.3	134.8	161.4	164.0	167.7	166.7	165.7	160.8	162.5	164.8	160.0	161.7	159.9	157.8	157.7	158.5
	2	126.0	125.4	163.3	163.7	164.8	161.8	166.5	165.8	165.9	162.0	157.1	152.0	160.6	159.2	160.8	161.2
	3	137.2	129.1	163.7	163.9	166.8	163.3	167.4	161.8	164.4	163.5	159.4	159.7	158.0	159.9	159.3	157.6
	4	152.3	144.8	159.9	159.8	167.0	162.9	161.4	163.4	162.2	158.7	159.8	159.3	154.5	156.2	156.3	152.2
	5	142.7	140.6	164.4	162.3	165.5	162.8	164.5	166.0	168.3	164.4	165.5	165.7	162.8	157.2	157.4	160.0
	Average		136.5		162.6		164.9		164.3		163.7		160.0		158.6		158.1
Sliding Angle (°)	1	Did Not Slide		Did Not Slide		10.0		7.5		8.0		5.5		8.0		9.5	
	2					9.0		8.0		7.5		6.5		7.5		11.5	
	3					9.0		7.0		8.0		5.5		7.5		11.5	
	Average					9.3		7.5		7.8		5.8		7.7		10.8	

Table A 9 Contact angle and sliding angle measurements of coatings with different stir methods and spray times under high flow volume

Spray Time		Magnetic Stirrer + Homogeniser								Magnetic Stirrer							
		5		10		15		20		5		10		15		20	
Contact Angle (°)	1	167.7	164.2	166.5	162.6	166.3	163.1	164.0	160.8	157.0	156.8	163.7	163.7	167.2	164.9	163.4	167.2
	2	167.7	164.9	163.5	160.7	162.6	162.2	165.3	164.6	163.9	164.2	165.2	168.1	158.1	160.3	161.7	164.4
	3	165.9	167.0	162.2	160.1	163.1	161.0	166.2	170.4	162.8	163.5	162.8	166.1	161.1	162.8	165.0	164.5
	4	164.1	161.9	161.8	163.8	164.4	162.0	167.4	163.4	164.8	161.2	159.1	160.6	165.2	165.7	161.8	165.5
	5	162.1	166.7	162.7	164.8	163.5	160.6	167.7	164.3	159.6	153.9	159.3	163.5	159.0	160.3	159.0	160.3
	Average		165.2		162.9		162.9		165.4		160.8		163.2		162.5		163.3
Sliding Angle (°)	1	5.5		7.0		7.0		6.5		Did Not Slide	10.0		9.0		20.0		
	2	6.0		7.0		8.0		5.0			12.0		10.0		18.0		
	3	4.5		6.0		6.5		5.0			14.0		8.5		17.5		
	4	5.5		5.0		7.0		5.5			11.0		11.0		18.0		
	5	6.5		4.0		8.0		4.5			9.0		11.5		20.0		
	Average	5.6		5.8		7.3		5.3			11.2		10.0		18.7		

Table A 10 Contact angle and sliding angle measurements of coatings with different spray distance and spray times

Spray Distance (cm)		15								20							
Spray Time (s)		5		10		15		20		5		10		15		20	
Contact Angle (°)	1	162.7	163.2	165.5	163.6	167.5	165.4	168.7	162.7	168.8	167.7	165.4	163.2	166.6	165.3	169.7	167.0
	2	161.0	160.7	160.3	160.0	163.9	159.0	163.1	165.4	170.0	165.6	164.3	165.1	160.3	162.7	166.5	165.7
	3	160.7	164.5	161.6	165.1	162.2	165.2	160.3	158.9	169.5	169.4	163.1	163.3	166.2	166.8	169.0	168.5
	4	160.6	164.4	161.2	164.5	161.5	166.2	164.5	166.3	167.8	168.5	163.2	163.5	165.7	166.0	169.1	168.8
	5	164.1	166.5	162.0	165.0	160.0	162.1	164.3	160.2	168.5	167.3	162.0	161.9	166.2	168.8	168.3	168.7
	Average		162.8		162.9		163.3		163.4		168.3		163.5		165.5		168.1
Sliding Angle (°)	1	10.5		7.5		Did Not Slide		11.5		9.5		8.0		4.0		5.0	
	2	9.0		9.5				10.0		10.0		9.0		6.0		4.0	
	3	11.5		8.5				12.0		10.0		9.5		4.5		4.0	
	4	11.0		8.0				12.0		8.0		9.0		6.5		3.0	
	5	7.5		7.0				11.0		9.0		9.0		6.0		4.0	
	Average	9.9		8.1				11.3		9.3		8.9		5.4		4.0	

Table A 11 Contact angle and sliding angle measurements of coatings using homogeniser with 5000 and 7000 rpm stirring speed

Stir speed (rpm)		5000		7000	
Contact Angle (°)	1	165.4	165.1	166.4	164.5
	2	170.9	164.9	163.1	166.3
	3	171.8	169.8	172.6	167.7
	4	166.6	169.2	167.8	166.3
	5	170.7	168.1	164.4	165.3
	Average	168.3		166.4	
Sliding Angle (°)	1	5.0		5.0	
	2	5.5		6.0	
	3	4.5		5.5	
	4	5.0		6.5	
	5	5.5		7.0	
	Average	5.1		6.0	

Table A 12 Contact angle and sliding angle measurements of coatings with different spray times

Spray Time (s)		15		20		25		30	
Contact Angle (°)	1	171.7	166.0	170.7	169.3	166.3	163.5	167.2	172.8
	2	166.7	166.5	167.8	167.0	166.0	160.1	173.2	167.9
	3	171.8	173.6	171.3	167.9	172.1	165.1	164.1	168.2
	4	173.5	167.2	170.5	168.7	169.9	166.0	163.4	161.1
	5	167.5	172.4	170.8	168.6	167.4	165.9	167.5	164.7
	Average	169.7		169.3		166.2		167.0	
Sliding Angle (°)	1	6.5		5.0		8.0		8.5	
	2	6.0		4.5		7.5		9.0	
	3	6.5		5.0		7.0		9.5	
	4	6.5		4.0		7.5		10.0	
	5	5.0		5.0		8.5		10.0	
	Average	6.1		4.7		7.7		9.4	

Table A 13 Contact angle and sliding angle measurements of coatings with 20s of spray times (4×5s)

Sample		1		2		3		4		5		6	
Contact Angle (°)	1	166.4	162.3	165.8	166.6	166.8	165.1	171.9	162.7	171.4	166.3	166.3	165.6
	2	170.5	169.3	172.0	166.2	166.9	167.3	171.1	171.6	166.0	169.0	165.6	167.6
	3	169.5	170.7	164.1	165.1	165.4	163.7	168.2	169.6	167.0	164.9	163.1	164.2
	4	169.8	169.4	170.2	164.5	168.2	168.8	168.2	166.9	167.0	171.6	172.9	167.7
	5	166.9	168.6	170.0	166.5	167.4	168.0	168.9	169.9	168.8	168.3	168.1	169.8
	Average	168.3		167.1		166.8		168.9		168.0		167.1	
Sliding Angle (°)	1	3.0		4.0		3.0		4.0		4.5		4.0	
	2	3.0		4.5		3.5		3.5		2.5		2.5	
	3	4.0		3.5		4.5		4.5		3.5		5.0	
	4	4.0		4.0		4.0		5.0		4.0		3.0	
	5	5.0		3.0		4.0		4.0		3.0		5.0	
	Average	3.8		3.8		3.8		4.2		3.5		3.9	

Table A 14 Contact angle and sliding angle measurements before and after thermal ageing and thermal cycling

Thermal Ageing & Cycling		NeverWet								Laser Patterning	
		Sample 1		Sample 2		Sample 3		Sample 4			
Before Ageing	Contact Angle (°)	170.3	168.2	166.7	166.1	164.6	166.1	163.7	167.6	Could Not Be Measured	
		167.1	171.5	168.3	165.4	165.1	166.9	165.4	166.8		
		168.7	171.3	166.2	165.8	167.1	168.4	164.4	168.1		
	Average (°)	169.5		166.4		166.4		166.0			
	Sliding Angle (°)	1.0		2.0		1.5		2.5			
		1.5		1.5		2.5		1.5			
		2.0		2.0		1.5		1.5			
Average (°)	1.5		1.8		1.8		1.8				
Thermal Ageing	Contact Angle (°)	168.0	164.7	163.7	167.7	166.2	167.6	164.9	169.2	Could Not Be Measured	
		167.0	166.4	165.8	168.3	166.2	167.6	164.8	164.6		
		164.9	167.4	167.6	168.1	163.9	168.1	168.8	169.7		
	Average (°)	166.4		166.9		166.6		167.0			
	Sliding Angle (°)	1.5		2.5		1.5		1.5			
		1.0		2.5		1.0		1.5			
		2.0		1.5		2.0		2.0			
Average (°)	1.5		2.2		1.5		1.7				
Thermal Cycling Week 1	Contact Angle (°)	166.0	165.2	166.5	164.0	165.1	164.2	161.3	166.3	164.1	165.0
		161.6	168.1	165.6	168.0	161.2	164.9	162.3	167.0	165.3	163.9
		168.3	165.9	160.2	166.8	161.6	163.4	168.4	169.2	164.2	166.3
	Average (°)	165.9		165.2		163.4		165.8		164.8	

	Sliding Angle (°)	1.0		3.0		2.0		1.5		2.0	
		2.0		2.0		2.5		1.5		3.0	
		3.0		2.0		2.5		2.0		2.5	
	Average (°)	2.0		2.3		2.3		1.7		2.5	
Week 2	Contact Angle (°)	163.1	168.4	163.5	167.0	160.4	164.0	165.0	168.7	166.8	167.4
		164.3	169.3	163.2	167.1	159.3	164.7	166.9	166.4	162.9	167.8
		163.9	166.3	163.6	169.2	164.7	161.3	161.8	166.8	166.1	167.8
	Average (°)	165.9		165.6		162.4		165.9		166.5	
	Sliding Angle (°)	3.0		3.5		3.0		2.0		2.0	
		2.0		3.5		2.0		2.0		2.5	
		2.0		2.5		2.0		2.5		3.0	
Average (°)	2.3		3.2		2.3		2.2		2.5		
Week 3	Contact Angle (°)	161.4	162.1	165.5	168.1	159.2	162.3	162.6	163.6	165.6	166.5
		162.3	163.5	162.7	163.7	166.7	163.6	163.4	166.2	165.9	169.3
		162.7	165.8	164.3	167.3	160.2	160.3	159.3	165.1	163.8	163.8
	Average (°)	163.0		165.3		162.1		163.4		165.8	
	Sliding Angle (°)	3.0		3.0		4.5		2.0		3.0	
		3.5		3.5		6.0		3.0		3.0	
		3.0		3.5		4.0		5.0		2.5	
Average (°)	3.2		3.3		4.8		3.3		2.8		
Week 4	Contact Angle (°)	160.6	164.9	163.8	165.6	159.8	161.1	164.0	161.7	164.4	167.8
		161.7	165.2	161.6	164.9	163.3	165.2	158.8	163.2	163.4	166.9
		163.8	162.6	161.4	165.6	160.7	162.1	164.3	166.9	164.2	163.5

	Average (°)	163.1		163.8		162.0		163.2		165.0		
	Sliding Angle (°)	5.0		3.0		5.5		4.5		2.5		
		3.0		3.5		4.0		6.0		3.5		
		3.0		3.0		8.0		2.5		2.5		
	Average (°)	3.7		3.2		5.8		4.3		2.8		
Week 5	Contact Angle (°)	161.8	159.9	162.2	161.8	161.3	162.5	164.1	163.5	162.3	166.3	
		162.0	162.0	164.8	166.3	161.6	162.9	162.1	160.4	166.2	165.0	
		162.1	162.9	164.9	163.5	163.8	160.9	163.8	165.5	164.9	164.7	
		Average (°)	161.8		163.9		162.2		163.2		164.9	
	Sliding Angle (°)	4.0		5.5		5.5		3.0		2.5		
		3.0		5.5		4.0		4.5		3.0		
		5.0		4.5		8.5		6.5		2.5		
	Average (°)	4.0		5.2		6.0		4.7		2.7		
Week 6	Contact Angle (°)	163.3	165.1	161.0	161.7	159.0	162.6	158.7	159.9	165.5	164.0	
		158.9	161.3	164.2	166.1	160.8	162.2	160.5	162.4	163.7	166.4	
		160.3	161.5	163.6	165.4	159.7	162.9	162.4	163.5	165.3	166.2	
		Average (°)	161.7		163.7		161.2		161.2		165.2	
	Sliding Angle (°)	3.0		4.0		10.0		8.5		3.0		
		4.0		7.5		6.0		3.5		3.0		
		5.0		5.0		8.5		6.0		2.0		
	Average (°)	4.0		5.5		8.2		6.0		2.7		

Table A 15 Contact angle and sliding angle measurements before and after UV exposure

UV Exposure		Stearic Acid with SiO ₂								NeverWet							
		Sample 1		Sample 2		Sample 3		Sample 4		Sample 1		Sample 2		Sample 3		Sample 4	
Before Ageing	Contact Angle (°)	158.7	159.5	168.3	170.3	164.6	166.4	168.1	165.4	166.3	165.3	169.1	163.8	165.7	164.7	167.3	168.7
		160.3	162.8	162.7	160.3	166.8	166.7	165.9	167.9	163.1	167.1	166.0	168.0	169.4	168.5	163.4	164.1
		160.0	160.0	162.3	160.8	165.5	166.0	164.1	166.5	164.0	168.7	162.7	168.6	163.1	166.4	165.5	169.1
	Average (°)	160.2		164.1		166.0		166.3		165.8		166.4		166.3		166.4	
	Sliding Angle (°)	6.0		5.5		6.0		5.5		2.0		2.5		2.0		2.0	
		5.5		4.5		5.5		6.5		2.5		2.0		1.5		2.0	
		6.0		6.5		6.0		4.5		1.5		1.5		2.0		1.5	
Average (°)	5.8		5.5		5.8		5.5		2.0		2.0		1.8		1.8		
Week 1	Contact Angle (°)	161.8	161.9	162.5	163.3	164.4	162.4	161.1	164.7	164.5	163.9	163.6	165.3	162.7	165.8	164.4	163.4
		157.6	159.4	162.9	163.4	162.8	164.7	164.6	163.5	163.2	165.6	166.5	165.3	162.4	165.2	162.4	163.7
		160.7	160.5	164.5	165.4	162.0	162.2	161.0	163.9	161.1	164.3	164.7	164.6	164.7	164.2	163.3	162.6
	Average (°)	160.3		163.7		163.1		163.1		163.8		165.0		164.2		163.3	
	Sliding Angle (°)	7.0		8.0		7.5		8		2.0		1.5		2.0		2	
		6.0		7.5		8.5		8.5		2.5		2.0		1.5		2	
		8.0		8.5		9.0		8.5		2.0		2.5		2.5		2.0	
Average (°)	7.0		8.0		8.3		8.3		2.2		2.0		2.0		2.0		
Week 2	Contact Angle (°)	162.4	159.5	162.9	160.7	160.7	162.8	159.7	158.5	164.3	164.6	165.7	164.8	165.5	164.4	164.8	164.6
		158.4	161.1	163.1	164.3	164.4	162.8	159.4	160.9	163.9	164.7	165.2	163.4	161.3	163.8	162.5	162.9
		162.4	161.6	164.1	161.0	160.2	160.3	160.9	160.7	161.9	163.5	160.1	164.2	162.4	166.4	161.6	162.4
	Average (°)	160.9		162.7		161.9		160.0		163.8		163.9		164.0		163.1	

	Sliding Angle (°)	7.5		9.0		9.5		8		2.0		1.5		2.0		2.5	
		7.0		8.5		10.0		9		2.0		2.0		2.5		1.5	
		7.0		10.0		11.0		10.0		2.5		2.5		2.0		2.0	
	Average (°)	7.2		9.2		10.2		9.0		2.2		2.0		2.2		2.0	
Week 3	Contact Angle (°)	155.0	153.9	155.0	157.1	156.1	159.2	151.3	154.0	164.7	162.5	163.9	164.1	166.0	166.8	163.0	165.9
		156.6	155.0	157.6	156.0	155.8	158.0	159.2	158.4	162.4	165.0	162.5	163.9	163.7	162.8	161.9	164.7
		154.9	154.6	155.3	157.4	158.3	155.3	158.6	156.9	163.1	162.4	163.0	164.1	161.7	162.5	161.4	160.9
	Average (°)	155.0		156.4		157.1		156.4		163.4		163.6		163.9		163.0	
	Sliding Angle (°)	17.0		15.0		13.5		14		2.0		1.5		2.0		2.5	
		21.5		14.5		16.0		19.5		2.5		2.0		2.0		2	
20.0		17.0		16.5		20.0		1.5		2.5		2.5		1.5			
Average (°)	19.5		15.5		15.3		17.8		2.0		2.0		2.2		2.0		
Week 4	Contact Angle (°)	153.9	155.0	154.4	155.9	152.6	154.1	157.4	156.3	164.3	164.5	163.8	164.8	164.5	162.3	162.2	163.1
		154.6	153.6	154.9	156.3	155.7	157.1	152.4	154.0	163.6	162.8	161.6	162.5	163.3	164.0	162.5	162.8
		154.8	156.8	154.0	154.5	157.2	159.8	152.5	156.0	162.2	163.8	162.6	163.5	161.8	163.1	163.4	164.0
	Average (°)	154.8		155.0		156.1		154.8		163.5		163.1		163.2		163.0	
	Sliding Angle (°)	19.0		22.5		17.5		25.5		2.5		2.0		2.5		2	
		25.0		19.5		16.0		26		2.0		2.5		2.5		1.5	
26.5		18.5		22.0		27.5		2.0		2.0		2.0		2.5			
Average (°)	23.5		20.2		18.5		26.3		2.2		2.2		2.3		2.0		

Table A 16 Contact angle and sliding angle measurements of stearic acid with SiO₂ coating before and after outdoor exposure

Outdoor Exposure		Stearic Acid with SiO ₂							
		Sample 1		Sample 2		Sample 3		Sample 4	
Before Ageing	Contact Angle (°)	165.1	162.2	162.5	166.6	165.0	165.5	166.1	163.4
		165.2	164.9	162.8	161.6	165.7	162.7	160.8	164.0
		161.4	162.4	163.8	160.4	166.4	160.2	165.4	162.0
	Average (°)	163.5		163.0		164.3		163.6	
	Sliding Angle (°)	6.5		6.0		5.0		6.0	
		6.0		7.0		7.0		7.0	
		6.5		5.5		6.0		5.5	
Average (°)	6.3		6.2		6.0		6.2		
Week 1	Contact Angle (°)	160.3	159.9	158.6	161.5	159.1	159.6	160.4	161.9
		161.2	160.0	161.9	161.6	160.9	161.6	159.8	158.7
		161.6	158.3	159.8	159.8	162.6	160.6	162.5	162.1
	Average (°)	160.2		160.5		160.7		160.9	
	Sliding Angle (°)	34.0		28.0		30.5		26.5	
		33.0		31.0		25.0		30	
		31.5		30.5		29.5		29.0	
Average (°)	32.8		29.8		28.3		28.5		
Week 2	Contact Angle (°)	157.1	157.3	162.2	158.6	159.5	162.1	160.3	161.6
		159.3	159.9	159.8	161.4	158.4	160.0	157.0	161.0
		159.2	159.3	159.0	162.2	162.7	160.6	159.8	162.4
	Average (°)	158.7		160.5		160.6		160.4	

	Sliding Angle (°)	32.0		27.0		32.5		32	
		35.5		32.0		26.0		29.5	
		27.5		30.5		29.5		28.0	
	Average (°)	31.7		29.8		29.3		29.8	
Week 3	Contact Angle (°)	155.6	157.1	155.3	158.6	161.6	160.3	159.3	157.9
		161.2	161.1	158.3	160.1	158.5	159.4	156.6	160.7
		158.0	158.4	160.4	157.4	157.6	156.6	160.5	161.2
	Average (°)	158.6		158.4		159.0		159.4	
	Sliding Angle (°)	28.5		26.5		26.0		26.5	
		34.5		31.0		29.5		32	
33.0		33.0		33.5		31.5			
Average (°)	32.0		30.2		29.7		30.0		
Week 4	Contact Angle (°)	158.0	157.2	153.8	156.9	159.2	158.4	157.4	158.1
		159.1	160.3	159.5	157.6	158.5	156.2	158.1	156.5
		157.6	158.5	157.0	159.3	157.5	158.9	154.1	156.7
	Average (°)	158.5		157.4		158.1		156.8	
	Sliding Angle (°)	34.0		31.0		33.5		34	
		35.0		34.5		26.5		26.5	
		27.5		26.0		29.5		31.0	
Average (°)	32.2		30.5		29.8		30.5		

Table A 17 Contact angle and sliding angle measurements of NeverWet coating and laser patterning before and after outdoor exposure

Outdoor Exposure		NeverWet								Laser Patterning			
		Sample 1		Sample 2		Sample 3		Sample 4		Sample 1	Sample 2	Sample 3	Sample 4
Before	Contact Angle (°)	167.8	163.3	165.6	162.0	167.7	166.8	163.5	167.6	Could Not Be Measured			
		167.5	165.1	167.0	165.3	167.1	166.9	165.3	167.4				
		164.9	166.5	166.4	164.6	167.4	164.3	168.7	168.3				
	Average (°)	165.9		165.2		166.7		166.8					
	Sliding Angle (°)	2.5		3.0		1.5		2.5					
		3.0		2.5		2.5		2.5					
		1.5		2.0		1.0		3.0					
Average (°)	2.3		2.5		1.7		2.7						
Week 1	Contact Angle (°)	164.5	165.4	163.7	164.9	164.4	163.9	165.3	162.5	Could Not Be Measured			
		163.9	167.8	165.1	167.9	163.8	165.8	167.9	165.9				
		161.3	162.3	162.6	164.3	163.9	166.2	166.0	167.7				
	Average (°)	164.2		164.8		164.7		165.9					
	Sliding Angle (°)	2.0		2.5		2.0		3					
		2.5		2.5		1.5		2.5					
		2.5		2.0		2.0		2.5					
Average (°)	2.3		2.3		1.8		2.7						
Week 2	Contact Angle (°)	165.2	165.2	161.8	163.0	164.5	162.1	164.2	162.2	Could Not Be Measured			
		164.3	163.2	164.7	166.1	166.3	163.1	163.4	167.9				
		163.9	163.3	163.8	164.0	163.9	164.7	164.6	162.7				

	Average (°)	164.2	163.9	164.1	164.2					
	Sliding Angle (°)	1.5	2.0	1.5	3					
		2.5	2.5	2.0	2.5					
		3.0	2.5	1.5	3.0					
	Average (°)	2.3	2.3	1.7	2.8					
Week 3	Contact Angle (°)	163.1	162.2	166.8	167.0	162.6	164.9	165.1	164.3	Could Not Be Measured
		164.2	164.0	161.9	163.4	161.4	162.7	162.9	164.5	
		164.7	164.3	162.2	161.1	165.6	165.1	162.8	164.4	
	Average (°)	163.8	163.7	163.7	164.0					
	Sliding Angle (°)	2.5	2.0	2.0	2.5					
		3.0	2.5	1.5	3					
		2.0	2.0	2.0	2.5					
Average (°)	2.5	2.2	1.8	2.7						
Week 4	Contact Angle (°)	163.3	164.4	162.1	164.3	162.4	162.2	164.5	164.4	Could Not Be Measured
		163.2	162.5	163.5	165.7	163.1	163.6	162.8	163.0	
		163.7	163.8	162.5	163.7	164.0	164.4	162.8	163.5	
	Average (°)	163.5	163.6	163.3	163.5					
	Sliding Angle (°)	2.0	2.0	2.0	3					
		3.0	2.5	2.0	3					
		2.5	2.5	1.5	2.5					
Average (°)	2.5	2.3	1.8	2.8						
Week 6	Contact Angle (°)	164.0	165.4	165.3	163.7	163.7	163.9	162.3	163.4	Could Not Be Measured
		161.7	163.3	164.0	162.4	163.2	162.6	163.4	163.8	
		162.0	163.9	162.2	163.9	163.2	163.7	163.6	162.5	

	Average (°)	163.4	163.6	163.4	163.2					
	Sliding Angle (°)	2.5	2.0	2.0	3.5					
		2.0	3.0	2.5	2.5					
		3.0	2.0	1.5	3.0					
	Average (°)	2.5	2.3	2.0	3.0					
Week 8	Contact Angle (°)	164.4	163.9	163.4	161.4	164.0	164.1	162.0	162.5	Could Not Be Measured
		163.3	163.5	162.8	163.8	162.9	162.1	163.7	164.0	
		162.1	163.0	164.4	164.5	162.4	164.4	163.7	163.3	
	Average (°)	163.4	163.4	163.3	163.2					
	Sliding Angle (°)	2.5	2.0	2.0	3					
		3.0	2.5	2.5	3.5					
		2.0	2.5	2.0	2.5					
Average (°)	2.5	2.3	2.2	3.0						
Week 10	Contact Angle (°)	161.1	164.3	162.2	163.1	163.8	163.6	162.9	163.3	Could Not Be Measured
		163.2	165.0	164.0	163.2	160.7	163.1	163.3	163.0	
		160.1	163.7	163.0	162.2	163.2	163.0	161.5	163.2	
	Average (°)	162.9	163.0	162.9	162.9					
	Sliding Angle (°)	2.0	2.0	1.5	2.5					
		3.5	2.5	3.0	4					
		2.0	3.0	2.0	2.5					
Average (°)	2.5	2.5	2.2	3.0						
Week 12	Contact Angle (°)	162.6	160.6	161.5	161.4	161.8	162.2	164.0	164.4	Could Not Be Measured
		164.1	164.0	163.9	162.9	162.8	162.8	161.5	163.5	
		163.1	163.2	162.5	162.7	161.5	164.2	160.7	161.9	

	Average (°)	162.9	162.5	162.6	162.7												
	Sliding Angle (°)	2.5	2.0	2.0	2.5												
		2.0	3.0	2.5	3												
		3.5	2.5	2.0	3.5												
	Average (°)	2.7	2.5	2.2	3.0												
Week 16	Contact Angle (°)	161.7	162.5	163.0	161.3	163.3	161.9	163.6	162.3	163.1	164.2	166.7	164.6	164.1	164.6	166.1	165.8
		164.1	162.5	162.6	162.8	161.4	162.9	162.9	161.3	166.3	165.6	165.4	165.1	164.6	164.0	165.4	166.2
		162.4	163.5	162.9	162.4	162.0	162.2	162.7	163.2	166.2	164.9	165.1	165.4	164.4	163.5	166.2	165.5
	Average (°)	162.8	162.5	162.3	162.7	165.1	165.4	164.2	165.9								
	Sliding Angle (°)	2.5	2.5	1.5	3	2.0	1.0	3.0	1.5								
		2.5	3.0	2.5	3.5	1.5	1.0	3.5	1.5								
		3.0	2.5	3.0	2.5	2.0	1.5	2.0	1.5								
Average (°)	2.7	2.7	2.3	3.0	1.8	1.2	2.8	1.5									
Week 20	Contact Angle (°)	162.8	160.2	161.8	162.0	163.1	161.3	163.4	161.0	166.0	166.4	165.0	165.1	164.1	164.6	166.8	167.3
		161.6	161.0	163.0	162.3	161.7	161.1	161.5	161.4	163.0	165.7	163.0	164.3	165.4	164.3	163.9	165.6
		163.3	164.0	162.9	161.5	162.7	163.2	162.1	162.7	162.9	164.5	165.6	165.6	162.5	162.2	163.8	164.3
	Average (°)	162.2	162.3	162.2	162.0	164.8	164.8	163.9	165.3								
	Sliding Angle (°)	2.5	4.0	2.0	3	2.5	2.5	2.0	2								
		3.0	3.0	3.5	4	2.5	2.0	3.5	1.5								
		3.5	3.0	2.0	5.0	2.0	2.0	2.5	2.0								
Average (°)	3.0	3.3	2.5	4.0	2.3	2.2	2.7	1.8									
Week 24	Contact Angle (°)	163.0	160.9	161.8	162.8	162.8	163.2	161.9	160.9	164.3	165.6	163.0	165.3	163.8	163.2	163.0	165.5
		162.1	162.5	161.0	162.3	162.4	162.0	162.7	161.7	163.9	163.4	164.6	164.1	163.4	164.8	165.1	165.4
		162.5	162.3	163.0	162.8	161.0	161.4	162.0	162.4	165.1	162.9	164.0	163.6	162.4	165.2	165.4	164.1

	Average (°)	162.2	162.3	162.1	161.9	164.2	164.1	163.8	164.8									
	Sliding Angle (°)	3.5	3.5	3.0	3.5	3.5	3.0	3.5	2.5									
		3.0	3.0	2.5	4	3.5	3.5	3.0	2.5									
		3.0	4.5	3.0	5.0	3.0	3.5	3.0	2.0									
	Average (°)	3.2	3.7	2.8	4.2	3.3	3.3	3.2	2.3									
Week 28	Contact Angle (°)	158.8	161.8	161.5	163.6	162.7	161.7	163.0	162.2	162.5	163.7	162.8	162.7	163.0	162.4	163.3	164.1	
		165.0	164.0	161.2	161.6	160.0	163.0	161.2	162.0	164.4	164.2	165.0	163.2	164.2	164.5	163.2	164.4	
		161.7	161.3	161.2	163.8	161.8	163.5	161.8	161.5	164.1	163.1	165.5	164.4	162.6	163.9	163.4	164.7	
		Average (°)	162.1	162.2	162.1	162.0	163.7	163.9	163.4	163.9								
		Sliding Angle (°)	3.0	3.5	3.0	3.5	3.5	4.0	3.5	3								
			3.0	3.5	3.0	4	4.0	3.0	3.0	3								
			3.5	4.0	3.5	5.0	3.5	3.5	3.5	3.0								
	Average (°)	3.2	3.7	3.2	4.2	3.7	3.5	3.3	3.0									
Week 32	Contact Angle (°)	162.5	161.5	164.5	162.6	162.7	163.0	161.8	164.5	163.6	164.2	163.2	164.6	163.0	163.3	163.0	162.9	
		162.8	161.9	161.5	160.4	160.7	162.8	160.0	161.7	162.7	163.5	164.1	163.3	163.0	163.5	163.7	164.0	
		162.1	161.7	161.0	162.3	161.4	162.0	159.5	161.0	163.0	164.0	162.6	163.6	163.0	164.1	164.1	163.7	
		Average (°)	162.1	162.1	162.1	161.4	163.5	163.6	163.3	163.6								
		Sliding Angle (°)	3.0	3.5	3.5	5	5.0	3.5	4.0	3.5								
			3.0	3.5	4.0	3.5	4.0	4.0	4.0	5.0	4							
			3.5	4.0	3.0	4.5	5.5	5.0	5.0	4.0								
	Average (°)	3.2	3.7	3.5	4.3	4.8	4.2	4.7	3.8									
Week 36	Contact Angle (°)	160.2	161.1	157.5	157.8	159.4	160.1	160.1	159.0	163.8	162.0	163.6	163.5	162.9	161.9	162.7	162.4	
		157.6	157.5	158.8	161.7	157.6	158.1	160.8	159.7	163.3	162.9	163.3	162.6	163.8	161.3	163.5	164.0	
		159.6	160.3	160.9	160.9	160.8	160.8	161.5	161.9	163.0	162.0	162.5	163.3	163.7	163.8	162.6	163.0	

	Average (°)	159.4	159.6	159.5	160.5	162.8	163.1	162.9	163.0									
	Sliding Angle (°)	7.0	6.0	7.0	7	5.0	4.5	4.5	4									
		6.0	6.5	5.0	6	5.0	5.0	4.5	4									
		5.5	5.5	6.0	6.0	4.5	5.0	5.0	4.0									
	Average (°)	6.2	6.0	6.0	6.3	4.8	4.8	4.7	4.0									
Week 40	Contact Angle (°)	161.0	160.5	158.2	159.3	159.0	158.8	160.5	159.6	162.6	162.6	162.2	162.5	163.0	162.8	162.7	162.2	
		157.7	157.0	161.5	159.9	159.0	159.4	161.1	159.4	163.0	162.9	163.2	162.6	162.8	162.5	162.5	162.3	
		159.5	158.8	158.2	159.3	160.3	159.6	158.2	160.0	162.3	162.1	163.4	163.1	162.9	162.5	162.9	163.6	
		Average (°)	159.1	159.4	159.4	159.8	162.6	162.8	162.8	162.7								
		Sliding Angle (°)	9.0	9.5	8.5	8.5	4.0	4.5	4.5	4.5								
			9.5	10.0	10.0	9	5.5	5.0	5.0	4								
			8.0	9.5	9.5	8.5	5.0	5.0	5.0	4.0								
	Average (°)	8.8	9.7	9.3	8.7	4.8	4.8	4.8	4.2									
Week 44	Contact Angle (°)	161.0	160.8	157.3	157.0	159.3	160.2	160.6	158.9	162.7	163.4	162.4	162.8	163.2	161.9	162.2	162.3	
		155.5	156.5	159.1	159.0	158.8	159.4	158.6	159.0	163.6	161.4	162.1	161.8	161.3	161.8	162.5	161.8	
		160.5	159.9	159.5	160.5	157.3	160.7	160.4	160.6	161.3	161.3	161.5	161.3	160.9	162.1	162.1	161.7	
		Average (°)	159.0	158.7	159.3	159.7	162.3	162.0	161.9	162.1								
		Sliding Angle (°)	12.0	11.5	10.0	10.5	6.0	6.0	6.0	5.5								
			11.0	12.0	12.0	11	5.0	6.5	6.0	5								
			12.0	11.0	11.0	10.0	6.0	6.0	6.5	5.5								
	Average (°)	11.7	11.5	11.0	10.5	5.7	6.2	6.2	5.3									
Week 48	Contact Angle (°)	159.6	160.0	158.1	158.1	158.7	158.5	158.6	158.6	160.0	160.8	162.1	162.5	160.7	161.7	162.4	161.8	
		158.0	158.3	157.0	158.5	158.0	158.4	158.7	159.6	163.0	162.6	160.5	162.0	162.5	161.9	161.4	161.6	
		159.5	157.9	156.1	158.4	158.8	157.9	157.2	158.8	160.8	161.0	160.9	162.6	162.4	160.6	161.8	162.5	

	Average (°)	158.9	157.7	158.4	158.6	161.4	161.8	161.6	161.9								
	Sliding Angle (°)	11.5	12.0	12.0	10	6.0	6.0	6.5	6								
		12.0	12.0	12.5	11	6.0	6.5	6.0	5.5								
		12.0	12.5	12.0	11.5	6.5	6.0	6.5	5.5								
	Average (°)	11.8	12.2	12.2	10.8	6.2	6.2	6.3	5.7								
Week 52	Contact Angle (°)	158.3	159.2	159.6	159.5	158.4	157.1	155.5	157.5	161.0	161.8	161.3	161.5	161.1	162.0	161.3	160.6
		159.0	158.1	157.9	157.3	157.6	157.6	159.6	160.0	161.1	161.4	161.0	161.0	160.9	160.5	160.9	162.0
		158.8	158.8	155.9	155.6	159.0	155.8	156.6	157.7	161.2	161.2	161.4	161.8	159.8	160.0	162.0	162.5
		Average (°)	158.7	157.6	157.6	157.8	161.3	161.3	160.7	161.6							
	Sliding Angle (°)	13.5	14.0	13.0	12.5	7.0	8.0	7.5	6								
		12.5	14.0	13.0	13	8.0	7.0	8.0	6								
		13.5	14.5	14.0	13.0	6.5	7.5	7.5	7.0								
	Average (°)	13.2	14.2	13.3	12.8	7.2	7.5	7.7	6.3								

Table A 18 Contact angle hysteresis (CAH) measurements of laser patterning before and after outdoor exposure

Outdoor Exposure	Contact Angle Hysteresis (CAH) of Laser Patterning							
	Sample 1		Sample 2		Sample 3		Sample 4	
	Advancing Angle	Receiving Angle	Advancing Angle	Receiving Angle	Advancing Angle	Receiving Angle	Advancing Angle	Receiving Angle
Before Ageing	169.1	168.9	169.2	168.9	169.0	168.9	169.1	168.7
	169.0	168.6	168.0	167.3	168.2	168.0	168.5	168.1
	169.2	168.9	169.8	169.8	168.8	168.1	168.7	168.5
Average CAH (°)	0.3		0.3		0.3		0.3	
Week 1	168.9	168.7	167.9	167.3	168.7	168.4	167.9	167.3
	168.2	167.6	168.4	168.0	168.3	168.0	168.3	168.0
	168.8	168.3	168.5	167.9	167.8	167.2	168.3	167.9
Average CAH (°)	0.4		0.5		0.4		0.4	
Week 2	165.5	165.4	164.6	164.2	166.1	166.1	166.0	164.9
	164.4	163.7	166.2	165.5	166.2	165.3	165.2	165.1
	165.8	165.2	166.1	165.5	166.0	164.9	165.7	164.9
Average CAH (°)	0.5		0.6		0.7		0.7	
Week 3	165.9	165.4	166.2	165.9	166.5	165.2	165.7	165.2
	166.0	164.7	166.5	166.3	166.1	165.9	165.8	165.0
	164.7	164.6	165.9	164.7	166.6	166.0	166.2	165.3
Average CAH (°)	0.6		0.6		0.7		0.7	
Week 4	167.8	167.1	164.5	163.5	167.5	167.0	165.8	164.9
	167.5	166.0	165.3	164.5	165.8	165.5	166.1	164.8

	166.9	166.6	166.0	165.5	166.6	165.6	166.0	165.5
Average CAH (°)	0.8		0.8		0.6		0.9	
Week 6	165.9	164.8	166.5	165.9	166.5	166.2	167.6	166.9
	165.7	164.9	168.3	167.2	165.8	165.1	168.1	167.2
	166.8	166.0	166.5	165.5	168.6	167.1	167.2	166.0
Average CAH (°)	0.9		0.9		0.8		0.9	
Week 8	167.5	166.6	167.2	166.5	165.9	165.3	166.0	165.1
	167.6	165.8	164.9	164.0	165.5	163.9	166.5	165.0
	168.5	167.9	166.3	165.2	165.5	164.9	165.2	164.5
Average CAH (°)	1.1		0.9		0.9		1.0	
Week 10	166.9	166.2	166.2	164.7	166.1	164.9	164.6	164.0
	166.7	165.5	166.0	165.5	166.1	165.4	165.9	164.1
	164.9	163.1	165.3	164.2	166.1	164.8	165.2	163.9
Average CAH (°)	1.2		1.0		1.1		1.2	
Week 12	166.2	164.8	166.6	165.4	167.7	167.3	167.0	166.1
	167.6	166.4	167.0	165.3	169.0	167.3	167.6	166.0
	167.4	166.0	165.6	164.2	168.9	167.5	166.3	164.8
Average CAH (°)	1.3		1.4		1.2		1.3	
Week 16	166.9	165.2	166.0	165.0	166.5	164.9	162.4	160.7
	165.9	164.6	164.6	163.5	165.9	163.6	164.5	162.6
	164.2	161.4	166.0	163.7	165.2	164.9	163.7	161.9
Average CAH (°)	1.9		1.5		1.4		1.8	
Week 20	165.0	160.5	165.0	161.9	166.0	162.9	167.0	164.0
	164.7	160.4	168.5	166.5	168.0	162.9	166.6	164.6

	163.3	159.4	168.0	164.9	165.7	162.8	166.8	163.4
Average CAH (°)	4.2		2.7		3.7		2.8	
Week 24	165.0	157.8	165.2	161.2	164.5	160.5	165.4	159.3
	166.3	160.8	163.7	159.6	164.6	159.5	163.8	159.2
	163.8	158.7	166.2	159.6	166.3	159.3	165.2	160.9
Average CAH (°)	5.9		4.9		5.4		5.0	
Week 28	166.9	160.7	166.3	162.7	162.1	156.9	163.7	157.7
	164.9	156.9	164.5	158.3	164.1	160.3	164.5	158.8
	164.0	158.0	165.0	157.2	163.6	155.1	164.5	157.8
Average CAH (°)	6.7		5.9		5.8		6.1	
Week 32	163.6	159.2	162.1	157.3	163.9	158.0	163.8	159.6
	164.6	155.1	164.5	156.1	164.3	157.5	165.5	158.3
	164.7	156.0	161.8	151.5	164.0	158.8	164.8	157.7
Average CAH (°)	7.5		7.8		6.0		6.2	
Week 36	165.7	157.2	166.6	159.8	162.7	154.0	163.9	157.6
	165.8	158.4	164.9	156.5	165.1	157.6	164.4	156.6
	166.7	159.0	164.5	155.9	164.0	157.9	166.6	159.0
Average CAH (°)	7.9		7.9		7.4		7.2	
Week 40	166.3	154.9	164.8	158.4	164.4	155.4	165.0	156.0
	163.6	157.4	164.2	154.9	164.0	156.4	164.0	157.0
	162.0	155.7	165.4	156.3	164.2	157.0	165.1	157.3
Average CAH (°)	8.0		8.3		7.9		7.9	
Week 44	162.0	153.3	164.0	155.0	160.0	152.6	162.2	152.5
	163.6	155.3	163.0	154.0	161.1	151.3	162.0	156.0

	164.2	156.0	163.4	156.0	161.0	152.0	160.6	151.8
Average CAH (°)	8.4		8.5		8.7		8.2	
Week 48	160.0	151.9	162.2	151.2	160.3	151.8	161.8	152.6
	161.0	149.6	160.5	155.3	159.5	151.0	159.4	150.6
	161.9	154.6	159.9	150.4	160.5	149.6	162.2	154.8
Average CAH (°)	8.9		8.6		9.3		8.5	
Week 52	165.0	157.0	161.7	152.6	159.3	151.6	163.0	151.0
	164.6	156.5	161.4	152.9	161.0	151.3	163.5	156.8
	163.9	153.0	163.5	154.9	160.0	149.0	162.9	155.9
Average CAH (°)	9.0		8.7		9.5		8.6	

Table A 19 Sag and %RTS of different conductors under different ice accretion thickness with or without wind load

Ice Thickness (mm)	Sag (m)						RTS (%)					
	AAAC Araucaria		AAAC Oak		ACCC Madrid		AAAC Araucaria		AAAC Oak		ACCC Madrid	
	Ice Only	Ice + Wind	Ice Only	Ice + Wind	Ice Only	Ice + Wind	Ice Only	Ice + Wind	Ice Only	Ice + Wind	Ice Only	Ice + Wind
0	5.2	5.9	0.5	1.1	7.2	7.9	22.5	27.1	25.8	30.7	20.7	23.4
5	5.7	6.5	0.8	1.6	7.8	8.6	25.9	31.2	28.1	37.2	23.1	26.4
10	6.3	7.1	1.2	1.9	8.5	9.4	29.8	35.6	32.4	44.2	25.8	29.4
15	6.9	7.6	1.6	2.3	9.2	10.1	34.1	40.1	38.3	51.2	28.8	32.6
20	7.4	8.2	2.0	2.6	10.0	11.0	38.7	44.8	45.2	58.6	32.0	35.7
25	8.0	8.7	2.3	2.9	10.8	11.9	43.5	49.6	52.9	66.1	35.2	38.5
30	8.6	9.3	2.7	3.2	11.8	12.9	48.6	54.6	61.1	73.8	38.2	41.5
35	9.2	9.8	3.0	3.5	12.8	13.8	53.6	59.7	69.6	81.6	41.3	44.6
40	9.8	10.4	3.3	3.8	13.8	14.7	59.2	64.8	78.2	89.5	44.5	47.9
45	10.4	11.0	3.7	4.0	14.7	15.6	64.7	70.0	86.9	97.8	48.0	51.3
50	11.0	11.6	4.0	4.3	15.6	16.4	70.1	75.2	95.8	106.4	51.5	54.9
55	11.6	12.2	4.3	4.6	16.5	17.3	75.5	80.2	105.1	115.5	55.3	58.6
60	12.3	12.9	4.6	4.9	17.4	18.1	80.8	85.2	114.7	124.9	59.2	62.5
65	13.0	13.5	4.9	5.1	18.3	19.0	86.0	90.3	124.7	134.6	63.2	66.4
70	13.7	14.2	5.2	5.4	19.2	19.8	91.3	95.5	135.1	144.7	67.4	70.6
75	14.4	14.8	5.4	5.7	20.0	20.6	96.8	100.9	145.7	155.1	71.6	74.8
80	15.0	15.5	5.7	5.9	20.8	21.4	102.4	106.5	156.6	165.7	76.0	79.1